MADE-TO-MEASURE DYNAMICAL PARTICLE MODELS OF ELLIPTICAL GALAXIES

Inauguraldissertation

zur
Erlangung der Würde eines Doktors der Philosophie
vorgelegt der
Philosophisch-Naturwissenschaftlichen Fakultät
der Universität Basel

von

Flavio De Lorenzi

aus Schaffhausen

Basel, 2007

CONTENTS

1 Introduction **1**
- 1.1 The aim of the present work . . . 1
- 1.2 Evolution of a collisionless system . . . 1
- 1.3 Dynamical modeling of elliptical galaxies . . . 3
- 1.4 N-particle simulations . . . 4
- 1.5 General properties of elliptical galaxies . . . 5
- 1.6 Cosmological context . . . 6
- 1.7 Measuring the kinematics of elliptical galaxies . . . 7
- 1.8 Evidence for dark matter in elliptical galaxies . . . 9
- 1.9 Outline . . . 10

2 NMAGIC: A χ^2-Made-To-Measure Algorithm **11**
- 2.1 Introduction . . . 11
- 2.2 Syer & Tremaine's Made-To-Measure Algorithm . . . 12
- 2.3 χ^2-based Made-to-Measure Algorithm . . . 14
- 2.4 Densities . . . 15
- 2.5 Kinematics . . . 16
- 2.6 Implementation: the NMAGIC parallel code . . . 17
- 2.7 Target Models and Their Observables . . . 21
  - 2.7.1 Spherical Target . . . 21
  - 2.7.2 An Oblate Three-Integral Target made with NMAGIC . . . 23
  - 2.7.3 Making Triaxial Models with NMAGIC . . . 25
- 2.8 Tests of NMAGIC . . . 27
  - 2.8.1 Spherical Models . . . 27
  - 2.8.2 Oblate Models . . . 35
  - 2.8.3 Triaxial Models . . . 41
- 2.9 Conclusions . . . 42

3 NMAGIC models of NGC 4697 **47**
- 3.1 Introduction . . . 47
- 3.2 Observational Data . . . 49
  - 3.2.1 Surface Photometry . . . 49
  - 3.2.2 Deprojection . . . 50
  - 3.2.3 Kinematic Data . . . 51
- 3.3 NMAGIC models . . . 54
  - 3.3.1 Luminous and dark matter distribution . . . 54
  - 3.3.2 Model observables . . . 56
  - 3.3.3 Seeing effects . . . 57
  - 3.3.4 The merit function . . . 59
  - 3.3.5 Discrete PNe velocities . . . 59
  - 3.3.6 Efficient mass-to-light estimate . . . 60

3.3.7 Initial conditions . . . 61
3.4 Testing the modelling with isotropic rotator targets . . . 61
3.4.1 Entropy parameter μ . . . 61
3.4.2 Mass-to-light ratio . . . 66
3.5 Dynamical models of NGC 4697 . . . 67
3.6 Summary and Conclusions . . . 72

4 NMAGIC models of NGC 3379 77
4.1 Introduction . . . 77
4.2 Observational Data . . . 79
4.2.1 Photometric Data . . . 79
4.2.2 Deprojection . . . 79
4.2.3 Kinematic Data . . . 81
4.3 NMAGIC modelling . . . 85
4.3.1 Luminous and dark mass distributions . . . 85
4.3.2 Model and target observables . . . 86
4.3.3 Fitting a particle model to the observations . . . 87
4.3.4 Isotropic γ-model . . . 87
4.4 Dynamical models of NGC 3379 . . . 92
4.4.1 Spherical models . . . 94
4.4.2 Oblate models including dark matter halos . . . 100
4.4.3 Models without axisymmetry constraint . . . 106
4.4.4 Likelihoods and quality of the fits to the data . . . 107
4.5 Summary and conclusions . . . 111

5 Summary and outlook 113
5.1 Summary . . . 113
5.2 Outlook . . . 115
5.2.1 Technical improvements . . . 115
5.2.2 Future applications . . . 117

A Some technical details 119
A.1 Potential solver . . . 119
A.2 Initial conditions . . . 121
A.3 Integration scheme . . . 124
A.4 Parallelization . . . 125

B Photometric and kinematic data of NGC 4697 127
B.1 Photometric and kinematic data . . . 128

C Abbreviations 135

Bibliography 137

List of Figures 149

List of Tables 151

Acknowledgments 153

CHAPTER 1

INTRODUCTION

1.1 The aim of the present work

The first main goal of this thesis is to develop and test a new way of modelling galaxies, based on the original ideas of Syer and Tremaine (1996). This method is new in the sense that a N-particle system is tailored to reproduce galaxy observations, rather than superposing orbits as done in Schwarzschild's method. The new χ^2-made-to-measure (χ^2M2M) algorithm properly accounts for observational errors, is flexible, and can be applied to various systems and geometries. The χ^2M2M is implemented in a parallel code NMAGIC and various tests using known dynamical models are carried out to illustrate its performance.

The second goal of this thesis is to apply NMAGIC to real galaxies and to investigate the issue of dark matter in the intermediate luminosity elliptical galaxies NGC 4697 and NGC 3379. These two galaxies are particularly interesting because recent studies (Méndez et al., 2001; Douglas et al., 2007) revealed a dearth of dark matter in these systems, which conflicts with the prevailing cosmological paradigm.

1.2 Evolution of a collisionless system

The evolution of a stellar system, where the stars can be considered as point masses, is determined by the mutual gravitational forces of the stars. The collision rate of a star in a stellar system with equal mass stars and a constant total mass is inversely proportional to the total number of stars. This can be understood as follows: If the total number of stars is doubled, then also the number of encounters is doubled, but the strength of a single scattering event is reduced by a factor of four, since the mass of each star is halved and the gravitational force is proportional to the square of the mass. One can show that for galaxies, which typically have $N \approx 10^{11}$ stars, encounters are unimportant. Hence, galaxies can be considered as collisionless systems (*e.g.* Binney and Tremaine, 1987) and the motions of the stars are governed by the smooth gravitational potential, generated by the entire system.

The collisionless Boltzmann equation

A collisionless stellar system can be described by its phase-space distribution function (DF) $f(\mathbf{x}, \mathbf{v}, t)$, which gives the density of stars in the six-dimensional phase space of $\mathbf{x}, \mathbf{v}$ and is positive everywhere. For example, the surface brightness μ and the mean line-of-sight velocity v_{los} are then given by integrals:

$$\mu = \int f \mathrm{d}^3 v \mathrm{d}z, \qquad v_{los} = \frac{1}{\mu} \int v_z f \mathrm{d}^3 v \mathrm{d}z, \tag{1.1}$$

where the line-of-sight is assumed along the z-direction.

The evolution of the DF under the influence of the total gravitational potential ϕ, is determined by the collisionless Boltzmann equation (CBE) (*cf.* Binney and Tremaine, 1987):

$$\frac{\partial f}{\partial t} + \mathbf{v} \cdot \nabla f - \nabla\phi \cdot \frac{\partial f}{\partial \mathbf{v}} = 0, \tag{1.2}$$

which follows from the conservation of stars in phase-space. The CBE states that the phase-space flow is incompressible. The total gravitational potential $\phi(\mathbf{x}, t)$ is generated by the combined stellar mass and dark matter distributions and is given by

$$\phi = \phi_\star + \phi_{DM}, \tag{1.3}$$

where the stellar potential $\phi_\star$ is related to the DF via Poisson's equation

$$\Delta\phi_\star = 4\pi G\rho_\star, \tag{1.4}$$

with the volume density

$$\rho_\star = \int f \mathrm{d}^3 v. \tag{1.5}$$

The Poisson's equation together with the CBE are the fundamental equations in stellar dynamics. Once a solution of these equations has been found, all the interesting information about the system can be extracted as illustrated in equations (1.1).

In stellar dynamics, the CBE is typically solved like an initial value problem: An initially specified system of particles, representing the initial $f(\mathbf{x}, \mathbf{v}, t_0)$, is integrated in a smooth gravitational potential to study the evolution of the system and to possibly compare the final model with observations. For example, Fux (1997) realized various models of the Galaxy by self-consistent evolution of bar unstable models and compared them posterior with observations of the Milky Way.

Moment Equations

Generally, to solve the CBE poses a difficult problem. Valuable insight can be obtained by considering velocity moments of the CBE. This results in a hierarchy of equations, beginning with the continuity equation, followed by the higher order ones. Combining the continuity equation and the second moment equation yields the *Jeans equations*, which are closely related to the Euler equations of fluid dynamics (*e.g.* Binney and Tremaine, 1987; Gerhard, 1994):

$$\rho\frac{\partial \bar{v}_l}{\partial t} + \rho\bar{v}_k\frac{\partial \bar{v}_l}{\partial x_k} = -\rho\frac{\partial \phi}{\partial x_l} - \frac{\partial(\rho\sigma^2_{kl})}{\partial x_k}, \tag{1.6}$$

where the symmetric tensor σ^2_{kl} measures the random motions of the stars with respect to the mean streaming motion. At each position in space, the principal axes of σ^2_{kl} define the velocity ellipsoid. Unfortunately, the principal axes of the velocity ellipsoid are not known in general, and hence solutions can only be obtained by making assumptions about the shape of the velocity ellipsoid or the form of the DF.

Jeans theorem

Often one is interested in solutions of the CBE that describe stars moving in a gravitational potential which is constant in time, such that the DF is also constant. For such a steady-state solution ($\frac{\partial f}{\partial t} = 0$) of the CBE Jeans theorem states that the DF depends on the phase-space coordinates only through the integrals of motion for the stellar orbits in the gravitational potential. On the other hand, any non-negative function of the integrals of motion is a steady-state solution of the CBE. For a steady-state system, the Jeans theorem implies, that the phase-space density is constant along individual orbits. This is the basis of many methods for constructing equilibrium models of galaxies, such as the Schwarzschild method (Schwarzschild, 1979) or DF-based methods.

1.3 Dynamical modeling of elliptical galaxies

The central problem in dynamical modelling of galaxies is to find a DF which solves the CBE and reproduces the observations, such as the surface brightness distribution and the mean line-of-sight velocity field (*cf.* equation 1.1), to gain some information about the distribution of mass and the orbital structure. These are interesting because the first one may gives a hint on the distribution of dark matter, where as the latter one is likely to have preserved some record of the formation of the galaxy.

Unfortunately, estimating the distribution of mass is complicated by the fact that the intrinsic shape of an elliptical galaxy is not known at the outset and that the deprojection of its surface brightness distribution is not unique. Consequently, different intrinsic shapes have to be probed. In addition, constraining the dynamical models by only the mean velocity and velocity dispersion is insufficient to derive the mass of the system due to the mass-anisotropy degeneracy (Binney and Mamon, 1982). Using the full LOSVD instead, allows to reconstruct the DF given the potential is known (Dejonghe and Merritt, 1992) and to constrain the DF and the potential, if the latter is not given (Gerhard, 1993; Merritt, 1993).

Several techniques have been developed to construct dynamical models of galaxies with the attempt to recover the mass distribution (including dark matter) and the DF consistent with the observational data.

DF-based methods assume that the integrals of motion can be expressed or approximated in terms of analytic functions. This approach has been applied to spherical or other integrable systems (*e.g.* Dejonghe 1984; Bishop 1987; Dejonghe and de Zeeuw 1988; Gerhard 1991; Hunter and de Zeeuw 1992; Carollo et al. 1995; De Bruyne et al. 2000; Kronawitter et al. 2000), nearly integrable potentials where perturbation theory can be used (*e.g.* Saaf, 1968; Dehnen and Gerhard, 1993; Matthias and Gerhard, 1999) and to axisymmetric models assuming that the DF is a function of energy E and angular momentum L_z only (*e.g.* Hunter and Qian, 1993; Dehnen and Gerhard, 1994; Kuijken, 1995; Magorrian, 1995; Qian et al., 1995; Merritt, 1996). However, there is no physical reason why the DF should only depend on the classical integrals and most orbits in axisymmetric systems have an additional third integral I_3, which is not known in general (Ollongren, 1962).

Another class of models solve the Jeans equations or higher order velocity moments of the CBE. This approach does not require the knowledge of the integrals of motion, but since the Jeans equations are not closed, assumptions about the shape of the velocity ellipsoid have to be made. For example, M87 was studied by Binney and Mamon (1982) using spherical Jeans models. Binney et al. (1990) constructed axisymmetric models for NGC 4697 assuming $f(E, L_z)$. But the Jeans approach has the limitation that the DF associated with the velocity moments is not guaranteed to be positive everywhere.

Schwarzschild (1979) developed an orbit based method for numerically building models of galaxies, without explicit knowledge of the integrals of motion. It makes use of the fact that the DF is constant along orbits and can be interpreted as a superposition of the DFs of the individual orbits. A library of orbits is computed and orbits are then superposed with positive definite weights to reproduce observed photometry and kinematics. The Schwarzschild method has been used to model stellar systems for measurements of global mass-to-light ratios, internal kinematics and the masses of central black holes (*e.g.* Gebhardt et al., 2003; Thomas et al., 2005; Cappellari et al., 2006; Shapiro et al., 2006). However, most Schwarzschild models in the literature to date are axisymmetric.

Syer and Tremaine (1996) invented a particle-based method for generating models of stellar systems. This "made-to-measure" (M2M) method is allied to the Schwarzschild technique, but rather than superposing orbits from a library, it works by varying the weights of the particles in the system as a function of time, until the model converges to the observational data. This allows for arbitrary geometries and is not restricted necessarily to stationary systems. So far, the only

practical application of the M2M method was made by Bissantz et al. (2004). These authors constructed a dynamical model of the Milky Way's barred bulge and disk by constraining the projected density map. One goal of this thesis is to extend the M2M algorithm to incorporate kinematic observations and to properly account for observational errors.

1.4 N-particle simulations

Much of what is known today about the dynamical evolution of stellar systems comes from N-body simulations. N-body problems and their solutions divide into two types, depending on the importance of binary collisions. In a collision dominated simulation each particle represents an individual star, as for example in studies of the dynamical evolution of star clusters (*e.g.* von Hoerner 1960; Aarseth 1963; Hénon 1964).

On the other hand, stellar systems such as galaxies are collisionless for time scales much longer than a Hubble time. As discussed in section 1.2, such a system is completely described by a DF $f(\mathbf{x}, \mathbf{v}, t)$ along with the smooth potential $\phi(\mathbf{x}, \mathbf{v}, t)$ generated by the DF and any external contributions. The evolution of the DF is determined by the CBE, *cf.* equation (1.2). The CBE is solved by sampling phase-space using a Monte-Carlo approach in which selected "fluid" elements are represented as particles and are integrated along the characteristic curves of the CBE, defined by (*e.g.* Hernquist and Ostriker 1992; Leeuwin et al. 1993)

$$\frac{\mathrm{d}\mathbf{x}}{\mathrm{d}t} = \mathbf{v} \tag{1.7}$$

$$\frac{\mathrm{d}\mathbf{v}}{\mathrm{d}t} = \mathbf{a}, \tag{1.8}$$

where $\mathbf{a} = -\nabla\phi$ is the acceleration. The potential ϕ is computed from the mass densities of the particles. In reality, N-body simulations are never perfectly collisionlness due to the particle noise in the estimation of the accelerations. One should therefore make the number of particles as large as possible to reduce the effects of the shot noise.

The task of the potential solver is to estimate the accelerations $\mathbf{a}$ from the discrete sample of particles. Various techniques have been proposed in the literature and in the following I give only an incomplete list. The simplest technique is the particle-particle method (PP) in which the potential is computed by a direct summation of the pair-wise interactions (*e.g.* Aarseth, 1985). Another approach is the so-called particle-mesh (PM) method which solves Poisson's equation on a grid (PM) (*e.g.* Hockney and Brownrigg, 1974), using for example a fast Fourier transform (FFT). Sellwood (2003) developed a surface harmonic method (PM+SH) which is described in more detail in section A.1. The PM+SH method is used as the potential solver in the NMAGIC code.

Collisionless N-body simulations have been applied to many problems in astrophysics such as galaxy evolution (*e.g.* Hockney and Brownrigg 1974; Debattista and Sellwood 2000), merger simulations (*e.g.* Gerhard 1981; Barnes 1990; Hernquist 1992; Naab et al. 2006) and in cosmological simulations (*e.g.* Efstathiou and Eastwood 1981; Navarro et al. 1996).

In a "standard" N-body simulation, one specifies a set of initial conditions ($f(\mathbf{x}, \mathbf{v}, t_0)$) and follows the evolution of the particle system and any quantity of interest (*e.g.* mass density or line-of-sight-velocity). The only way one can influence the final model is by changing the initial conditions. As already mentioned in section 1.2, this approach was employed by Fux (1997) to model the Milky Way. In contrast to that, the M2M method allows to tailor an initially specified system by gently adjusting the individual adaptable particle weights during the evolution of the particle system until it matches the observations (*cf.* section 2.2).

1.5 General properties of elliptical galaxies

Elliptical galaxies are usually smooth and almost structureless; devoid of photometric structures such as spiral arms, rings or bars. They are among the brightest galaxies in the universe and reach total B-band magnitudes of $M_B \approx -24$ mag, but elliptical galaxies populate the hole range of luminosities down to very faint dwarf ellipticals (dE). They vary in shape from round to highly flattened in appearance with isophotes, contours of constant surface brightness, remarkably close to being true ellipses. Accordingly, they are designated En where $n = 10(1 - a/b)$ and a/b describes the apparent axis ratio (Binney and Merrifield, 1998). There are few, if any, more flattened than E7.

Elliptical galaxies are preferentially found in clusters, and the largest of them, the cD galaxies, are found at the cluster centers (Dressler, 1980). The surface brightness profiles of elliptical galaxies are well described by the empirical Sersic (1968) law

$$I(R) = I(R_e) \exp(-b[(R/R_e)^{1/n} - 1]), \tag{1.9}$$

where the constant b is chosen such that half the light is enclosed within the effective radius R_e. For $n > 1$, $b \approx 1.999n - 0.327$. For $n = 4$, one obtains the $R^{1/4}$ or de Vaucouleurs (1948) law, which provides a fairly good description of the surface brightness profile over a large radial range. Unless an elliptical galaxy is circular symmetric, different values for R_e will be measured along the major and the minor axes, and the quoted values are typically the geometric mean of them.

The central regions of elliptical galaxies have attracted a lot of interest, because ellipticals have long been suspected to harbor central black holes. Due to the high spatial resolution needed, observations of the centers of ellipticals became possible only with the Hubble Space Telescope (HST). Lauer et al. (1995); Gebhardt et al. (1996); Faber et al. (1997) analysed HST surface brightness profiles of dozens of elliptical galaxies and discovered a bimodality in the central profile slopes. Nearly all the galaxies in these samples have central cusps, *i.e.* the logarithmic slope of the luminosity profile is significantly different from zero. The brightest galaxies with $M_v < -22$ have *cores* with a shallower inner profile, breaking at a break radius R_b to the steep outer profile. Faint galaxies with $M_V > -22.5$ have largely structureless steep *power-law* profiles and are therefore called power-law galaxies. In the intermediate luminosity range, both forms exist.

The appearance of an elliptical galaxy depends on its orientation with respect to the observer. For instance, an axisymmetric galaxy observed along the symmetry axis, looks as an E0 irrespective of the intrinsic flattening. Hence, it is not possible to determine the intrinsic shape for a single galaxy, but since ellipticals are observed along random directions, one can use the distribution of apparent flattening to constrain an average three dimensional shape, *i.e.* the probability distribution of intrinsic shapes. The distribution of apparent ellipticities of elliptical galaxies peak between E2 and E3. There is a lack of exactly circular objects and no galaxy is flatter than E7, possibly due to a dynamical instability. (*e.g.* Binggeli, 1980; Bender et al., 1988; Franx et al., 1991; Ryden, 1992). The apparent shapes of faint ellipticals are more flattened than those of more luminous ones. On average, the faint ellipticals are E3 and the brighter ones E1.5. The apparent shape distribution of the fainter galaxies is consistent with oblate symmetry, but the brighter ones are not, due to a lack of E0 galaxies. The apparent shape distribution of either group is successfully reproduced by a triaxial intrinsic light distribution (Tremblay and Merritt, 1996). Isophote twists, *i.e.* the change of the position angle (PA) with radius, further indicate that some elliptical galaxies are triaxial.

With the availability of CCD devices, accurate photometry became feasible and revealed deviations of the isophotes from being true ellipses. These deviations are between $0-2$ percent of the isophotal radius. (*e.g.* Carter, 1978, 1987; Jedrzejewski et al., 1987; Peletier et al., 1990). Usually, the deviations from an ellipse fit are quantified by means of a Fourier analysis (*cf.*

Bender and Moellenhoff, 1987). A positive a_4 coefficient indicates disky isophotes and a negative a_4 results from boxy isophotes. Boxy ellipticals are more likely to show isophote twists. Often they tend to be brighter and are radio and X-ray loud. By contrast, disky ellipticals are fainter, fast rotating and have less X-ray emission (*cf.* Bender et al., 1989; Cappellari et al., 2007). They resemble S0 galaxies with a low disk-to-bulge ratio. Hence, they may form a sequence with S0 galaxies (*cf.* Simien and Michard, 1990; Rix and White, 1990; Scorza and Bender, 1990; Cinzano and van der Marel, 1993). Boxy ellipticals have possibly formed by galaxy mergers, which could have destroyed any disks, and leave a triaxial remnant. The merger hypothesis is supported by the observations of kinematically decoupled components (*e.g.* Bender, 1988; Franx and Illingworth, 1988; Cappellari et al., 2007).

In contrast to spiral galaxies, ellipticals lack luminous young blue stars with most of their light coming from red giants. They are old and α-enriched. Brighter galaxies are redder than fainter ones (*e.g.* Visvanathan and Sandage, 1977; Bower et al., 1992). In general, ellipticals are redder at their centers than in the outer parts (*e.g.* Peletier et al., 1990).

Among the basic structural parameters of elliptical galaxies exist various correlations. For instance the central velocity dispersion is tightly linked with the luminosity: Brighter ellipticals have larger central velocity dispersions and roughly $L \propto \sigma^4$. This correlation is often called the *Faber-Jackson* relation, after Faber and Jackson (1976). The Faber-Jackson relation can be used to estimate galaxy distances from velocity dispersion measurements. But it is difficult to determine the total luminosity of a galaxy, because a significant amount of light comes from the faint outer parts. Distances derived from the Faber-Jackson relation are therefore not very accurate.

The $D - \sigma$ relation (Dressler et al., 1987), where D measures the diameter of the isophote within which the mean surface brightness equals $I = 20.75\mu_B$, was found to provide a tighter correlation than the Faber-Jackson relation and is particularly used as a tool in distance estimation.

The *fundamental plane* (FP) relation (*cf.* Faber et al., 1987; Djorgovski and Davis, 1987; Dressler et al., 1987) is a generalization of the Faber-Jackson relation, which turned out to be a projection of the FP. The FP relation relates the effective radius R_e with the mean surface brightness I_e within one R_e and the velocity dispersion σ. It is approximately

$$R_e \propto \sigma^{1.2} I_e^{-0.8}, \tag{1.10}$$

which implies under the assumption of homology $(M/L) \propto L^{0.24}$ (Faber et al., 1987), known as the tilt of the FP. The luminosity dependence of the M/L is confirmed by dynamical studies (Gerhard et al., 2001; Cappellari et al., 2006) and is primarily due to population effects, while a varying DM fraction is less important.

1.6 Cosmological context

Observations of the temperature anisotropies in the cosmic microwave back ground imply that the universe is flat, consists mainly of cold dark matter and dark energy, with a small amount of ordinary mater, which formed its structure through gravitational instability starting from an inflationary epoch (*e.g.* Peacock, 1999; Hu and Dodelson, 2002; Spergel et al., 2003, 2007)

Numerical N-body simulations offer a powerful tool to study the formation of structure in the universe, starting from small density perturbations derived from temperature fluctuations in the cosmic microwave background. The growth of structure is determined by the amount and type of dark matter. High resolution ΛCDM simulation reveal a universal DM halo density profile, which is well approximated over a large range of masses by a functional two parameter form

$$\rho_{NFW}(r) = \frac{\rho_s}{(r/r_s)(1 + r/r_s)^2}, \tag{1.11}$$

where r_s is a characteristic scale length and ρ_s a corresponding density (*e.g.* Navarro et al., 1996, 1997; Moore et al., 1998). A useful alternative parameter for describing the shape of the density profile is the concentration parameter c_{vir} which is the ratio of the virial radius r_{vir} to r_s (*e.g.* Bullock et al., 2001; Wechsler et al., 2002). For a given cosmology, the halo concentration tends to increase with decreasing halo mass. This reflects the fact that low-mass halos typically collapse earlier, when the universe was denser. In the prevailing ΛCDM cosmology, the structure forms hierarchically bottom-up: dense low mass halos form first and merge successively to build up the high mass objects.

In the standard picture of galaxy formation, the dark matter halos carry withe them gas, which eventually cools and collapses within the potential wells of the surrounding halos to form disk galaxies. This suggests that galaxies trace a similar hierarchical formation path as their surrounding DM halos. The merger hypothesis as first proposed by Toomre and Toomre (1972) envisions that most elliptical galaxies form by major mergers of pairs of galaxies. The hierarchical formation picture is consistent with the fact that the fraction of early-type galaxies increases with increasing density of the environment whereas the fraction of late-type galaxies decreases (Dressler, 1980), and that some ellipticals show arc-like shells or have kinematically decoupled central cores (*e.g.* Malin and Carter, 1983; Bender, 1988; Franx and Illingworth, 1988; Cappellari et al., 2007). The merger scenario is supported by numerical simulations which have been successful in explaining observed properties of ellipticals like the surface brightness profiles, kinematics and isophotal shape parameters (*e.g.* Gerhard 1981; Barnes 1990; Hernquist 1992; Naab et al. 2006). However the picture has become more complex. For example, boxy ellipticals can form via disk-disk mergers (*e.g.* Naab and Burkert, 2003) or from multiple mergers (Weil and Hernquist, 1996); and the most massive ellipticals should have experienced a last elliptical-elliptical merger (Naab et al., 2006). Hence, it seems likely that ellipticals are remnants of mergers of both small ellipticals and spiral galaxies.

An ongoing test of ΛCDM is measuring the concentration, mass and extent of DM halos on different scales. There is compelling evidence for dark matter in galaxy clusters. Already in 1933, Zwicky concluded by means of the virial theorem that most of the mass in the Coma cluster is invisible. More recent studies using X-ray measurements (*e.g.* Schindler et al., 1999) and gravitational lensing (*e.g.* Mellier et al., 1993; Bartelmann, 1995) confirm these results.

On galactic scales, dark matter was first found in spiral galaxies. The most direct method to estimate the distribution of mass in spiral galaxies is provided by their circular-speed curves $v_c(R)$, which allow to deduce the mass inside radius R via

$$v_c^2(R) \propto \frac{M(R)}{R}. \tag{1.12}$$

Rotation curves can be measured optically from emission lines in HII (*e.g.* Burstein et al., 1982; Rubin, 1985; Kent, 1986), or from the 21-cm emission line of HI (*e.g.* van Albada et al., 1985; Begemann, 1987), which allows to measure the rotation curves out to radii, containing all but a negligible fraction of the total luminosity of a spiral galaxy.

These studies revealed that the rotation curves of spiral galaxies are flat out to the last measured data points and hence provide the most direct evidence for dark matter in these systems.

The search for dark matter in elliptical galaxies is more difficult due to the lack of a simple mass tracer such as HI, and due to their complex orbital structure (*cf.* section 1.8).

1.7 Measuring the kinematics of elliptical galaxies

Kinematic information about elliptical galaxies can be obtained from the integrated spectrum, which is the sum of all the individual stellar spectra along the line-of-sight, each Doppler-shifted in wavelength according to the velocity of the star. The random motions of the stars cause the lines in the integrated spectrum to be broadened. Thus, the absorption lines contain information

about the line-of-sight velocity distribution (LOSVD) of the stars. To first order, the line profile can by described by a Gaussian, characterized by a mean velocity equal to the bulk motion of the stars (rotation) and a width equal to the velocity dispersion of the stars. High-quality CCD spectra with high signal-to-noise ratio and high spectral resolution allow to extract the full LOSVD (*e.g.* Franx and Illingworth, 1988; Bender, 1990; Kuijken and Merrifield, 1993). The LOSVD can be described by a truncated Gauss-Hermite series (van der Marel and Franx, 1993; Gerhard, 1993):

$$\mathscr{L} \propto \exp(-w^2/2) \left[1 + \sum_{k=3}^{n} h_k H_k(w)\right], \tag{1.13}$$

where $w = (v_{los} - v)/\sigma$ and v and σ describe the underlying Gaussian. Here h_k are the Gauss-Hermite coefficients and $H_k(w)$ are the Hermite polynomials. The odd and even Gauss-Hermite coefficients measure asymmetric and symmetric deviations from a Gaussian, respectively. For example, $h_3 < 0$ characterizes a LOSVD with a prograde wing steeper than the retrograde one and $h_4 < 0$ corresponds to a flat-topped LOSVD.

The steeply decreasing surface brightness profiles of ellipticals make it difficult to measure stellar kinematics at large radii. Hence, absorption line measurements are confined to within approximately two effective radii.

Studies of the velocity profile shapes (Bender et al., 1994a) have revealed that the rotation velocity often increases within the central few arcsec and then flattens out. The velocity dispersion profiles either remain flat or fall in the outer parts. In general, rotating galaxies have flat-topped, asymmetric LOSVDs with $h_3 < 0$. The degree of asymmetry correlates with v/σ, so that disky ellipticals have more asymmetric velocity profiles than the boxy ones.

The recent development of integral-filed spectrographs, such as the SAURON instrument (*cf.* Bacon et al., 2001), provide two-dimensional kinematic information out to approximately one effective radius. However, measuring stellar kinematics at larger distances from the galaxy center remains difficult.

Other dynamical tracers such as globular clusters and planetary nebulae offer an alternative to measure the kinematics at large radii. For most galaxies within a distance of $\approx$ 20 Mpc, globular cluster velocities can be measured and have been used to study the outer halo of ellipticals (*e.g.* Pierce et al., 2006), but the modest numbers that have been observed today make it difficult to rule out constant mass-to-light ratios.

Planetary nebulae (PNe) are stars at the end of their lives. They have exhausted their nuclear fuel and have ejected their outer envelope. The core's intense ultraviolet radiation ionizes the ejected envelope, which emits in bright emission lines, of which the $[\mathrm{OIII}]\lambda 5007$ line is the most prominent one. By searching for objects emitting in this line, PNe can be detected at distances up to 100 Mpc and can be found even between galaxies in the intra cluster light (*e.g.* Gerhard et al., 2007). Once the PNe are identified, their line-of-sight velocities can be obtained from the Doppler shift of the narrow emission line.

PNe have been used to study the kinematics of elliptical galaxies at large radii out to $\approx 5R_e$ (*e.g.* Ciardullo et al., 1993; Arnaboldi et al., 1998; Douglas et al., 2002; Romanowsky et al., 2003; Douglas et al., 2007), where the dark matter is expected to dominate. Different techniques are in use to study PNe kinematics. Méndez et al. (2001) used a dispersed-undispersed imaging technique to measure the PNe velocities in NGC 4697. The Planetary Nebulae Spectrograph (PN.S) utilizes counterdispersed imaging in conjunction with two spectrographic cameras (Douglas et al., 2002) providing an efficient tool to measure the PNe kinematics up to 25 Mpc. The primary purpose of the PN.S instrument is to study the dynamics of a sample of ordinary early-type galaxies.

The PN population in elliptical galaxies is expected to arise from the underlying galactic population of old stars and hence the PNe can be used as kinematic tracers for the stellar distribution. This seems to be true in general except in one case: Sambhus et al. (2006) analyzed the correlations between the magnitudes, velocities and positions of a sample of PNe belonging to

NGC 4697 and found kinematic evidence for more than one PN sub-population. In addition to the main PN population, they found evidence for a population of preferably bright PNe which appeared to be not in dynamical equilibrium in the galactic potential.

1.8 Evidence for dark matter in elliptical galaxies

Estimates of the total gravitating mass in ellipticals is in principle offered through various channels. Among them are studies of the kinematics of occasional cold gas disks, the X-ray emitting hot gas, gravitational lensing and stellar dynamical modelling.

Constraints on the dark matter halo from extended HI rings are only available in a few cases (*e.g.* Franx et al., 1994; Oosterloo et al., 2002). For example, Oosterloo et al. (2002) find that in NGC 3108 the HI rotation curve remains flat out to 6 R_e consistent with a mass-to-light ratio $M/L \sim 18$, which implies that a significant amount of dark matter is present at large radii.

A significant fraction of elliptical galaxies, especially giant ones, contain hot X-ray emitting gas atmospheres. From measuring the X-ray luminosity and spectrum, the spatial density and the temperature of the hot gas can be inferred, and allows to estimate the total mass assuming the gas is in hydrostatic equilibrium. These studies indicate that dark matter halos are common in elliptical galaxies and almost follow the NFW profile (*e.g.* Awaki et al., 1994; Loewenstein and White, 1999; Humphrey et al., 2006; Fukazawa et al., 2006). The dark matter contribution inside R_e is about 20 percent and up to $40-80$ percent at $5-6$ R_e. Gravitational lensing studies reveal similar dark matter fractions (*e.g.* Griffiths et al., 1996; Treu and Koopmans, 2004; Rusin and Kochanek, 2005).

In more ordinary ellipticals, mass estimates come from stellar dynamical studies, which have been limited to within $R \lesssim 2R_e$ by the faintness of the galaxies' outer surface brightness (*e.g.* Kronawitter et al., 2000; Gerhard et al., 2001; Thomas et al., 2007). Two larger samples consisting of roughly 20 apparently round, non-rotating galaxies have been analyzed in spherical approximation using spherical basis DFs (Kronawitter et al., 2000) and parameterized DFs with constant anisotropy (Magorrian and Ballantyne, 2001). Thomas et al. (2007) analyzed 17 Coma early-type galaxies, consisting of flattened, rotating as well as non-rotating galaxies, with axisymmetric Schwarzschild models (*cf.* Thomas et al., 2005). These three studies predict dark matter fractions of $\sim 10-50$ percentage inside R_e.

Cappellari et al. (2006) constructed self-consistent, axisymmetric Schwarzschild models for a sample of 25 E/S0 galaxies with SAURON kinematics extending to $\sim R_e$. A comparison of their dynamical M/L estimate with mass-to-light ratios derived from stellar population models revealed a DM fraction of ~ 30 percentage inside R_e.

In broad terms, the various methods using different dynamical traces agree with each other and the general result is that elliptical galaxies are surrounded by dark matter halos producing nearly flat rotation curves, and the dark matter contributes contributes $\sim 10-40\%$ of the mass within R_e. The central dark matter concentrations are higher than in spiral galaxies. This presumably reflects the earlier formation epoch (Gerhard et al., 2001; Thomas et al., 2007).

In the light of this, it is quite surprising that the derived PNe dispersion profiles in the intermediate luminosity elliptical galaxies NGC 4697 (Méndez et al., 2001) and NGC 821, 3379 and 4494 (Romanowsky et al., 2003; Douglas et al., 2007) were found to decline significantly with radius outside R_e.

Méndez et al. (2001) have fitted the PNe velocity dispersion profile of NGC 4697 using a spherical, isotropic Hernquist (1990) model, adopting a constant mass-to-light ratio. They concluded that the PNe velocity dispersion profile is consistent with no DM inside $4.5R_e$, but that DM can be present if the velocity distribution is anisotropic. Romanowsky et al. (2003) analyzed the PNe velocity dispersion profiles of three intermediate luminosity ellipticals (NGC 3379, NGC 4494, NGC 821), measured with the special Planetary Nebulae Spectrograph (PN.S) instruments, using spherically symmetric dynamical models allowing for orbital anisotropy.

They concluded that the galaxies in their sample apparently have only diffuse halos.

Subsequently, Dekel et al. (2005) argued that the Keplerian declining PNe velocity dispersion profiles were compatible with their spiral merger simulations carried out within the ΛCDM cosmology framework. They found that the merger remnants have very elongated orbits at large radii and hence are radially anisotropic. They suggested that the well known mass-anisotropy degeneracy (*e.g.* Binney and Mamon, 1982) allows for declining dispersion profiles even when a standard DM halo is present. However, Douglas et al. (2007) pointed out that Romanowsky et al. (2003) properly took into account orbital anisotropies in the data modelling process. Douglas et al. (2007) reanalyzed the velocity dispersion profile of NGC 3379, the strongest case of Romanowsky et al. (2003), obtained from a larger PNe sample by means of a spherical Jeans analysis. They argued that their result continues to conflict with the presence of a standard dark matter halo as predicted by cosmological simulations.

Thus the important question remains whether these intermediate luminosity ellipticals differ from most other galaxies in the way in which they formed, they did not acquire a dens massive halo; or whether they are embedded in massive halos which are difficult to see in their unusual kinematics.

1.9 Outline

The thesis is organized as follows.

In chapter 2, the χ^2-made-to-measure algorithm and its implementation in a parallel code NMAGIC is presented. Various tests, employing spherical, oblate and triaxial target models, are carried out to show its flexibility and performance. These tests illustrate the dependence of the results from χ^2M2M on the initial model, the geometry, and the amount of available data.

Chapter 3 presents the first application of NMAGIC to a real galaxy, the intermediate luminosity elliptical NGC 4697, combining new surface brightness photometry, new as well as published long-slit absorptionline kinematic data, and published PNe velocity data. The combined kinematic data set extends out to $\sim 4.5R_e$ and allows to probe the galaxy's outer halo.

NMAGIC is extended to include seeing effects, an efficient scheme to estimate the mass-to-light ratio is introduced, and a maximum likelihood technique to account for discrete velocity measurements is incorporated. Dynamical axisymmetric self-consistent models as well models including various dark matter halos are constructed.

A detailed dynamical study of NGC 3379, combining ground based long slit spectroscopy, integral-field data from the SAURON instrument, and PN.S data reaching to more than seven effective radii is the subject of chapter 4, with main focus on the galaxy's outer halo.

The photometric and combined kinematic data are fitted with spherical and axisymmetric models in a sequence of gravitational potentials whose circular velocity curves at large radii vary between a near-Keplerian decline and the nearly flat shapes generated by massive halos.

The dynamical studies of NGC 4697 and NGC 3379 show that their kinematic data are consistent with models including quite massive and moderately massive halos, respectively. Thus NGC 4697 and NGC 3379 may well have dark matter halos consistent with the current ΛCDM paradigm.

Finally, chapter 5 gives a short summary and an outlook.

CHAPTER 2

NMAGIC: A χ^2-MADE-TO-MEASURE ALGORITHM FOR MODELING OBSERVATIONAL DATA

Flavio De Lorenzi, Victor P. Debattista, Ortwin Gerhard, Niranjan Sambhus
published in *MNRAS*, 2007, 376, 71

We describe a made-to-measure algorithm for constructing N-particle models of stellar systems from observational data (χ^2M2M), extending earlier ideas by Syer and Tremaine. The algorithm properly accounts for observational errors, is flexible, and can be applied to various systems and geometries. We implement this algorithm in a parallel code NMAGIC and carry out a sequence of tests to illustrate its power and performance: (i) We reconstruct an isotropic Hernquist model from density moments and projected kinematics and recover the correct differential energy distribution and intrinsic kinematics. (ii) We build a self-consistent oblate three-integral maximum rotator model and compare how the distribution function is recovered from integral field and slit kinematic data. (iii) We create a non-rotating and a figure rotating triaxial stellar particle model, reproduce the projected kinematics of the figure rotating system by a non-rotating system of the same intrinsic shape, and illustrate the signature of pattern rotation in this model. From these tests we comment on the dependence of the results from χ^2M2M on the initial model, the geometry, and the amount of available data.

2.1 Introduction

Understanding the structure and dynamics of galaxies requires knowledge of the total gravitational potential and the distribution of stellar orbits. Due to projection effects the orbital structure is not directly given by observations. In equilibrium stellar systems, the phase-space distribution function (DF) fully determines the state of the galaxy. Dynamical models of observed galaxies attempt to recover their DF and total (*i.e.* due to visible and dark matter) gravitational potential consistent with the observational data. Several methods to tackle this problem exist. Jean's theorem (*e.g.* Binney and Tremaine 1987) requires that the DF depends on the phase-space coordinates only through the integrals of motion. If these integrals can be expressed or approximated in terms of analytic functions, one can parametrize the DF explicitly. This approach has been applied to spherical or other integrable systems (*e.g.* Dejonghe 1984, Dejonghe 1986; Bishop 1987; Dejonghe and de Zeeuw 1988; Gerhard 1991; Hunter and de Zeeuw 1992; Carollo et al. 1995, Kronawitter et al. 2000); nearly integrable potentials where perturbation theory can be used (*e.g.* Saaf 1968; Dehnen and Gerhard 1993, Matthias and Gerhard 1999) and to axisymmetric models assuming that the DF is a function of energy E and angular momentum L_z only (Hunter and Qian 1993; Dehnen and Gerhard 1994; Kuijken 1995; Qian et al. 1995;

Magorrian 1995; Merritt 1996). However there is no physical reason why the DF should only depend on the classical integrals and most orbits in axisymmetric systems have an approximate third integral of motion, which is not known in general (Ollongren, 1962).

Schwarzschild (1979) developed a technique for numerically building self-consistent models of galaxies, without explicit knowledge of the integrals of motion. In this method, a library of orbits is computed and orbits are then superposed with positive definite weights to reproduce observed photometry and kinematics. The Schwarzschild method has been used to model stellar systems for measurements of global mass-to-light ratios, internal kinematics and the masses of central supermassive black holes (*e.g.* Rix et al. 1997; Cretton et al. 1999; Romanowsky and Kochanek 2001; Cappellari et al. 2002; Verolme et al. 2002; Gebhardt et al. 2003; van de Ven et al. 2003; Valluri et al. 2004, Copin et al. 2004, Thomas et al. 2005). The method is well-tested, and modern implementations are quite efficient. However, it also has some draw-backs: symmetry assumptions are often made, and the potential must be chosen a priori. Initial conditions for a representative orbit library have to be carefully chosen, which becomes more complicated as the complexity of the potential's phase space structure increases, in terms of number of orbit families, resonances, chaotic and semi-chaotic regions. As a result, most Schwarzschild models in the literature to date are axisymmetric.

Thus there is scope for exploring alternative approaches. Syer and Tremaine (1996, hereafter ST96) invented a particle-based algorithm for constructing models of stellar systems. This "made-to-measure" (M2M) method works by adjusting individually adaptable weights of the particles as a function of time, until the model converges to the observational data. The first practical application of the M2M method constructed a dynamical model of the Milky Way's barred bulge and disk (Bissantz et al., 2004) and was able to match the event timescale distribution of microlensing events towards the bulge. This chapter illustrates some of the promise that lies in particle-based methods, in that it was relatively easy to model a rapidly rotating stellar system. However, other important modeling aspects were not yet implemented, such as a proper treatment of observational errors. The purpose of the present chapter is to show how this can be done, and to describe and test our modified χ^2M2M method designed for this purpose.

The chapter is organized as follows. In the Section 2.2 we describe the M2M algorithm of ST96. Then in Section 2.3 we extend the algorithm in order to include observational errors. We also discuss how we include density and kinematic observables in the same model, and describe the NMAGIC code, our parallel implementation of the χ^2M2M method. In Section 2.7 we present the models we use to test this implementation, and the results of these tests follow in Section 2.8. Finally, the chapter closes with the conclusions in Section 2.9.

2.2 Syer & Tremaine's Made-To-Measure Algorithm

The M2M algorithm is designed to build a particle model to match the observables of some target system. The algorithm works by varying the individually adaptable weights of the particles moving in the global potential until the model minimizes deviations between its observables and those of the target. An observable of a system characterized by a distribution function $f(\mathbf{z})$, is defined as

$$Y_j = \int K_j(\mathbf{z}) f(\mathbf{z}) \, \mathrm{d}^6 z \tag{2.1}$$

where K_j is a known kernel and $\mathbf{z} = (\mathbf{r}, \mathbf{v})$ are phase-space coordinates. Examples of typical observables include surface or volume densities and line-of-sight kinematics. The equivalent observable of the particle model is given by

$$y_j(t) = \sum_{i=1}^{N} w_i K_j \left[\mathbf{z}_i(t)\right], \tag{2.2}$$

where w_i are the weights and $\mathbf{z}_i$ are the phase-space coordinates of the particles, $i = 1, \cdots, N$. In the following, we use units and normalization such that

$$\sum_{i=1}^{N} w_i = 1, \tag{2.3}$$

so that the equivalent masses of the particles are $m_i = w_i M$ with M the total mass of the system.

Given a set of observables $Y_j,\ j = 1, \cdots, J$, we want to construct a system of N particles $i = 1, \cdots, N$ orbiting in the potential, such that the observables of the system match those of the target system. The heart of the algorithm is a prescription for changing particle weights by specifying the "force-of-change" (hereafter FOC):

$$\frac{\mathrm{d}w_i(t)}{\mathrm{d}t} = -\varepsilon w_i(t) \sum_j \frac{K_j\left[\mathbf{z}_i(t)\right]}{Z_j} \Delta_j(t). \tag{2.4}$$

Here

$$\Delta_j(t) = \frac{y_j(t)}{Y_j} - 1 \tag{2.5}$$

measures the deviation between target and model observables. The constant ε is small and positive and, to this point, the Z_j are arbitrary constants. The linear dependence of the FOC for weight w_i on w_i itself ensures that the particle weights cannot become negative, and the dependence on the kernel K_j ensures that a mismatch in observable j only has influence of the weight of particle i when that particle actually contributes to the observable j. The choice of Δ in terms of the ratio of the model and target observables makes the algorithm closely related to Lucy's (1974) method, in which one iteratively solves an integral equation for the distribution underlying the process from observational data.

Since in typical applications the number of particles greatly exceeds the number of independent constraints, the solutions of the set of differential equations (2.4) are under-determined, *i.e.* the observables of the particle model can remain constant, even as the particle weights may still be changing with time. To remove this ill-conditioning, ST96 maximize the function

$$F = \mu S - \frac{1}{2}\chi^2, \tag{2.6}$$

with

$$\chi^2 = \sum_j \Delta_j^2 \tag{2.7}$$

and the entropy

$$S = -\sum_i w_i \log(w_i/\hat{w}_i) \tag{2.8}$$

as a profit function. The $\{\hat{w}_i\}$ are a predetermined set of weights, the so-called priors. Since

$$\mu \frac{\partial S}{\partial w_i} = -\mu(\log(w_i/\hat{w}_i) + 1), \tag{2.9}$$

if a particle weight $w_i < \hat{w}_i/e$ then equation (2.9) becomes positive while it is negative when $w_i > \hat{w}_i/e$. Therefore the entropy term pushes the particle weights to remain close to their priors (more specifically, close to $\hat{w}_i/e$). Equation (2.4) is now replaced by

$$\frac{\mathrm{d}w_i(t)}{\mathrm{d}t} = \varepsilon w_i(t) \left(\mu \frac{\partial S}{\partial w_i}(t) - \sum_j \frac{K_j\left[\mathbf{z}_i(t)\right]}{Y_j} \Delta_j(t) \right), \tag{2.10}$$

with Z_j now fixed to Y_j by the requirement that equation (2.6) will be maximized, as discussed in Section 2.3. The constant μ governs the relative importance of the entropy term in equation (2.10): When μ is large the $\{w_i\}$ will remain close to their priors $\{\hat{w}_i\}$. In the following, we will generally set $\hat{w}_i = w_0 = 1/N$; i.e., the particle distribution follows the initial model, but this is not necessary.

To reduce temporal fluctuations, ST96 introduced temporal smoothing by substituting $\Delta_j(t)$ in Equations (2.7) and (2.10) with

$$\widetilde{\Delta}_j(t) = \alpha \int_0^\infty \Delta_j(t-\tau) e^{-\alpha\tau} \mathrm{d}\tau, , \tag{2.11}$$

which can be expressed in the form of the differential equation

$$\frac{\mathrm{d}\widetilde{\Delta}}{\mathrm{d}t} = \alpha \left(\Delta - \widetilde{\Delta}\right). \tag{2.12}$$

The smoothing time is $1/\alpha$. The temporal smoothing suppresses fluctuations in the model observables and hence in the FOC correction of the particle weights – in the computation of these quantities the effective number of particles is increased as each particle is effectively smeared backwards in time along its orbit. The smoothing time should satisfy $2\epsilon < \alpha$ to avoid excessive temporal smoothing[1], which slows down convergence.

2.3 χ^2-based Made-to-Measure Algorithm to Model Observational Data

The M2M algorithm as originally formulated by ST96 is well adapted to modeling density fields (*e.g.* Bissantz et al. 2004). It is not, however, well suited to mixed observables such as densities and kinematics, where the various ratios of model to target observable can take widely different values, or to problems where observables can become zero, when Δ diverges. Moreover, the χ^2 defined as in equations (2.7,2.5) is not the usual one, but is given by the relative deviations between model and data. Thus extremizing F (equation 2.6) with this χ^2 does not produce the best model given the observed data. We have therefore modified the M2M method as described in this section.

We begin by considering observational errors. We do this by replacing equation (2.5) by

$$\Delta_j(t) = \frac{y_j - Y_j}{\sigma(Y_j)}, \tag{2.13}$$

where $\sigma(Y_j)$ in the denominator is the error in the target observable. With this definition of Δ_j equation (2.7) now measures the usual absolute χ^2. As a result of this, if we now maximize the function of equation 2.6 with respect to the w_i's we obtain the condition

$$\mu \frac{\partial S}{\partial w_i} - \sum_j \frac{K_{ji}}{\sigma(Y_j)} \Delta_j = 0. \tag{2.14}$$

If we replace the FOC equation (2.10) by

$$\frac{\mathrm{d}w_i(t)}{\mathrm{d}t} = \varepsilon w_i(t) \left(\mu \frac{\partial S}{\partial w_i} - \sum_j \frac{K_j\left[\mathbf{z}_i(t)\right]}{\sigma(Y_j)} \Delta_j(t) \right) \tag{2.15}$$

then the particle weights will have converged once F is maximized with respect to all w_i, i.e., once the different terms in the bracket balance. For large μ, the solutions of eqn. 2.15 will have smooth weight distributions at the expense of a compromise in matching χ^2.

[1] This corrects the typo in equation (19) of ST96.

In the absence of the entropy term, the solutions of eqs. 2.15 near convergence can be characterized by an argument closely similar to that used by ST96 to study the solutions of their eqs. (4). For small ε, the weights $w_i(t)$ change only over many orbits, so we can orbit-average over periods $t_{\rm orb} \ll \tau \ll t_{\rm orb}/\varepsilon$ and write the equations for the orbit-averaged $< \Delta_j >$ as

$$\frac{{\rm d} < \Delta_j(t) >}{{\rm d}t} = \varepsilon \mathcal{A}_{jk} < \Delta_k(t) >, \tag{2.16}$$

where the matrix A has components

$$\mathcal{A}_{jk} = \Sigma_i \frac{< K_{ji} >< K_{ki} >}{\sigma_j \sigma_k} w_i^0, \tag{2.17}$$

and we have replaced $w_i(t)$ by the constant w_i^0, because near convergence the dominant time-dependence is in $< \Delta_k >$ rather than w_i. The matrix A is symmetric by construction and positive definite, i.e., $x^t \cdot \mathcal{A} \cdot x > 0$ for all vectors x; so all its eigenvalues are real and positive. The solutions to eqs. 2.16 then converge exponentially to $< \Delta_j(t) >= 0$. As for eqs. (4) of ST96, this argument suggests that if ε is sufficiently small and we start close to the correct final solution, then the model observables converge to their correct final values on $O(\varepsilon^{-1})$ orbital periods.

Substituting Δ_j in equation (2.11) leads to

$$\widetilde{\Delta}_j(t) = \frac{\widetilde{y}_j(t) - Y_j}{\sigma(Y_j)}, \tag{2.18}$$

which allows us to temporally smooth model observables directly

$$\widetilde{y}_j(t) = \alpha \int_0^\infty y_j(t-\tau) e^{-\alpha\tau} {\rm d}\tau. \tag{2.19}$$

In practice, $\widetilde{y}_j$ can be computed using the equivalent differential equation, in the same manner as before.

Since the uncertainty in any observable presumably never becomes zero, the Δ_j in equation (2.13) remain well-defined even when the observables themselves take zero values. However, if the data entering χ^2 have widely different relative errors, the FOC equation may be dominated by only a few of the Δ_j. This can slow down convergence of the other observables and thus lead to noisy final models. Also, notice that the cost of deriving the FOC from minimizing χ^2 is that equation (2.6) is maximized only if the observables are exactly of the form given by equation (2.2), *i.e.* the kernel K_{ij} may depend on the particle's phase-space coordinates but must not depend on its weight w_i.

We adopt the convention throughout this chapter in which the positive x-axis points in the direction of the observer, so that a particle with velocity $v_x < 0$ will be moving away from the observer.

Our implementation of the χ^2M2M algorithm models volume luminosity densities (equivalent to luminous mass densities for constant mass-to-light ratio), and line-of-sight velocities. As in the Schwarzschild method, dark matter, which generally has a different spatial distribution from the stars, can be included as an external potential, to be added to the potential from the luminous particles. The form of the dark matter potential can be guided by cosmological simulations, or also include information from gas velocities and other data.

2.4 Densities

For modeling the target distribution of stars one can use as observables the surface density or space density in various grids, or also some functional representations such as, *e.g.* , isophote

fits, multi-Gaussian expansions, etc. In this chapter we have chosen to model a spherical harmonics expansion of the three-dimensional density, where we expand the density in surface harmonics computed on a 1-D radial mesh of radii r_k. The expansion coefficients, A_{lm} are computed based on a cloud-in-cell scheme. The function

$$\gamma_k^{CIC}(r) = \begin{cases} \frac{r-r_{k-1}}{r_k-r_{k-1}} & \text{if } r \in [r_{k-1}, r_k) \\ \frac{r_{k+1}-r}{r_{k+1}-r_k} & \text{if } r \in [r_k, r_{k+1}] \\ 0 & \text{otherwise,} \end{cases}$$

gives the fractional contribution of the weight w of a particle at radius r to shell k. The model observable is then the mass on each shell k,

$$m_k = M \sum_i w_i \gamma_k^{CIC}(r_i) \equiv M \sum_i w_i \gamma_{ki}^{CIC}. \tag{2.20}$$

Comparing with equation (2.2), we recognize the kernel for this observable as

$$K_{ki} = M \gamma_{ki}^{CIC}. \tag{2.21}$$

Thus the FOC on a particle is computed by linear interpolation of the contributions from the adjacent shells. From equation (2.13), we obtain

$$\Delta_k[m] = \frac{m_k - M_k}{\sigma(M_k)} \tag{2.22}$$

where M_k is the target mass on shell k and $\sigma(M_k)$ its uncertainty.

The spherical harmonic coefficients for the particle model with $l > 0$ are computed via

$$a_{lm,k} = M \sum_i \gamma_{ki}^{CIC} Y_l^m(\theta_i, \varphi_i) w_i. \tag{2.23}$$

Now the kernel is given by

$$K_{\mathbf{j}i} = M \gamma_{ki}^{CIC} Y_l^m(\theta_i, \varphi_i), \;\; \mathbf{j} = \{lm, k\}, \tag{2.24}$$

and depends on the spherical harmonics; the same variation also holds therefore for the FOC. From equation (2.13), we obtain

$$\Delta_{\mathbf{j}}[a_{lm}] = \frac{a_{lm,k} - A_{lm,k}}{\sigma(A_{lm,k})}, \;\; \mathbf{j} = \{lm, k\}, \tag{2.25}$$

with $A_{lm,k}$ as the target moments and $\sigma(A_{lm,k})$ as their errors. $a_{00,k}$ and $A_{00,k}$ are of course related to the mass on shell k via the relation $\sqrt{4\pi} a_{00,k} = m_k$, etc., but we will use the masses on shells m_k, M_k as observables in the following.

2.5 Kinematics

Unlike for the density observables, we use kinematic observables computed in the plane of the sky to compare with the target model. Since kinematic data can either come from restricted spatial regions (*e.g.* slit spectra) or from integral fields, we do not specify any special geometry for computing these observables.

The shape of the line-of-sight velocity distribution (LOSVD) can be expressed in a truncated Gauss-Hermite series with coefficients $h_n, \;\; n = 1, \cdots, n_{max}$ (van der Marel and Franx 1993; Gerhard 1993). Since the kernel in equation (2.15) cannot depend on masses, this puts some constraints on which observables can be used in the FOC. For kinematics, suitable observables

are the *mass-weighted* Gauss-Hermite coefficients, which we use as follows. Particle weights are assigned to a spatial cell, $\mathcal{C}_p$, of the kinematic observable under consideration using the selection function

$$\delta_{pi} = \begin{cases} 1 & \text{if } (y_i, z_i) \in \mathcal{C}_p \\ 0 & \text{otherwise.} \end{cases}$$

This selection function can be replaced appropriately if seeing conditions need to be taken into account. In our present application this is not necessary. The mass-weighted kinematic moments are computed as

$$b_{n,p} \equiv m_p\, h_{n,p} = 2\sqrt{\pi} M \sum_i \delta_{pi} u_n(\nu_{pi}) w_i, \tag{2.26}$$

$$\nu_{pi} = (v_{x,i} - V_p)\,/\sigma_p, \tag{2.27}$$

and where m_p is the mass in cell $\mathcal{C}_p$, and the dimensionless Gauss-Hermite functions (Gerhard, 1993)

$$u_n(\nu) = \left(2^{n+1}\pi n!\right)^{-1/2} H_n(\nu) \exp\left(-\nu^2/2\right). \tag{2.28}$$

H_n are the standard Hermite polynomials. For the mass-weighted higher order moments we obtain the kernel

$$K_{\mathbf{j}i} = 2\sqrt{\pi} M \delta_{pi} u_n(\nu_{pi}), \;\; \mathbf{j} = \{n, p\}. \tag{2.29}$$

and as usual

$$\Delta_{\mathbf{j}}[m\, h_n] = \frac{b_{n,p} - B_{n,p}}{\sigma(B_{n,p})}, \;\; \mathbf{j} = \{n, p\}. \tag{2.30}$$

The velocity V_p and dispersion σ_p are not free parameters; rather we set V_p and σ_p to the mean line-of-sight velocity and velocity dispersion obtained from the best fitting Gaussian to the observed (target) LOSVD. This implies $B_{1,p} \equiv (m_p\, h_{1,p})_{\rm target} = B_{2,p} \equiv (m_p\, h_{2,p})_{\rm target} = 0$ for the first and second order mass-weighted target Gauss-Hermite coefficients. If the model $b_{1,p}$ and $b_{2,p}$ both converge to zero, then the LOSVD of the particle model automatically has the correct mean line-of-sight velocity and velocity dispersion. For describing the higher-order structure of the LOSVD we include terms $m\, h_n$ $(n = 1, \cdots, 4)$ in the test modeling described below.

2.6 Implementation: the NMAGIC parallel code

The routine for updating the particle weights includes three main steps: First, all the observables used in the modeling process are computed as described above. Then we change the particle weights in accordance with equation (2.15) by

$$w_{i,t+\delta t} = w_{i,t} + \varepsilon w_{i,t} \left(\mu \frac{\partial S}{\partial w_i} - \sum_j \frac{K_j\,[\mathbf{z}_{i,t}]}{\sigma(Y_j)} \widetilde{\Delta}_{j,t} \right) \delta t, \tag{2.31}$$

with

$$\widetilde{\Delta}_{j,t} = \frac{\widetilde{y}_{j,t} - Y_j}{\sigma(Y_j)}. \tag{2.32}$$

Finally, we update the temporally smoothed observables as follows:

$$\widetilde{y}_{j,t+1} = \widetilde{y}_{j,t} + \alpha(y_{j,t} - \widetilde{y}_{j,t})\delta t. \tag{2.33}$$

Here δt is the time between successive χ^2M2M steps. All the differential equations here are ordinary differential equations of the form $\mathrm{d}y_i(t)/\mathrm{d}t = f_i(t, y_1, \cdots, y_N)$, and the $y_{i,n}$'s in our case are the particle weights w_i or time-smoothed observables y_i at t_n. We integrate them using a simple Euler method $y_{i,n+1} = y_{i,n} + h\;\; f(t_n, y_{i,n})$ with $t_{n+1} = t_n + h$ and time

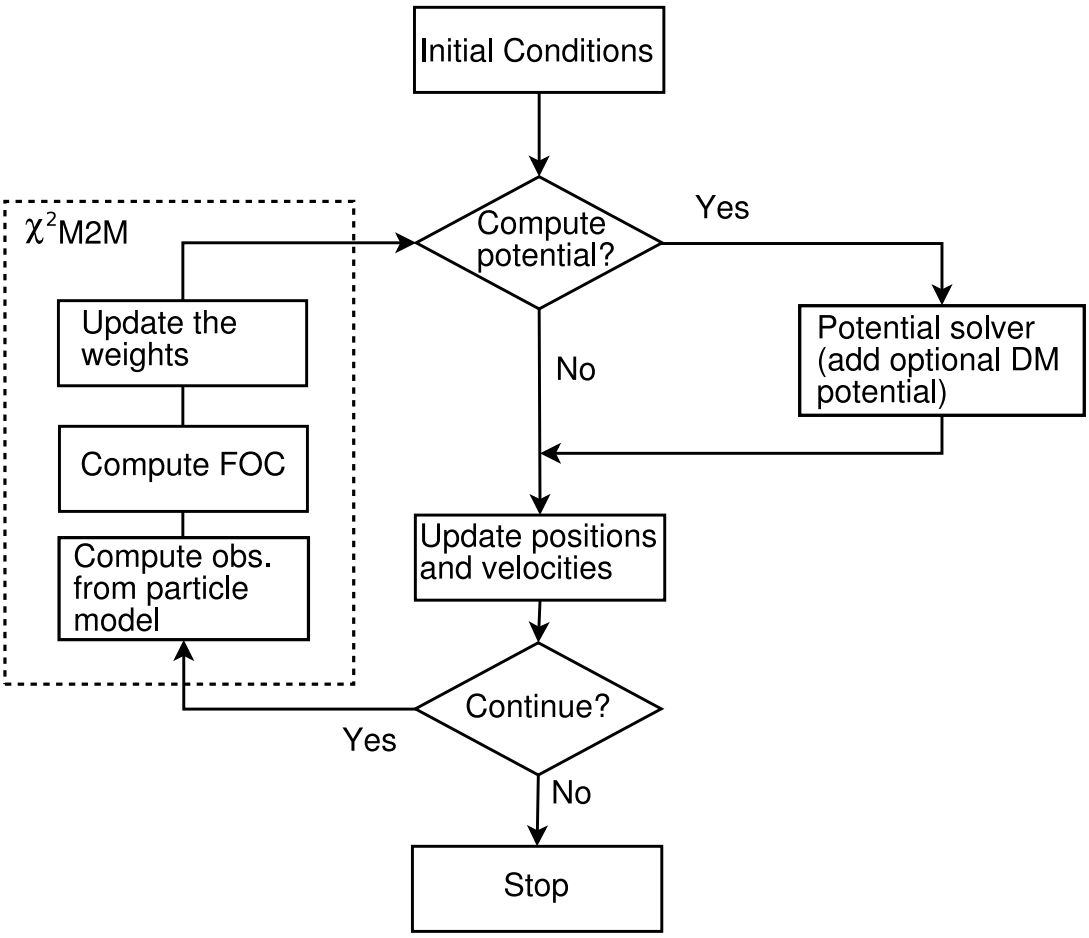

Figure 2.1: A high level flowchart describing NMAGIC. The main χ^2M2M algorithm is contained in the dashed block, the remainder is an optional potential solver and code for moving the particles, both of which are exchangeable. In our tests, χ^2M2M is generally applied only after a number of position/velocity updates.

step $h = \delta t$. We could replace the Euler method by the second-order Runge-Kutta method (*cf.* Press et al. 1992), which is more expensive and requires more memory. Since we are not interested in the details of how the weights converge, but only in the final converged system, a simple Euler method suffices for our purposes. We write ε in equation (2.31) as $\varepsilon = \varepsilon'\varepsilon''$ with $\varepsilon'' = 10/\max_{i,j}\{K_{ji}\widetilde{\Delta}_j/\sigma(Y_j)\}$. Thus ε'' times the last term in equation (2.15) is of order unity and we choose $2\varepsilon' < \alpha$ to avoid excessive temporal smoothing.

The NMAGIC (**N**-particle **M**ade-to-measure **A**l**G**orithm m**I**nimizing **C**hi squared) correction routine can be combined with a standard N-body code including a potential solver and time integrator, or a fixed-potential routine and integrator when the target is to be modeled in a given gravitational potential. This last case is most similar to the Schwarzschild method. In most of the tests below, we use a fixed potential expanded in spherical harmonics.

However, in test E we allow the potential to vary, as we evolve from one triaxial model to another. For advancing the particles we use a standard leap frog time integrator with fixed time-step. The time-step value chosen leads to fluctuations of energy and angular momentum with amplitudes 5×10^{-6} and 2×10^{-5} around their initial values, without systematic drift, over 80 half mass dynamical times in the fixed potential case.

For test E, which models a triaxial system, a simple spherical harmonic expansion suffices for solving for the potential. We follow the method described by Sellwood (2003): we tabulate coefficients of a spherical harmonic expansion of the density on a 1-D radial grid but retain the exact angular dependence up to some adopted $l_{\max}$, the maximum order of the spherical harmonic expansion. We include terms up to $l_{\max} = 4$ in this experiment. Particles are binned on the radial grid using the scheme described by Sellwood (2003). This then gives the forces on the grid, from which we interpolate back to a particle's position for the gravitational forces. Test E involves a cuspy model; in order to properly resolve this we use a radial grid at radii $r_\xi = e^{\gamma\xi} - 1$ with $\gamma = \ln(r_{\max} + 1)/\xi_{\max}$; we use $\xi_{\max} = 301$ for 301 shells and $r_{\max} = 40$.

NMAGIC is written in Fortran 90 and parallelized with the MPI library. We distribute the N particles as nearly evenly as possible over N_p processors. Parallelizing in only the observables would not scale well with large N_p, because of the different nature of the observables, and would require a large memory on each processor when N is large. In Figure 2.1 we present a high level flowchart of the operational logic of NMAGIC.

In order to test the scaling with N_p of NMAGIC we considered $N = 1.8\times10^6$ and $N_o = 816$ observables (640 density and 176 kinematic) with N_p varying from 1 to 120. These values of N_p and N_o are adequate for the experiments presented here and are used in test C of Table 2.1. Since we are only interested in the scaling of the χ^2M2M parallelization with N_p, we only execute the χ^2M2M 50 times, without recomputing the potential or advancing particles. In Figure 2.2 we present these scaling results as time per step (left hand axis, plus symbols) and steps per unit time (right hand axis, open squares) as functions of N_p. We generally find that our implementation of χ^2M2M scales very well with N_p. Defining the speedup $S(N_p, N)$ as

$$S(N_p, N) = \frac{T(1, N)}{T(N_p, N)} \tag{2.34}$$

where $T(N_p, N)$ is the time for computing N particles on N_p processors, we fit a standard Amdahl's law (Amdahl, 1967)

$$S(N_p, N) = \frac{1}{f + (1 - f)/N_p}, \tag{2.35}$$

in order to determine the fraction of sequential code, f. We obtained that $f \simeq 0.010$, i.e. the sequential part of the code accounts for only 1%.

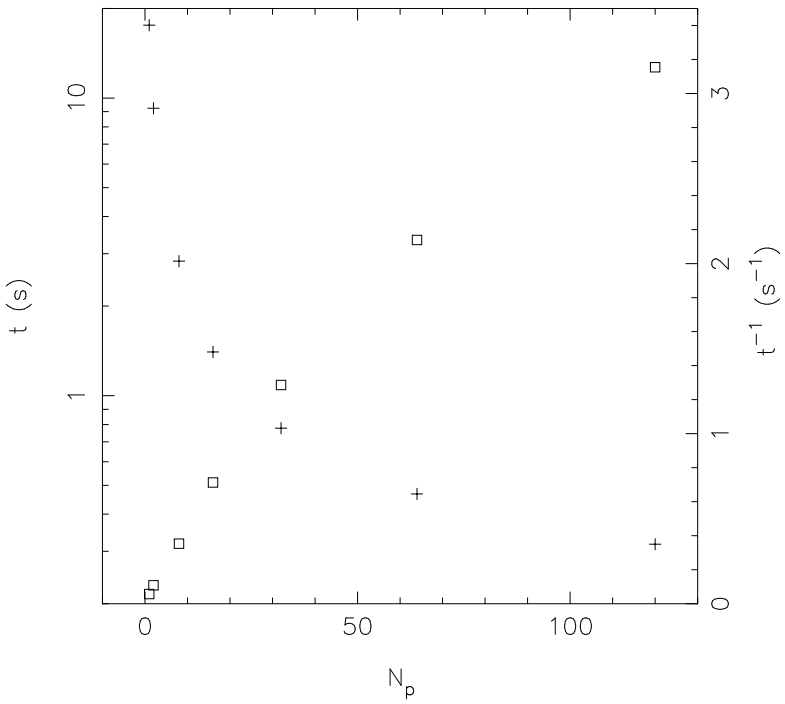

Figure 2.2: The performance of our implementation of χ^2M2M. We used 1.8×10^6 particles without potential calculations or particle motion. On the left hand axis we label time per step required, with the corresponding data indicated by plus symbols, while on the right hand axis we label steps per unit time, with the corresponding data now shown by open squares. Note that the scale is logarithmic on the left and linear on the right. The fraction of sequential code, f, from these data was computed at $\sim 1\%$.

2.7 Target Models and Their Observables

We will test the NMAGIC code on spherical, axisymmetric, and triaxial target models. The spherical target is a particle model constructed from the analytic density and distribution function of an isotropic Hernquist sphere. As oblate target we take a maximally rotating three-integral model. Finally, we construct both a stationary and a rotating triaxial target system. We use the NMAGIC code itself to generate a dynamical equilibrium structure for these models. It will be seen that the χ^2M2M method provides a very useful means to set up dynamical equilibrium models of galaxies for which no analytic distribution functions are known, in order to study the properties of such systems.

In the following subsections, we describe in turn each of these targets and their construction. We determine the target observables obtained from these models, and describe how we obtain errors for these observables. These will be needed in Section 2.8 where we present the results of building χ^2M2M models to match these targets. The reader who is mainly interested in these tests of NMAGIC can in a first reading directly go to that section.

2.7.1 Spherical Target

Our first target is a spherical isotropic Hernquist (Hernquist, 1990) model, which we will refer to as target SIH. Its density and potential are given by

$$\varrho(r) = \frac{aM}{2\pi r(r+a)^3}, \qquad \varphi(r) = -\frac{GM}{r+a}, \tag{2.36}$$

where a is the scale length, M is the total mass, and G is the gravitational constant. The projected effective (half-mass) radius equals $R_{\rm eff} \approx 1.8153a$. We use units such that $M = a = 1$. The target mass M_k on shell r_k is given by the sum of the contributions of the adjacent shells,

$$M_k = 4\pi \int \varrho(r)\gamma_k^{CIC}(r)r^2 {\rm d}r. \tag{2.37}$$

The innermost (outermost) shell is an exception because only the layer immediately exterior (interior) contributes.

We construct SIH models on a radial grid with 40 shells, quasi-logarithmically spaced in radius with inner and outer boundaries at $r_{\rm min} = 5 \times 10^{-4}$ and $r_{\rm max} = 20$. The distribution function is truncated at $E_{\rm max} \equiv \phi(r_{\rm max})$. At that truncation, the mass included is

$$M_{\rm trun} = \int_{E_{\rm min}=\varphi(0)}^{E_{\rm max}=\varphi(r_{\rm max})} \frac{dM}{dE} dE, \tag{2.38}$$

with (dM/dE) the differential energy distribution (*e.g.* Binney and Tremaine 1987) and thus $M_{\rm trun} = 0.86$. Figure 2.3 compares the mass on shells (hereafter "mass profile") $M_P(r_k)$ for a particle realization of this truncated distribution function (constructed using the method described in Debattista and Sellwood 2000), with the M_k from the Hernquist density profile as in equation (2.37). For small radii the mass profiles match but for larger radii $M_P(r_k)$ is significantly smaller than M_k due to the finite extent of the particle realization, consisting only of particles with $E < E_{\rm max} = \varphi(r_{\rm max})$. Using M_k as target observables would increase the mass of particles on the outer (near) circular orbits and would therefore increase the tangential velocity dispersion. We will thus use the $M_P(r_k)$ as targets and omit the subscript P in the following. We also include zero-valued higher order mass moments to enforce sphericity.

We assume Poisson errors for the radial mass: $\sigma(M_j) = \sqrt{M_j M_{\rm trun}/N}$ where N is the total number of particles used in the particle model. For the errors in the higher order mass moments, we use Monte-Carlo experiments in which we generate particle realizations of the

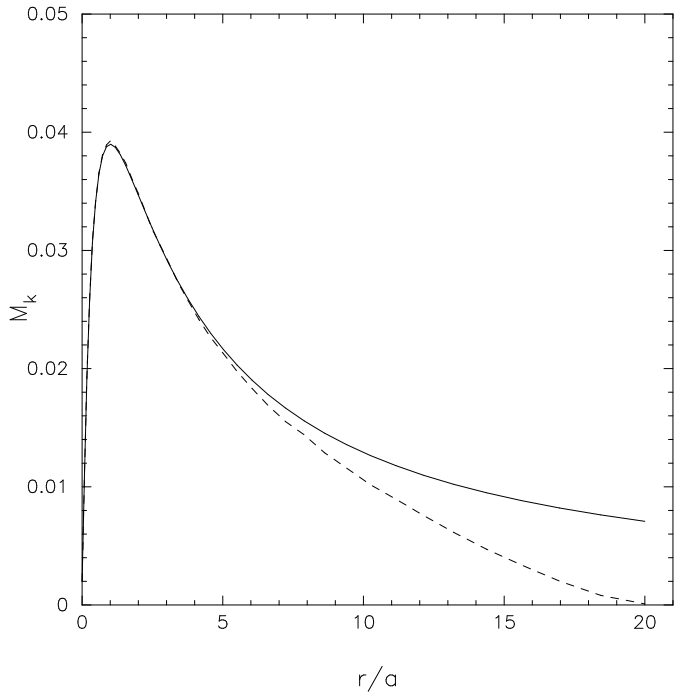

Figure 2.3: The mass in shells profile computed from equation (2.36) is shown as the solid line, whereas the dashed line illustrates the mass profile computed from a spherical Hernquist particle model generated from a truncated DF.

density field of the target model using 1.8×10^6 particles, which is the same number as in the χ^2M2M models.

Kinematics of the target can be computed from a DF. We use the isotropic DF (Hernquist 1990, Carollo et al. 1995)

$$f(E) \propto \frac{1}{(1-q^2)^{5/2}}\big(3\arcsin(q) + q(1-q^2)^{1/2} \times (1-2q^2)(8q^4-8q^2-3)\big) \tag{2.39}$$

with $q = \sqrt{-aE/GM}$, and E is the energy. We determine kinematic observables of the target on a projected radial grid with 30 shells, quasi-logarithmically spaced in radius and bounded by $R_{\rm min} = 0$ and $R_{\rm max} = 10 = 5.51 R_{\rm eff}$. On the shell midpoints we compute the h_2 and h_4 moments of the isotropic Hernquist model from the DF of equation (2.39). We will use integral field-like kinematic data to recover the spherical targets in Section 2.8. More precisely, we multiply the $h_{2,k}$ and $h_{4,k}$ moments by the projected mass of the truncated SIH model within each radial grid shell to obtain the mass-weighted higher order moments $M_k\, h_{2,k}$ and $M_k\, h_{4,k}$, which we use as the target observables. While this procedure is not perfectly self-consistent, because the moments are from the infinite extent analytic DF while the mass is from the truncated DF, the differences are very small. The main advantage of doing this is that it allows us to compute the uncertainties in these kinematic observables, which we assume $\sigma(M_k h_{n,k}) = \sigma(h_n) M_c \sqrt{M_k/M_c}$ with $\sigma(h_n) = 0.005$, M_k the target mass in shell k, and M_c the mass in the central grid shell.

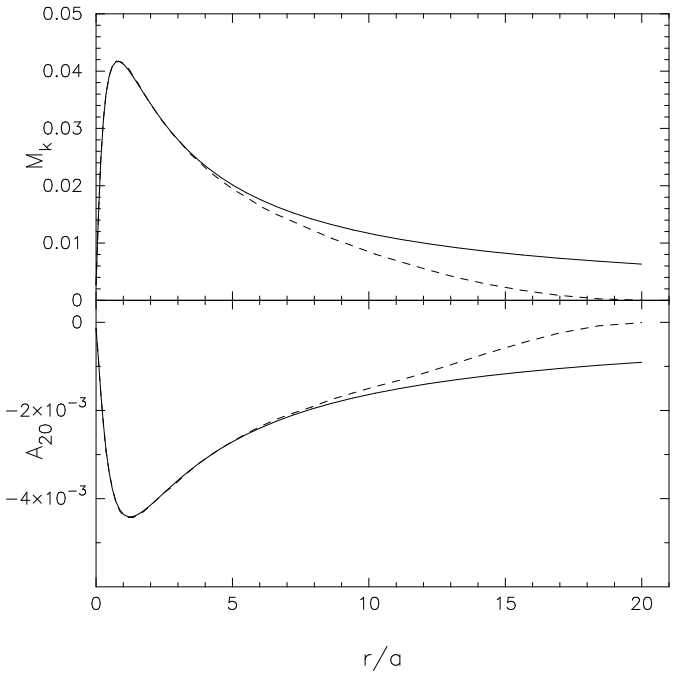

Figure 2.4: The upper panel shows the mass profile computed from equation (2.40) for $q = 0.6$ (solid line) and from a Hernquist particle model made from a DF and squeezed along the z-axis (dashed line). The lower panel is the same but for A_{20}.

2.7.2 An Oblate Three-Integral Target made with NMAGIC

Our oblate target model has density

$$\varrho(m) = \frac{aM}{2\pi q m(m+a)^3} \tag{2.40}$$

where M and a are total mass and scale radius, and $m^2 = R^2 + (z/q)^2$ with q being the flattening. This density belongs to the family of flattened γ models (Dehnen and Gerhard, 1994), with $\gamma = 1$. We compute the gravitational potential from (*cf.* Binney and Tremaine 1987, section 2.3)

$$\varphi(R,z) = -\frac{GM}{2a}\int_0^\infty \frac{\tilde{\psi}(\tilde{m})\mathrm{d}\tau}{(1+\tau)\sqrt{\tau+q^2}} \tag{2.41}$$

with

$$\tilde{m} = \sqrt{\frac{R^2}{\tau+1} + \frac{z^2}{\tau+q^2}}, \tag{2.42}$$

$$\tilde{\psi}(m) = 1 - \frac{m^2+2am}{(m+a)^2}. \tag{2.43}$$

by numerical integration, and tabulate it using a coarse and a fine linear grid in the meridional $(R-z)$ plane. The coarse grid extends to $R = z = 30a$ with 500×500 grid points. To increase the resolution at small R and z we replace the 20×20 "innermost" grid cells at $(R,z) = (0,0)$ to $(1.2a, 1.2a)$ by a finer grid also consisting of 500×500 grid points.

In our experiments, we view the model edge-on along the x-axis as line-of-sight. Our targets are the mass moments $A_{lm,k}$ of the three-dimensional density ρ, and – for these oblate models – the kinematic moments $m\ h_n$, $n = 1, ..., 4$. We define an effective radius $R_{\rm eff} \approx 1.8153a$ which is equal to that of the spherical Hernquist model. We set $M = a = 1$ and $q = 0.6$. The

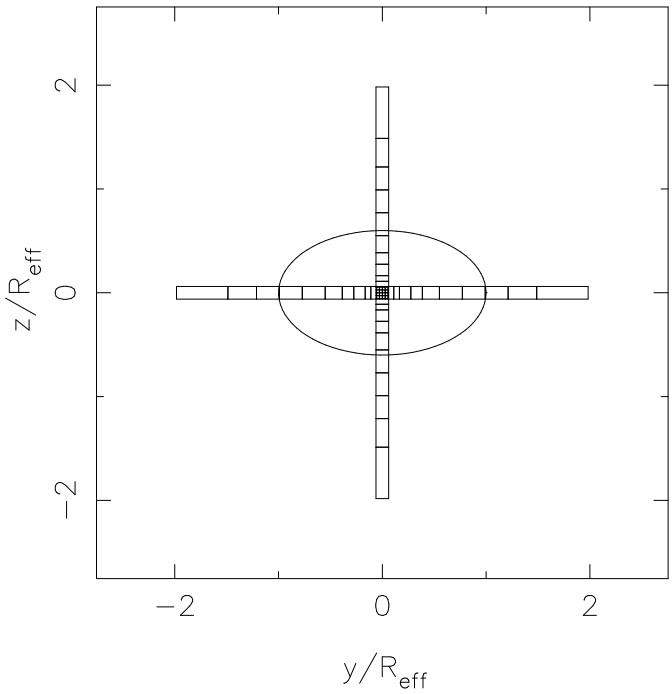

Figure 2.5: Kinematic major and minor axis slits for the oblate models, with the cells along each slit indicated. The ellipse corresponds to one $R_{\rm eff}$ of the equivalent Hernquist model squeezed by 0.6 in the z direction.

target mass moments $A_{lm,k}$ on shell r_k are given by the sum of the contributions of the adjacent shells and are computed through

$$A_{lm,k} = \int Y_{lm}(\theta,\phi)\varrho(\mathbf{x})\gamma_k^{CIC}(r)\mathrm{d}^3x. \tag{2.44}$$

The innermost (outermost) shell is an exception because only the layer immediately exterior (interior) contributes. The setup of the radial grid is identical to that used for the spherical model and for our tests below we use M_k, $A_{20,k}$, $A_{22,k}$, $\cdots$, $A_{66,k}$.

Figure 2.4 compares M_k and $A_{20,k}$ computed from equation (2.40) with $M_P(r_k)$ and $A_{P,20}(r_k)$ obtained from a spherical Hernquist particle realization built from a DF and squeezed along the z-axis by $q = 0.6$. As in Figure 2.3, $M_P(r_k)$ and $A_{P,20}(r_k)$ match M_k and $A_{20,k}$ within $r \lesssim 5a$ but then approach zero at larger radii towards $r_{\rm max}$. This difference is again due to the finite extent of the particle model. Below we therefore use the radial mass profile M_P and the higher mass moments $A_{P,lm}$ as targets, and again we omit the subscript P in the following.

We assume errors in the target mass profile $\sigma(M_j)$ as for the spherical model. For the errors in the higher order mass moments, we use Monte-Carlo experiments in which particle realizations of the density field of the target model are generated using 5×10^5 particles, which is the same number as in the χ^2M2M models.

In our oblate models we attempt to recover the target system from both slit and integral field kinematic data. Thus as kinematic target observables we use the projected mass-weighted Gauss-Hermite moments along the major and minor axes in Test C, and on a grid of 30×20 points covering positions on the sky in $[-3.6, 3.6] \times [-1.8, 1.8]$ in Test D. A schematic representation of the slit setup is shown in Figure 2.5. The slits extend out to about $2R_{\rm eff} \simeq 3.6$.

The target kinematics are determined from a 4×10^6 particle representation of a maximally rotating three-integral model for the density distribution of equation (2.40) with $q = 0.6$. This is constructed by first evolving an isotropic spherical Hernquist model to the desired shape, using χ^2M2M, and then switching the in-plane velocity vectors of all particles with positive

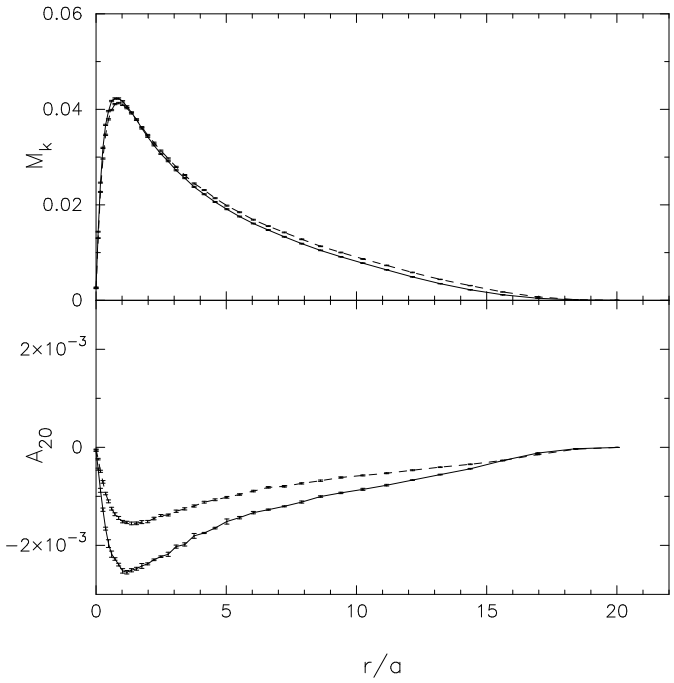

Figure 2.6: Target mass and A_{20} profiles for the triaxial models. The solid line shows target T54 while the dashed line shows target T53.

angular momentum J_z to negative J_z, leading to a DF which is still a valid solution of the Boltzmann equation (Lynden-Bell, 1960). For each slit or integral field cell p we obtain the mass in that cell M_p and the mass-weighted Gauss-Hermite moments $M_p\, h_{1,p}, \cdots, M_p\, h_{4,p}$. We assume errors for the mass-weighted Gauss-Hermite coefficients as for the spherical model: $\sigma(M_p h_{n,p}) = \sigma(h_n) M_c \sqrt{M_p/M_c}$, where M_p is the mass in slit cell p, computed by Monte-Carlo integration. In this case, we set $\sigma(h_n) = 0.005$ (0.003) for the central slit (integral field grid) cell m_c to approximate realistic errors.

2.7.3 Making Triaxial Models with NMAGIC

In the tests below we also explore triaxial Hernquist target models with stellar densities

$$\varrho(s) = \frac{Ma}{2\pi x_0 z_0 s (s+a)^3}, \tag{2.45}$$

where M is the total mass, a the scale radius, and $s = \sqrt{(x/x_0)^2 + y^2 + (z/z_0)^2}$. Here y is the longest axis, and the parameters x_0 and z_0 are the axis ratios. As before, we use units with $M = a = 1$ and we define the effective radius with reference to the spherical model, *i.e.* $R_{\rm eff} \approx 1.815$. We generate two targets with different triaxialities, characterized by the triaxiality parameter $T = (1 - x_0^2)/(1 - z_0^2)$ (Franx et al., 1991). The more triaxial target, hereafter T53, has $x_0 = 0.9$ and $z_0 = 0.8$ ($T = 0.53$) whereas the less triaxial target, hereafter T54, has $x_0 = 0.85$ and $z_0 = 0.7$ ($T = 0.54$). In both cases the target is observed along its intermediate (x-)axis.

Like our oblate target model, the triaxial models cannot be represented by a DF based on the integrals of motion. We therefore construct them through particle realizations via a two step process. Starting from a spherical Hernquist particle realization made from a DF as before, we squeeze this along the x- and z-axes by factors x_0 and z_0, respectively, and compute the desired target density observables M_k and the higher order mass moments $A_{20,k}$, $A_{22,k}$ up to $A_{60,k}$ using the same radial binning as in the spherical and oblate targets. A_{lm} components

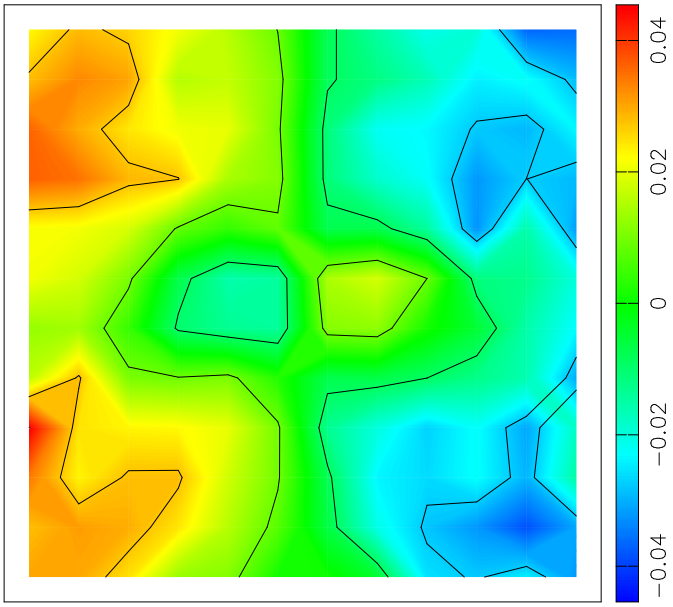

Figure 2.7: Line-of-sight velocity field of the rotating triaxial particle model (RT54K) as seen in the inertial frame. The co-rotation radius is $R_{\rm cor} \approx 10R_{\rm eff}$. The FoV extends from $-R_{\rm eff}$ to $R_{\rm eff}$ along each direction. Its lower edge is parallel to the major axis, the line-of-sight is parallel to the intermediate axis. Notice the counter-rotation near the center.

with $l > 6$ are small and we omit them. The squeezing is rigid, *i.e.* without regard to the internal motions. We repeat this 30 times, squeezing the spherical Hernquist model rigidly along random orientations to the desired shapes. From these 30 particle representations of the model we compute the means and one σ variations around the mean for the $A_{lm,k}$. The former are taken as target density observables, the latter as their errors. The uncertainties on the radial mass in shells profile are taken to be $\sigma(M_k) = \sqrt{M_k M_{\rm trun}/N}$ as before. Figure 2.6 shows the target mass and A_{20} profiles as functions of radius for T54 (solid line) and T53 (dashed line) as well as their uncertainties.

After this first step, which only gives target density observables, we then use χ^2M2M to evolve a spherical Hernquist model to generate self-consistent triaxial particle realizations of T54 and T53. In addition we generate a slowly tumbling version of T54 with corotation radius $R_{cor} \approx 10R_{\rm eff}$, by applying χ^2M2M in the appropriately rotating frame. The final models now have self-consistent kinematics; in order to distinguish them from the purely density targets we refer to them as models T53K and T54K for the non-tumbling models and RT54K for the tumbling model.

These final self-consistent models T54K and RT54K can now be used as targets in their own right, and we can compute (observer frame) target kinematics $m_p h_{n,p}$ from them. We compute the kinematics of both T54K and RT54K on a 12×12 grid extending from $-R_{\rm eff}$ to $R_{\rm eff}$. For the uncertainties in the kinematic observables we adopt $\sigma(m_p h_{n,p}) = \sigma(h_n) M_c \sqrt{M_p/M_c}$ with $\sigma(h_n) = 0.005$ the error in h_n, M_p the mass in grid cell p, and M_c the mass in the central grid cell. The M_p's were obtained directly from the particles. The velocity field of the target system RT54K in the observer's frame is shown in Figure 2.7. This velocity field is characterized by disk-like counter-rotation close to the mid-plane and near cylindrical rotation away from the plane. These kinematics for this slowly tumbling triaxial model represent a valid dynamical model, but are unlikely to be the unique dynamical solution for the model's density distribution.

TEST	ICS	TARGET	ε'	ε''	μ
A	RP	SIH	0.025	$6.32\ 10^{-7}$	$4.3\ 10^{-4}$
A2	RP	SIH	0.025	$1.32\ 10^{-6}$	$4.3\ 10^{2}$
A3	RP	SIH	0.050	$1.24\ 10^{-6}$	$4.3\ 10^{-4}$
A4	RP	SIH	0.100	$6.80\ 10^{-7}$	$4.3\ 10^{-4}$
B	SIH-2	SIH	0.025	$1.76\ 10^{-6}$	$4.3\ 10^{-4}$
C	ORIH	O3I	0.05	$3.94\ 10^{-7}$	0
D	ORIH	O3I	0.05	$3.94\ 10^{-7}$	0
E	T53K	T54K	0.15	$5.06\ 10^{-8}$	$4.3\ 10^{2}$
F	T54K	RT54K	0.15	$3.77\ 10^{-8}$	$4.3\ 10^{2}$

Table 2.1: Tests of NMAGIC carried out in this chapter, with model names and parameters. For all models, we have used $\alpha = 2.1\varepsilon'$.

2.8 Tests of NMAGIC

In this section we will use the χ^2M2M algorithm to solve some modeling problems of increasing dimensionality and complexity, starting with spherical systems and ending with rotating triaxial models. The goal of these experiments is to investigate the convergence of the code, the quality with which various data are modeled, and the degree to which known properties of the target models can be recovered from their simulated data. We will see how these issues depend on the initial model, geometry, and amount of data available.

Table 2.1 lists all the experiments that we have carried out, including the target and the initial model identifications. We will refer to the final χ^2M2M models by the prefix 'F' to the test model name (e.g., FA for the final model of Test A). Generally, these final models are obtained in two steps. First we use only the target density observables in the χ^2M2M algorithm, and once these have converged, we add the kinematic observables. Finally, we integrate all orbits for some time in the potential without χ^2M2M corrections to test whether equilibrium has been reached. Unless mentioned otherwise, we use 1.8×10^6 particles and set the entropy parameter μ to a small ($\ll 1$) value; see the discussion in Section 5.1.1. In most experiments, the particle distribution is evolved in the fixed target potential (this is analogous to the Schwarzschild modelling approach), but we include one test (model E) in which we also let the gravitational potential evolve.

2.8.1 Spherical Models

Initial model and time-evolution

The aim of our first experiment, Test A, is to reproduce a spherical isotropic Hernquist (SIH) model by a 1.8×10^6 particle model. We start by generating a Plummer model from its DF (*e.g.* Binney and Tremaine 1987), using the method described in Debattista and Sellwood (2000). The DF of the Plummer model is truncated at $\Phi(r_{\max})$, with $r_{\max} = 20$, and has a scale length $b = 1$ and unit total mass. We then relax these particles in the analytic Hernquist potential, which is held fixed while the particle orbits are integrated. We refer to the resulting particle distribution as initial model RP (relaxed Plummer).

Then with χ^2M2M we first adjust the density distribution of model RP to that of the target SIH, using as target observables $M_k = \sqrt{4\pi} A^t_{00,k}$ (equation 2.37) and $A^t_{lm,k} = 0$ for $1 < l \leq 6$, $0 < m \leq l$ (equation 2.23) with Monte Carlo errors estimated as described in Section 2.7.1. After convergence the even kinematic moment observables $M_k h_{2,k}$ and $M_k h_{4,k}$ are added with errors given also in Section 2.7.1. Finally the system is integrated for some time without applying the χ^2M2M corrections.

The second experiment B is identical to A except that instead of model RP we use a second

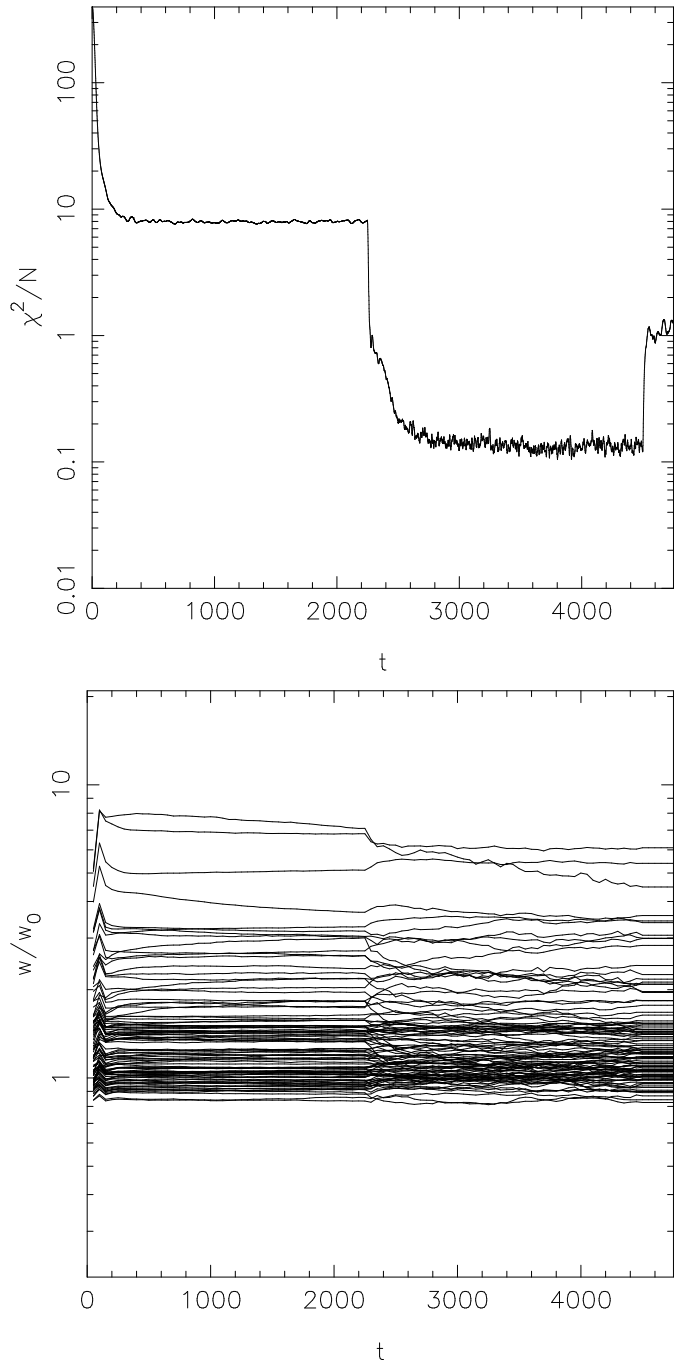

Figure 2.8: (a) Top: Time evolution of χ^2 in test A. (b) Bottom: Time evolution of a set of 100 particle weights in test A. w_0 is the initial weight of the particles; $w_0 = 1/N$. The time-interval plotted includes a first phase of density adjustment ($t \leq 2250$), a second phase of density and kinematic adjustment ($2250 < t \leq 4500$), and a final phase of free evolution during which the weights do not change ($t \geq 4500$). Time is in units where the dynamical time at the half-mass radius is 6.0, and the dynamical time at $r_{\max}$ is 150.

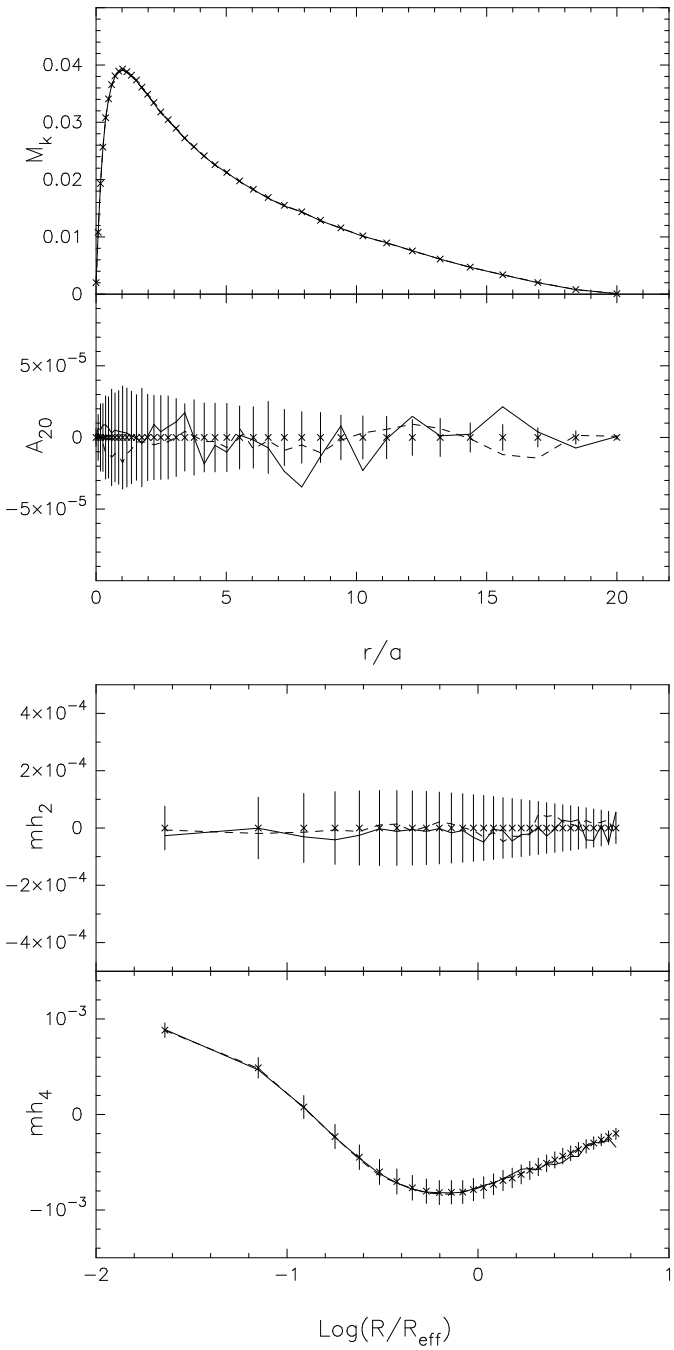

Figure 2.9: (a) Top: Radial mass and A_{20} profiles for the target model SIH and the final models FA from Test A (solid line) and FB from Test B (dashed line). (b) Bottom: Kinematic profiles $m\,h_2$ and $m\,h_4$, for the same models. – In all panels, the data points with errors correspond to the SIH target, the solid line to the final particle model FA, and the dashed line to the final model FB. The error bars in the target mass distribution are not shown as they are smaller than the symbol sizes. The absolute errors shown decrease outwards due to the mass weighting; the corresponding relative errors increase outwards.

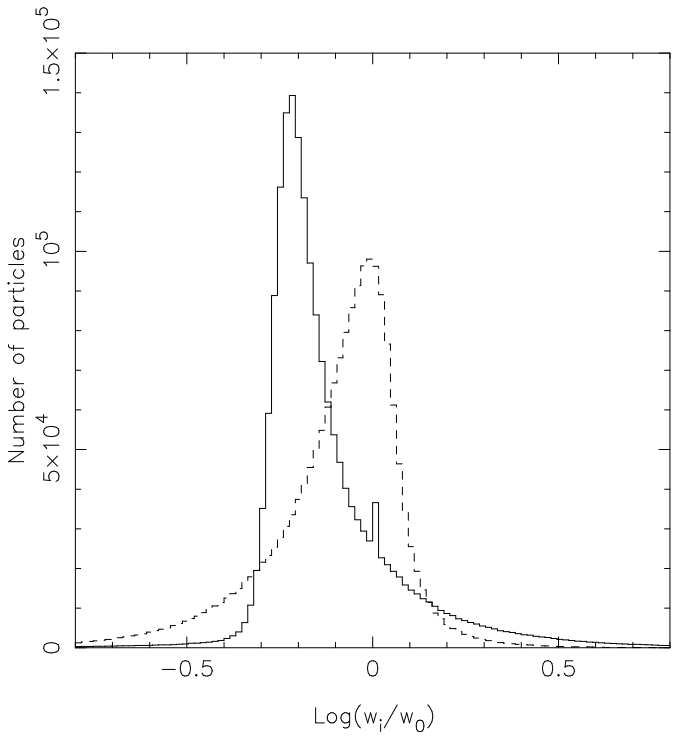

Figure 2.10: Histogram of the particle weights in the final FA model, obtained from Plummer model initial conditions (solid line). The dashed line shows the histogram of particle weights when spherical Hernquist ICs with scale length $a = 1.4$ were used (FB). w_0 is the initial weight of the particles; $w_0 = 1/N$ in all cases.

Hernquist model SIH-2 as initial conditions for NMAGIC. SIH-2 differs from the target model SIH in that its radial scale length $a = 1.4$ instead of $a = 1$.

Figure 2.8a shows the time evolution of χ^2/N_o of the particle model A during and after the χ^2M2M evolution. Throughout N_o refers to all the observables, density and kinematics, regardless of whether they are being used in the FOC or not; thus N_o is a constant. The time evolution of a sample of 100 particle weights of the SIH particle model is presented in Figure 2.8b. From these figures one sees that the overall χ^2/N_o decreases quickly at the beginning of both phases (density adjustment only phase, and a density and kinematic observable adjustment phase). However, particle weights keep evolving for significantly longer time-scales. For this reason we integrate and adjust particle weights in both phases for relatively long times, about 15 dynamical times at $r_{\max}$.

Convergence to the target observables for different initial conditions

The fit of the final particle models FA and FB to the observables is illustrated in Figure 2.9. The top panel shows the radial mass and A_{20} coefficient, whereas the bottom panel shows the kinematic targets and final model observables for $m\,h_2$ in the upper and $m\,h_4$ in the lower panel. As can also be seen from Fig. 2.8, the final model fits the input data to within 1σ. The corresponding error bars are smaller than the crosses in the top panel of Fig. 2.9; see Fig. 2.6 for an example. The same is true for A_{20} except when the target values are zero as in Fig. 2.9. Error bars for the mass observables are therefore not plotted in this and subsequent similar figures.

All model observables in Fig. 2.9 are temporally smoothed observables as in equation (2.19). After some free evolution with χ^2M2M turned off both models fit the target data within the errors. The free evolution is necessary because χ^2M2M pushes the model towards a perfect fit to the observables, at the expense of continually changing particle weights. Deviations are largest

in the outer parts where orbital time-scales are longest. Model FB, which had an initial particle distribution closer to the target, is generally smoother and fits the data better, but differences are within the errors. NMAGIC achieved satisfactory models even from the less favorable, cored Plummer initial conditions.

Figure 2.10 compares the histogram of final particle weights of the FA and FB models, all normalized by their initial weight. Model FA has a significant tail towards high weights, and a peak at correspondingly lower particle weight such that the mean particle weight is the same as for the more symmetric weight distribution of model FB. On average, the weights of particles in model FA had to change by more than those in model FB. We can quantify this by defining an *effective* particle number $N_{\rm eff}$ characterizing mass fluctuations through

$$N_{\rm eff} \equiv N \frac{\overline{w}^2}{\overline{w^2}}, \tag{2.46}$$

where $\overline{w}$ and $\overline{w^2}$ are the mean and mean-square particle weights. This reduces to N for equal-mass particles, to one when one particle dominates, and discards particles with near-zero weights. For the final models FA and FB the effective numbers of particles are $N_{\rm eff} = 5.7 \times 10^5$ and 1.5×10^6, respectively, while for both models $N = 1.8 \times 10^6$.

The origin of this difference between the two models can be seen from Figure 2.11a, which plots the radial density profile of the target SIH (stars), the initial models RP and SIH-2, and the temporally smoothed final models. We computed the densities using the identical radial grid as was used for the mass targets. The density profile of the SIH target is well reproduced by the final particle models FA and FB across more than a factor of 100 in radius. The largest relative deviation in the density $\delta\rho/\rho$ occurs at small radii and never reaches more than 5%. In this region, model RP has few particles and the large relative error is due to Poisson noise. Model FB, which starts out closer to the target SIH fits better in this region.

Model RP is clearly significantly less dense than SIH inside $r \simeq 0.3a$; it has a core whereas the target profile is cuspy. Also, it has a steeper outer density profile than the target model. To match model RP to SIH therefore requires NMAGIC to increase the particle masses both in the central regions and in the outer halo of the model. This causes the high-weight tail in the distribution in Fig. 2.10, as we verified by inspecting the positions of particles with $w_i > 2w_0$.

Figure 2.11b presents the differential energy distributions. The final particle model FA matches the analytic differential energy distribution of the isotropic Hernquist model (equation 2.39) very well.

As a final test, Figure 2.12a shows the intrinsic velocities (lower panel) and velocity dispersions (upper panel) of the analytic, untruncated DF and the final χ^2M2M model FA. The match to the target kinematics is good and model FA is nearly isotropic, despite the fact that it has evolved from an initial RP model that is moderately anisotropic. The anisotropy of the initial model RP is shown in Figure 2.12b which compares its intrinsic velocity dispersions σ_r, σ_φ and σ_θ with the analytic σ_r of the SIH target model. The residual anisotropy in model FA is caused by the relative absence of radial orbits resulting from truncating the DF.

Dependence on ϵ' and μ

In the tests described so far, we have used $\epsilon' = 0.025$ for the correction steps in the FOC. In general, small values of ϵ' result in a smooth evolution but slow convergence, whereas large values of ϵ' change the global model too rapidly to attain a properly phase-mixed stationary solution. Thus generally we have found $\epsilon' \lesssim 0.1$ to give good results. This is illustrated in Fig. 2.13, which shows that test A converges to essentially identical density distributions and differential energy distributions for values of $0.025 \leq \epsilon' \leq 0.1$ (models FA, FA3, FA4). Only for the largest value $\epsilon' = 0.1$ do we start seeing small deviations in the density profile of more than a few percent from the target model. Also, the effective particle number [equation (2.46)] decreases from

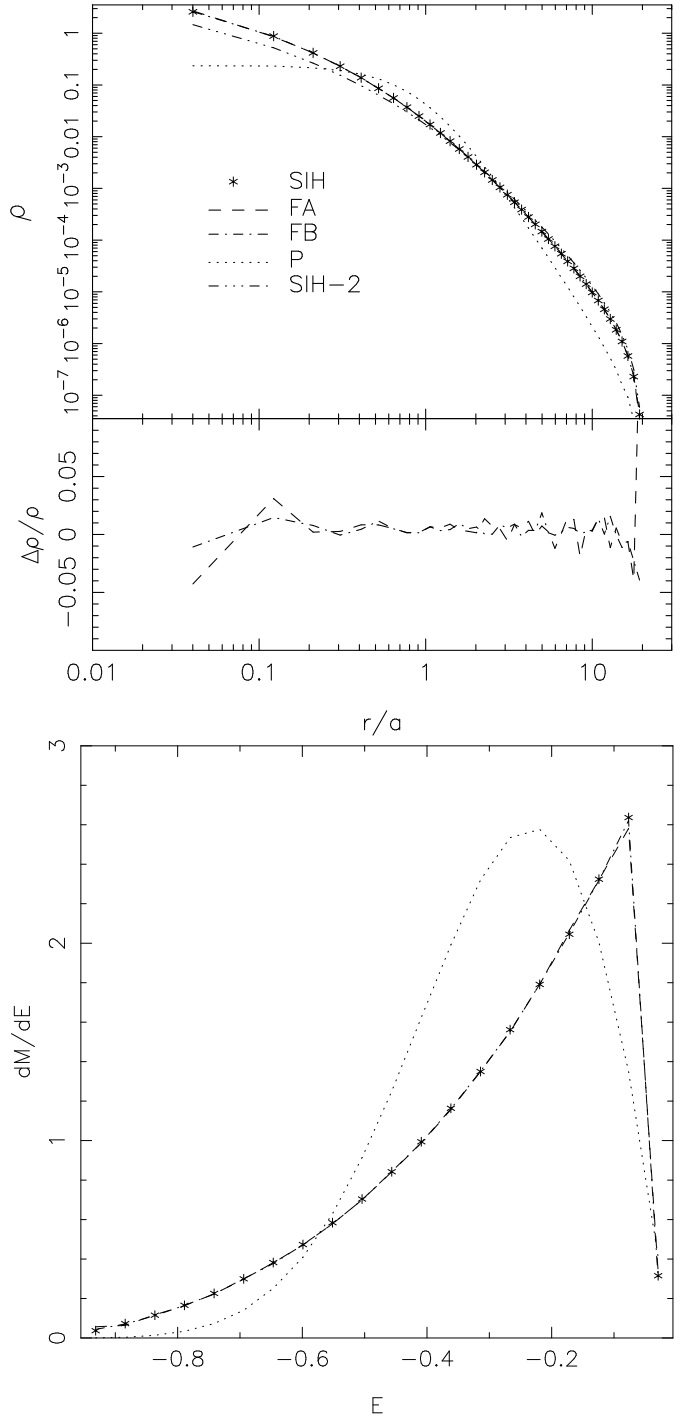

Figure 2.11: (a) Top: Radial density profiles in the spherical models. Uppermost panel: Density profiles for the Hernquist target profile, SIH (stars), the final models FA (dashed line) and FB (dash-dotted line), and their respective initial condition models RP and SIH-2 (dotted and dash-triple-dotted lines). Middle panel: Relative deviation from the target density $\Delta\rho/\rho$, for the two models FA and FB using the same line styles. (b) Bottom: Differential energy distributions. The truncated analytic Hernquist DF used for target SIH is shown by the star symbols. The dashed line corresponds to the final χ^2M2M model FA, and the dotted line indicates the relaxed Plummer initial conditions RP.

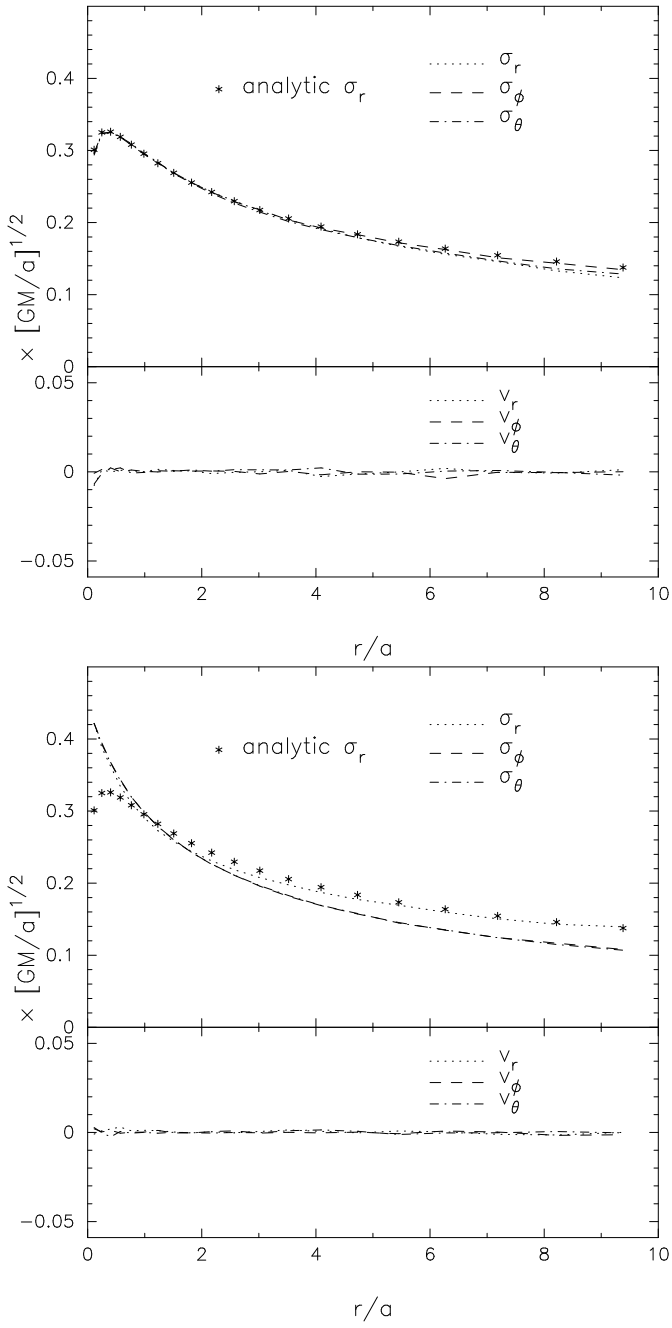

Figure 2.12: (a) Top: Internal kinematics of the final model FA. The upper panel show σ_r, σ_φ and σ_θ, the lower panel the v_r, v_φ and v_θ. The stars correspond to the analytic σ_r from the untruncated DF. Model FA is very nearly isotropic and has negligible rotation, despite starting from anisotropic initial conditions. (b) Bottom: Anisotropic internal kinematics of the initial model RP. The dotted, dashed, and dash-dotted lines show σ_r, σ_φ, and σ_θ of the RP particle model. For comparison, the solid line corresponds to the analytic σ_r of the untruncated analytic DF of the SIH target model.

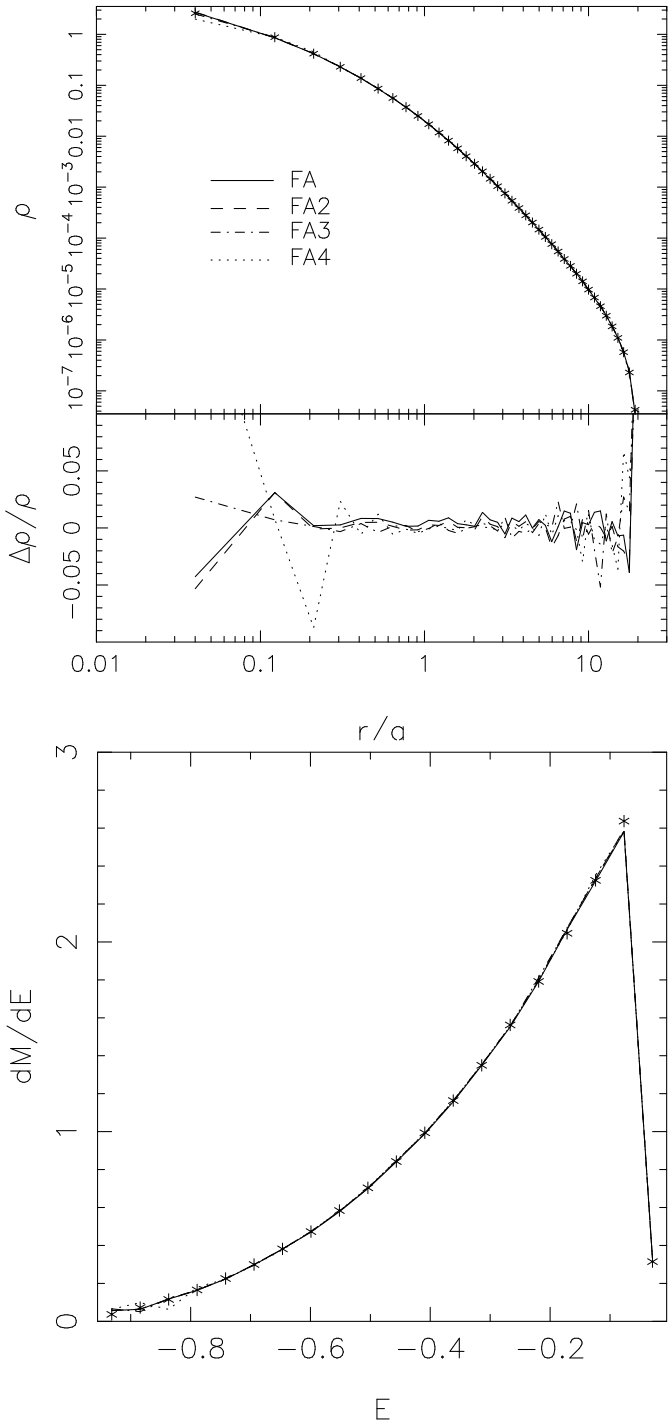

Figure 2.13: (a) Top: Radial density profiles for various spherical models constructed for the Hernquist target profile, SIH. Upper panel: Density profiles for the target model (stars), the model FA (dashed line) and several tests that differ from model FA by the values of the parameters ε' and μ (see Table 1). Middle panel: Relative deviation from the target density $\Delta\rho/\rho$, for the same models. (b) Bottom: Differential energy distributions. Stars: target model SIH. Lines: same models as in top panel.

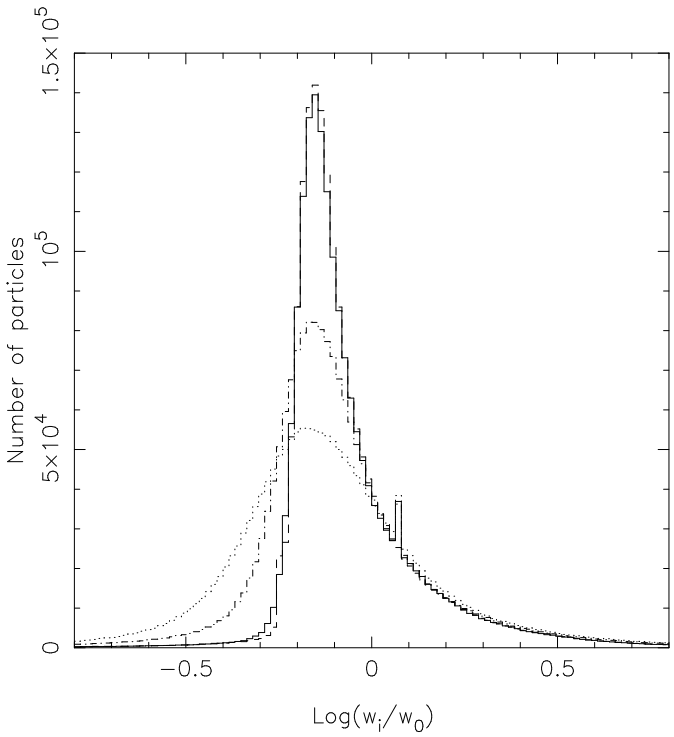

Figure 2.14: Histogram of the particle weights in the final FA model, obtained from Plummer model initial conditions (solid line). The other histograms show the particle weight distributions for models FA2 (dashed), FA3(dash-dotted), and FA4 (dotted). w_0 is the initial weight of the particles; $w_0 = 1/N$ in all cases.

5.7×10^5 through 3.3×10^5 to 1.0×10^5 for models FA, FA3, and FA4, respectively. Thus we will generally use $\epsilon' < 0.1$, but because the speed of convergence also depends on the number and kind of observables used for the corrections, we have sometimes also increased ϵ' slightly. Figure 2.14 shows the distributions of particle weights for these models. They develop larger wings for larger values of ϵ'. Because particles weights are then changed by larger amounts, the reshuffling is greater until convergence is reached.

In models FA and FB, we have also set the entropy parameter μ to a small ($\ll 1$) value, which allows the NMAGIC code to concentrate on fitting the data. (Note that, because the term $K_{ij}\,\widetilde{\Delta}_j/\sigma(Y_j)$ in the FOC is large, even $\mu = 1.0$ leads to only a small contribution of the entropy terms in the FOC). While the purpose of not setting μ to zero exactly originally was to prevent overly large fluctuations in the particle weights, in fact, a test with $\mu = 0$ has given essentially identical results to the ones reported. Fig. 2.13 shows that also for model FA2 with 10^6 times larger entropy parameter than in model FA, the target density and differential energy distribution are fitted equally well as before. Generally, the best value to use for the entropy depends on the initial model, the data to be fitted, and the intrinsic structure of the target, and it must be determined separately for each application. A more systematic investigation of the effect of the entropy term is therefore deferred to the next chapter in which we will use χ^2M2M to model and determine mass-to-light ratio, anisotropy, etc., for a real galaxy.

2.8.2 Oblate Models

The task we set the algorithm here is a difficult one: starting from a non-rotating system, we see whether we can recover the maximally rotating three-integral model described in Section 2.7.2, in which the weights of all counter-rotating particles should be zero. We perform two such experiments, one using slit data as kinematic targets (Test C), the second using integral field

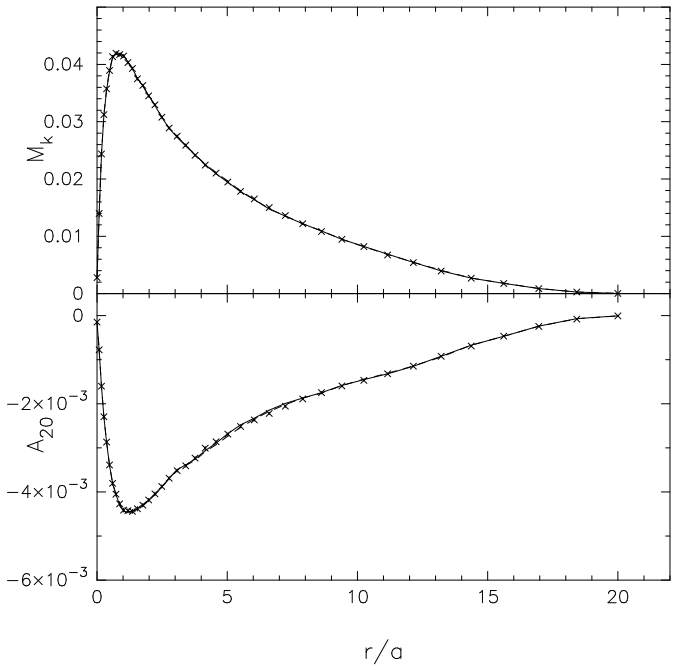

Figure 2.15: The mass and mass A_{20} profiles for the oblate models. The data points show the target and the lines shows the converged models FC (dashed) and FD (full).

kinematic targets (Test D). As in the spherical experiments, we keep the potential fixed while evolving the system with χ^2M2M in runs C and D.

Both experiments start from an initial model which is constructed by relaxing a spherical Hernquist particle model consisting of 5×10^5 particles in the oblate potential. As in experiments A and B, we then apply χ^2M2M in 2 steps, first for the density alone, and when this has converged, for both the density and kinematics. The density part of the runs is identical for experiments C and D.

Figure 2.15 plots the mass and A_{20} radial profiles of the target (error bars) and the final χ^2M2M models FC and FD. As in the spherical tests, the target density distribution is very well fitted by the χ^2M2M models.

The mass-weighted kinematics along the major and minor axes of model FC are shown in Figure 2.16, while Figure 2.17 show the as-observed kinematics of both models. The latter are calculated by dividing the mass-weighted moments by the mass in the slit resp. grid cell, and using the relations $v = v_{\rm targ} - \sqrt{2}\sigma_{\rm targ}h_1$ and $\sigma = \sigma_{\rm targ} - \sqrt{2}\sigma_{\rm targ}h_2$ (*e.g.* , Rix et al. 1997). All kinematic quantities for the reconstructed models are shown $\Delta t = 500$ ($\gtrsim 3$ dynamical times at $r_{\rm max}$) after switching off the χ^2M2M corrections. The fits are generally excellent except for the higher order moments near the boundaries of the kinematic fit regions, where counter-rotating particles with high energies still make significant contributions, because their weights have not yet been sufficiently reduced.

Figure 2.18 showing the weight distributions for both models FC and FD clearly illustrates the stronger constraints placed on the model by the integral field data. In both models, the NMAGIC code works at reducing the weights of the counter-rotating particles, but has clearly gone a lot further in model FD.

Finally, in Figure 2.19 we show the distribution of weights in the (E, L_z) plane for the target model, initial relaxed model, and the two models FC and FD. The success of the χ^2M2M method in removing the counter-rotating particles amply present in the initial model is apparent, particularly for model FD. Of course, in applications aimed at obtaining a best-fit representation of some galaxy kinematic data it would have been smart to start the iterations from an initial

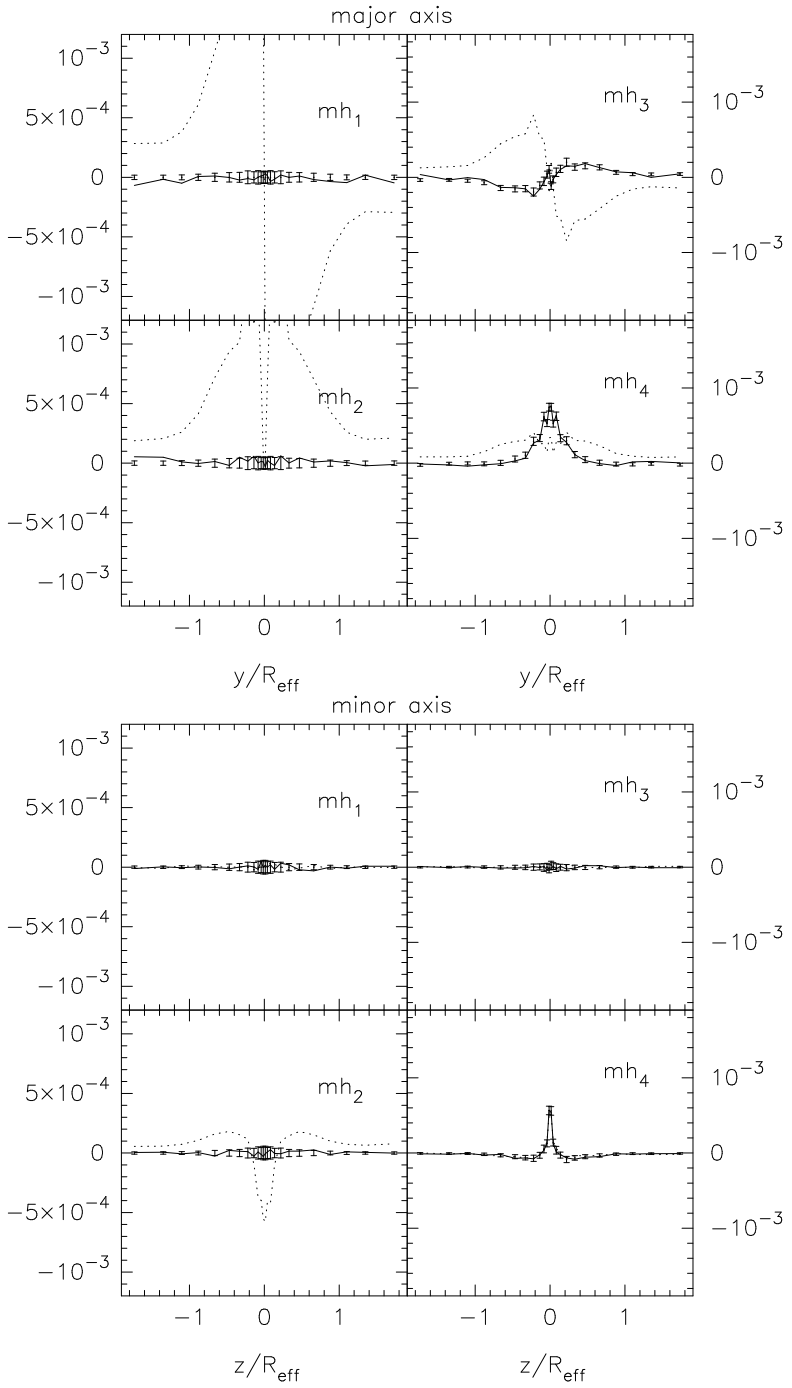

Figure 2.16: Mass-weighted higher order moments along the major and minor axes for the slit-reconstructed oblate model FC. The target observables are shown as error bars, whereas the model observables for model FC are indicated by the dashed lines, respectively. Kinematics along the major axis are shown on the left and those along the minor axis on the right.

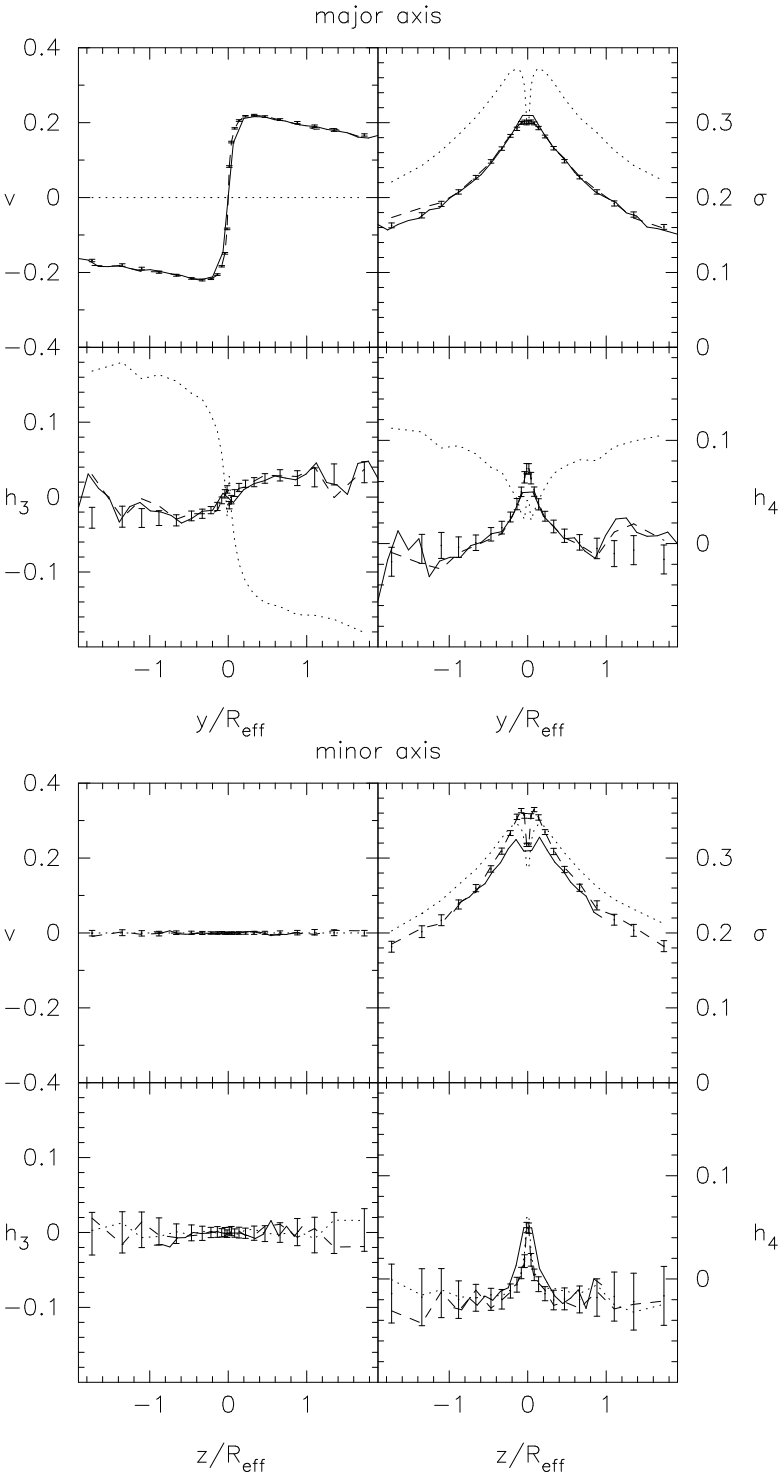

Figure 2.17: Gaussian best fit velocity (top left), velocity dispersion (top right), Gauss-Hermite moments h_3 (bottom left) and h_4 (bottom right) along the major axis (left) and minor axis (right), for the models with slit data targets (dashed line), integral field kinematic targets (full), and the initial model (dotted). The error bars show the target kinematics.

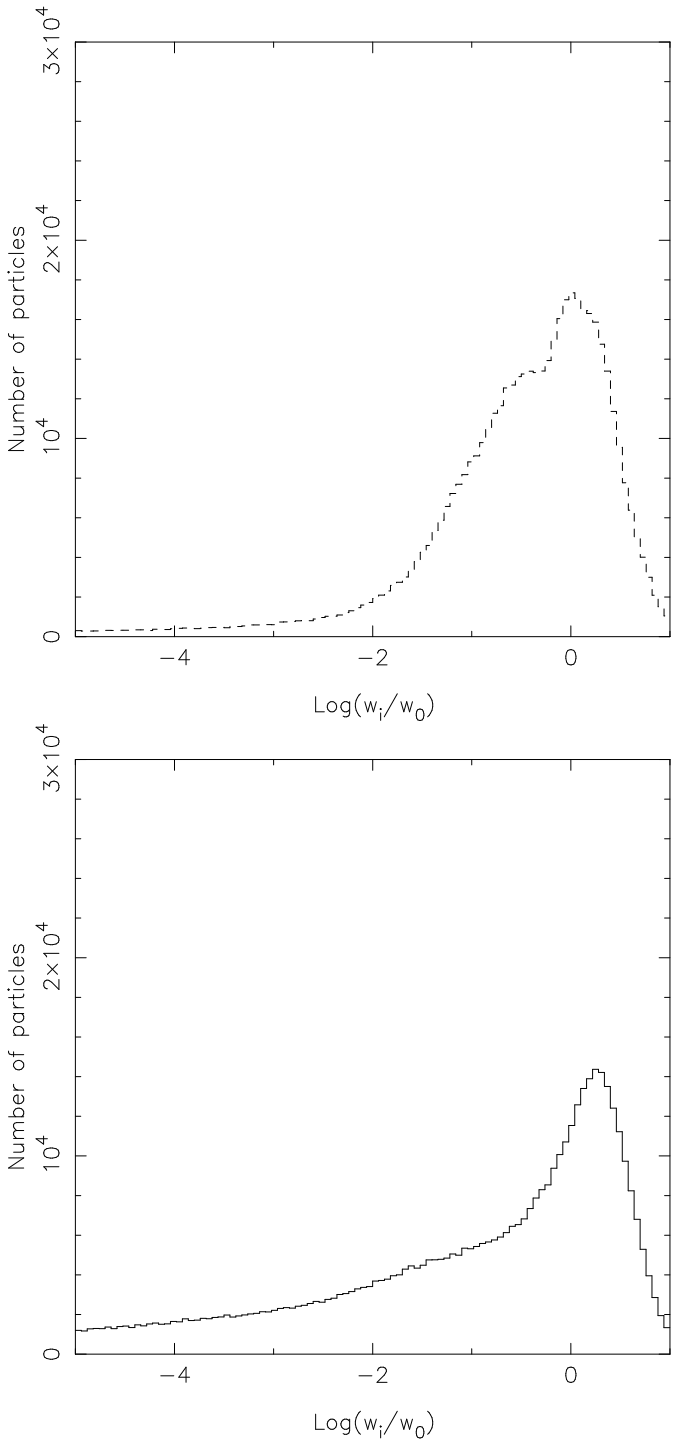

Figure 2.18: Distribution of particle weights in the final models FC (top) and FD (bottom).

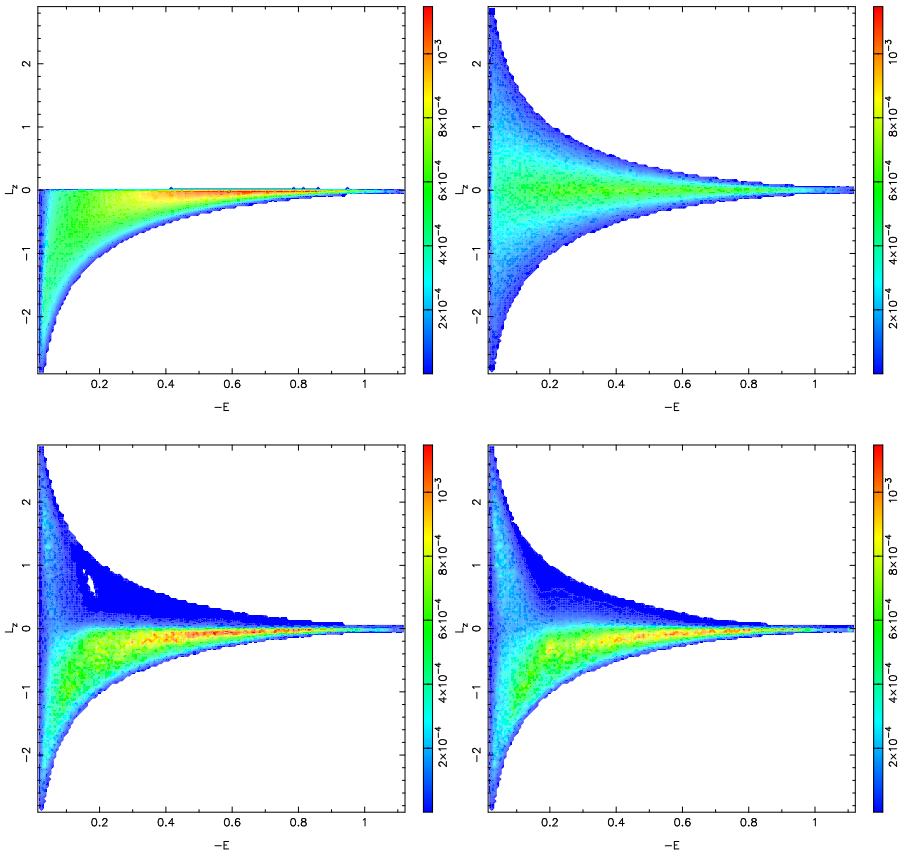

Figure 2.19: Particle weight distributions projected onto the (E, L_z) plane, for the maximally rotating three-integral target (top left), the initial relaxed isotropic Hernquist model (top right), and the two models reconstructed from density and slit kinematic targets (FC, bottom right) and from density and integral field kinematics (bottom left).

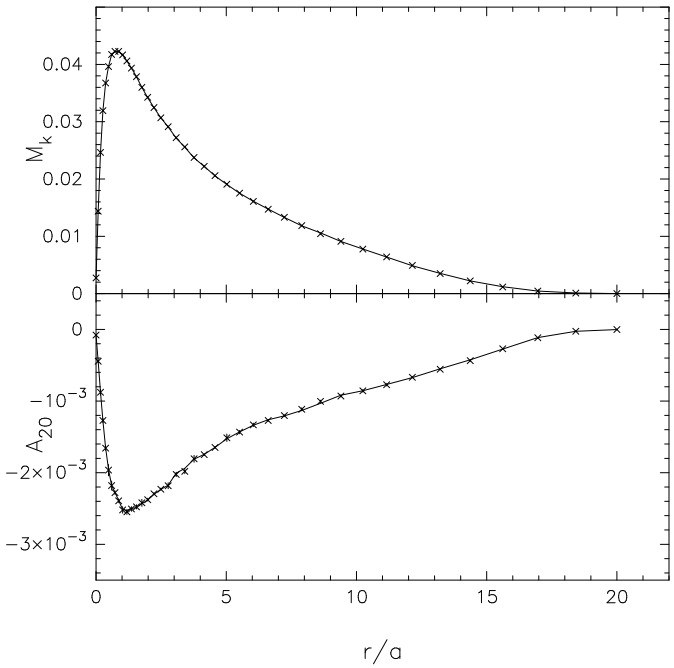

Figure 2.20: Mass and A_{20} profiles for experiment E. The dots show the target T54K and the solid lines show FE.

model that is better adapted to the problem at hand.

2.8.3 Triaxial Models

Evolving the potential self-consistently

We illustrate NMAGIC's capabilities with two very different triaxial model experiments. In run E, we start with the self-consistent model T53K as initial conditions and use NMAGIC to converge to target T54K. With this model, we test the full capabilities of χ^2M2M, which make this technique more general than Schwarzschild's method: in model E, we solve for the potential as the system evolves and follow the model in its self-consistent potential throughout, akin to an N-body experiment. For this purpose we use the spherical harmonic potential solver described in Section 2.3 above and update the potential after every 25 χ^2M2M steps.

The resulting final model FE gives an excellent match to the density of the target model T54K, as is apparent from comparing the M_k and A_{20} profiles in Figure 2.20. Figure 2.21 shows the kinematics within $R_{\rm eff}$ of the models T54K and FE. All mass-weighted kinematic observables $m\,h_1$,..., $m\,h_4$ of the final model match the target observables at better than one σ over almost the entire FoV, except for a few isolated regions reaching two σ. The random location of these deviations imply that they are due only to Poisson noise in the target model, the observables of which have not been temporally smoothed.

Rotating vs. non-rotating models

Test F is an interesting experiment in different ways. Starting from T54K, we use NMAGIC to attempt to converge to the observables of the tumbling target model RT54K, with a triaxial model which does not tumble but remains stationary relative to the observer. Thus this experiment explores whether it is possible to identify a kinematic signature of slow figure rotation in elliptical galaxies. Since the initial conditions possess neither rotation nor internal net stellar streaming, if this model fails to converge it may well be because the problem admits no solution. Because of this, test F is interesting in its own right, apart from as a validation of NMAGIC.

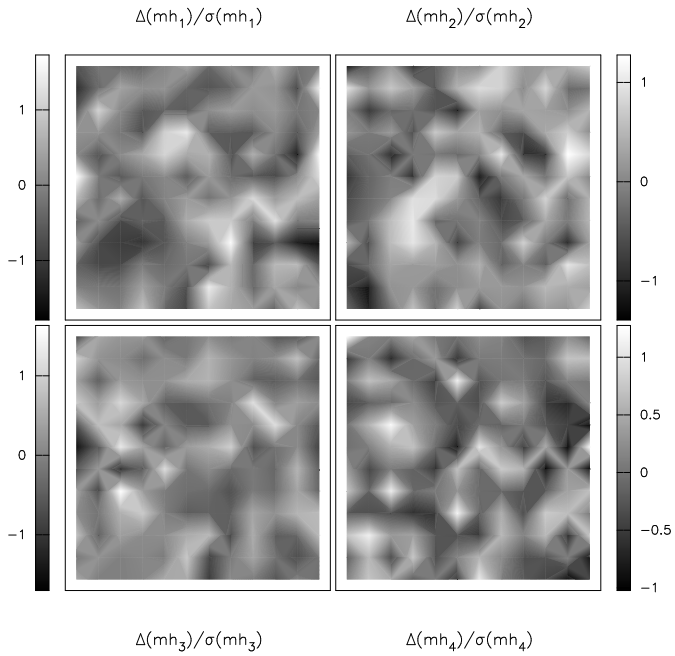

Figure 2.21: The difference between kinematics in model T54K and model FE. The observables of FE are the temporally smoothed mass-weighted moments while those of T54K are not temporally smoothed. The differences have been divided by the corresponding assumed errors. The FoV extends from $-R_{\rm eff}$ to $R_{\rm eff}$ along each direction.

In fact, NMAGIC was able to converge the mass-weighted kinematic moments to within about one σ of their target values; however, the residuals maps (Figure 2.22) show spatially correlated residuals in mh_1. When we compare the global velocity field of model FF with that of RT54K we find that the degree of cylindrical rotation around the tumbling axis (z-axis) is higher in RT54K than it is in model FF (Figure 2.23). Near the mid-plane, instead, the velocity field of both models is very similar, including the counter-rotation seen near the center. We can explore whether the residual differences are due to having assumed too large errors in the mass-weighted moments by decreasing the errors by a factor of five. The corresponding final model looks very similar to model FF but now with reduced $\chi^2 > 4$. Thus the difference is likely intrinsic and can be used to recognize a tumbling galaxy. A more complete analysis of this problem will be undertaken elsewhere (De Lorenzi et al. in progress).

2.9 Conclusions

We have presented a made-to-measure algorithm for constructing particle models of stellar systems from observational data, building on the made-to-measure method of Syer and Tremaine (1996, ST96). An important element of our new method is the use of the standard χ^2 merit function at the heart of the algorithm, in place of the relative error used by ST96. The improved algorithm, which we label χ^2M2M, allows us to assess the quality of a model for a set of target data directly, using a statistically well-defined quantity (χ^2). Moreover, this quantity is well-defined and finite also when a target observable takes on zero values.

This property has enabled us to incorporate kinematic observables including higher-order Gauss-Hermite moments into the force-of-change equation. Kinematic and density (or surface density) observables can then be used simultaneously to correct the particle weights. The price of changing to χ^2M2M from the original formulation is that the kernels which project the particle weights and phase-space coordinates into model observables cannot themselves depend on the particle weights. In general this is quite natural for (volume or surface) density observ-

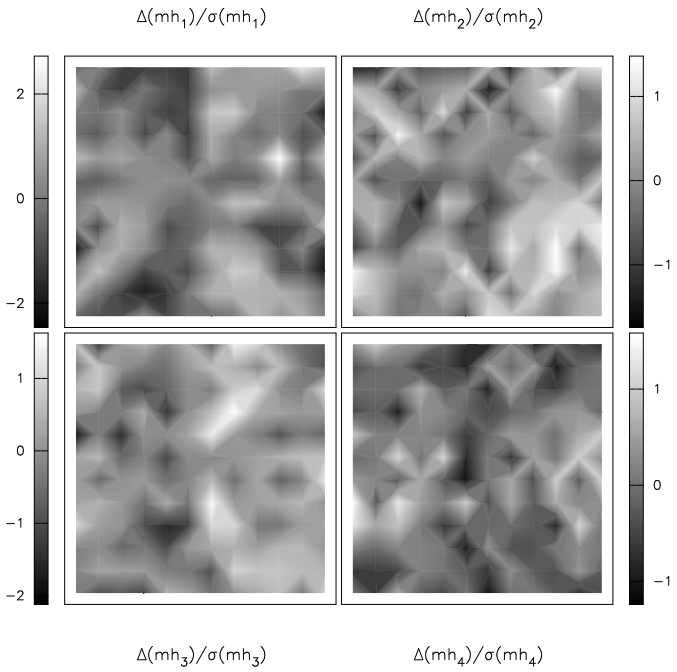

Figure 2.22: The difference between kinematics in target RT54K and model FF. The observables are the mass-weighted higher order moments, and have been divided by the corresponding assumed errors. The kinematics of RT54K are instantaneous but those of FF are time-averaged. The FoV extends from $-R_{\rm eff}$ to $R_{\rm eff}$ along each direction.

ables. For the kinematics this means that we need to use mass-weighted kinematic observables. Nonetheless, this is not a significant limitation.

We have implemented the χ^2M2M method in a fast, parallel code, NMAGIC. This code also incorporates an optional but fast potential solver, allowing the potential to vary along with the model density. Its implementation of the χ^2M2M algorithm is highly efficient, with a sequential fraction of only $\sim 1\%$. This has allowed us to build various models with large numbers of particles and based on many observables, and to run them for $\sim 10^6$ steps.

Then we have carried out a number of tests to illustrate the capabilities and performance of NMAGIC, employing spherical, oblate and triaxial target models. The geometric flexibility by itself is one of the main strengths of the method – no symmetry assumptions need to be made.

In the spherical experiments NMAGIC converged to the correct isotropic model from anisotropic initial conditions, demonstrating that a unique solution, if present, can be recovered. Both the truncated distribution function and the intrinsic velocity dispersions were recovered correctly. Two initial models with different density distributions were used in these experiments. While both converged to the final isotropic model, that with density closer to the density of the final model had smaller final deviations from the target observables, and a narrower distribution of weights. In both experiments, the observables (density and integral field-like kinematics) each converged in a few dynamical times at the outer boundary $t_{d,o}$, whereas the particle weights kept evolving for significantly longer, $\sim 10t_{d,o}$.

In the oblate experiments we gave the algorithm a difficult problem to solve. The target system was a maximally rotating three-integral model in which the weights of all counter-rotating particles were zero. Using density observables and either slit or integral field kinematics, NMAGIC was asked to recover this maximally rotating model starting from an isotropic spherical system relaxed in the oblate potential. After about 100'000 correction steps, particle weights on the counter-rotating side were reduced by a factor of ~ 50, the distribution of weights approached that of the target, and a good fit to the kinematic constraint data was achieved. Only near the boundary of the kinematic data did particles on orbits further out, whose weights had

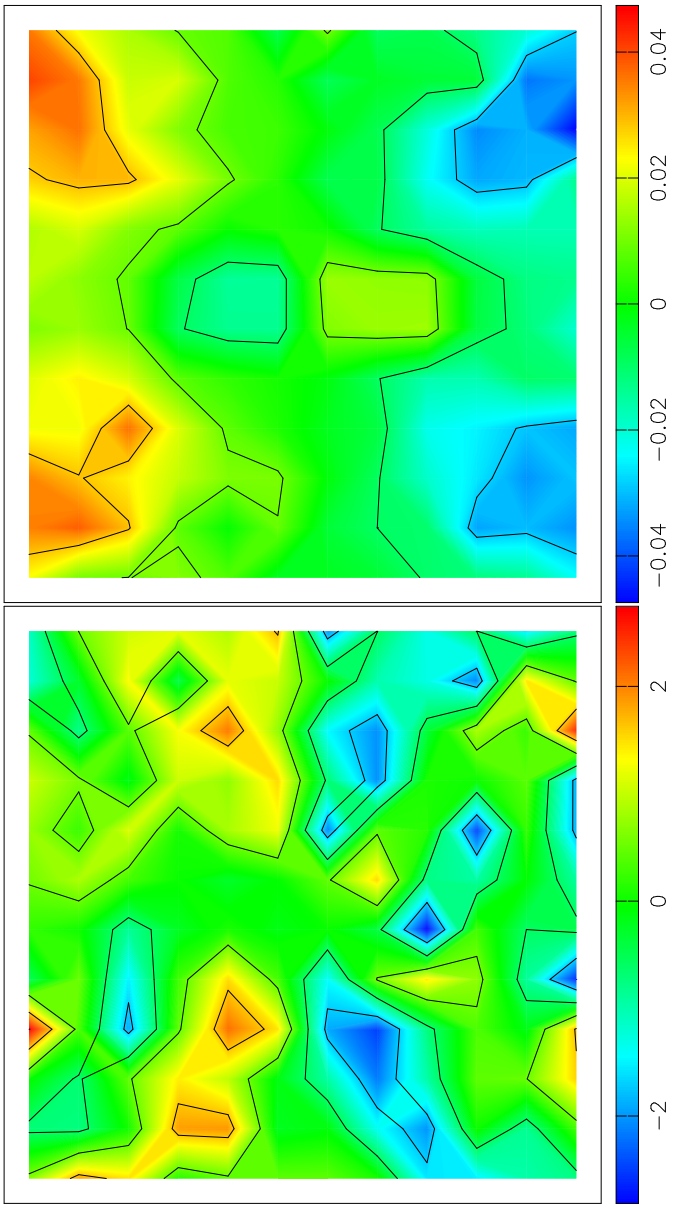

Figure 2.23: Left: Line-of-sight velocity field of the final non-tumbling triaxial particle model FF. Right: Difference of the line-of-sight velocity fields between the non-tumbling triaxial particle model FF and the tumbling target galaxy RT54K divided by the errors as described in the text. We assume an error in the mean velocity $\sigma(v_j) = \sqrt{2}\sigma(h_1)\sqrt{m_c/m_j}\sigma_j$, where we assumed $\sigma(h_1) = -\sqrt{1/2}\sigma(v)/\sigma$ (Rix et al., 1997). In both panels the FoV extends from $-R_{\rm eff}$ to $R_{\rm eff}$ along each direction.

not yet converged, still cause some deviations from the target kinematics. These experiments also clearly showed the advantage of integral field data over slit data for constraining the model.

Our triaxial experiments showed that it is possible to start from one triaxial model and converge to another. We anticipate that this ability will be very useful in constructing models for the triaxial elliptical galaxies with which nature confronts us. One of these triaxial experiments included a potential update step every 25 χ^2M2M steps, demonstrating that including an evolving potential is also practical.

In the final experiment, we first generated a particle model of a slowly tumbling triaxial system to use as a target. We then matched its volume density and line-of-sight kinematics with a stationary model. We showed that the mass-weighted kinematic moments of the figure rotating system was fitted to within one σ by the non-rotating system out to $R_{\rm eff}$. However the residuals in the first order kinematic moment are correlated, which gives a clear signature of tumbling which the non-tumbling model is not able to match, even when the assumed errors are decreased by a significant factor. We thus conclude that, at least for this triaxial system, it is possible to distinguish between internal stellar streaming and pattern rotation within $R_{\rm eff}$ provided a full velocity field is available. A more complete study of this problem will be presented elsewhere.

This experiment also demonstrates the usefulness of the χ^2M2M algorithm for modeling mock (rather than real) galaxies in order to learn about their dynamics. We note that such an experiment would not have been practical with standard N-body simulations.

Compared to the Schwarzschild method, the main advantages of the χ^2M2M algorithm as implemented in NMAGIC are that (i) stellar systems without symmetry restrictions can be handled relatively easily, (ii) it avoids complicated procedures for sampling, binning, and storing orbits, and (iii) the potential can be evolved self-consistently if needed. In the examples given, a simple isotropic spherical model was evolved into a suitable initial model, which contained the required wide range of orbital shapes. Every χ^2M2M model corresponds to a new set-up of a complete orbit library in the Schwarzschild method; so in problems where the same orbit library can be reused, Schwarzschild's method will be faster. However, NMAGIC is highly parallel, so suites of models with $\sim 10^6$ particles are feasible on a PC cluster.

There is clearly room for improving the current implementation of the χ^2M2M algorithm, and there is a need to study carefully the parameters that enter the algorithm, such as magnitude and frequency of the correction steps, entropy, etc., which we will address in future work.

However, the different applications presented in this chapter show that the χ^2M2M algorithm is practical, reliable and can be applied to various dynamically relaxed systems. High quality dynamical models of galaxies can be achieved which match targets to $\sim 1\sigma$ for plausible uncertainties in the observables, and without symmetry restrictions. We conclude that χ^2M2M holds great promise for unraveling the nature of galaxies.

CHAPTER 3

DARK MATTER CONTENT AND INTERNAL DYNAMICS OF NGC 4697: NMAGIC PARTICLE MODELS FROM SLIT DATA AND PLANETARY NEBULAE VELOCITIES

Flavio De Lorenzi, Ortwin Gerhard, Roberto P. Saglia, Niranjan Sambhus, Victor P. Debattista, Maurilio Panella, Roberto H. Méndez
submitted to *MNRAS*, 2007

We present a dynamical study of NGC 4697, an almost edge-on, intermediate-luminosity, E4 elliptical galaxy, combining new surface brightness photometry, new as well as published long-slit absorption line kinematic data, and published planetary nebulae (PNe) velocity data. The combined kinematic data set extends out to $\simeq 5' \simeq 4.5R_e$ and allows us to probe the galaxy's outer halo.

For the first time, we model such a dataset with the new and flexible χ^2-made-to-measure particle code NMAGIC. We extend NMAGIC to include seeing effects, introduce an efficient scheme to estimate the mass-to-light ratio, and incorporate a maximum likelihood technique to account for discrete velocity measurements.

For modelling the PNe kinematics we use line-of-sight velocities and velocity dispersions computed on two different spatial grids, and we also use the individual velocity measurements with the likelihood method, in order to make sure that our results are not biased by the way we treat the PNe measurements.

We generate axisymmetric self-consistent models as well models including various dark matter halos. These models fit all the kinematic data with $\chi^2/N < 1$, both in the case with only luminous matter and in potentials including quite massive halos. There is a slight but not yet statistically significant tendency that the massive halos fit the PN data better; to firm this up would require PN velocities at even larger radii. Thus with the present kinematic data it is not possible to determine the amount of dark matter in NGC 4697. The best fitting models are slightly radially anisotropic; the anisotropy parameter $\beta =\simeq 0.3$ at the center, increasing to $\beta \simeq 0.5$ at radii $\gtrsim 2R_e$.

3.1 Introduction

The presence of dark matter (DM) has long been inferred around spiral galaxies from their flat rotation curves, and galaxies are now generally believed to be surrounded by extended dark matter halos. Indeed, in the current Λ-cold dark matter (ΛCDM) cosmology, galaxies form within the potential wells of their halos. The standard picture for the formation of elliptical

galaxies is through mergers of smaller units. Ellipticals should thus also be surrounded by dark matter halos. Their halos are particularly interesting because ellipticals are among the oldest galaxies and are found in the densest environments.

Unfortunately, mass measurements in elliptical galaxies have been difficult because of the lack of a suitable ubiquitous tracer such as neutral hydrogen rotation curves in spirals. In giant ellipticals, there is evidence for dark matter from gravitational lensing (*e.g.* Griffiths et al. 1996; Treu and Koopmans 2004; Rusin and Kochanek 2005) and X-ray emission (*e.g.* Awaki et al. 1994; Loewenstein and White 1999 Humphrey et al. 2006). In more ordinary ellipticals, mass estimates come from stellar dynamical studies, which have been limited by the faintness of the galaxies' outer surface brightness to radii less than two effective radii from the centre, $R \lesssim 2R_e$ (*e.g.* Kronawitter et al. 2000; Thomas et al. 2007). These studies suggest that the dark matter contributes $\sim 10 - 40\%$ of the mass within R_e (Gerhard et al. 2001; Cappellari et al. 2006), consistent with the lensing results.

The strong emission line at $[\mathrm{OIII}]\lambda 5007$ from planetary nebulae offers a promising tool to overcome this limitation and to extend stellar kinematic studies to larger radii (Hui et al., 1995; Tremblay et al., 1995; Arnaboldi et al., 1996, 1998). Also, in the less massive, X-ray faint ellipticals, PNe may be the primary tool for constraining the dynamics at large radii. Once the PNe are identified, their line-of-sight velocities can be obtained from the Doppler shift of the narrow emission line. Interestingly, the derived PNe dispersion profiles in the elliptical galaxies NGC 4697 (Méndez et al., 2001) and NGC 821, 3379 and 4494 (Romanowsky et al., 2003; Douglas et al., 2007) were found to decline significantly with radius outside $1R_e$. Their spherically symmetric dynamical analysis led Romanowsky et al. (2003) to the conclusion that these galaxies lack massive dark matter halos; however, Dekel et al. (2005) argued that the well known mass-anisotropy degeneracy allows for declining dispersion profiles even when a standard DM halo is present.

In the present chapter we focus on NGC 4697, a normal and almost edge-on E4 galaxy located along the Virgo southern extension. Méndez et al. (2001) obtained a planetary nebula luminosity function (PNLF) distance of 10.5 ± 1 Mpc from magnitudes of 531 PNe, and Tonry et al. (2001) measured a surface brightness fluctuation (SBF) distance of 11.7 ± 0.1 Mpc. This fairly isolated galaxy has a total B magnitude $B_T = 10.14$ and harbors a central super massive black hole (SMBH) of mass $1.2 \times 10^8 M_\odot$ (Pinkney et al., 2000). A Sersic law with $R_e = 66$ arcsec gives a good fit to the surface brightness profile out to about 4 arcmin (see Section 2). Based on the disky isophote shapes Carter (1987) and Goudfrooij et al. (1994) inferred a stellar disk along the major axis. The contribution of the disk kinematics to the major axis line-of-sight velocity distributions was estimated by Scorza et al. (1998). X-ray observations with ROSAT (Sansom et al., 2000) show a lack of large scale hot gas in the halo of this galaxy. Using more recent Chandra data, Irwin et al. (2000) could resolve most of this emission into non-uniformly distributed low mass X-ray binary (LMXB) point sources, suggesting that NGC 4697 is mostly devoid of interstellar gas and perhaps does not have substantial amounts of DM.

Dynamical axysimmetric models of NGC 4697 have been constructed by Binney et al. (1990) and Dejonghe et al. (1996), both based on photometry and absorption line kinematic data within $\sim 1R_e$. The data were consistent with a constant mass-to-light-ratio and none of these models showed evidence for dark matter. Méndez et al. (2001) obtained velocities for 531 PNe and derived a velocity dispersion profile out to approximately $4.5R_e$. Assuming an isotropic velocity distribution, Méndez et al. (2001) found that the PNe velocity dispersion profile is consistent with no DM inside $4.5R_e$, but that DM can be present if the velocity distribution is anisotropic. This was also argued by Dekel et al. (2005) to be the main cause of the finding by Romanowsky et al. (2003), that their three intermediate luminosity galaxies lacked significant dark matter halos (but see Douglas et al., 2007). Contrary to these three galaxies, which are nearly round on the sky, NGC 4697 is strongly flattened and likely to be nearly edge-on, thus easier to model since shape degeneracies are much less severe.

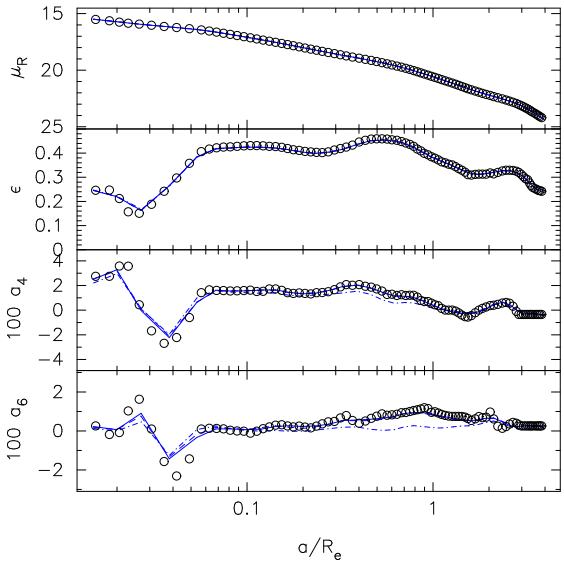

Figure 3.1: Comparison of the photometry of NGC 4697 with reprojected three-dimensional luminosity models. The data points correspond to the observed photometry for NGC 4697 (for the deprojection, the a_4 and a_6 values have been set to constants beyond $\simeq 3R_e$). The solid line shows the edge-on deprojected model reprojected, the dashed line the $i = 80°$ deprojected model reprojected, and the dash-dotted line the $i = 67°$ model. The panels show, from top to bottom, surface brightness μ_R, ellipticity ϵ and the isophotal shape parameters a_4 and a_6.

In the light of this, it is important enough to perform a further careful analysis of this galaxy. In this chapter we construct dynamical models of NGC 4697 with the very flexible NMAGIC particle code, making use of new and published slit kinematics and the Méndez et al. (2001) PN data. The chapter is organized as follows. In Section 3.2 we describe our new observational data and all other data that are used for the dynamical models. In Section 3.3 we give a brief explanation of the NMAGIC modeling technique. We extend the method to include seeing effects, introduce an efficient scheme to estimate the mass-to-light ratio, and show how discrete velocity measurements may be taken into account. In Section 3.4 we construct isotropic rotator models to test and calibrate the method, preparing for the dynamical modeling of NGC 4697 which is then performed in Section 3.5. Finally, the chapter closes with our conclusions in Section 3.6.

3.2 Observational Data

In this section, we describe the observational data used in the present study, including new CCD photometry and new long-slit absorption line kinematics. We also describe here the procedure employed for the deprojection of the photometric data. In the following we adopt a distance 10.5 Mpc to NGC 4697 (Méndez et al., 2001).

3.2.1 Surface Photometry

The R-band data used in the present work were taken in April 2000 as part of the ESO Proposal 064.N-0030 (P.I. R.P. Saglia) at the Wide Field Imager on the ESO-MPIA $2.2m$ telescope. Six 5 minutes, dithered exposures where taken in sub-arcsec seeing conditions. After the usual data reduction procedures (performed using the IRAF task mscred), the data were tabulated as radial profiles of surface brightness μ, ellipticity ϵ, position angle PA and Fourier shape coefficients (Bender and Moellenhoff, 1987). The surface brightness was calibrated using the

R band photometry of Peletier et al. (1990). Systematic errors due to sky subtraction ($\mu_{sky} = 20.18$ Rmag arcsec^{-2}) are always smaller than 10%. Fig. B.1 shows the derived profiles and Table B.1 gives them in tabular form. The isophotes of NGC 4697 do not show any appreciable twist in PA and have a positive a_4 coefficient in the galaxy's inner parts, which is well-explained by a near-edge-on embedded disk (Scorza and Bender, 1995). The galaxy has some dust in the inner regions (Pinkney et al., 2003), but the R-band observations are relatively unaffected by it. The outer isophotes are progressively slightly off-centered. A Sersic fit to the surface brightness profile results in Sersic index $n = 3.5$ and effective radius $R_e = 66$ arcsec. The older value of 95 arcsec from Binney et al. (1990) was based on photometry reaching only 120 arcsec; thus we use $R_e = 66$ arcsec in the following. For a distance of 10.5 Mpc this corresponds to 3.36 kpc.

3.2.2 Deprojection

For our dynamical study, we will fit particle models to the deprojected luminosity density using NMAGIC, *cf.* Section 3.3. To obtain the luminosity density we need to deproject the surface brightness. This inversion problem is unique only for spherical or edge-on axisymmetric systems (Binney and Tremaine, 1987). For axisymmetric systems inclined at an angle i, the Fourier slice theorem (Rybicki, 1987) shows that one can recover information about the density only outside a "cone of ignorance" of opening angle $90^\circ - i$. The deprojection of photometry for galaxies with i significantly less than 90° can thus be significantly in error because of undetermined konus densities (Gerhard and Binney, 1996; Kochanek and Rybicki, 1996).

Fortunately, NGC 4697 is seen almost edge-on and hence does not suffer from this ill-condition. Dejonghe et al. (1996) observed a nuclear dust lane with a ring-like appearance, elongated along the major axis of NGC 4697. Assuming that the ring is settled in the equatorial plane, they estimated an inclination angle $i = 78^\circ \pm 5^\circ$. Applying a disk-bulge decomposition to the isophote shapes of the galaxy, and assuming a thin disk, Scorza and Bender (1995) derived an inclination $i = 67^\circ$. This was updated by Scorza et al. (1998) to $i = 70^\circ$. Scorza and Bender (1995) also estimated the velocity dispersion σ_d of the disk component from the major axis line-of-sight velocity distributions. From their plots we estimate $\sigma_d \simeq 95 km\ s^{-1}$ at the half-mass radius of the disk, $r_D \simeq 13$". Assuming that the vertical dispersion in the disk is comparable, we can estimate the intrinsic flattening of the disk $\propto \sigma_d^2/v_c^2 \simeq 0.2$, using the measured rotation velocity. A disk with intrinsic thickness $h/R \simeq 0.2$ would give the same isophote distortions for inclination $i \simeq 80^\circ$ as a thin disk with $i = 67 - 70^\circ$, in agreement with the value found by Dejonghe et al. (1996).

We have deprojected NGC 4697 for inclinations $i = 90^\circ$, $i = 80^\circ$ and $i = 67^\circ$, using the method and program of Magorrian (1999). This algorithm uses a maximum penalized likelihood method with a simulated annealing scheme to recover a smooth three-dimensional luminosity density distribution which, when projected onto the sky-plane, has minimal deviations from the observed SB. The three-dimensional luminosity density so obtained extends beyond the radial range of the data, where the penalized likelihood scheme favours an outer power-law density profile. Figure 3.1 compares the observed photometry with the three deprojected luminosity models reprojected on the sky. In the range from $0.2R_e$ to $2R_e$ the $i = 67^\circ$ deprojection yields a significantly less good fit to the observed a_4 and a_6. Figure 3.2 compares the radial run of the isophotal shape parameters for the $i = 80^\circ$ and $i = 67^\circ$ luminosity models projected edge-on, with the observed photometry of NGC 4697. The $i = 80^\circ$ deprojection produces again somewhat better results. It is also more physical because it allows for a finite thickness of the inner disk of NGC 4697, as discussed above. Hence we will adopt it for the dynamical study of NGC 4697 to follow.

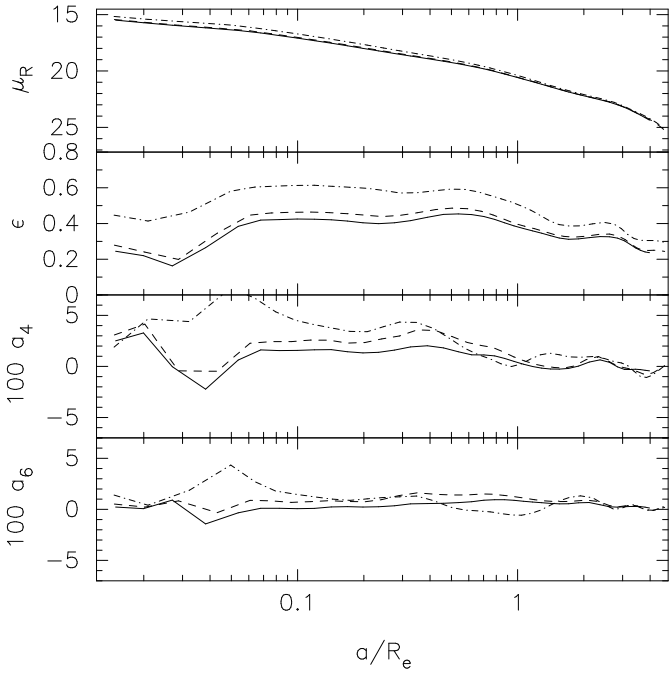

Figure 3.2: Isophote parameter profiles for the NGC 4697 photometry compared with those of the deprojected luminosity models shown in Figure 3.1 but now as seen in edge-on projection. NGC 4697 is coded as the solid line, whereas the $i = 80°$ and $i = 67°$ luminosity models are presented by the dashed and the dash-dotted lines, respectively.

3.2.3 Kinematic Data

Stellar-absorption line data

Long slit absorption line kinematics within $\sim R_e$ have been reported, amongst other works, by Binney et al. (1990) and Dejonghe et al. (1996). The Binney et al. (1990) kinematic data (BDI data) consist of line-of-sight velocity v and velocity dispersion σ profiles along the major axis, along slits $10''$ and $20''$ parallel to the major axis, along the minor axis, and along a slit $22''$ parallel to the minor axis. They are derived using the Fourier Quotient (FQ) method (Illingworth and Schechter, 1982). Dejonghe et al. (1996) have published further v and σ measurements (DDVZ data) at various position angles, also measured with the FQ method.

Along the major and minor axes we have derived additional line-of-sight velocity distribution (LOSVD) kinematics from the high S/N integrated absorption line spectra obtained by Méndez et al. (2005) with FORS2 at the VLT, a slit width of 1 arcsec and seeing $1'' - 1.''5$. We refer to this paper for a description of the data acquisition and reduction. The LOSVDs were measured using the Fourier Correlation Quotient (FCQ) method, as in Bender et al. (1994b) and Mehlert et al. (2000), and the K3III star HD132345 as a template. From these LOSVDs, profiles of v, σ, h_3 and h_4, the Gauss-Hermite coefficients (Gerhard, 1993; van der Marel and Franx, 1993), were obtained; these are shown in Figure 3.3. Tables B.1 and B.2 give the data in tabular form. The statistical errors derived from Monte Carlo simulations are minute and much smaller than the rms scatter observed between the two sides of the galaxy. These differences are particularly obvious along the major axis in the radial range 10-20 arcsec. As noted in Méndez et al. (2005), in this region we detect patchy [OIII] emission that is affecting to some extent the kinematics. Judging from the asymmetries in the kinematics on both sides of the galaxy, we estimate the residual systematic errors affecting the data, which amount to ≈ 3 km/s in V, ≈ 3.5 km/s in σ, ≈ 0.02 in h_3 and h_4.

In the following we discuss the comparison between the kinematic data derived here and the

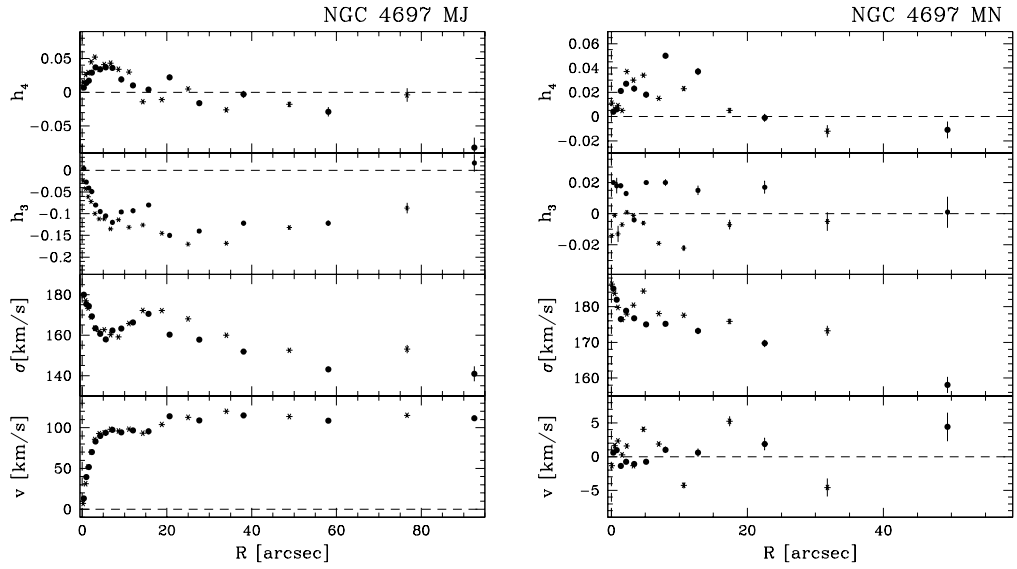

Figure 3.3: The kinematics along the major (left panel) and minor (right panel) axis of NGC 4697. The filled and starred symbols refer to the data folded along the axes.

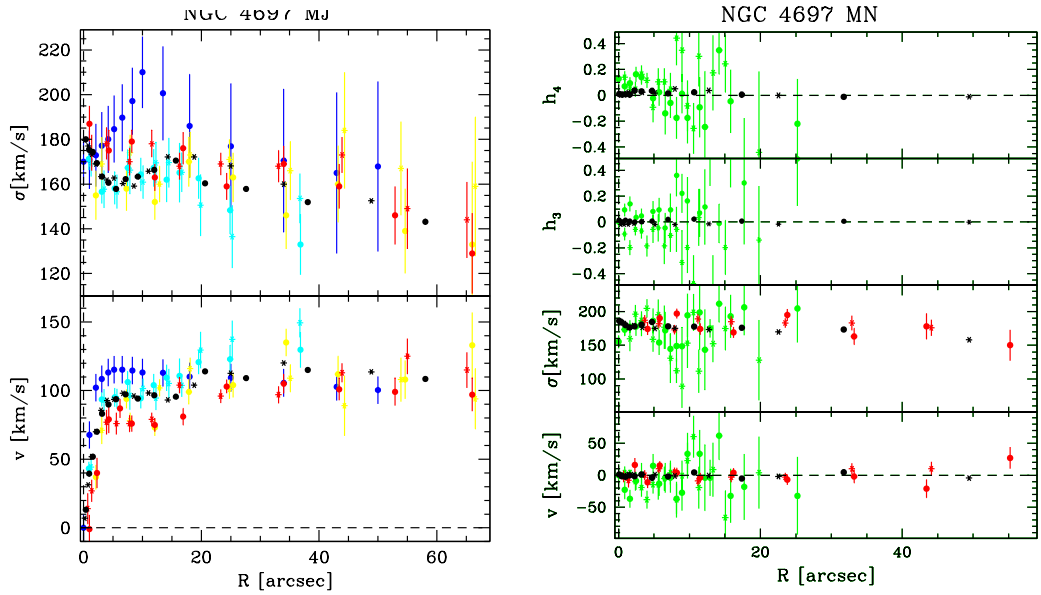

Figure 3.4: Comparison between the different absorption line kinematics along the major (left panel) and the minor (right panel) axis. Black: our data; red: BDI; blue: DDVZ; cyan: SB; green: KZ; yellow: FI.

kinematics published in the literature. Note that part of the differences seen below arise from the different observational setups (along the major axis different slit widths probe different relative amounts of the central disk structure present in the galaxy and related [OIII] emission regions) and methods used. In particular, the FQ method fits Gaussian profiles to the LOSVDs, ignoring the higher order Gauss-Hermite terms. In general the systematic effect on the measured mean velocity and velocity dispersion profiles is small (van der Marel et al., 1994). When applied to our major axis data set, FQ gives systematically slightly smaller mean velocities and larger velocity dispersions.

In the inner 10 arcsec along the major axis we confirm the clear kinematic signature of the central disk discussed by Scorza and Bender (1995, SB) and agree well with their mean v and σ derived also with the FCQ method and 1.8 arcsec slit width (see Figure 3.4, left, cyan points). Along the same axis we find good agreement with Fried and Illingworth (1994) (FI, yellow, derived using the FQ method and 1.1 arcsec slit width). Overall, the BDI data (Figure 3.4, red points, 2.6 arcsec slit width), agree well with our data, although at $15''$ along the major axis, the two data sets differ systematically. The σ profiles of DDVZ (blue points, 0.7 arcsec slit width) differ significantly in the sense that at small semi-major axis distances the DDVZ σ is increasing with radius but our σ is decreasing. Finally, the right panel of Figure 3.4 compares our data along the minor axis with the data sets of BDI (red points) and Koprolin et al. (2000) (KZ, green points, 2 arcsec slit width), who use the Fourier Fitting method of van der Marel and Franx (1993). Both agree within their respective (larger) errorbars.

Based on the radial extent and quality of the different datasets, and taking into account the discussion above, we have decided to use in the subsequent modeling only our data combined with BDI. For our kinematic data, the errors in v and σ are $\lesssim 0.5 \mathrm{km}\ s^{-1}$, which is small compared to the scatter in the data. This suggests, as already discussed above, that systematic errors dominate. For the modelling we have therefore replaced these errors with the smallest errors in v and σ of the BDI data along the major and minor axis, respectively ($5-7 \mathrm{km}\ s^{-1}$). Similar arguments hold for h_3 and h_4 and we set their errors to 0.01. In addition, the h_3 coefficients along the minor axis scatter significantly around zero while the minor axis velocities are consistent with zero; thus we replace these h_3 values by $h_3 = 0.0$.

Figure 3.5 gives a schematic view of the arrangement of the kinematic slits used in the modelling process.

Planetary nebula velocities

Planetary nebulae (PNe) are dying stars that emit most of their light in a few narrow lines of which the $[\mathrm{OIII}]\lambda 5007$ is the most prominent one. The PN population in elliptical galaxies is expected to arise from the underlying galactic population of old stars and hence the PNe can be used as kinematic tracers for the stellar distribution. Méndez et al. (2001) detected 535 PNe in NGC 4697 and were able to measure radial velocities for 531 of these with a typical error of $40\ \mathrm{km}\ s^{-1}$.

Sambhus et al. (2006) analyzed the correlations between the magnitudes, velocities and positions of these 531 PNe and found kinematic evidence for more than one PN sub-population in NGC 4697. In addition to the main PN population, they found evidence for a population of preferably bright PNe which appeared to be not in dynamical equilibrium in the galactic potential. To remove these possible kinematic contaminants, and to also ensure completeness for $R > R_e$ (Méndez et al., 2001), we discard all PNe with magnitudes outside the range $26.2 < m(5007) \leq 27.6$. The positions and velocities of the remaining 381 PNe are shown in Figure 3.6. In the following, we use a doubled sample of 762 PNe for our analysis, obtained by applying a point-symmetry reflection. Every PN with observed position coordinates (x, y) on the sky and line-of-sight velocity v_{PN} is reflected with respect to the center of the galaxy to generate a new PN with coordinates $(-x, -y, -v_{PN})$. Such point-symmetric velocity fields are

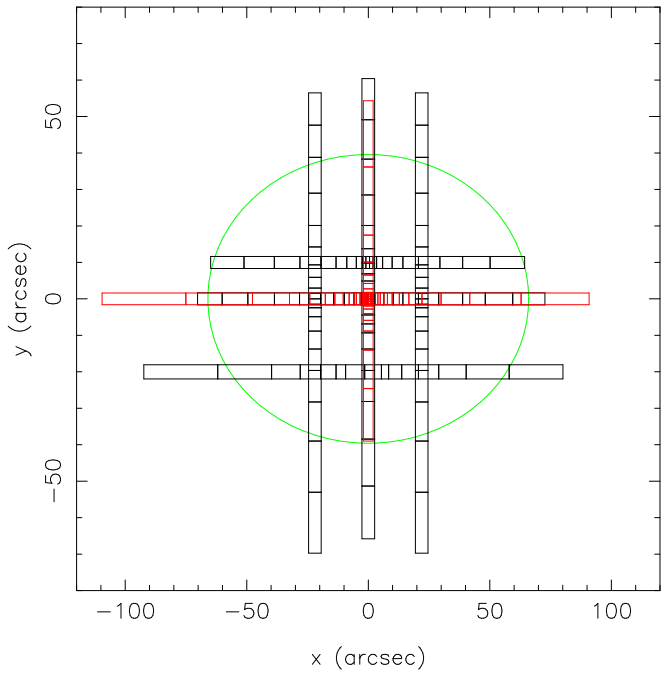

Figure 3.5: Schematic view of the slit setup used to construct the particle models. BDI slits are shown in black and our slits are shown in red. The ellipse has a semi-major axis of length R_e and axis ratio $q = 0.6$.

expected for axisymmetric and non-rotating triaxial potentials. Moreover, this reflection will help to further reduce any PN sub-population biases which might still be present.

We compute v and σ on two slightly different spatial grids, subtracting $40\ \mathrm{km}\ s^{-1}$ in quadrature from all PN velocity dispersions to account for the measurement uncertainties (Méndez et al., 2001). We use the spatial bins defined by the solid lines displayed in Figure 3.6 to obtain data set PND1, which is shown together with the models in Section 3.5. The second data set, PND2, is computed using the same grid but replacing the outermost ellipse by the dashed ellipse with semi-major axis $a = 280''$. This second grid is used to make sure that the dynamical models we generate are not affected by the way we define the outermost bins.

3.3 NMAGIC models

In this section we give a brief introduction to NMAGIC and present a few extensions to the method described in de Lorenzi et al. (2007). Syer and Tremaine (1996) invented a particle-based method for constructing models of stellar systems. This "made-to-measure" (M2M) method works by adjusting individual particle weights as the model evolves, until the N-particle system reproduces a set of target constraints. de Lorenzi et al. (2007) improved the algorithm to account for observational errors and to assess the quality of a model for a set of target data directly, using the standard χ^2 statistics in the function to be maximized upon convergence of the weights (χ^2M2M). NMAGIC is a parallel implementation of the improved χ^2M2M algorithm.

3.3.1 Luminous and dark matter distribution

Luminous mass

We assume that the luminous mass distribution of NGC 4697 follows the deprojected luminosity density. The mass density of the luminous matter is then given by $\rho_\star = \Upsilon j$, with mass-to-light

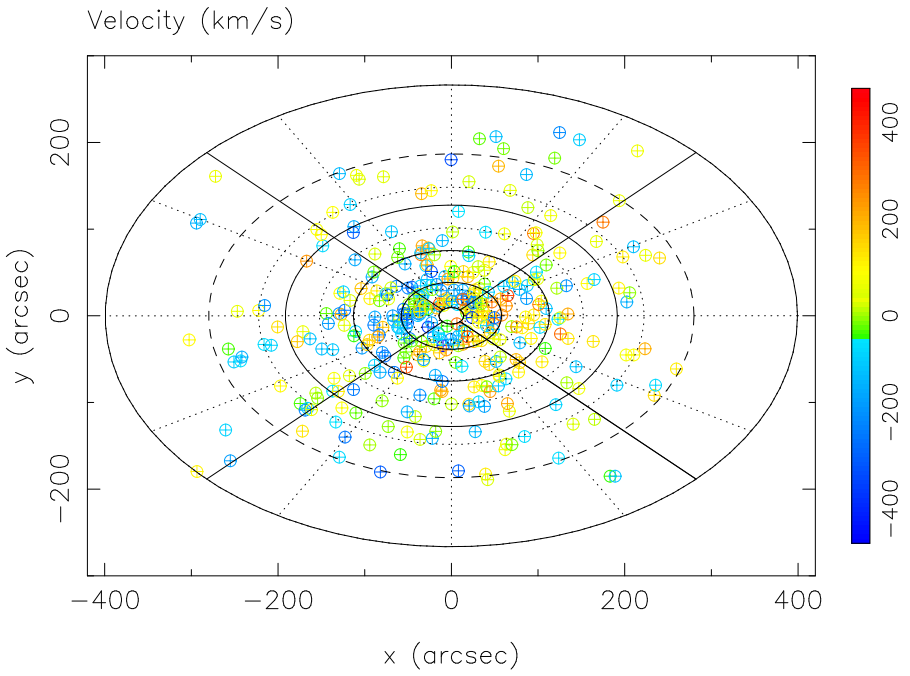

Figure 3.6: The positions and velocities of the cleaned PN sample of 381 PNe. The lines indicate the different grids used for binning the PNe. Details are given in the text.

ratio Υ and luminosity density j represented by the discrete ensemble of particles with positions $\mathbf{x}_i$ and luminosities L_i.

Dark halo potential

The prevailing cosmological paradigm predicts that galaxies have massive, extended dark matter halos. Numerical cold dark matter (CDM) simulations reveal universal halo density profiles with steep central density cusps (*e.g.* Navarro et al., 1996; Moore et al., 1999). On the other hand, observations of many dwarf and low-surface brightness galaxies find shallower inner density cores (*e.g.* de Blok et al., 2003; McGaugh et al., 2007). Here our aim is not to determine the detailed shape of the dark matter halo in NGC 4697, but rather to first see whether the PN velocities allow or require any dark matter at all in this galaxy. To answer this question we will investigate a one-dimensional sequence of potentials whose circular velocity curves vary at large radii between the near-Keplerian decline expected when the mass in stars dominates, and the nearly flat shapes generated by massive dark halos. Thus for our dynamical studies of NGC 4697, we represent the dark matter halo by the logarithmic potential (Binney and Tremaine, 1987)

$$\phi_D(R', z') = \frac{v_0^2}{2} \ln(r_0^2 + R'^2 + \frac{z'^2}{q_\phi^2}), \tag{3.1}$$

which is generated by the density distribution

$$\rho_D(R', z') = \frac{v_0^2}{4\pi G q_\phi^2} \frac{(2q_\phi^2 + 1)r_0^2 + R'^2 + 2(1 - \frac{1}{2}q_\phi^{-2})z'^2}{(r_0^2 + R'^2 + q_\phi^{-2}z'^2)^2}, \tag{3.2}$$

where v_0 and r_0 are constants, q_ϕ is the flattening of the potential, and R' and z' are cylindrical coordinates with respect to the halo's equatorial plane. When $q_\phi < 1/\sqrt{2}$ the density becomes negative along the z' axis. The density given in equation 3.2 has a shallow inner density profile, but since we are mainly interested in the circular velocity curve in the outer halo of NGC 4697,

this is inconsequential: it is always possible to reduce the stellar mass-to-light ratio in exchange for an additional centrally concentrated dark matter cusp.

The total gravitational potential

The total gravitational potential is generated by the combined luminous mass and dark matter distributions and is given by

$$\phi = \phi_\star + \phi_D, \tag{3.3}$$

where $\phi_\star$ is generated by the N-particle system assuming a constant mass-to-light ratio for each stellar particle. We estimate $\phi_\star$ via a spherical harmonic decomposition (Sellwood, 2003; de Lorenzi et al., 2007). The stellar potential is allowed to change during a NMAGIC modelling run, but the dark matter potential is constant in time and is given by equation (3.1). The particles are integrated in the global potential using a drift-kick-drift form of the leapfrog scheme with a fixed time step.

3.3.2 Model observables

Typical model observables are surface or volume densities and line-of-sight kinematics. An observable y_j of a particle model is computed via

$$y_j(t) = \sum_{i=1}^{N} w_i K_j \left[\mathbf{z}_i(t)\right], \tag{3.4}$$

where w_i are the particle weights, $\mathbf{z}_i$ are the phase-space coordinates of the particles, $i = 1, \cdots, N$, and $K_j[\mathbf{z}_i(t)]$ is a kernel corresponding to y_j. We use units such that the luminosity L_i of a stellar particle can be written as $L_i = Lw_i$, where L is the total luminosity of the model galaxy. We use temporally smoothed observables to increase the effective number of particles in the system, *cf.* Syer and Tremaine (1996); de Lorenzi et al. (2007).

Luminosity constraints

For modeling the luminosity distribution of NGC 4697 one can use as observables the surface density or space density on various grids, or some functional representations of these densities. We have chosen to model a spherical harmonics expansion of the deprojected luminosity density. We determine the expansion coefficients A_{lm} for the target galaxy on a 1-D radial mesh of radii r_k. The spherical harmonic coefficients for the particle model are computed via

$$a_{lm,k} = L \sum_i \gamma_{ki}^{CIC} Y_l^m(\theta_i, \varphi_i) w_i, \tag{3.5}$$

where L is the total luminosity of the model galaxy, w_i the particle weights, Y_l^m the spherical harmonic functions and γ_{ki}^{CIC} is a selection function, which maps the particles onto the radial mesh using a cloud-in-cell scheme (see de Lorenzi et al., 2007).

Kinematic constraints

Since in the χ^2M2M algorithm the kernel in equation (3.4) cannot depend on the particle weights themselves, this puts some constraints on which observables can be used. For kinematics, suitable observables are the luminosity-weighted Gauss-Hermite coefficients or the luminosity-weighted velocity moments. We implement them as follows.

Spectroscopic data The shape of the line-of-sight velocity distribution (LOSVD) can be expressed as a truncated Gauss-Hermite series and is then characterized by V, σ and h_n ($n > 2$), where V and σ are free parameters. If V and σ are equal to the parameters of the best fitting Gaussian to the LOSVD, then $h_1 = h_2 = 0$ (van der Marel and Franx, 1993; Rix et al., 1997). The luminosity-weighted Gauss-Hermite coefficients are computed as

$$b_{n,p} \equiv l_p\, h_{n,p} = 2\sqrt{\pi} L \sum_i \delta_{pi} u_n(\nu_{pi}) w_i, \tag{3.6}$$

with

$$\nu_{pi} = (v_{z,i} - V_p)\,/\sigma_p. \tag{3.7}$$

Here $v_{z,i}$ denotes the line-of-sight velocity of particle i, l_p is the luminosity in cell $\mathcal{C}_p$, V_p and σ_p are the best-fitting Gaussian parameters of the target LOSVD in cell $\mathcal{C}_p$, and the dimensionless Gauss-Hermite functions are (Gerhard, 1993)

$$u_n(\nu) = \left(2^{n+1}\pi n!\right)^{-1/2} H_n(\nu) \exp\left(-\nu^2/2\right). \tag{3.8}$$

H_n are the standard Hermite polynomials and δ_{pi} is a selection function which is one if particle i is in cell $\mathcal{C}_p$ and zero otherwise. The errors in h_1 and h_2 can be computed from those of V and σ via

$$\Delta h_1 = -\frac{1}{\sqrt{2}} \frac{\Delta V}{\sigma} \tag{3.9}$$

and

$$\Delta h_2 = -\frac{1}{\sqrt{2}} \frac{\Delta \sigma}{\sigma}, \tag{3.10}$$

valid to first order (van der Marel and Franx, 1993; Rix et al., 1997). Since we use the observed V_p and σ_p from a Gauss-Hermite fit to the LOSVD as expansion parameters for the model line profiles, the final fitted h_1 and h_2 of a model will be small, and so we can also use relations (3.9) and (3.10) to compute the model V and σ from V_p and σ_p.

Spatially binned PNe data We have computed mean PN velocities and velocity dispersions for the ellipse sector bins shown in Figure 3.6. The ellipticity of the grid corresponds to the mean ellipticity of the photometry. As suitable observables we take the *luminosity-weighted* velocity moments in these bins, which are computed as

$$v_p^n = L \sum_i \delta_{pi} v_{z,i}^n w_i, \tag{3.11}$$

where $v_{z,i}$ is the velocity along the line-of-sight of particle i and δ_{pi} is a selection function, which is equal to one if particle i belongs to the bin segment under consideration and zero otherwise. In the following, we use only the moments v_p^1 and v_p^2.

3.3.3 Seeing effects

To account for seeing effects we apply a Monte Carlo approach (*e.g.* Cappellari et al., 2006) instead of convolving the observables with the PSF. As long as the particles move along their orbits no PSF effects need to be taken into account, only when the observables of the system are computed, the effects of seeing may matter.

When computing an observable including PSF effects, we replace the "original" particle at position (x_i, y_i) on the sky plane temporarily by a cloud of N_{pp} pseudo particles. The position of a pseudo particle is obtained by randomly perturbing (x_i, y_i) with probability given by the PSF. Note that neither extra storage is needed nor additional time to integrate the particles along their orbits. Usually, only a small number of pseudo particles are needed to model PSF effects,

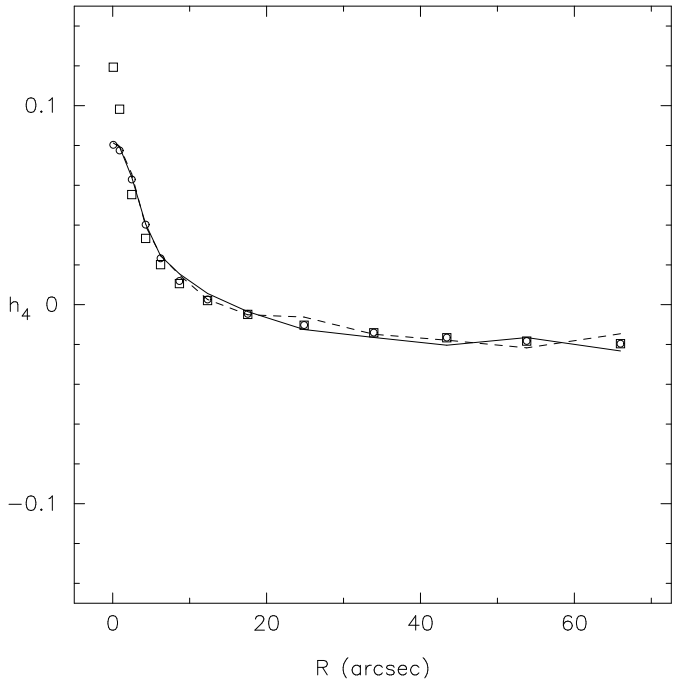

Figure 3.7: Seeing convolution test, comparing the radial run of h_4 along a $2''$ slit for a spherical target model and its particle representation. The squares (circles) were computed for the target from higher order Jeans equations without (with) seeing. The lines correspond to the particle model including seeing, for which the PSF was represented using $N_{pp} = 5$. The full and dashed lines refer to the major axis slit data at positive resp. negative radii with respect to the origin. The heavily seeing-affected central profile is well recovered by the model.

even one is often sufficient. This procedure is implemented in the kernel K_{ij} as defined in equation (3.4). The same kernel then enters the force-of-change equation, *cf.* de Lorenzi et al. (2007).

To test how well PSF effects are modeled using only a few pseudo particles we computed mock observations for a spherical isotropic galaxy of mass $M = 10^{10} M_{\odot}$, located at a distance 10 Mpc. The intrinsic density of the galaxy is given by a Hernquist (1990) profile with scale length $a = 55.1''$. We assumed a major axis slit of width $2''$ and a Gaussian PSF with $\mathrm{FWHM} = 4''$. We computed the LOSVD of the target galaxy along the major axis using higher order Jeans moments (Magorrian and Binney, 1994), and compared it with the LOSVD of a particle realization of the mock galaxy, applying the above procedure. The particle realization of the Hernquist model was generated from an isotropic distribution function (*e.g.* Debattista and Sellwood, 2000). As an example, Figure 3.7 shows the h_4 profile along the major axis slit. The square symbols are the target data computed using higher order Jeans equations without seeing, the circles are computed the same way but including PSF effects. The lines are the temporally smoothed h_4 profiles of the particle model using $N_{pp} = 5$ to represent the PSF. One sees that the heavily seeing-affected central profile is well recovered by the model.

In the dynamical modeling of NGC 4697 we include seeing only for our new kinematic data. We represent the PSF by a single Gaussian with $FWHM = 1.25''$. For the BDI data we do not know the PSF but since the slit cells are relatively large, seeing is likely to be negligible.

3.3.4 The merit function

By fitting the particle model to the observables, the weights w_i are gradually changed such that the merit function

$$F = \mu S - \frac{1}{2}\chi^2 \tag{3.12}$$

is maximized, where S is a profit function and χ^2 measures the quality of the fit. The parameter μ controls the relative contribution of the profit function to F; incrementing μ increases the influence of S in equation (3.12). The χ^2 statistics is computed as usual

$$\chi^2 = \sum_j \Delta_j^2, \tag{3.13}$$

where $\Delta_j = (y_j - Y_j)/\sigma(Y_j)$. y_j is a model observable (*e.g.* $a_{lm,k}$ with $\mathbf{j} = \{lm, k\}$), Y_j is the corresponding target and $\sigma(Y_j)$ its error.

For the profit function S, we use the entropy

$$S = -\sum_i w_i \ln(w_i/\hat{w}_i) \tag{3.14}$$

where $\{\hat{w}_i\}$ are a predetermined set of weights, the so-called priors (here equal for all particles). The entropy term pushes the particle weights to remain close to their priors (more specifically, close to $\hat{w}_i/e$). This implies that models with large μ will have smoother distribution functions than those with small μ. The best choice for μ depends on the observational data to be modeled, *e.g.* their spatial coverage, on the phase-space structure of the galaxy under consideration, but also on the initial conditions. For the dataset at hand, the best value of μ will be determined in Section 3.4.1

3.3.5 Discrete PNe velocities

The likelihood of a model fit to photometric as well absorption line kinematic data is measured by the standard χ^2 statistics given in equation (3.13). To treat discrete PN velocity measurements the same way, we must bin them to estimate the underlying mean v and σ fields. This gives the corresponding model observables as discussed in section 3.3.2.

As an alternative, one can measure the likelihood of a sample of discrete velocities v_j and positions $\mathbf{R}_j = (x_j, y_j)$ on the sky via

$$\mathcal{L} = \sum_j \ln \mathcal{L}_j \tag{3.15}$$

using the likelihood function for a single PN (Romanowsky and Kochanek, 2001)

$$\mathcal{L}_j(v_j, \mathbf{R}_j) = \frac{1}{\sqrt{2\pi}} \int \frac{\mathrm{d}L}{\mathrm{d}v_z}(v_z, \mathbf{R}_j) e^{-(v_j - v_z)^2/2\sigma_j^2} \mathrm{d}v_z, \tag{3.16}$$

where σ_j is the error in velocity and $\mathrm{d}L/\mathrm{d}v_z$ is the LOSVD assuming as before that the line-of-sight is along the z-axis.

We can then add equation (3.15) to the function F given in equation (3.12) and maximize

$$F^+ = F + \mathcal{L} \tag{3.17}$$

with respect to the particle weights w_i. Hence, we obtain an additional contribution to the force-of-change as given in de Lorenzi et al. (2007). We will now derive this extra term. Let us consider the selection function

$$\delta_{ji} = \begin{cases} 1 & \text{if } (x_i, y_i) \in \mathcal{C}_j \\ 0 & \text{otherwise.} \end{cases}$$

which assigns particle weights to a spatial cell $\mathcal{C}_j$, which contains the j-th PNe. We can then write $\mathrm{d}L/\mathrm{d}v_z$ at position j as

$$\left(\frac{\mathrm{d}L}{\mathrm{d}v_z}\right)_j = \frac{1}{l_j}\sum_i \delta_{ji} w_i \delta(v_z - v_{z,i}) \tag{3.18}$$

with

$$l_j = \sum_i \delta_{ji} w_i, \tag{3.19}$$

and $\delta(x)$ being the standard delta function. Hence, equation (3.16) can be expressed in terms of the particles via

$$\mathcal{L}_j = \frac{\widehat{\mathcal{L}}_j}{l_j} \tag{3.20}$$

with

$$\widehat{\mathcal{L}}_j = \frac{1}{\sqrt{2\pi}}\sum_i \delta_{ji} w_i e^{-(v_j - v_{z,i})^2/2\sigma_j^2}. \tag{3.21}$$

Finally, we find for the additional term in the FOC

$$\frac{\mathrm{d}w_i}{\mathrm{d}t} = \varepsilon w_i \sum_j \delta_{ji}\left(\frac{1}{\sqrt{2\pi}}\frac{e^{-(v_j - v_{z,i})^2/2\sigma_j^2}}{\widehat{\mathcal{L}}_j} - \frac{1}{l_j}\right), \tag{3.22}$$

where the sum runs over all individual PNe. For small errors, the $\mathrm{d}w_i/\mathrm{d}t$ from the likelihood term is positive for particles with $v_j = v_{z,i}$, but reduces the weights of the other particles and hence drives the LOSVD to peak at v_j. In the implementation, we replace l_j and $\widehat{\mathcal{L}}_j$ with the corresponding temporally smoothed quantities.

When we use this method to account for the PN velocities in NGC 4697, we adopt the grid defined in Figure 3.6 by the dotted lines, including the innermost and outermost full ellipses. In this way, we assign each of the 762 PNe to a cell $\mathcal{C}_j$. It follows, that more than one PNe share the same spatial bin, but this is not a problem.

3.3.6 Efficient mass-to-light estimate

It is common practice to evolve N-particle systems in internal units (IU), in which the gravitational constant and the units of length and mass are set to unity, and to scale the system to physical units (PU) a posteriori to compare with galaxy observations. Similarly, the velocities of a system with mass-to-light ratio Υ of unity may be scaled to any Υ via $v_{\mathrm{PU}} = \gamma\, v_{\mathrm{IU}}$ where $\gamma \propto \sqrt{\Upsilon}$ and v_{PU} and v_{IU} are the velocities in physical and internal units, respectively. It follows that the kinematic observables of the model and hence also χ^2 can be regarded as functions of Υ. Equation (3.13) then reads

$$\chi^2 = \sum_j \Delta_j(\Upsilon)^2. \tag{3.23}$$

In the following we will only consider the luminosity-weighted Gauss-Hermite moments as given in equation (3.6) and neglect the PNe kinematic constraints. Taking the partial derivative with respect to Υ of equation (3.23) leads to

$$\frac{1}{2}\frac{\partial\chi^2}{\partial\Upsilon} = \sum_{\mathbf{j}} \frac{\Delta_j(\Upsilon)}{\sigma(B_{n,p})}\frac{\partial b_{n,p}}{\partial\Upsilon}, \quad \mathbf{j} = \{n,p\} \tag{3.24}$$

where $B_{n,p}$ is the target observable and $\sigma(B_{n,p})$ its error. We define a force-of-change (FOC) for the mass-to-light ratio Υ

$$\frac{\mathrm{d}\Upsilon}{\mathrm{d}t} = -\eta\Upsilon\frac{\partial\chi^2}{\partial\Upsilon} \tag{3.25}$$

which equals

$$\frac{\mathrm{d}\Upsilon}{\mathrm{d}t} = -\eta\Upsilon \sum_{\mathbf{j}} 2\Delta_j(\Upsilon)\frac{\partial\Delta_j(\Upsilon)}{\partial\Upsilon} \tag{3.26}$$

with

$$\frac{\partial\Delta_j(\Upsilon)}{\partial\Upsilon} = \frac{\sqrt{\pi}L}{\Upsilon\sigma_p\sigma(B_{n,p})}\sum_i \delta_{pi}w_i\frac{\partial u_n(x)}{\partial x}\Big|_{x=\nu_{pi}} v_{z,i}, \tag{3.27}$$

where we used $\partial v_{z,i}/\partial\Upsilon = v_{z,i}/2\Upsilon$ for $v_{z,i}$ given in physical units, and $\mathbf{j} = \{n, p\}$. The line-of-sight is along the z axis. In practice, we use the temporally smoothed quantities to compute the FOC for the mass-to-light ratio.

In principle, the proposed scheme can be understood as a gradient search along the $\chi^2(\Upsilon)$ curve when simultaneously the particle model is fitted to the observational constraints. Hence the same NMAGIC run allows us to estimate Υ as well. We test the scheme and illustrate its accuracy in Section 3.4.

3.3.7 Initial conditions

As initial conditions for NMAGIC, we generate a particle realization of a spherical γ-model (Dehnen, 1993; Carollo et al., 1995) made from a distribution function (DF) using the method of Debattista and Sellwood (2000). The model consists of $N = 5 \times 10^5$ particles and has $\gamma = 1.5$, scale length $a = 1$ and $r_{\max} = 40$. When scaled to NGC 4697 one unit of length corresponds to 2.3810 kpc, i.e., this model has $R_e = 3.8$ kpc.

In some cases, we have found it useful to give the initial particle system some angular momentum about an axis of symmetry. For axisymmetric stellar systems, the density is determined through the even part in L_z of the DF (Lynden-Bell, 1962). Thus the component of the angular momentum of a particle along the symmetry axis may be reversed without affecting the equilibrium of the system. Kalnajs (1977) showed, however, that a discontinuity at $L_z = 0$ can affect the stability of the particle model. Therefore, if desired, we switch retrograde particles with a probability

$$p(L_z) = p_0\frac{L_z^2}{L_z^2 + L_0^2}, \tag{3.28}$$

which ensures a smooth DF.

3.4 Testing the modelling with isotropic rotator targets

In this section, we use axisymmetric, isotropic rotator models with known intrinsic properties to determine the optimal value of the entropy "smoothing" parameter μ in equation (3.12), and to test our procedure for determining the optimal mass-to-light ratio simultaneously with modelling the data.

3.4.1 Entropy parameter μ

Our approach to determine suitable values for μ is similar as in Gerhard et al. (1998) and Thomas et al. (2005). We first generate a "mock" kinematic data set from an isotropic rotator model whose information content (number and density of points, errors) is similar as for the real data set to be modelled. To this data set we perform a sequence of particle model fits for various μ, and determine the values of μ for which (i) a good fit is obtained, and (ii) the known intrinsic velocity moments of the input "mock" system are well reproduced by the corresponding moments of the final particle model. Using an isotropic rotator model for this purpose here makes sense, because such a model is a fair representation of NGC 4697 (Binney et al., 1990).

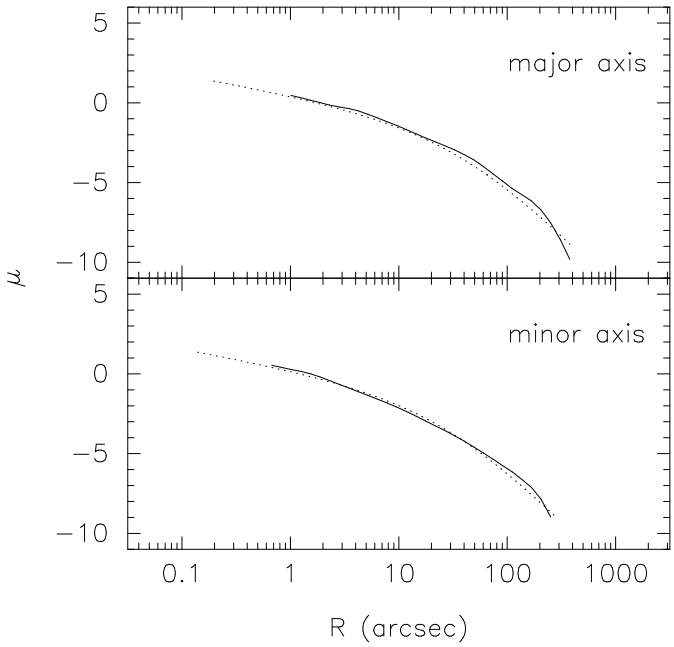

Figure 3.8: Comparison of the surface brightness of NGC 4697 (solid lines) with the γ-model described in the text and seen under $i = 80°$ inclination (dotted lines). Top: Surface brightness profile along the major axis. (b) Along the minor axis.

We have chosen to describe the luminosity density of the mock galaxy by one of the flattened γ-models of Dehnen and Gerhard (1994),

$$j(m) = \frac{(3-\gamma)L}{4\pi q} \frac{a}{m^{\gamma}(m+a)^{4-\gamma}}. \tag{3.29}$$

Here L and a are the total luminosity and scale radius, $m^2 = R'^2 + (z'/q)^2$, and q is the flattening. The parameters are chosen such that the surface brightness closely resembles that of NGC 4697, i.e., $q = 0.7$, $\gamma = 1.5$, $L = 2 \times 10^{10}\ L_{\odot,R}$ and $a = 2.5$ kpc, which corresponds to $a \approx 49''$ at a distance of 10.5 Mpc. Figure 3.8 shows a comparison of the surface brightness of NGC 4697 with the mock galaxy projected under $i = 80°$. The major and minor axis surface brightness profiles are well approximated by the γ-model, except for some differences at larger radii, so we will use this model for the calibration of μ.

We determine mock kinematic profiles from internal velocity moments, obtained from higher-order Jeans equations (Magorrian and Binney, 1994) in the self-consistent potential generated by the density of equation (3.29) for a mass-to-light ratio $\Upsilon = 5$. Before calculating the line-of-sight velocity profiles, the velocity moments are slit-averaged to account for the observational setup of the kinematic slits given in Section 3.2.3. We add Gaussian random variates to the isotropic rotator kinematics with 1σ dispersion corresponding to the respective measurement error in NGC 4697 at that position. Figure 3.9 shows a comparison of our new kinematic data for NGC 4697 with the isotropic rotator mock data, along the galaxy's major axis.

We do not construct mock PNe data for inclusion in the entropy tests, but we need to compute the photometric observables to construct a complete observational data set. We expand the luminosity distribution of equation (3.29) in a spherical harmonics series (*cf.* Section 3.3.2) on a radial grid with 40 shells at radii r_k. The radii are quasi-logarithmically spaced with $r_{\min} = 1.0''$ and $r_{\max} = 700''$. We use the luminosity on radial shells $L_k = \sqrt{4\pi} A_{00,k}$ and the higher order coefficients $A_{20,k}$, $A_{22,k}$, $\cdots$, $A_{66,k}$ and $A_{80,k}$ to constrain the luminosity distribution of the particle model. The $m \neq 0$ terms are set to zero to force the models to remain nearly axisymmetric, i.e., within the limits set by the A_{lm} errors. We assume Poisson errors for the

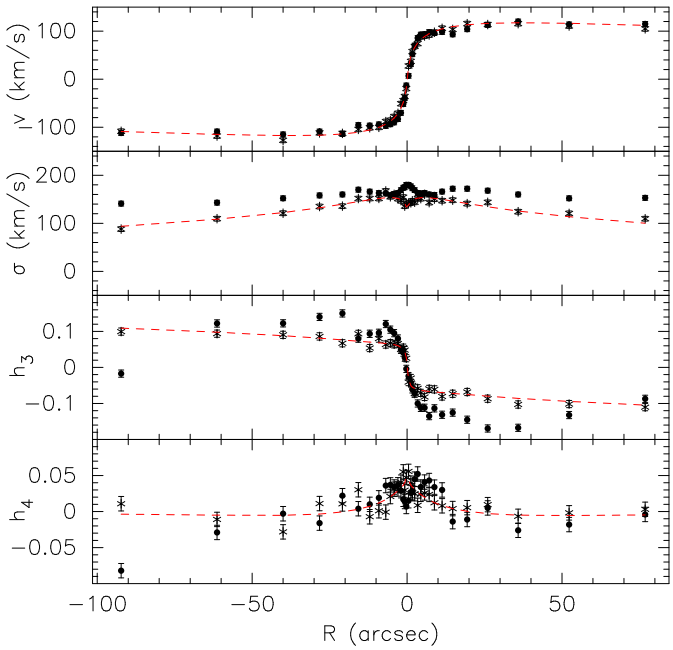

Figure 3.9: Comparison of v, σ, h_3 and h_4 of NGC 4697 and an isotropic rotator model with approximately the same projected surface brightness as the galaxy. The filled circles show our new kinematic data for NGC 4697 from Section 3.2.3, the star symbols show the isotropic rotator mock data, and the dashed red lines show the underlying smooth model kinematics, all along the major axis.

L_k: $\sigma(L_k) = \sqrt{L_k L/N}$ where N is the total number of particles used in the particle model and L is the total luminosity of the system. To estimate the errors in the higher order luminosity moments, we use Monte-Carlo experiments in which we generate particle realizations of a spherical approximation of the density field of the target system with 5×10^5 particles, which is the same number as in the χ^2M2M models for NGC 4697.

We then construct self-consistent particle models for the isotropic rotator target in a three step process, using the mock data as constraints. (i) Density fit: we start with the spherical initial conditions described in Section 3.3.7 and evolve them using NMAGIC to generate a self-consistent particle realization with the desired luminosity distribution (γ-particle model), fitting only the luminosity constraints. (ii) Kinematic fit: because the target galaxy has a fair amount of rotation, it is worth starting the kinematic fit from a rotating model. Hence, following Section 3.3.7, we switch a fraction of retrograde particles in the γ-particle model to prograde orbits, using $p_0 = 0.3$ and $L_0 \simeq L_{\rm circ}(0.03R_e)$. This rotating system we then use as a starting point to construct a series of self-consistent dynamical isotropic rotator models, by fitting the target photometry *and* kinematics for different values of μ. For each model, we evolve the particle system for $\sim 10^5$ NMAGIC correction steps while fitting the complete set of constraints. During this correction phase, the potential generated by the particles is updated after each correction step. (iii) Free evolution: to ensure that any correlations which might have been generated during the correction phase are phase-mixed away, we now keep the potential constant and evolve the system freely for another 5000 steps, without further correction steps. For reference, 5000 of these steps correspond to ≈ 20 circular rotation periods ("dynamical times")at R_e in spherical approximation.

The results are presented in Figure 3.10. The lower panel shows the quality of the fit as a function of μ, both in terms of normalized χ^2 values and in terms of the merit function F from equation (3.12). The upper panel shows the $\rm rms$ Δ relative difference between the internal velocity moments of the isotropic rotator input model and those of the particle models

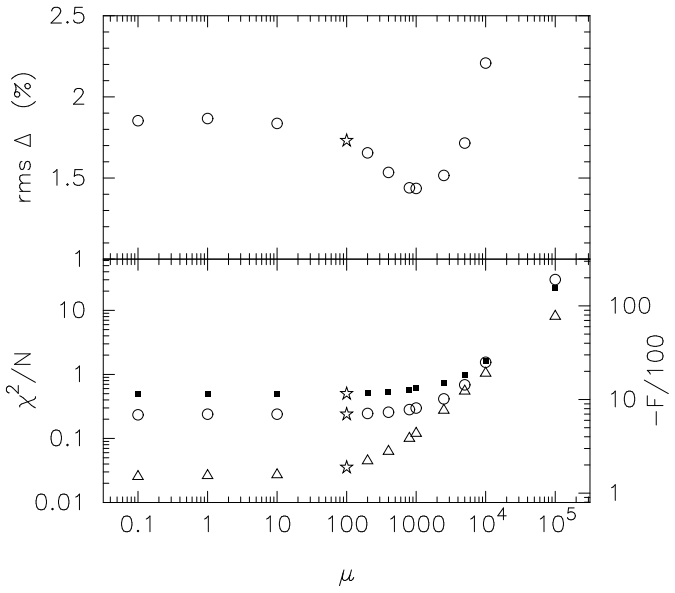

Figure 3.10: Entropy tests. Top: Deviation $\mathrm{rms}\ \Delta(\mu)$ of the particle models from the isotropic rotator internal velocity moments. The point for the rightmost value of μ is at a large value of Δ outside the diagram. Bottom: χ^2 deviation per data point of the particle model fit to the photometric and kinematic target observables (open circles) and to the kinematic observables alone (filled squares), as a function of entropy parameter μ. The triangles show the same dependence for the merit function $(-F)$, *cf.* equation (3.12). The starred symbol indicates the value of μ chosen for the subsequent modelling.

reconstructed from the mock kinematics. For the particle models intrinsic velocity moments are computed by binning the particles in spherical polar coordinates, using a quasi-logarithmic grid with 20 radial shells bounded by $r_{\min} = 0.01''$ and $r_{\max} = 200''$, 12 bins in azimuthal angle ϕ, and 21 bins equally spaced in $\sin\theta$. The $\mathrm{rms}\ \Delta$ shown in Figure 3.10 is obtained by averaging over all grid points in the radial region constrained by the data ($R \leq 1.5R_e$). The minimum in $\mathrm{rms}\ \Delta$ determines the value of μ for which the model best recovers the internal moments of the input model. This occurs at $\mu \simeq 10^3$, and the value of $\mathrm{rms}\ \Delta$ at the minimum is $\simeq 1.4\%$. For larger (smaller) μ, the $\mathrm{rms}\ \Delta$ is larger because of oversmoothing (excess fluctuations) in the model.

χ^2/N values are given in the lower panel of Fig. 3.10 for all (photometric and kinematic) data points, and for the kinematic data points alone. Generally the χ^2/N for the photometric points is significantly better than for the kinematic points, because (i) the A_{lm} come from averages over many particles, thus have little noise, and we have not added Gaussian variances, and (ii) all particles contribute to the A_{lm} force-of-change at all timesteps, so the A_{lm} are weighted strongly during the evolution. The kinematic χ^2 per data point in the lower panel is of order 0.5 for a large range of μ and then increases starting from $\mu \gtrsim 300$ to 1 at $\mu \simeq 5 \times 10^3$, whereas $-F$ already increases around $\mu \gtrsim 100$.

Some results for the isotropic rotator dynamical models obtained with $\mu = 10^2$, $\mu = 10^3$, $\mu = 5 \times 10^3$ are presented in Figures 3.11 and 3.12. Figure 3.11 shows a comparison of the target kinematics with the kinematics of the self-consistent particle models along the major axis slit. Note the excellent fit of the central velocity gradient and velocity dispersion dip, for all μ values. However, the models with higher μ begin to fail matching the target data at the largest radii. This is because the number of data points decreases with radius, whereas the number of particles and hence entropy constraints is roughly proportional to luminosity L_k, i.e. changes much more slowly with radius. The result is that the constraints from the data become relatively weaker at larger radii. The entropy term tries to enforce a dynamical structure related to the

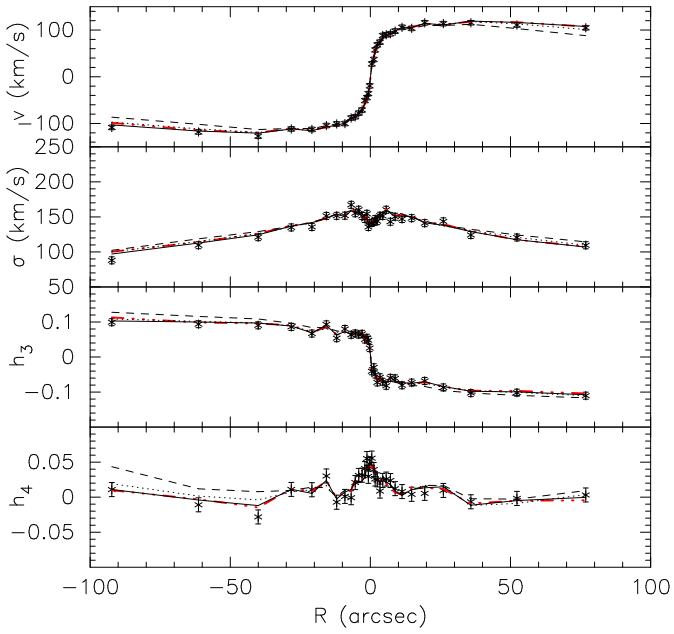

Figure 3.11: Particle model fits to the isotropic rotator mock kinematic data along the model's major axis. The points with error bars show the target data and the lines represent the model kinematics. The model data points are averages over the same slit cells as the target data (see Fig. 3.5), and are connected by straight line segments. The model v, σ are determined via eqs. (3.9) and (3.10) and h_3, h_4 are the fitted values based on the observed scale parameters V_p and σ_p. The full, dotted and dashed lines correspond to the models obtained with $\mu = 10^2$, $\mu = 10^3$, and $\mu = 5 \times 10^3$, respectively. The red dashed line shows the $\mu = 100$ model kinematics 20 dynamical times later, reflected with respect to the origin, and obtained from direct fitting of the model line profiles. This proves that this model is accurately axisymmetric and stationary; see text for details.

initial particle model, in which all particles have equal weights. In the present case this works to cause a bias against both fast rotation and anisotropy. This first becomes apparent where the relative statistical power of the data is weakest, i.e., at large radii.

Because our goal in this chapter is to determine the range of potentials in which we can find valid dynamical models for NGC 4697, we need to ensure that the answer to this question is not biased by overly strong entropy smoothing in the galaxy's outer regions. Thus in the modelling in Section 3.5 we will conservatively choose $\mu = 100$ for the smoothing parameter (indicated by the starred symbol in Fig. 3.10). Similar caution is common practice in determining black hole masses in galaxies (e.g., Gebhardt et al., 2003). The resulting dynamical models will then be somewhat less smooth than could be achieved, but this price is rather modest; between $\mu = 10^2$ and its minimum value at $\mu = 10^3$, the rms Δ in Fig. 3.10 decreases from $\simeq 1.7\%$ to $\simeq 1.4\%$, i.e., by $\simeq 15\%$. Certainly it would not be appropriate to rule out potentials in which the solutions differ by this degree in smoothness.

Using $\mu = 100$ in the modelling leads to a slight overfitting of the slit kinematic data, especially for the higher order kinematic moments which themselves take only values of order percents. It is worth pointing out that, contrary to first appearances from Fig. 3.11, this implies neither that these models are not axisymmetric, not that they are out of equilibrium. The model kinematics shown in Fig. 3.11 are obtained after 20 dynamical times of free evolution in the axisymmetric potential, so are thoroughly phase-mixed. The model data points shown are averages over the same slit cells as the target data (see Fig. 3.5), and are connected by straight line segments. The plotted v, σ are determined via eqs. (3.9) and (3.10) and h_3, h_4 are the fitted values based on the observed scale parameters V_p and σ_p. The red dashed line in Fig. 3.11 also corresponds to the $\mu = 100$ model, but has been determined as follows: (i) from the particle distribution after a total of 40 dynamical times of free evolution; (ii) from a mirror-symmetric set of slit cells, with respect to the major-axis slit shown in Fig. 3.5, (iii) using the (v, σ, h_3, h_4) parameters obtained by direct fits to the model line profiles, and (iv) finally reflecting the kinematics so obtained anti-symmetrically with respect to the origin. The excellent agreement between this curve and the original major axis kinematics of this model in Fig. 3.11 shows that (i) the $\mu = 100$ model is a true equilibrium, (ii) it is accurately axisymmetric, and (iii) the left-right differences in the kinematics in Fig. 3.11 are due to slightly different slit cell averages over the model on both sides. That these averages can be slightly different is made possible by low-level (axi-symmetric) structure in the model consistent with the slight under-smoothing for this value of μ. What happens is that the algorithm adds a few near-circular orbits in the relevant radial ranges. When added to the corresponding model LOSVDs and averaged over the asymmmetric slit cells these orbits change the kinematic moments h_n, $n \geq 3$ at the $\simeq 0.01$ level so as to improve the agreement with the observed major axis h_3, h_4. In the other slits the models interpolate more smoothly between points when needed because fluctuations in the particle distribution to follow local kinematic features are less easily arranged; see the corresponding figure for NGC 4697 in Section 3.5.

A comparison of the internal velocity moments of the input model and the particle model in the equatorial plane is presented in Figure 3.12. The figure shows σ_R, σ_ϕ and σ_z, followed by v_ϕ. The last panel displays the anisotropy parameter $\beta_\theta = 1 - \sigma_\theta^2/\sigma_r^2$, which is zero for the input isotropic rotator model. Within the radial extent of the target data, the internal moments of the input model are well reproduced; outside this region, where the model is poorly constrained by the input data, the particle model increasingly deviates from the target. Indeed, if we add PN velocity data in this test, the corresponding particle model agrees with the internal moments of the input model out to larger radii.

3.4.2 Mass-to-light ratio

We will now use such isotropic rotator models to explore how accurately we are able to recover the input mass-to-light ratio, given the spatial coverage of the data. Further, we will test our new

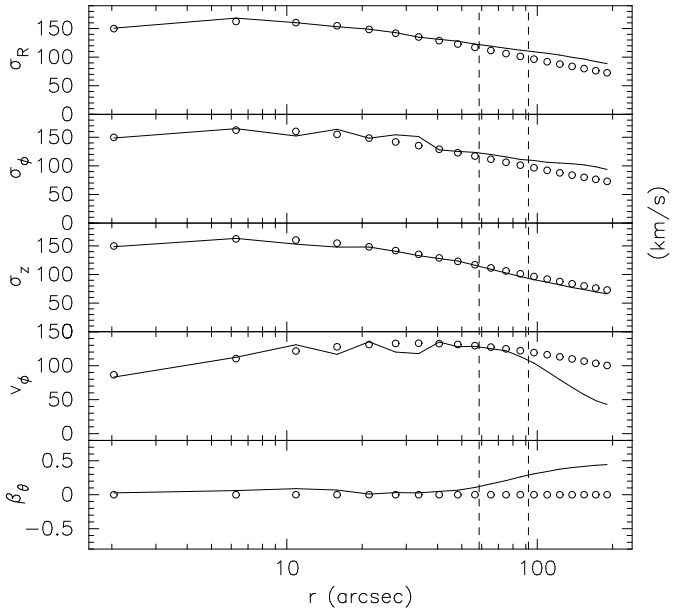

Figure 3.12: Comparison of the intrinsic velocity moments in the equatorial plane of the axisymmetric isotropic rotator particle model and target model. The points represent the target system and the lines correspond to the final particle model for $\mu = 100$, averaged over azimuth. The dashed vertical lines show the maximum radial extent of the minor axis (left line) and major axis target kinematic data (right line). At larger radii the particle model is poorly constrained by the input target data.

procedure, described in Section 3.3.6, for estimating the mass-to-light ratio efficiently. As input models we take both the self-consistent isotropic rotator model described above and a model constructed in the same way but including a dark matter halo. The halo potential is of the form of equation (3.1), with $r_0 = 190$ arcsec ($9.7\,\mathrm{kpc}$), $v_0 = 220\ \mathrm{km}\ s^{-1}$ and $q_\phi = 1.0$. The mass-to-light ratio of the stars in both input models is fixed to $\Upsilon = 5$.

The results for a "classical" approach, in which we fit a dynamical particle model to the data for different values of Υ, are presented in Figure 3.13, which shows the quality of the fit as function of Υ for the self-consistent case. The input value of Υ is recovered well. The results with the new procedure presented in Section 3.3.6 are summarized in Figure 3.14. The figure shows the evolution of the mass-to-light ratio as a function of time during NMAGIC model fits. Models for both the self-consistent input galaxy and for the target model including a dark halo potential are shown, with both low and high initial choices of Υ. The tests show that for the self-consistent case the input mass-to-light ratio is recovered very well. The uncertainties are slightly larger when a dark matter halo is included, but the maximum fractional error is less than three percent. We conclude that the new scheme works very well and that Υ is recovered within a few percent (for the amount and quality of data used in the present work). The advantage of the new method is its efficiency, only one run is needed to estimate Υ instead of order 10, but at the cost of not knowing the shape of χ^2 as a function of Υ near the minimum, i.e., the confidence interval.

3.5 Dynamical models of NGC 4697

After these tests we are now ready to use NMAGIC for constructing axially symmetric dynamical models of NGC 4697. We investigate self-consistent models as well as models including dark matter halos, and fit the photometry, slit kinematics and PNe data. Our aim in this chapter

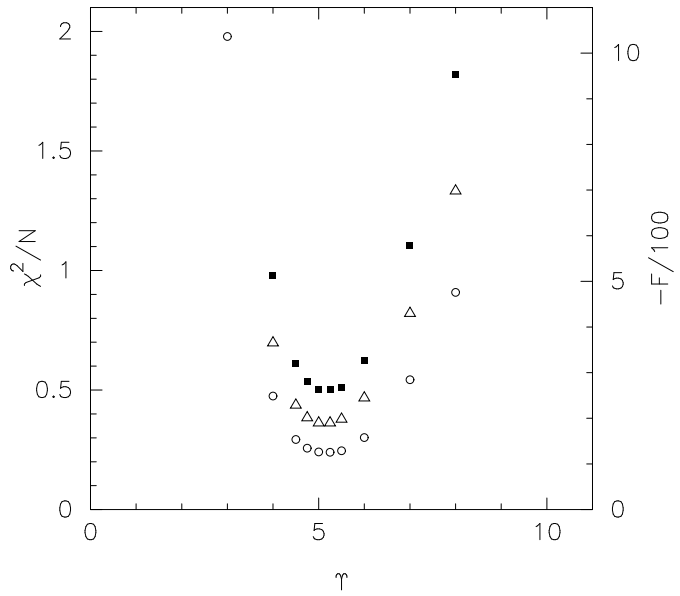

Figure 3.13: Quality of the particle model fit to the self-consistent isotropic rotator input model, as a function of assumed mass-to-light ratio Υ. χ^2 values per data point are given for the particle model fit to the photometric and kinematic target observables (open circles) and to the kinematic observables alone (filled squares). The triangles correspond to the measured merit function F. The input mass-to-light ratio is $\Upsilon = 5$. All models are built using $\mu = 100$.

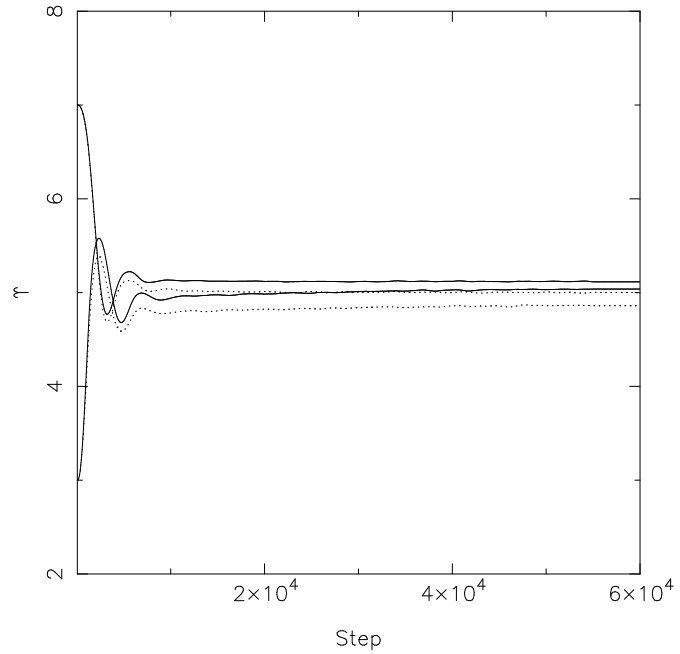

Figure 3.14: Direct mass-to-light ratio fits with NMAGIC. The plot shows the evolution of Υ with time during NMAGIC runs with different initial Υ, for the self-consistent isotropic rotator target (solid lines), and the isotropic rotator in a potential including a dark halo (dotted lines). The input mass-to-light ratio $\Upsilon = 5$ in all cases. Time is given in terms of elapsed time steps where 10^4 steps correspond to $\simeq 40$ circular rotation periods at $1R_e$.

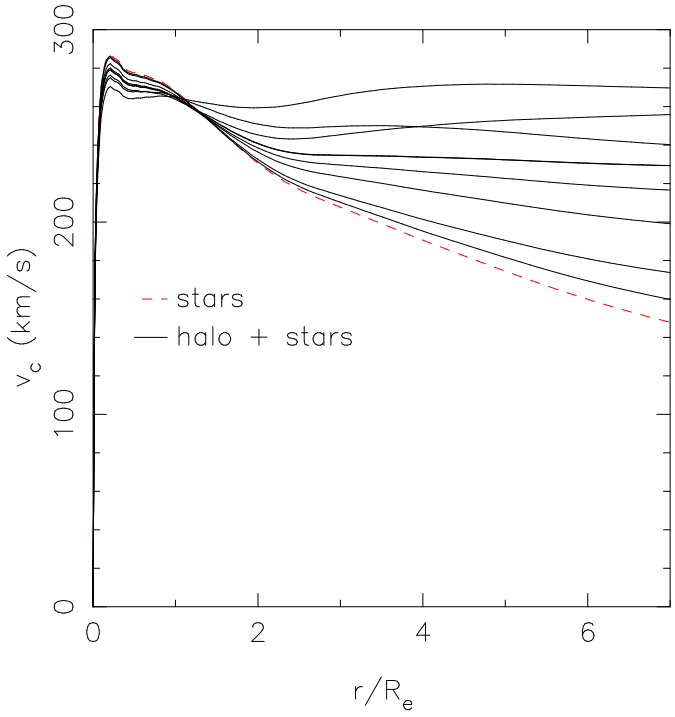

Figure 3.15: Circular velocity curves of the potentials used in the modelling, including the self-consistent model A (dashed line), and a sequence of dark matter halos (solid lines). The lines at $r/R_e = 7$ run from model A (bottom) to K (top), with models F and G represented by the same curve; *cf.* Table 3.1.

is not to attempt to constrain detailed halo mass profiles, but only to ascertain whether a dark matter component is allowed, or required, by the kinematic data. Thus we investigate a simple sequence of potentials A to K which include the contribution from the stellar component and a halo potential as in equation (3.1), with parameters given in Table 3.1. The parameters are chosen to result in a sequence of circular speed curves ranging from falling according to the distribution of stars to nearly flat over the whole range of radii. This sequence is shown in Figure 3.15; all these circular velocity curves are computed in the galaxy's equatorial plane and include the stellar component with the respective best-fitting mass-to-light ratio as given in Table 3.1.

To construct the models, we proceed as in Section 3.4. First, we compute the photometric observables. We expand the deprojected luminosity distribution of NGC 4697 in a spherical harmonics series on a grid of 40 shells in radius, quasi-logarithmically spaced with $r_{\rm min} = 1.0''$ and $r_{\rm max} = 700''$. As observables we use the luminosity on radial shells L_k and the higher order coefficients $A_{20,k}$, $A_{22,k}$, $\cdots$, $A_{66,k}$ and $A_{80,k}$, at radii r_k. The $m \neq 0$ terms are set to zero to force the models to remain nearly axisymmetric, i.e., within the limits set by the specified A_{lm} errors. Because the photometry is not seeing-deconvolved, for the innermost two points ($R < 3$") we only fit the A_{00} term. Errors for the luminosity terms A_{lm} are estimated by Monte Carlo simulations as in Section 3.4.1. As kinematic constraints we use the luminosity weighted Gauss-Hermite moments from the slit data, and the PNe kinematics, either represented by binned line-of-sight velocity and velocity dispersion points, or as discrete velocity measurements; see Sections 3.2.3 and 3.3.5.

Again we fit particle models in a three step process. (i) First, we start with the spherical particle model described in Section 3.3.7 and evolve it using NMAGIC to generate a self-consistent particle realization with the luminosity distribution given by the deprojection of the photometry. (ii) Because NGC 4697 shows significant rotation, we then switch retrograde particles similarly as in Section 3.4.1, using $p_0 = 0.3$ and $L_0 \simeq L_{\rm circ}(0.03R_e)$. The resulting rotating parti-

HALO	r_0/R_e	$v_0/\mathrm{km\ s^{-1}}$	q_ϕ	χ^2/N	χ^2_{alm}/N_{alm}	χ^2_{sl}/N_{sl}	χ^2_{PN}/N_{PN}	$-F$	Υ
A	0	0	1.0	0.453	0.0323	0.900	0.968	370.2	5.78
B	5.76	80	1.0	0.415	0.0254	0.828	0.884	343.9	5.74
C	5.76	120	1.0	0.439	0.0343	0.877	0.784	358.6	5.71
D	4.32	160	1.0	0.404	0.0288	0.816	0.610	333.7	5.58
E	4.32	190	1.0	0.404	0.0244	0.826	0.520	332.8	5.49
F	4.32	210	1.0	0.386	0.0229	0.791	0.476	320.0	5.45
G	4.32	210	0.8	0.382	0.0203	0.785	0.439	315.4	5.46
H	2.88	210	0.8	0.376	0.0232	0.773	0.397	310.2	5.28
J	4.32	250	0.8	0.383	0.0242	0.786	0.377	313.7	5.34
K	2.88	250	0.8	0.377	0.0212	0.771	0.506	309.6	5.10

Table 3.1: Table of model parameters and fit results. Columns (1)-(4) give the model code and the parameters r_0, v_0 and q_ϕ used in equation (3.1) for the respective dark halo potential in this model. The next four columns list the χ^2 values per data point, for all observables [column (5)], and for the density constraints, slit kinematic observables, and PN observables (data set PND1) separately [columns (6)-(8)]. Column (9) gives the numerical value of the merit function in equation 3.12, and column (10) the final (r-band) mass-to-light ratio. The respective number of constraints are $N = 1316$, $N_{alm} = 680$, $N_{sl} = 604$, $N_{PN} = 32$.

HALO	r_0/R_e	$v_0/\mathrm{km\ s^{-1}}$	q_ϕ	χ^2/N	χ^2_{alm}/N_{alm}	χ^2_{sl}/N_{sl}	$-\mathcal{L}$	$-F$	Υ
A	0	0	1.0	0.415	0.0331	0.845	2042.9	2382.5	5.81
B	5.76	80	1.0	0.405	0.0282	0.830	2038.2	2371.5	5.76
C	5.76	120	1.0	0.419	0.0331	0.853	2033.7	2374.2	5.72
D	4.32	160	1.0	0.406	0.0314	0.828	2028.3	2357.9	5.60
E	4.32	190	1.0	0.391	0.0271	0.801	2026.3	2344.9	5.54
F	4.32	210	1.0	0.402	0.0304	0.820	2025.6	2350.1	5.49
G	4.32	210	0.8	0.396	0.0232	0.815	2024.8	2343.9	5.48
H	2.88	210	0.8	0.373	0.0245	0.766	2026.3	2329.2	5.31
J	4.32	250	0.8	0.374	0.0203	0.773	2025.6	2329.0	5.37
K	2.88	250	0.8	0.369	0.0198	0.763	2030.8	2329.9	5.14

Table 3.2: Table of model parameters and fit results, similar to Table 3.1, but with all models computed using the likelihood scheme for the PNe as discrete kinematic tracers. Columns (8) and (9) now give the likelihood of the PN data set $\mathcal{L}$ and the merit function including $\mathcal{L}$ [equation 3.17]. The other columns are equivalent to those in Table 3.1.

cle model (hereafter, model RIC) is used as a starting point to construct a series of dynamical models by fitting the photometry and kinematics in different halo potentials, as follows. For every dark matter halo from Table 3.1, we first relax RIC for 5000 time steps in the total gravitational potential, assuming a mass-to-light ratio of 5.74. For reference, 10000 time steps in the self-consistent potential correspond to ≈ 40 circular rotation periods at R_e in spherical approximation. After this relaxation phase, we evolve the particle system for $\sim 10^5$ NMAGIC correction steps while fitting the complete set of constraints. During this correction phase, the potential generated by the particles is updated after each correction step but the dark matter potential (if present) is constant in time. (iii) Subsequently, we keep the global potential constant and evolve the system freely for another 5000 steps, without further correction steps. Models A, D, G and K were in addition evolved for a further 10000 steps with all potential terms active, to confirm that the modest radial anisotropy required in these models does not lead to dynamical instabilities.

To make sure that the results are not biased by the way we incorporate the PNe data, we have constructed three models in most halo potentials. Each time the PNe data are represented differently, using the binnings PND1, PND2, or the likelihood method.

The quality of the fit for different halo models can be characterized by the quantity F defined in equation (3.12) or (3.17) and is given in Tables 3.1 and 3.2. In addition, the value of χ^2 per data point is also shown, globally and for each data set separately, as are the stellar mass-to-light ratios. For the same reasons as for the isotropic rotator test models, the density constraints are very accurately fit. The slit kinematics are typically fit within about 0.9σ per point, slightly better than required. This is due to the relatively low value used for the entropy smoothing, needed not to bias the range of allowed potentials by the imposed smoothing. The PN χ^2 and likelihood values show that the PN data are consistent with all models.

Figures 3.16, 3.17, 3.18 present results from some of these models, comparing the stars-only model A and the three halo models D, G, and K to the data. Figure 3.16 shows the comparison of models A, D, G with the photometric constraints. The model lines match the target data points perfectly, in accordance with the very small χ^2_{alm}/N_{alm} values in Table 3.1. Figure 3.17 compares the projected absorption line kinematics of the three models with our measurements and the BDI data. The fits are generally excellent. Along the major and minor axes one can see how the models have found compromises to deal with asymmetries of the data on both sides of the galaxy, and slight discrepancies between our and the BDI data, e.g., in the region around $\pm 10''$ along the major axis. As for the isotropic rotator, the major axis higher order moments in Fig. 3.17 are even somewhat overfitted; see the discussion in Section 3.4.1.

Figure 3.18 compares the final A, D, G, and K models with the PNe kinematic constraints along the major axis (left) and minor axis (right); on each axis we show mean velocity (top) and velocity dispersion (bottom). The model curves in Fig. 3.18 and the χ^2 per data point values in Table 3.1 are computed for PN dataset PND1. There was no difference between these values and those obtained with PN dataset PND2 in all cases where we modelled both. The two additional lines in the panels of Fig. 3.18 show the mean velocities and velocity dispersions for the variants of models A, K obtained with the likelihood scheme for the PNe (see Section 3.3.5), computed by binning the particles in these models a posteriori in the same bins as for dataset PND1. While there is little difference for model K, the likelihood variant of model A fits the observed PN data points actually better than the original model A based on the PND1 data.

Overall, this figure illustrates that with increasing halo mass the fit to the PNe kinematic data improves slightly. Models G and K bracket the best-fitting models to the binned data in Fig. 3.18. However, also model A without dark matter still has a χ^2_{PN}/N_{PN} just below one, despite being systematically a little low in the minor axis dispersion plot. When we force the self-consistent model to improve the PN data fit at the expense of the slit kinematic data fit, the model starts to develop specific anisotropy features at the radii of the outer PN data. This suggests that with PN data extending to somewhat larger radii, ≈ 400 arcsec ($R \simeq 6R_e$), the

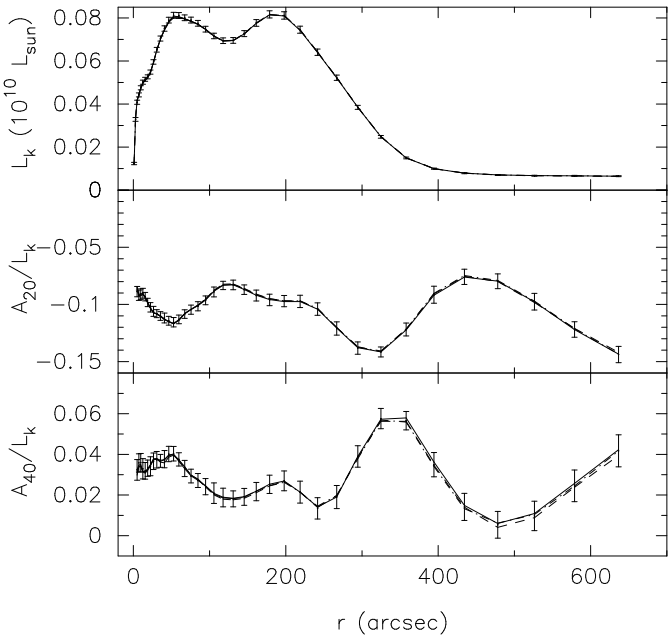

Figure 3.16: Comparison of the photometric constraints with the final models A (self-consistent, dashed), D (dotted), and G (full line). The points correspond to the target input data. From top to bottom: luminosity on radial shells profile $L_k = \sqrt{4\pi}A_{00}$, and normalized A_{20} and A_{40} profiles.

model without dark halo might start to fail. However, given the present PN data the differences between our models are not yet large enough to rule out constant mass-to-light ratio models for NGC 4697 (see also the likelihood values in Table 3.2).

The conclusion that both models with and without dark halos are consistent with the data currently available for NGC 4697 is also confirmed by considering the model fits to all the data in Figures 3.16-3.18. Models with massive dark halos overall fit slightly better, having slightly lower χ^2 values in Table 3.1, but these variations are all within $\chi^2 < 1$. Certainly these differences are not sufficient to rule out any of the models, given also the possibility of residual systematic effects.

Finally, Figure 3.19 shows the internal kinematics of the particle models A, D, G, and K. The upper panels give σ_R, σ_ϕ and σ_z, followed by v_ϕ. The last panel displays the anisotropy parameter $\beta_\theta = 1 - \sigma_\theta^2/\sigma_r^2$, which is zero for an isotropic rotator model. All quantities are given as averages over the models' equatorial plane. The more massive halo models become more radially anisotropic in the outer parts in terms of σ_R vs. σ_ϕ, but β_θ does not increase beyond model D because σ_R and σ_z increase in parallel while σ_ϕ remains constant. Thus the additional kinetic energy that stars at large radii must have in these models, is hidden in the plane of the sky. Conversely, at small radii the velocity dispersions in models G-K are slightly lower, compensating for the larger radial velocities of halo stars along the line-of-sight to the center. These models have $\beta \simeq 0.3$ at the center, which increases with radius and reaches $\beta \simeq 0.5$ at $\gtrsim 2R_e$.

3.6 Summary and Conclusions

In this chapter, we have presented new surface brightness measurements and long slit spectroscopic data for the E4 galaxy NGC 4697, and combined these data with existing long slit kinematics and discrete PNe position and velocity measurements to construct dynamical models for this galaxy. The combined data set runs from the center of the galaxy to about 4.5 effective radii.

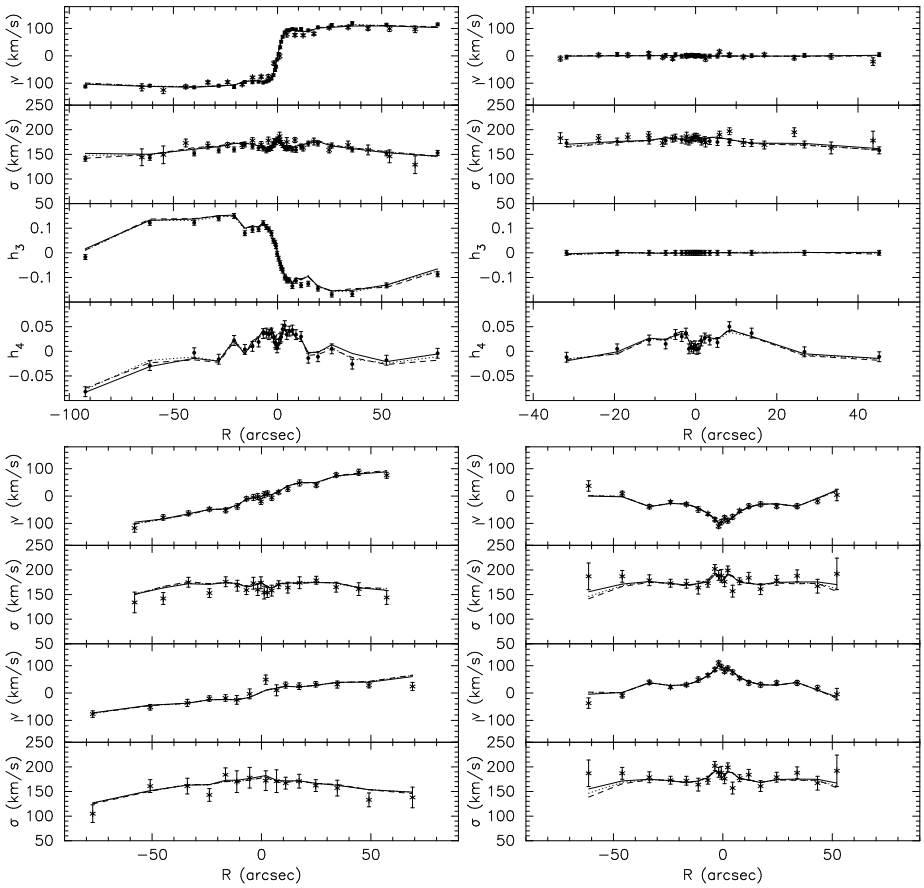

Figure 3.17: Comparison of models A, D, and G to the absorption line kinematic data along the major axis (top left), minor axis (top right), the slits parallel to the major axis (bottom left), and the slits parallel to the minor axis (bottom right). Full and starred data points show our new data and the BDI data, respectively. The model data points are averages over the same slit cells as the target data (see Fig. 3.5), and are connected by straight line segments. Linestyles for the models are the same as in Fig. 3.16.

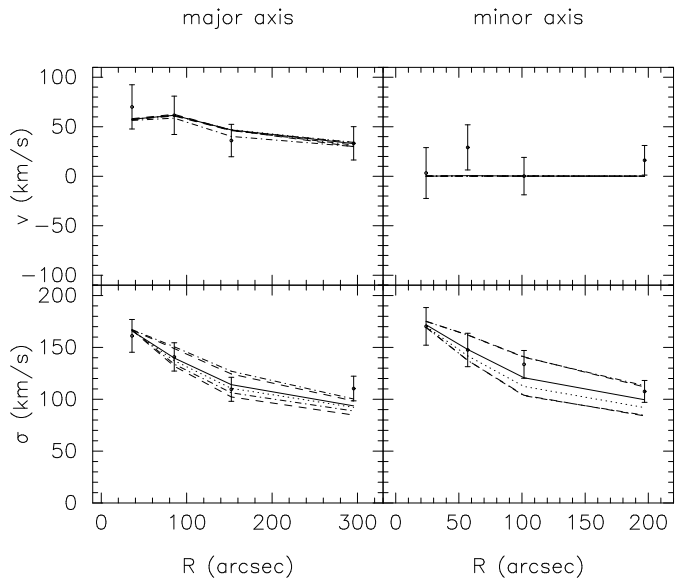

Figure 3.18: Comparison of the PNe velocity and velocity dispersion data (PND1, points) with models A, D, G, and K. Top left: v along the positive major axis. Top right: The same for the minor axis. Bottom left: σ along the positive major axis. Bottom right: The same but for the minor axis. Dashed, dotted, full, and upper dashed lines show models A, D, G, and K; the two dash-dotted lines show the variants of models A and K obtained with the likelihood scheme for the PNe.

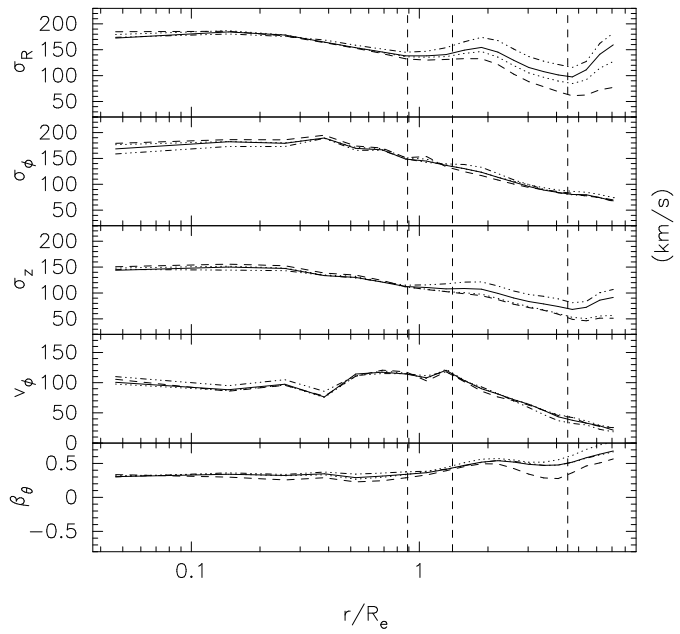

Figure 3.19: Internal velocity moments in the equatorial plane for models A, D, G, K (dashed, dotted, full, and dash-triple dotted lines, respectively). The vertical dashed lines indicate the radial extent of the minor axis slit data, major axis slit data, and PN data, from left to right.

For the first time, we have modelled such a dataset with the new and flexible χ^2-made-to-measure (χ^2M2M) particle code NMAGIC. We have extended NMAGIC to include seeing effects and have implemented an efficient method to estimate the mass-to-light ratio Υ. Tests of this scheme using isotropic rotator input models have shown that the method recovers Υ within a few percent both for self-consistent and dark matter dominated target galaxies. In addition, we have implemented a likelihood scheme which allows us to treat the PNe as discrete velocity measurements, so that no binning in velocities is needed. The modelling presented in this chapter shows that the χ^2M2M/NMAGIC particle method is now competitive with the familiar Schwarzschild method. In fact, it has already gone further in that the gravitational potential of the stars has been allowed to vary in the modelling, the mass-to-light ratio has been adapted on the fly, the stability of the models has been checked, and, in de Lorenzi et al. (2007), NMAGIC has been used to construct triaxial and rotating triaxial models.

Even though NMAGIC does not require any symmetry assumptions for the modelling, we have in this chapter forced the method to generate axisymmetric particle models for NGC 4697. Both self-consistent models without dark matter, and models following a sequence of circular speed curves with increasing dark halo contributions have been investigated. The PN data have been used both binned on two different spatial grids, as well as with the new likelihood scheme, to make sure that the results are not biased by the way the PNe data are incorporated.

Our main astronomical result is that models both with and without dark matter are consistent with all the data for NGC 4697. These models fit all kinematic data with $\chi^2/N < 1$, both in potentials with only luminous matter and in potentials including sufficiently massive halos to generate nearly flat circular rotation curves. The massive dark halo models tend to fit the data slightly better in the sense of lower χ^2/N, for both the slit kinematics and the PN data, but these variations are small and not yet statistically significant. To exclude models without dark matter would require PN velocities at even larger radii than currently available, out to an estimated $\simeq 6R_e$ from the center.

Our models differ from earlier studies performed by Méndez et al. (2001) in the sense that we generate axisymmetric models instead of spherical ones and that our models are flexible with regard to anisotropy. The best-fitting models are slightly radially anisotropic, with $\beta \simeq 0.3$ at the center, increasing to $\beta \simeq 0.5$ at $\gtrsim 2R_e$. This is consistent with the value given by Dekel et al. (2005) obtained from merger simulations carried out within the ΛCDM cosmology framework.

CHAPTER 4

DEARTH OF DARK MATTER OR MASSIVE DARK HALO? MASS-SHAPE-ANISOTROPY DEGENERACIES REVEALED BY NMAGIC DYNAMICAL MODELS OF THE ELLIPTICAL GALAXY NGC 3379

Flavio De Lorenzi, Ortwin Gerhard, L. Coccato, M. Arnaboldi, M. Capaccioli, N.G Douglas, K.C. Freeman, K. Kuijken, M.R. Merrifield, N.R. Napolitano, E. Noordermeer, A.J. Romanowsky, V.P. Debattista
to be submitted to *MNRAS*, 2007

Recent results from the Planetary Nebula Spectrograph (PN.S) survey have revealed a rapidly falling velocity dispersion profile in the nearby elliptical galaxy NGC 3379, casting doubts on whether this intermediate-luminosity galaxy has the kind of dark matter halo expected in ΛCDM cosmology. We present a detailed dynamical study of this galaxy, combining ground based long slit spectroscopy, integral-field data from the SAURON instrument, and PN.S data reaching to more than seven effective radii.

We construct dynamical models with the flexible χ^2-made-to-measure particle method implemented in the NMAGIC code. We fit spherical and axisymmetric models to the photometric and combined kinematic data, in a sequence of gravitational potentials whose circular velocity curves at large radii vary between a near-Keplerian decline and the nearly flat shapes generated by massive halos.

Assuming spherical symmetry we find that the data are consistent both with near-isotropic systems dominated by the stellar mass, and with models in moderately massive halos with strongly radially anisotropic outer parts ($\beta \simeq 0.8$). Formal likelihood limits would exclude (at 1σ) the model with stars only, as well as halo models with $v_{circ}(7R_e) \gtrsim 250\mathrm{kms}^{-1}$. A sequence of more realistic axisymmetric models of different inclinations confirms the spherical results. All valid models fitting all the data are dynamically stable over Gyrs, including the most anisotropic ones.

Overall the kinematic data for NGC 3379 out to $7R_e$ do not give strong constraints on the mass distribution in this galaxy. NGC 3379 may well have a dark matter halo consistent with the current ΛCDM paradigm.

4.1 Introduction

There is strong evidence that most galaxies are surrounded by massive dark matter (DM) halos. This is most evident in spiral galaxies, where the rotation curves of extended cold gas disks

remain flat out to large radii. In elliptical galaxies the evidence for dark halos has built up more slowly, and their halo properties are not so well known, because of a lack of ubiquitous tracer similar to the HI rotation curves in spirals. Only in a few cases is it possible to measure masses from extended HI ring velocities (*e.g.* Franx et al. 1994; Oosterloo et al. 2002).

However, at least for giant elliptical galaxies stellar-dynamical studies from integrated light spectra (*e.g.* Kronawitter et al. 2000; Gerhard et al. 2001; Cappellari et al. 2006; Thomas et al. 2007) analyses of the X-ray emitting hot gas atmospheres (*e.g.* Awaki et al. 1994; Matsushita et al. 1998; Loewenstein and White 1999; Humphrey et al. 2006; Fukazawa et al. 2006), and gravitational lensing data (*e.g.* Wilson et al. 2001; Treu and Koopmans 2004; Rusin and Kochanek 2005; Koopmans et al. 2006; Gavazzi et al. 2007) are now giving a fairly consistent picture. The general result from these studies is that these ellipticals are surrounded by dark matter halos, the inferred mass profiles (luminous plus dark) are nearly isothermal, i.e., the circular velocity curves approximately flat, and the dark matter contributes $\sim 10-50\%$ of the mass within R_e. The central dark matter densities in ellipticals are higher than in spirals, presumably reflecting their earlier formation epochs (Gerhard et al. 2001; Thomas 2006).

In light of this, the finding of Romanowsky et al. (2003); Douglas et al. (2007), that several intermediate luminosity ellipticals (NGC 3379, NGC 4494, NGC 821) apparently have only diffuse dark matter halos if any, is quite surprising. Could the dark matter properties of these ellipticals be different from those of giant ellipticals (*e.g.* Napolitano et al., 2005), perhaps related to the fact that these lower-luminosity galaxies are less often found in groups or clusters? The result of Romanowsky et al. (2003) is based on the outer velocity dispersion profiles of the three galaxies, determined from individual planetary nebulae (PNe) velocities measured with the special PN.S instrument (Douglas et al., 2002). Two of the three galaxies are nearly round on the sky, and therefore the dynamical analysis was carried out with spherical models. A fourth galaxy with a fairly rapidly declining outer velocity dispersion profile is NGC 4697 (Méndez et al., 2001); however, de Lorenzi et al. (2008) have recently shown that models both with and without massive dark halos can be constructed that fit all the data for this galaxy essentially perfectly. Unfortunately, the diffuse gas envelopes of these intermediate luminosity ellipticals have very low densities, so an independent confirmation with X-ray data is difficult.

The results of Romanowsky et al. (2003) were criticized by Dekel et al. (2005). These authors pointed out that the well known mass-anisotropy degeneracy in the study of velocity dispersion profiles does not allow one to unambiguously determine the mass profile, that the triaxial nature of elliptical galaxies can cause low line-of-sight dispersions at some viewing angles, or that the PNe could trace young stars generated during the merger formation instead of the bulk of the old stars as usually assumed. Douglas et al. (2007) argued that Romanowsky et al. (2003) properly took into account orbital anisotropies in the data fitting process, that the effect of triaxiality is very unlikely to be present in all three galaxies, that the PN number density and dispersion profiles match the corresponding integrated light profiles reasonably well, and that this as well as the universality of the bright end of the PN luminosity function rules out that PNe only trace a young stellar population. Douglas et al. (2007) concluded that their results continue to conflict with the presence of dark matter halos as predicted in cosmological merger simulations.

The issue is important enough to merit a further careful analysis. In this paper we construct dynamical models of NGC 3379 with the very flexible NMAGIC particle code, making use of a variety of kinematic data, including SAURON integral field data, slit kinematics, and the PN dispersion profile.

The NMAGIC method is flexible not only with regard to anisotropy, but also in allowing axisymmetric or triaxial shapes with radially varying axis ratios. This is important since the intrinsic shape of NGC 3379 is still in doubt. Capaccioli et al. (1991); Statler and Smecker-Hane (1999) have suggested that NGC 3379 is a triaxial S0 galaxy seen almost face-on. Statler (2001) considered triaxial dynamical models and constrained the shape of this galaxy to be axisymmet-

ric and oblate in the inner parts and triaxial in the outer parts. Shapiro et al. (2006) argue that the most likely model is one of a moderately inclined oblate system.

The outline of the paper is as follows. In Section 4.2 we describe briefly how the various observational data for NGC 3379 are used in the modelling. In Section 4.3 we give a few details of the χ^2M2M NMAGIC method, and show how it performs on a mock galaxy data set similar to that for NGC 3379. In Section 4.4 we then construct various dynamical models for the real galaxy data, both spherical and flattened, in a sequence of potentials with increasing circular velocity at large radii. As summarized in the final Section 4.5 of the paper, our main conclusion is that the combined kinematic data for NGC3379 is consistent with a variety of models with or without massive dark matter halos.

4.2 Observational Data

We begin by describing the observational data used in this study, which are all taken from the literature. We also describe here the procedure employed for obtaining the three-dimensional luminosity density from the surface brightness data. In the following we adopt a distance 9.8 Mpc to NGC 3379 (Jensen et al., 2003), effective radius $R_e = 47''$ (2.23 kpc), and an absolute B magnitude $M_B = -19.8$ (Douglas et al., 2007).

4.2.1 Photometric Data

The photometric data used in the present work consists of the wide-field B-band photometry of Capaccioli et al. (1990), combined with the HST V-band observations of Gebhardt et al. (2000) to increase the spatial resolution within the inner $10''$. The photometry has been matched up by assuming a constant color offset $B - V = 1.03$. The last eight surface brightness (SB) points from Capaccioli et al. (1990), outside $R \simeq 500''$, show fluctuations of an amplitude which we judged unphysical; these points we have replaced with a Sersic (1968) profile fitted to the galaxy further in. The same Sersic fit is used to extrapolate the SB profile outside the last measured point at $R = 676''$. Similarly, we have replaced the measured ellipticities for $R > 81''$, where the observational uncertainties become large, by $\epsilon = 0.14$. Figure 4.1 presents the combined photometric data, showing surface brightness and ellipticity ϵ. The isophotal shape parameters a_4 and a_6 are not available for these data and are thus set to zero. For the spherical models, we have used the SB profile rescaled to a mean radius $R_m \equiv \sqrt{ab} = a\sqrt{1-\epsilon}$. For the axisymmetric models, we have used a constant PA of $70°$; the isophotal PA measured by Capaccioli et al. (1990) are within $\pm 3°$ of this value.

4.2.2 Deprojection

In our implementation of NMAGIC a particle model can be fitted to the surface brightness and/or the deprojected luminosity density, *cf.* Section 4.3. Below we use both options, so first need to construct models for the three-dimensional luminosity density, j.

In the spherical case the surface brightness can be deprojected uniquely. For an axisymmetric system the deprojection is unique only for edge-on galaxies; for systems inclined at an angle i with respect to the line-of-sight, the SB map contains information about the luminosity density only outside a "cone of ignorance" in Fourier space, of opening angle $90° - i$, when $i = 90°$ denotes edge-on (Rybicki, 1987). Thus, the deprojection of a moderately inclined galaxy results in undetermined konus densities (Gerhard and Binney, 1996; Romanowsky and Kochanek, 1997).

We deproject the surface brightness of NGC 3379, without correcting for PSF effects, using the program of Magorrian (1999). The program finds a smooth axisymmetric density distribution consistent with the SB distribution for the specified inclination angle, by imposing that the solution maximizes a penalized likelihood. This ensures that the shape of the 3D luminosity

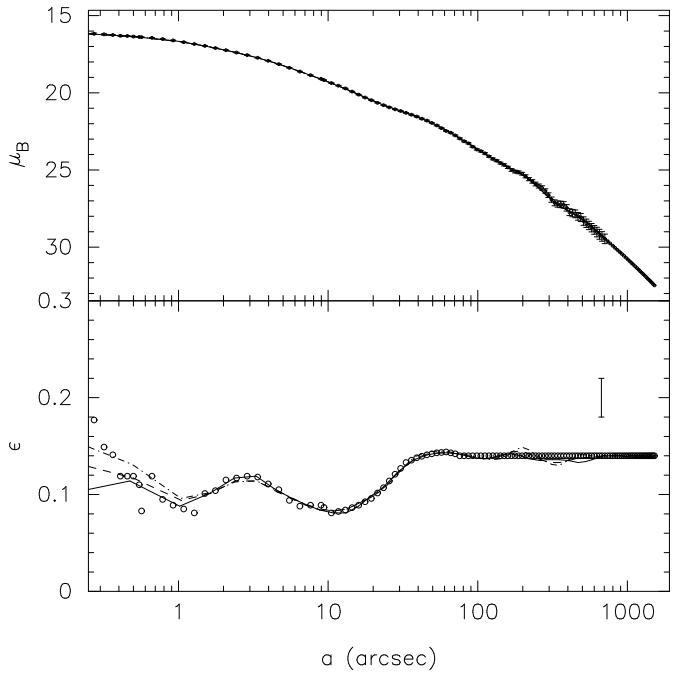

Figure 4.1: Combined photometry of NGC 3379 from Capaccioli et al. (1990) and Gebhardt et al. (2000) (black points). The two panels show the surface brightness (SB) profile and the ellipticity ϵ as a function of major axis distance. Beyond $500''$ the SB points are from a Sersic model fitted to the interior data, and outside $81''$, the ellipticity has been set to $\epsilon = 0.14$. In the ellipticity panel the error bar with size 0.02 illustrates the typical errors in the outer ellipticity measurements. The isophotal shape parameters a_4 and a_6 are not measured; they are set to zero. The lines show three-dimensional luminosity models determined from these data and reprojected onto the sky, for assumed inclinations of $i = 90°$ (edge-on, full lines), $i = 50°$ (dashed lines), and $i = 40°$ (dash-dotted lines).

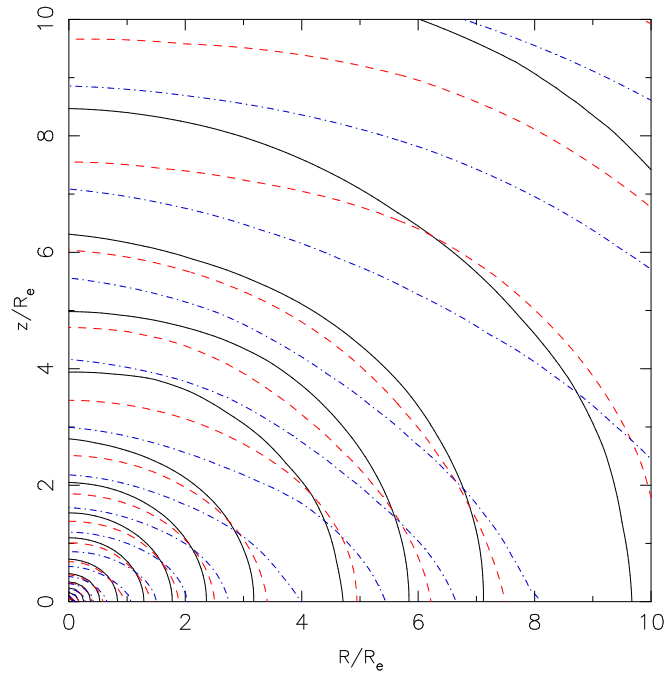

Figure 4.2: Iso-density contours of the deprojected B-band luminosity distribution of NGC 3379 for different inclinations. Solid, dashed, and dash-dotted contours refer to the $i = 90°$ edge-on, $i = 50°$, and $i = 40°$ deprojected models.

density is smooth, but for $i \neq 90°$, there would exist other smooth, slightly different, density distributions that also fit the SB data. We have used the program to compute luminosity densities for NGC 3379 for the inclinations $i = 90°$, $i = 50°$ and $i = 40°$. Figure 4.1 compares the observed photometry with the three deprojections reprojected onto the sky. Figure 4.2 shows the corresponding density isocontours of the deprojected B-band luminosity distributions in the meridional plane. Varying the inclination from $90°$ to $40°$ changes the intrinsic shape of the galaxy from E1 to E3.

4.2.3 Kinematic Data

Stellar-absorption line data

We have taken long-slit absorption line kinematics from the literature. We use data from Statler and Smecker-Hane (1999) at four different position angles, extending out to radii of $\simeq 80''$. We complement these kinematics with the spectroscopic data from Kronawitter et al. (2000). The major axis slits from Statler and Smecker-Hane (1999) and Kronawitter et al. (2000) are misaligned by $10°$ in PA; however, the data along both major axis slits follow each other closely. The measurements along the shifted slit of Kronawitter et al. (2000) reach $100''$ from the center. From both kinematic data sets we have the line-of-sight velocity, velocity dispersion, and higher order Gauss-Hermite moments h_3 and h_4 (Gerhard, 1993; van der Marel and Franx, 1993). Figure 4.3 shows the schematic arrangement of the kinematic slits used in the dynamical modeling.

In addition to the long-slit kinematics we also use the integral-field spectroscopy obtained with the SAURON instrument. These kinematic data were kindly provided by Shapiro et al. (2006) and consist of line-of-sight velocity, velocity dispersion and higher order Gauss-Hermite moments up to h_6. The SAURON field-of-view (FoV), shown by the (blue) rectangle in Figure 4.3, extends from $-19.6''$ to $24.4''$ along its short boundary and from $-34.8''$ to $35.6''$ along the long boundary. It consists of 9612 small grid cells, which serve as the basis grid to de-

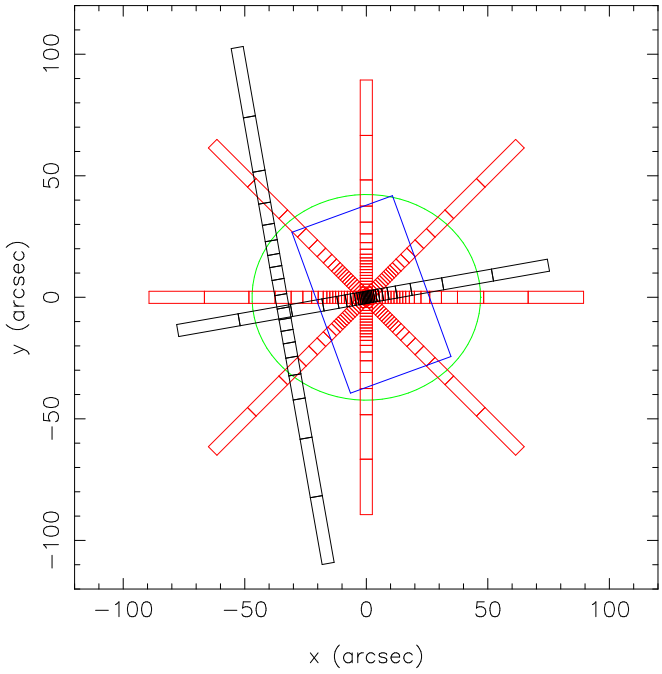

Figure 4.3: Schematic view of the positions with kinematic data as used to construct the dynamical models. The slits from Statler and Smecker-Hane (1999) and Kronawitter et al. (2000) are coded in red and black, respectively. Boxes along the slits show the region of the galaxy for which respective kinematic data points were derived; these boxes are used to determine the luminosity-weighted Gauss-Hermite moments. The blue rectangle indicates the SAURON field-of-view. The ellipse shown is oriented along PA=70°, the average major axis of the photometry, and has a semi-major axis of length R_e and axis ratio $q = 0.9$.

fine the 1602 voronoi cells on which the kinematic measurements are given. This results in a total of 9612 kinematic SAURON observables, as well as 1602 bin-luminosity observables. The SAURON data are compared to dynamical models in Section 4.4, and are reproduced in some of the figures there. Each of the six panels shows the 1602 voronoi bins, giving (from left to right) v, σ, h_3, h_4, h_5 and h_6. A comparison of the SAURON data with the data of Kronawitter et al. (2000) along their major axis is given in Figure 4.4. Overall, the two data sets agree well with each other. The same is true for the comparison of the SAURON data with Statler and Smecker-Hane (1999), as shown by Shapiro et al. (2006).

Both the SAURON data and the slit data are slightly asymmetric with respect to the center of the galaxy. If we denote the original SAURON dataset with $I(x, y|v_{\rm los}, \sigma_{\rm los}, h_3, h_4, h_5, h_6)$, and with $I^*(x, y|v_{\rm los}, \sigma_{\rm los}, h_3, h_4, h_5, h_6) = I(-x, -y, | - v_{\rm los}, \sigma_{\rm los}, -h_3, h_4, -h_5, h_6)$ the dataset obtained from I by point-symmetrical reflection with respect to the origin, we can construct a symmetrized dataset $\bar{I} \equiv 0.5(I + I^*)$. This symmetrized dataset $\bar{I}$ has a χ^2 per data point with respect to I of $\chi^2/N = 1.01$ when the original errors are used. Any point-symmetric model fit (spherical, axisymmetric, triaxial) to the original data I will therefore have a systematic error floor of this magnitude. In the models below, we will actually fit the symmetrized SAURON data to avoid any systematic effects, but keep the original errors on both sides of the galaxy separately (see also Shapiro et al., 2006).

In a similar fashion, we have constructed symmetrized slit data sets. To do this we average the two points at nearly similar radius on both sides of the slit with respect to the center. Taking into account the sign reversals of v and h_3, we take for the symmetrized data point the weighted mean of the points on both sides, with weights proportional to the inverse square of the measurement errors, and assign a new weighted error for the averaged point. If σ_+ and σ_- are the errors on both sides, the weights are $w_+ = 1/\sigma_+^2$, $w_- = 1/\sigma_-^2$, and the new error σ is given by the maximum of $2/\sigma^2 = 1/\sigma_+^2 + 1/\sigma_-^2$ and half of the deviation between the original data points on both sides. Again, the symmetrized data have a $\chi^2/N = 1.0$ systematic deviation from the original data, and therefore we will fit the symmetrized data below to avoid the model being pulled around by points with small error bars but large systematic deviations. The second panel of Figure 4.4 compares the symmetrized SAURON data with the symmetrized Kronawitter et al. (2000) data along the same slit as before. Again, the two data sets agree well with each other.

PNe data

Planetary nebulae (PNe) are dying low- to intermediate mass stars that emit most of their light in a few narrow lines of which the $[\mathrm{OIII}]\lambda 5007$ is the most prominent one. Because there are hardly other emission sources in elliptical galaxies, they can be detected fairly easily, and once identified, their line-of-sight velocity can be estimated from the Doppler shift of the emission line. The PN population in elliptical galaxies is expected to arise from the underlying galactic population of old stars and hence the PNe can be used as kinematic tracers for the stellar distribution. Their number relative to the luminosity of the galaxy is parametrized by the α parameter, which is a function of colour (Hui et al., 1995).

Douglas et al. (2007) processed observations of NGC 3379 conducted with the Planetary Nebula Spectrograph (PN.S) instrument and detected 214 spatially and spectrally unresolged PN candidates of which 191 are assigned to NGC 3379. Using the "friendless" algorithm applied by Merrett et al. (2003) they identified a small number of velocity outliers, probably unresolved background galaxy contaminants, which would be uniformly spread in velocity. The algorithm determined that 2 emission objects were more than $n = 5$ standard deviations away from the centroid of the velocity distribution of their $N = 15$ nearest neighbours, and $m = 5$ more than $n = 3$ standard deviations σ (see Fig. 8 of Douglas et al., 2007). The 3σ line itself has considerable uncertainty at large radii, due to the small number of PNe found there. Thus the exclusion of the outermost outlier is somewhat uncertain. Because this object does have some influence on the outermost velocity dispersion point, we will compare the models to the data

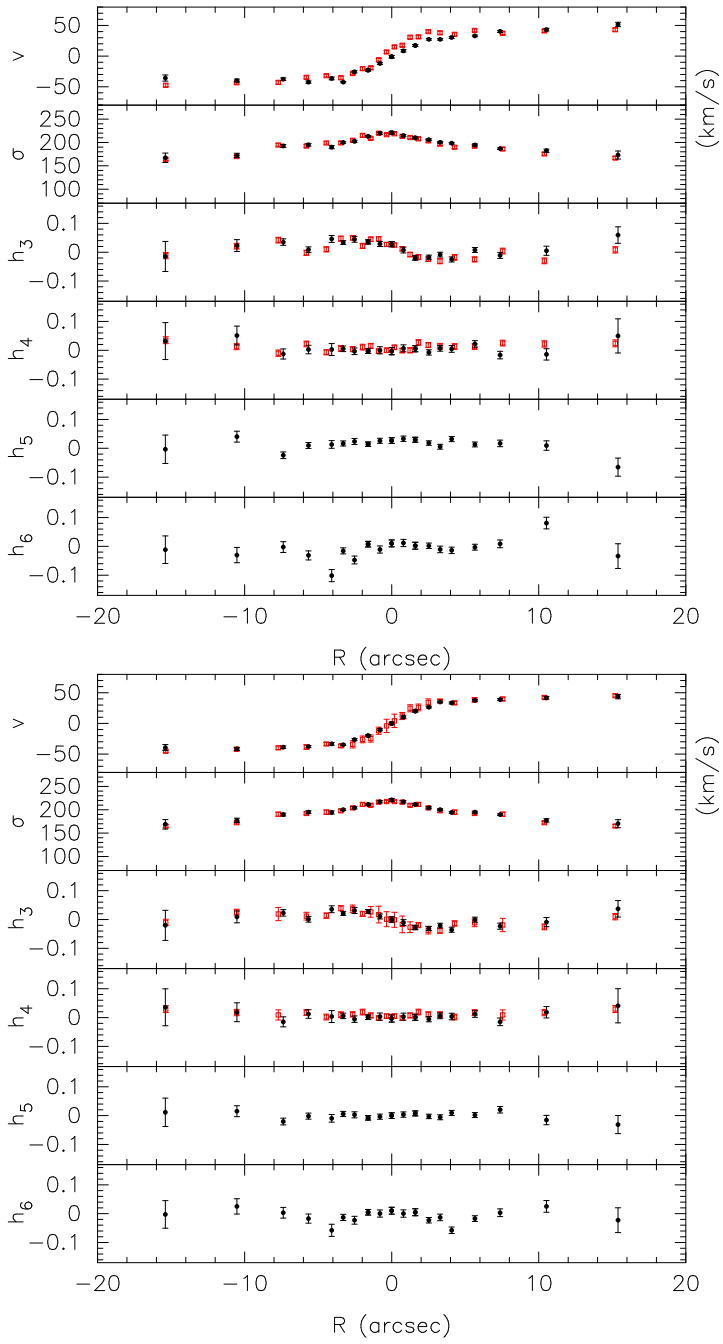

Figure 4.4: Comparison of the line-of-sight velociy distribution data along the galaxy's major axis ($PA = 70°$). The black circles correspond to the SAURON data and the open square symbols in red show the Kronawitter et al. (2000) data. The upper panel compares the original datasets, the lower panel is for the symmetrized data. In each panel from top to bottom are shown: v, σ, h_3, h_4, h_5, and h_6, for the latter two there are only SAURON data.

obtained both with and without this PN.

The radial distribution of the PNe in NGC 3379 was found to be consistent with the stellar density profile, and their kinematics consistent with absorption-line data in the region where the data sets overlap. Because the kinematics of the PNe in NGC 3379 are dominated by random motions with little azimuthal variation, the velocity dispersion can be computed in radial annuli without losing significant dynamical structure. We will thus use the radial run of the azimuthally averaged PN velocity dispersion in the dynamical modelling, but also compare the models to the individual velocities in a relative likelihood sense (cf. the tables and figures in Section 4.4).

4.3 NMAGIC modelling

To investigate the amount of dark matter consistent with the kinematic data for NGC 3379, we construct a range of dynamical models for the stellar component of this galaxy. We use the flexible χ^2-made-to-measure (χ^2M2M) particle method as described and implemented in the NMAGIC code by de Lorenzi et al. (2007, 2008). χ^2M2M is a development of the M2M algorithm of Syer and Tremaine (1996) that is suitable for modelling observational data. The M2M methods work by gradually adjusting individual particle weights as the model evolves, until the N-particle system reproduces a set of target constraints. In χ^2M2M the standard χ^2 statistics is used in the function to be maximized upon convergence of the weights. This allows for a proper treatment of observational errors, and the quality of the final model can be assessed directly from the target data.

Compared to the familiar Schwarzschild method the particle approach is relatively new and there are as yet only a few galactic dynamics studies in which it has been employed. Bissantz et al. (2004) made a first practical application of the M2M method of Syer and Tremaine (1996) and constructed a dynamical model of the Milky Way's barred bulge and disk by constraining the projected density map. First attempts to extend the M2M method to account for kinematic observables in addition to density constraints were made by De Lorenzi et al. (2006); Jourdeuil and Emsellem (2007). However, a proper treatment of observational errors was not yet included in their implementations. de Lorenzi et al. (2007) incorporated this in their χ^2M2M algorithm and demonstrated the potential of the NMAGIC code by constructing particle models for spherical, axisymmetric, triaxial and rotating target stellar systems. Some extensions of the method and the first detailed modelling of slit kinematic and PN data for an elliptical galaxy (NGC 4697) are described in de Lorenzi et al. (2008).

The NMAGIC method is flexible not only with regard to the orbit structure, but also in allowing axisymmetric or triaxial shapes with varying axis ratios. Contrary to Schwarzschild's method, the final stellar density and potential need not be known beforehand. This makes it ideal for the present study because different intrinsic shapes have been suggested for NGC 3379 (see the Introduction) and the issue of whether the kinematics require or allow dark matter may well be connected not only with the orbital anisotropies but also with the detailed shape of the stellar density distribution of the galaxy. Given that NGC 3379 is nearly round on the sky, we have constrained the models in this paper to be axisymmetric but have allowed radial variations in axis ratio. This has proved sufficient for answering our main science question.

4.3.1 Luminous and dark mass distributions

As in de Lorenzi et al. (2008), we assume that the luminous mass of NGC 3379 follows the light and we can characterize it by a constant mass-to-light ratio Υ, so that the stellar mass density is given by $\rho_\star = \Upsilon j$. The total gravitational potential is generated by the combined luminous mass and dark matter distributions, $\phi = \phi_\star + \phi_L$, where $\phi_\star$ is generated by $\rho_\star = \Upsilon j$. Only the luminosity density j is represented by the N-particle system. Its potential is computed using

a spherical harmonic decomposition as described in Sellwood (2003); de Lorenzi et al. (2007). The stellar potential is allowed to vary during the modeling process, but the DM halo is rigid.

Here our aim is not to determine the detailed shape of the dark matter halo in NGC 3379, but rather to first see whether the PN velocities allow or require any dark matter at all in this galaxy. To answer this question we will investigate a one-dimensional sequence of potentials whose circular velocity curves vary at large radii between the near-Keplerian decline expected when the mass in stars dominates, and the nearly flat shapes generated by massive dark halos. As in de Lorenzi et al. (2008) we thus represent the dark matter halo by the logarithmic potential (Binney and Tremaine, 1987)

$$\phi_L(r) = \frac{v_0^2}{2} \ln(r_0^2 + r^2). \tag{4.1}$$

4.3.2 Model and target observables

Target observables include surface or volume densities and line-of-sight kinematics. For modelling the luminosity distribution of NGC 3379, we generally use the deprojected luminosity density of NGC 3379, expanded in spherical harmonic coefficients A_{lm} on a 1-D radial mesh of radii r_k. The corresponding model observables are computed from the particles based on a cloud-in-cell (CIC) scheme; see de Lorenzi et al. (2007).

In some models, we do not constrain the three-dimensional luminosity density but only the stellar surface density, leaving the former free to evolve. In the remaining cases, we constrain the model by both the deprojected luminosity density and the projected surface density. In a similar spirit as for the volume density, we use as target constraints for the observed SB distribution the coefficients of a Fourier expansion in the azimuthal angle, computed on a 1-D radial mesh of projected radii R_k. For the corresponding model observables, the particles are assigned to the radial grid using a CIC scheme, and the Fourier coefficients a_m and b_m for the particle model on shell k are computed via

$$a_{m,k} = L \sum_i \gamma_{ki}^{CIC} \cos(m\varphi_i) w_i \tag{4.2}$$

$$b_{m,k} = L \sum_i \gamma_{ki}^{CIC} \sin(m\varphi_i) w_i, \quad m > 0 \tag{4.3}$$

where w_i are the particle weights, φ_i their angular positions, and γ_{ki}^{CIC} is a radial selection function. We use units for which the light L_i of a stellar particle can be written as $L_i = L w_i$ with L the total luminosity of the galaxy.

As kinematic constraints, we use the luminosity-weighted Gauss-Hermite coefficients from the SAURON or slit data, and luminosity-weighted velocity moments for the PN data. For the SAURON data (Shapiro et al., 2006), the luminosity-weighted coefficients are determined from the truncated Gauss-Hermite representation of the line-of-sight velocity distribution (LOSVD) up to order h_6 and the luminosity in the corresponding Voronoi bin. For the slit kinematics (Statler and Smecker-Hane 1999; Kronawitter et al. 2000), they are constructed again from the measured Gauss-Hermite moments, up to order h_4, and the luminosity in the slit section corresponding to the relevant LOSVD. The PN data (Douglas et al., 2007) are modelled either as 1-D radial dispersion profile or as a discrete set of velocities; in the former case we use as suitable observables the second velocity moments v_{los}^2, luminosity-weighted by the number of PNe per radial bin.

The corresponding model observables y_j are construced from the particles via equations of the form

$$y_j(t) = \sum_{i=1}^{N} w_i K_j \left[\mathbf{z}_i(t)\right], \tag{4.4}$$

where w_i are the particle weights and $\mathbf{z}_i$ are the phase-space coordinates of the particles, $i = 1, \cdots, N$. Here the Kernel K_j corresponds to the observable y_j. Detailed expressions for the kinematic model observables are given in de Lorenzi et al. (2007, 2008).

In general, we replace the observables by the corresponding temporally smoothed quantities to increase the effective number of particles in the system, *cf.* Syer and Tremaine (1996); de Lorenzi et al. (2007). For the parameters chosen, the smoothing is typically over $\sim 10^3$ correction time steps.

4.3.3 Fitting a particle model to the observations

Performing an NMAGIC fit to the observational constraints proceeds by evolving the force-of-change (FOC) equations for the particle weights,

$$\frac{\mathrm{d}w_i(t)}{\mathrm{d}t} = \varepsilon w_i(t) \left(\mu \frac{\partial S}{\partial w_i} - \sum_j \frac{K_j\left[\mathbf{z}_i(t)\right]}{\sigma(Y_j)} \Delta_j(t) \right) \tag{4.5}$$

depending on the discrepancies between model (y_j) and target observables (Y_j), $\Delta_j(t) = (y_j - Y_j)/\sigma(Y_j)$. Here $\sigma(Y_j)$ in the denominator is the error in the target observable. Evolving the particle weights to convergence in this way is equivalent to maximizing the merit function

$$F = \mu S - \frac{1}{2}\chi^2 \tag{4.6}$$

with respect to the particle weights w_i, where for the profit function S we use the entropy, and the standard χ^2 measures the goodness of the fit. The parameter μ controls the contribution of the entropy function to F. The entropy term pushes the particle weights to remain close to their priors, so models with large μ will have smoother distribution functions than those with small μ. The best choice for μ depends on the observational data to be modeled, *e.g.* spatial coverage and phase-space structure of the galaxy under consideration, but also on the initial conditions, and will be determined for the NGC 3379 dataset in the following Section 4.3.4.

Any NMAGIC model fit starts from a suitable initial model. For the models presented in this paper, we have used as initial conditions a Hernquist (1990) model particle realization generated from a distribution function (DF) using the method described in Debattista and Sellwood (2000). The particle realization consists of 7.5×10^5 particles, has a scale length $a = 1$, maximum radius $r_{\max} = 60$, and a total luminosity of unity. In model units, the gravitational constant is $G = 1$. When we match the model lengthscale to the effective radius of NGC 3379 at a distance of $9.8\mathrm{Mpc}$, one model unit length corresponds to $50''$.

4.3.4 Isotropic γ-model

To prepare for the modeling of NGC 3379, we now construct a spherical isotropic mock galaxy with known intrinsic properties to determine the optimal value of the entropy "smoothing" parameter μ in equation (4.6). Following a similar approach as in Gerhard et al. (1998) and Thomas et al. (2005) we determine for which value of μ the fitted particle model best reproduces the intrinsic velocity moments of the input mock galaxy model. The "best" value of μ depends on the observational data to be modelled and their spatial coverage, on the phase-space structure of the galaxy, but also on the initial conditions from which the NMAGIC modelling starts. The same value can then be used for the modelling of NGC 3379, provided the mock galaxy is a reasonable approximation to the real galaxy.

For the luminosity density of the mock galaxy we choose a flattened γ-model,

$$j(m) = \frac{(3-\gamma)L}{4\pi q} \frac{a}{m^\gamma (m+a)^{4-\gamma}} \tag{4.7}$$

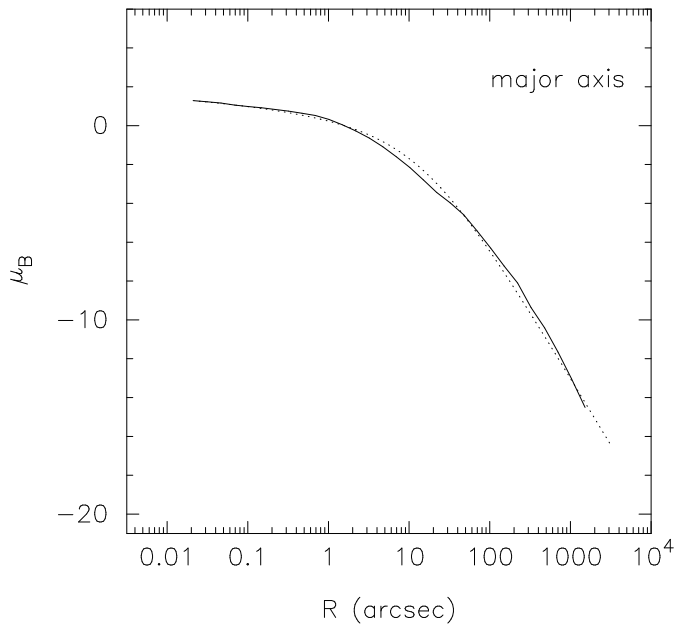

Figure 4.5: A comparison of the surface brightness profile of the isotropic γ-model (dotted line) with that of NGC 3379 (full line), along the major axis of NGC 3379.

where L and a are the total luminosity and scale radius, $m^2 = R^2 + (z/q)^2$, and q is the flattening (Dehnen and Gerhard, 1994). We choose the parameters such that the surface brightness closely resembles that of NGC 3379, i.e., $q = 1.0$, $\gamma = 1.0$, $L = 1.24 \times 10^{10}\ L_{\odot,B}$ and $a = 0.8$ kpc, which corresponds to $R_e \approx 30''$. Figure 4.5 shows that the surface brightness profile of the mock galaxy is an excellent approximation for NGC 3379.

We calculate LOSVD kinematics for the mock galaxy from internal higher-order velocity moments, using a program of Magorrian and Binney (1994) that solves the higher-order Jeans equations in the model's self-consistent potential. We set the mass-to-light ratio of the isotropic γ-model as $\Upsilon_B = 5$. Before calculating the LOSVD parameters, the velocity moments are slit-averaged to account for the observational setup of the slits given in Section 4.2.3. To the final LOSVD parameters we add Gaussian random variates with 1σ dispersions equal to the respective error bars of the corresponding NGC 3379 measurements at that point. In this way we compute v, σ, h_3 and h_4 for the γ-model along all slits shown in Figure 4.3. Figure 4.6 compares the kinematics of NGC 3379 with the isotropic γ-model along the major axis.

In addition, we construct SAURON mock kinematics for each voronoi cell in the NGC 3379 data as follows. We first compute the velocity profiles from higher order velocity moments at a few nearby radial positions. Using the spherical symmetry, we interpolate v, σ and the higher order moments to the mid-cell positions of the fine grid described in Section 4.2.3, using a spline interpolation scheme. Then we compute the mock data for each voronoi bin by a luminosity weighted average over those cells of the fine grid which contribute to the voronoi cell under consideration. Finally, we add Gaussian random variates to the kinematics with 1σ dispersions corresponding to the respective SAURON error bars in this voronoi bin. The SAURON pseudo data are shown in the top panels of Figure 4.7.

We do not construct mock PNe data and neglect them for the entropy tests, but we need to complete the mock observational data set with the photometric constraints. In the entropy tests here, we restrict ourselves to spherical models, so in the expansion of the luminosity density (equation 4.7) the only non-zero term in the spherical harmonics series (*cf.* Section 4.3.2) is the radial light in shells, $L_k = \sqrt{4\pi} A_{00,k}$. However, to ensure sphericity, we also need to use the higher order coefficients $A_{20,k}, \cdots, A_{22,k}$ and $A_{66,k}$ as constraints, set to zero. We define these photometric observables on a grid of radii r_k, quasi-logarithmically spaced in radius with

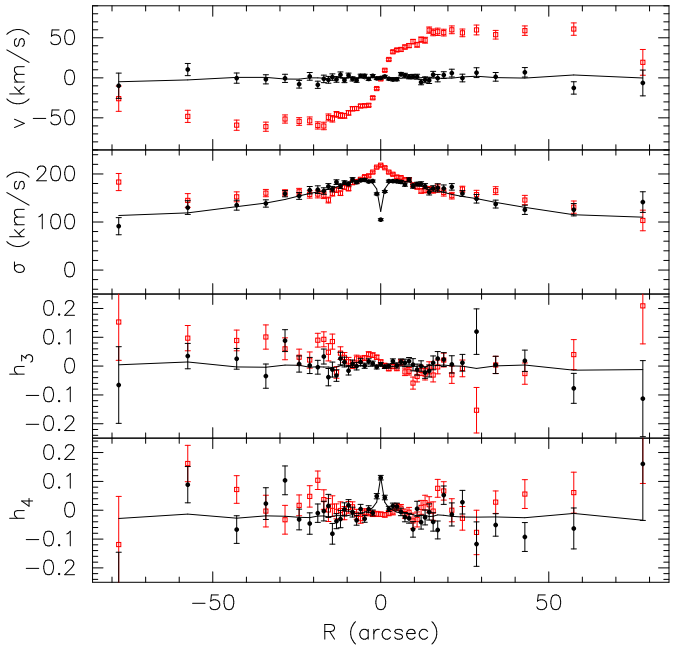

Figure 4.6: Comparison of the LOSVD kinematics of the γ-model mock galaxy with those of NGC 3379 along its major axis, and with γ-the particle model fit for $\mu = 2 \times 10^4$. The red open squares show the NGC 3379 data from Statler and Smecker-Hane (1999), the black circles show the γ-model pseudo data, and the solid line the self-consistent particle model obtained from fitting the pseudo data. The model data points are averages over the same slit cells as the target data (see Fig. 4.3), and are connected by straight line segments. The panels from top to bottom are for v, σ, h_3 and h_4.

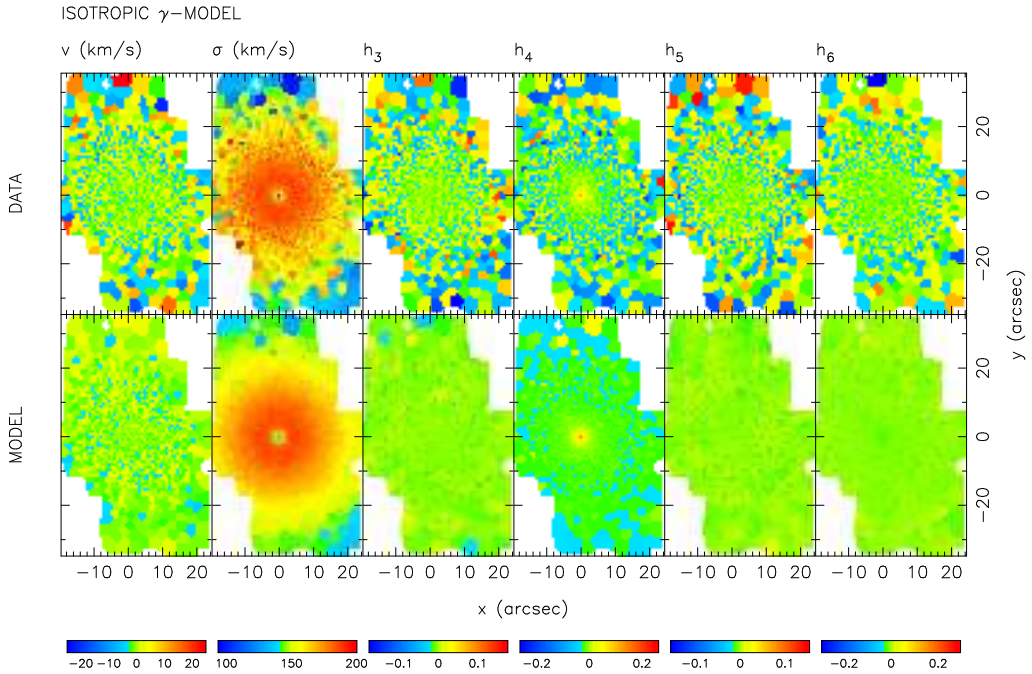

Figure 4.7: Top panel: SAURON mock kinematic data for a spherical isotropic γ-model. Bottom panel: Self-consistent particle realization obtained from a model fit with $\mu = 2 \times 10^4$. From left to right: v, σ and the higher order moments h_3-h_6.

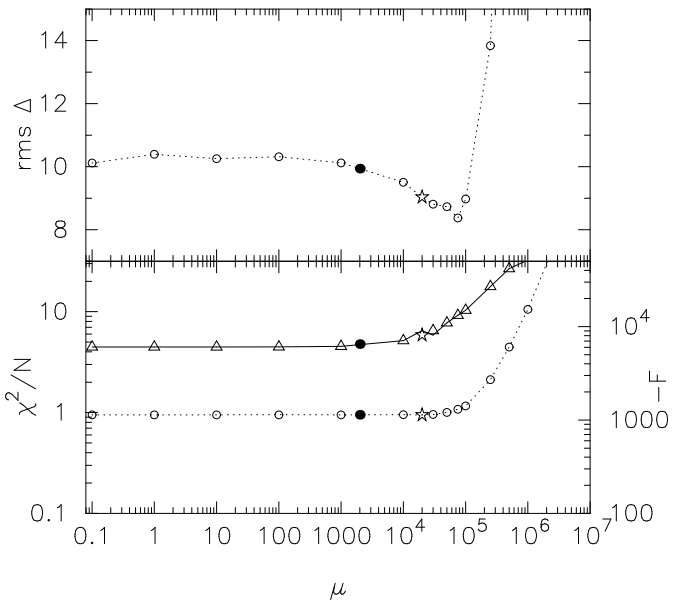

Figure 4.8: Top: Deviation rms $\Delta(\mu)$ between the internal velocity moments of the final γ-particle model and the input model. Bottom: The circles show χ^2 per data point of the model fit to the kinematic and photometric targets as a function of entropy parameter μ. The triangles display the same but for F, *cf.* equation (4.6). The starred symbol indicates the optimal value of μ, the full dot the μ value appropriate to avoid bias against rotation and anisotropy.

inner and outer boundaries at $r_{\rm min} = 0.01''$ and $r_{\rm max} = 2500''$. We assume Poisson errors for the radial light $\sigma(L_k) = \sqrt{L_k L/N}$ where N is the total number of particles used in the particle model and L is the total light of the system. To estimate the errors in the higher order luminosity moments, we use Monte-Carlo experiments in which we generate particle realizations of the density field of the target system with 7.5×10^5 particles, which is the same number as in the χ^2M2M models.

We then construct self-consistent particle models for the isotropic γ-model target in a two step process, using the mock observations as constraints for NMAGIC. First, we start with the particle model described in section 4.3.2 and evolve it using NMAGIC to generate a self-consistent particle realization with the desired luminosity distribution (γ-particle model), fitting only the photometric constraints. Then, we use the γ-particle model as initial conditions to fit both the kinematic and photometric target constraints for different values of μ.

The results are presented in Figure 4.8. The lower panel shows the goodness of the fit as a function of μ, both in terms of the normalized χ^2 per data point and in terms of the merit function F from equation (4.6). The upper panel shows the rms Δ difference between the internal velocity moments of the mock galaxy and the particle model realizations obtained for different values of μ. The intrinsic kinematics of the particle models are computed by binning the particles in spherical polar coordinates, using a quasi-logarithmic grid with 20 radial shells bounded by $r_{\rm min} = 0.01''$ and $r_{\rm max} = 500.0''$, 12 bins in azimuthal angle ϕ, and 21 bins equally spaced in $\sin\theta$. As can be seen from the top panel of Figure 4.8, the minimum in the rms Δ as a function of μ for which the model best recovers the internal moments of the input model is at $\mu \simeq 7.5 \times 10^4$. For larger (smaller) μ, the rms Δ is larger because of oversmoothing (excess fluctuations) in the model. Especially at μ values larger than the minimum rms Δ increases rapidly. The lower panel of the figure shows that χ^2 per data point is of order unity for a large range of μ but then increases for $\mu \gtrsim 3 \times 10^4$.

At first sight $\mu = 7.5 \times 10^4$ at the minimum of rms Δ might seem to be the best choice. However, a more conservative value is $\mu = 2 \times 10^4$, such that the entropy has not yet degraded

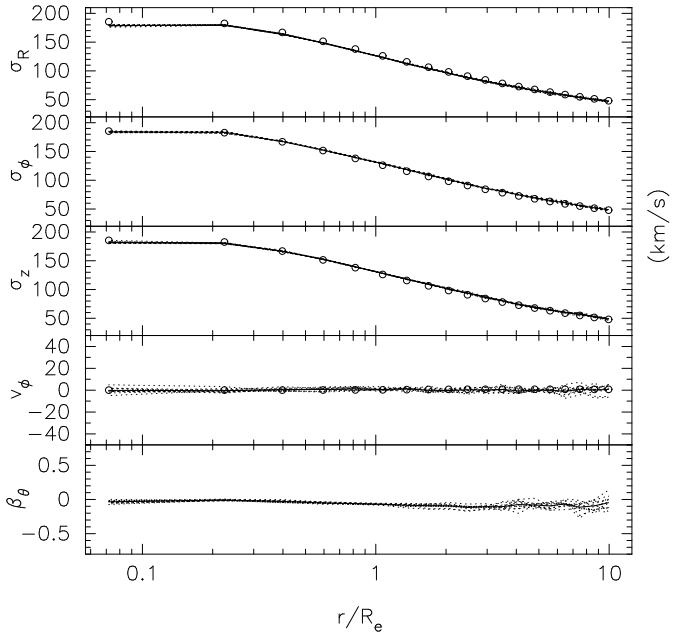

Figure 4.9: Internal kinematics of the isotropic target galaxy and its particle realization in the equatorial plane. From top to bottom: σ_R, σ_ϕ, σ_z, v_ϕ and anisotropy parameter β_θ. The kinematic quantities of the input mock galaxy (circles) are very well fitted by the particle model generated for $\mu = 2 \times 10^4$ (lines). Dotted lines show the model kinematics in different azimuthal bins in the equatorial plane, and the solid lines show the azimuthal average.

the fit to the data (oversmoothing). This also takes into account that the Hernquist (1990) model we have used as a starting point for this test is not very different from the target galaxy, so that the particle weights did not need to change too much. The choice of $\mu = 2 \times 10^4$ has proved good for near-isotropic models; it is indicated by the starred symbol in Fig. 4.8.

However, in our modelling of NGC 3379 we have found that for strongly anisotropic targets, this value of μ is too large. The reason for this is that the entropy term tries to retain a narrow distribution of particle weights around their priors which, because our initial conditions are near-isotropic, biases the model against anisotropic orbit distributions. To allow the models to converge towards strongly anisotropic orbit distributions we have therefore used in Section 4.4 a lower value of $\mu = 2 \times 10^3$. This is indicated by the solid symbol in Fig. 4.8.

The fit of the particle model to the kinematic data of the isotropic γ-model obtained with $\mu = 2 \times 10^4$, and its intrinsic kinematic properties, are illustrated in Figures 4.6, 4.7 and 4.9. Figure 4.6 compares the target kinematics and the self-consistent particle realization along the galactic major axis. Figure 4.7 shows the SAURON mock data and compares them to the corresponding kinematics obtained from the particle model. The model fit to all kinematic data is excellent. In fact, it is evident from Fig. 4.7 that the model is smoother than the mock data themselves, which is a consequence of orbit-smoothing and time-smoothing.

Figure 4.9 shows how well the internal kinematics of the particle model for $\mu = 2 \times 10^4$ compare with the intrinsic kinematics of the mock galaxy target. All velocity dispersions σ_R, σ_ϕ and σ_z, the streaming rotation v_ϕ, and even the anisotropy parameter $\beta_\theta = 1 - \sigma_\theta^2/\sigma_r^2$ (zero for this isotropic model) are very well reproduced by the model fit. The final particle realization is indeed isotropic.

Mass-to-light ratio So far all model fits have been made with the mass-to-light ratio fixed to the actual value used for the mock galaxy, $\Upsilon = 5$. Now we investigate how accurately we can *recover* Υ with the dynamical models, given the spatial extent and quality of the observational

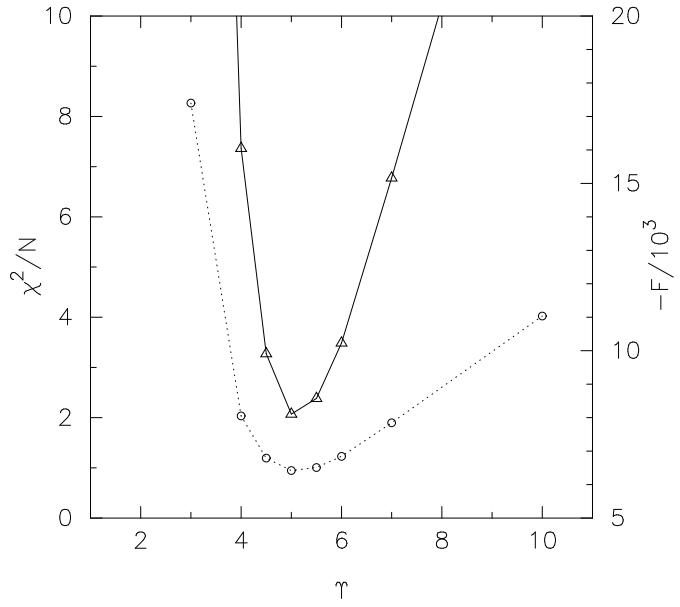

Figure 4.10: Recovering the mass-to-light ratio of the mock galaxy. The quality of the model fit as a function of mass-to-light Υ is shown in terms of χ^2 per data point (circles) and merit function F (triangles). All models are generated from the target pseudo data for $\mu = 2 \times 10^4$. The input mass-to-light ratio $\Upsilon = 5$ is recovered as the minimum in the curve $\chi^2/N(\Upsilon)$, where the model fit has $\chi^2/N \simeq 1$.

data. To this end we fit particle models to the mock galaxy observations for different mass-to-light ratios in the range $\Upsilon \in [3, 10]$, keeping the entropy parameter fixed at $\mu = 2 \times 10^4$. The results are presented in Figure 4.10, which shows how the quality of the model fit varies as a function of Υ, both in terms of χ^2 per data point and merit function F. As expected, the best model is obtained for $\Upsilon = 5$ and has χ^2 per data point approximately unity.

4.4 Dynamical models of NGC 3379

In this section we construct dynamical models for NGC 3379 to learn about its stellar and dark matter distribution. We investigate spherical and axisymmetric models with and without dark matter halos, and fit the photometry, SAURON integral field data, slit kinematics, and PNe velocity data. Our aim in this paper is not to constrain the detailed halo mass profile of the galaxy, but only to ascertain whether a dark matter halo is allowed, or required, by the kinematic data. Thus, as in de Lorenzi et al. (2008) we investigate a simple sequence of potentials which include the contribution from the stellar component and a halo potential as in equation (4.1). The circular speed curves corresponding to these potentials vary at large radii from the near-Keplerian decline expected when the mass in stars dominates, to the nearly flat shapes generated by massive halos. They are shown in Figure 4.11 and their halo potential parameter are given in Table 4.1.

In the following subsections, we describe spherical models (§4.4.1) and oblate models (§4.4.2), as well as a few models without imposed axisymmetry constraints (§4.4.3), and then discuss the significance of the fits to the data in a separate subsection (§4.4.4). To begin with we construct self-consistent particle models for NGC 3379 in which the distribution of stars is spherical. This allows for an easy comparison with previous work (Romanowsky et al., 2003; Douglas et al., 2007).

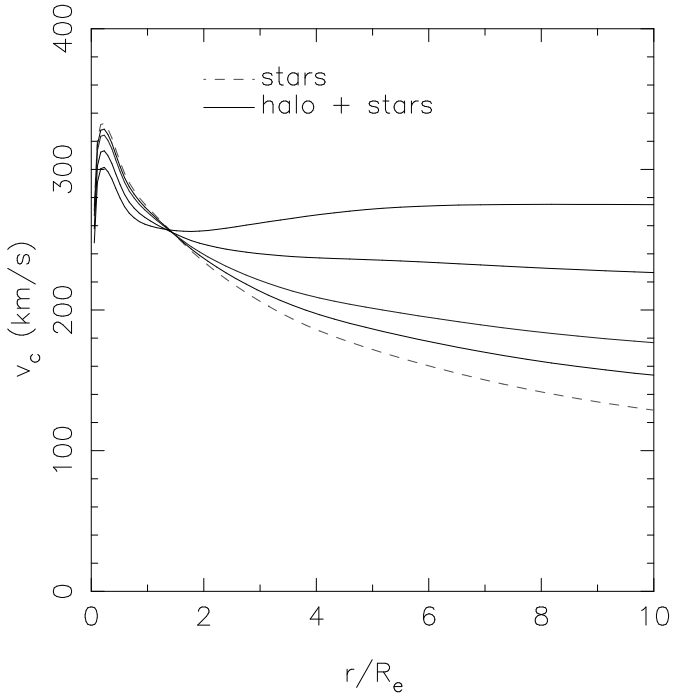

Figure 4.11: Circular velocity curves for the potentials used in the dynamical modelling, including the self-consistent stars-only model A (dashed line), and models including different spherical dark matter halos in addition to the stellar component (solid lines, from bottom to top: models B, C, D and E). For this figure the distribution of stars is assumed to be spherical with mass-to-light ratio as given by the final NMAGIC fit to the data in the respective spherical potential.

HALO	r_0/R_e	v_0/kms^{-1}	χ^2/N	χ^2_{alm}/N_{alm}	χ^2_{sb}/N_{sb}	χ^2_{sau}/N_{sau}	χ^2_{sl}/N_{sl}	χ^2_{PN}/N_{PN}	$-F$	Υ
A	0	0	0.208	0.137	–	0.176	0.565	0.371	2131.3	8.23
B	3	90	0.215	0.162	–	0.184	0.548	0.323	2231.9	8.03
C	3	130	0.216	0.201	–	0.184	0.539	0.340	2320.1	7.82
D	3	200	0.219	0.271	–	0.186	0.522	0.564	2622.9	7.28
D^+	3	200	0.362	0.641	–	0.300	0.814	1.002	4409.2	7.57
E	3	260	0.237	0.484	–	0.192	0.535	1.557	3175.2	6.73
E^*	3	260	0.241	–	0.084	0.215	0.522	0.504	2649.4	6.52

Table 4.1: Table of parameters and fit results for models of NGC 3379 with spherical potentials. Models A-E correspond to the circular rotation curves in Fig. 4.11. Model D^+ is the same as D but for a higher value of the entropy. Model E^* is the self-flattened oblate model in halo E of Section 4.4.2. For these models columns (1)-(3) give the model code and the parameters r_0 and v_0 used in equation (4.1) for the respective dark halo potential. The next six columns list the χ^2 values per data point, for all observables [column (4)] and for the luminosity density and surface brightness constraints, the SAURON kinematic observables, slit kinematic observables, and PN observables separately [columns (5)-(9)]. Column (10) gives the numerical value of the merit function in equation (4.6), and column (11) the final (B-band) mass-to-light ratio. The respective number of constraints are $N = 12997$ for A-E and $N = 12557$ for E^*, whith $N_{alm} = 640$, $N_{sb} = 200$, $N_{sau} = 11214$, $N_{sl} = 1135$, $N_{PN} = 8$.

4.4.1 Spherical models

Model fits

First we must determine the photometric and kinematic observables. Analogous to Section 4.3.4, we use the spherical harmonics expansion coefficients A_{lm} of the deprojected luminosity density as target data to constrain the particle models. Specifically, we use A_{00}, A_{20}, A_{22}, $\cdots$, A_{66}, but set all terms higher than A_{00} to zero, adopting the same radial grid as in Section 4.3.4. Errors for the luminosity terms are estimated as in Section 4.3.4. As kinematic observables, we use the SAURON and slit kinematics, as well as the binned PN velocity dispersion profile; see Sections 4.2.3 and 4.3.2. The SAURON data and most slit data are symmetrized, only the slit parallel to their minor axis of Kronawitter et al. (2000) cannot be symmetrized and for this slit the original kinematic data points are used.

We fit the particle models to these data in the following three-step process. (i) We start from the initial particle realization described in Section 4.3.3 and evolve it with NMAGIC to a self-consistent model that reproduces the target A_{lm}. (ii) Starting with this density model we then construct dynamical models, fitting the full set of photometric *and* kinematic target observables. If the potential includes a dark matter halo, we first relax the density model for 1000 steps in the total gravitational potential (*cf.* Section 4.3.1), assuming a mass-to-light ratio of 8. This is to make sure that the model is in approximate equilibrium before we start the fit. After this relaxation phase, we evolve the particle system for $\sim 10^5$ NMAGIC correction steps while fitting the complete set of constraints. During the correction phase the mass-to-light ratio Υ is adjusted in parallel, using its own force-of-change equation as given in de Lorenzi et al. (2008). After each correction step, the potential generated by the particles is updated but the dark matter potential (if present) is constant in time. In the fitting process the entropy parameter has value $\mu = 2 \times 10^3$; cf. the discussion below. (iii) In the final step, we keep the global potential constant and evolve the system freely for another 5000 steps, without changing the particle weights (phase-mixing). With this the fitting process is complete. Thereafter we generally evolve the model with all potential terms active for a further 10000 steps to test its stability. For reference, 10000 correction steps in the self-consistent potential correspond to ≈ 110 circular rotation periods at R_e, or 5.8 Gyr.

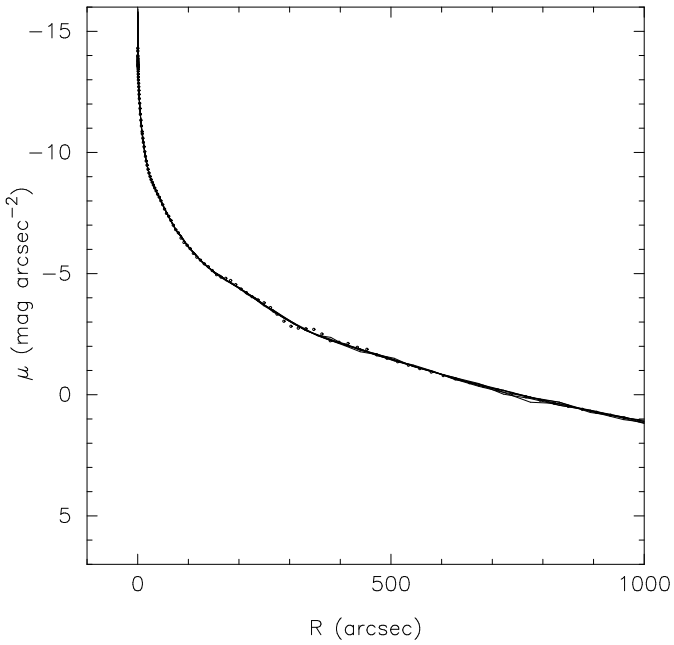

Figure 4.12: Comparison of the surface brightness profiles of the spherical models with the photometric data (points). The lines are for the spherical models A-E and the self-flattened model E*.

Results

In this way we obtain spherical dynamical models for NGC 3379, fitting to the density expansion and all kinematic data including the PN velocity dispersion profile. Model A is the self-consistent model without dark matter halo, models B-E have halos of increasing circular velocities, as shown in Figure 4.11 and Table 4.1. The quality of fit for these models can be judged from Table 4.1, which gives the numerical values of the merit function F and lists various values of χ^2 per data point, both those obtained globally for all the data, and those found for each of the four data sets separately (density expansion, SAURON, slit, and PNe). The 3σ outlier point discussed in Section 4.2.3 is not included in the fits and in the χ^2_{PN} in Table 4.1, but its influence will be discussed below.

Figures 4.12-4.15 compare the different data with the models. Fig. 4.12 shows the surface brightness profiles, Fig. 4.13 the integral field LOSVD parameter fields, Fig. 4.14 the kinematics along several slits, and Fig. 4.15 the PN velocity dispersion profiles. The model SB profiles fit the observed profile very well, and agree with each other within the thickness of the lines in the plot. The SAURON data are fitted with $\chi^2_{sau}/N_{sau} \simeq 0.2$ by all our spherical models. Notice that the particle noise in the models is significantly smaller than the noise in the symmetrized data. Also the χ^2_{sl}/N_{sl} for the combined slit data are less than unity; the plots for models (B,D) in Fig. 4.14 show a few small systematic deviations but generally the fits are very good. In the central 30 arcsec the slit data are dominated by the SAURON data. Notice that these spherical models are not constrained to be spherically symmetric also in their *kinematic* properties; hence they can also fit the small rotation of NGC 3379 with high accuracy.

The comparison of the models to the PN.S data is shown in Fig. 4.15. If we use the outermost dispersion point as given in Douglas et al. (2007), models A-D with no or moderate halos provide a good match to the data, but the most massive halo model E fits less well, being high by $\simeq 2\sigma$ with respect to the outermost dispersion point and by $\simeq 1.3\sigma$ with respect to the second-outermost point. If we include the object classified as 3σ "friendless" outlier (see Section 4.2.3and Douglas et al., 2007) in the outermost bin, the corresponding outer PN dispersion point increases significantly; see the red open circle and error bar in Fig. 4.15. Then model E

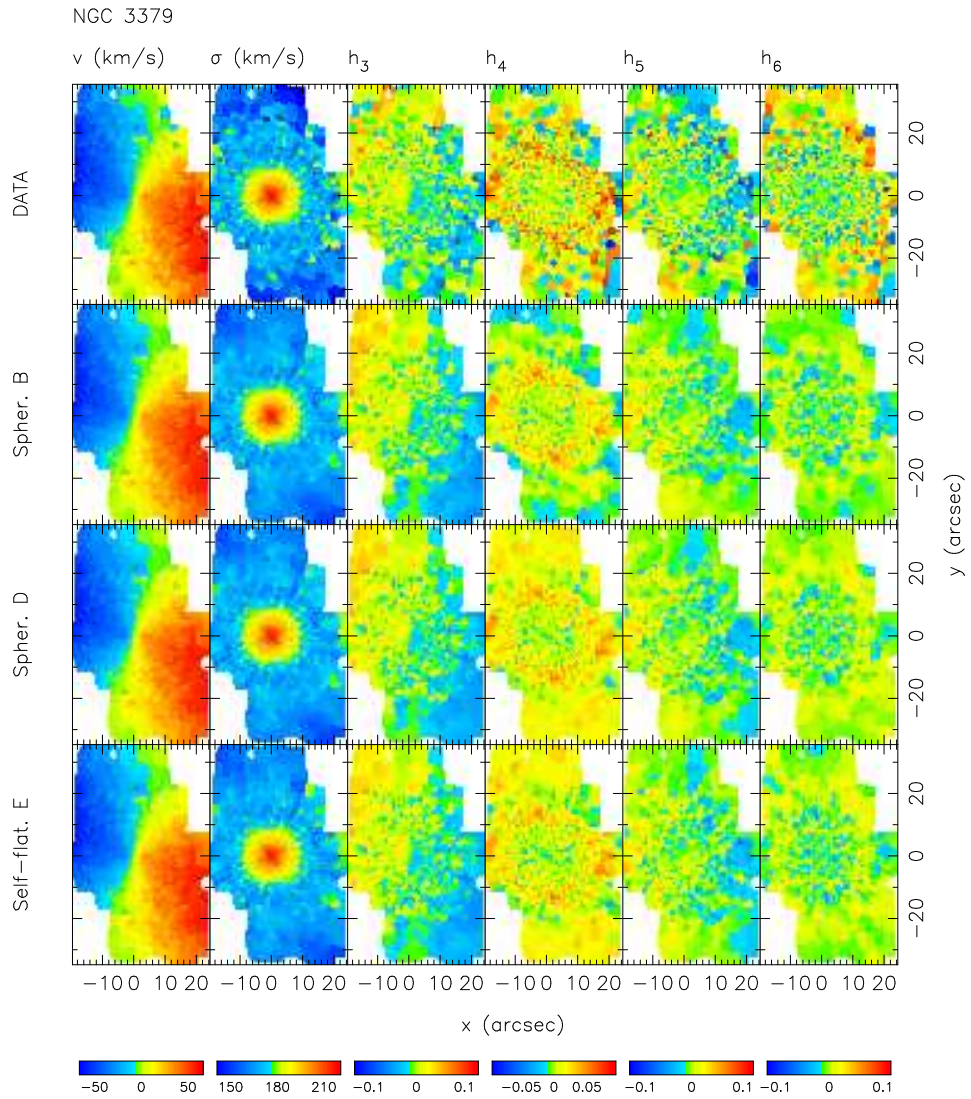

Figure 4.13: Symmetrized SAURON kinematic data for NGC 3379 (top row) compared with similar data extracted for the spherical models B and D and the self-flattened model E* (lower three rows). Notice that the particle noise in the model panels is significantly smaller than the noise in the corresponding data fields for all LOSVD parameters shown. In the panels for σ and h_4 a slightly colder ring-like structure with larger h_4 hints at some deviations from spherical symmetry.

also fits the PN dispersion profile, overestimating the outermost velocity dispersion point by less than 1σ.

The intrinsic kinematics of these spherical models is shown in Figure 4.16. One recognizes the expected signature of the well-known mass-anisotropy degeneracy (Binney and Mamon, 1982): In the more massive halos, the same falling line-of-sight dispersion profile requires larger radial anisotropy. Thus in the models with halo the radial anisotropy rises outside 1-2R_e. Particularly the more massive halo models D and E require strongly radially anisotropic orbit distributions ($\beta \simeq 0.9$) to be consistent with the falling dispersion profile of NGC 3379. Radial anisotropy was suggested as one of the possible causes for the measured profile by Dekel et al. (2005), based on a comparison with their merger models. However, the typical anisotropies in these models are more moderate ($\beta \simeq 0.5$).

Despite their strong radial anisotropy, the massive halo models D and E show no sign of an instability when evolved freely after the model fitting and phase-mixing. Rather, they evolve very slowly, reaching after 5.8 Gyr of evolution a configuration with slightly triaxial shape ($\epsilon < 0.1$) in which the initial slow rotation has mostly gone away. A similar evolution is seen for the near-isotropic model A without dark matter halo, indicating that this evolution may be connected to these equlibria being spherically symmetric only in their mass distribution but, due to the rotation. not in their kinematics. In any case, the PN dispersion profiles do not change during the evolution, i.e., the constraints on the dark matter halo remain as before.

In conclusion, the results of this section show that both near-isotropic spherical models with low density dark matter halos, and radially anisotropic spherical models with massive halos provide excellent fits to the available kinematic data for NGC 3379, including the PN dispersion profile to $\sim 7R_e$. A more quantitative discussion is deferred to Section 4.4.4.

Entropy smoothing

The entropy term in the force-of-change equation (4.5) smoothes the particle models by trying to maintain the values of the particle weights near their priors, here chosen as $1/N$. Because all fits start from an isotropic system with equal weight particles, the entropy smoothing thus biases the final models towards isotropy and slow rotation. To allow the models to develop strong radial anisotropy in their outer parts, it is necessary to reduce the value of the entropy parameter below that appropriate for an isotropic system (see Section 4.3.4). Otherwise the constraints from the small number of PN dispersion points with their relatively large Poisson error bars are overwhelmed by the entropy smoothing. Fig. 4.15 and Table 4.1 show that model D^+ constructed with $\mu = 2 \times 10^4$ is indeed degraded in its ability to fit the PNe data, relative to model D which is for $\mu = 2 \times 10^3$ in the same halo. On the other hand, the results from model D^0 with $\mu = 0$ are only slightly different from those for model D. Hence our choice of using $\mu = 2 \times 10^3$ throughout.

Contrary to second derivative regularisation, say, entropy smoothing does not distinguish between local and global uniformity of the particle weights; it likes to have *all* particle weights similar to their priors. Thus if μ is chosen such as to allow large differences in weight between radial and circular orbits, it also allows similar differences between particles on neighbouring orbits if this is preferred by the data. With $\mu = 2 \times 10^3$ the models can therefore fit the data with $\chi^2/N < 1$ as seen in Table 4.1. The effect is strongest for the spherical models because these have a larger number of independent orbits than less symmetric systems. However, Fig. 4.16 shows that the intrinsic velocity moments are smooth functions of radius, and below we will see that also the LOSVDs are smooth functions. Thus the good fits of the various models to the PN data are not achieved by large local variations of the orbital weights for orbits near the PN data points.

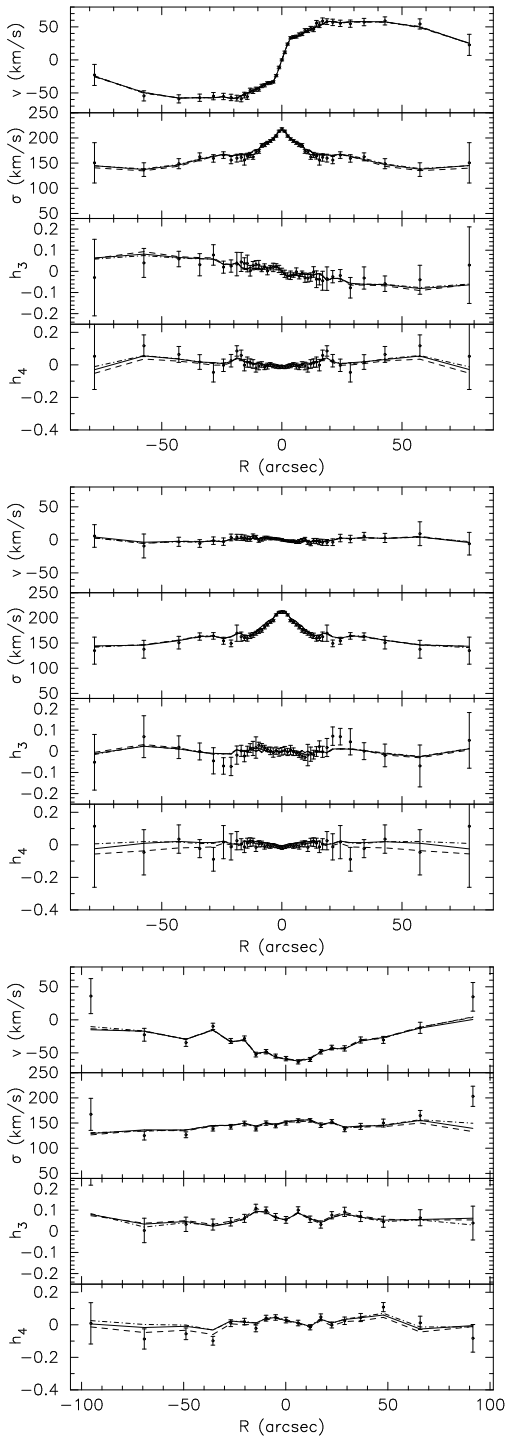

Figure 4.14: Comparison of models B (dashed lines), D (full lines) and E* (dash-dotted lines) with the symmetrized slit data along the major and minor axes from Statler and Smecker-Hane (1999) (top and middle panel) and the unsymmetrized minor-axis parallel slit from Kronawitter et al. (2000) (bottom panel). The model data points are averages over the same slit cells as the target data (see Fig. 4.3), and are connected by straight line segments.

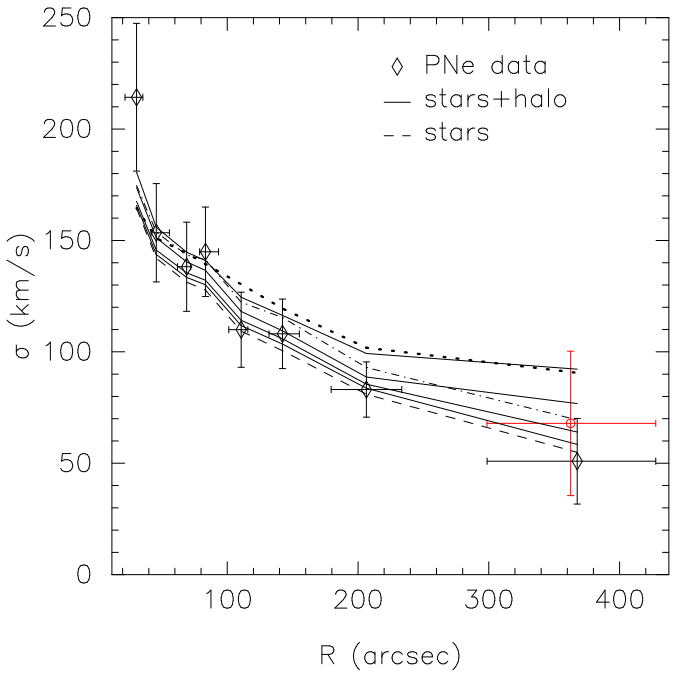

Figure 4.15: Comparison of the PNe velocity dispersion profiles of the spherical models with the PN.S data (diamonds). The dashed line shows the self-consistent particle model A. The solid lines represent the dynamical models including a DM halo, i.e., from bottom to top models B, C, D, and E. The heavy dotted line is for the higher-entropy model D^+, and the dash-dotted line is for the self-flattened model E^*.

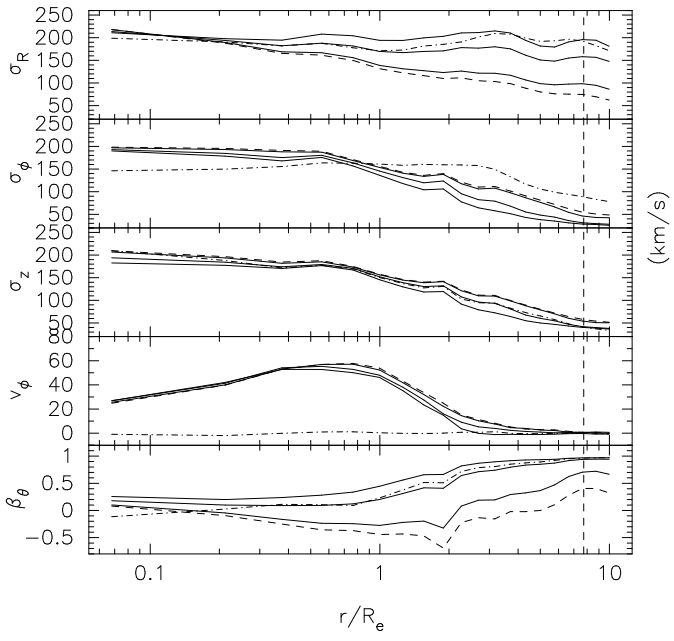

Figure 4.16: Intrinsic kinematics of the final spherical models A (dashed lines) and B,D,E (full lines), and the self-flattened model E^* (dash-dotted lines). Panels from top to bottom show the radial, azimuthal, and vertical velocity dispersion profiles, the mean azimuthal streaming velocity, and the meridional anisotropy profile, all computed in the equatorial plane through the models that coincides with the sky plane. The models in the more massive dark matter halos are more radially anisotropic, as expected.

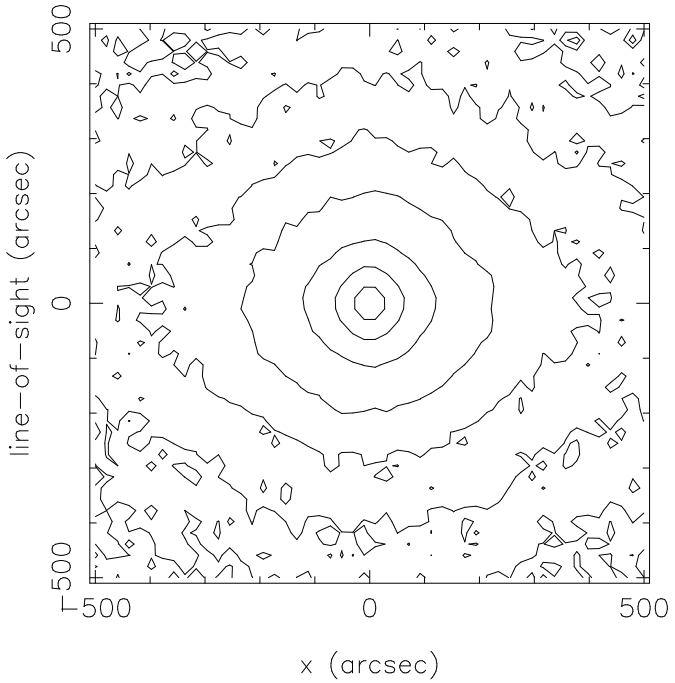

Figure 4.17: Edge-on surface brightness contours obtained when viewing the kinematically deprojected oblate model E* perpendicular to the line-of-sight.

4.4.2 Oblate models including dark matter halos

There is some evidence that NGC 3379 may be non-spherical. Capaccioli et al. (1991) argued that the bulge of NGC 3379 is remarkably similar to the one of NGC 3115, a well-known S0 galaxy. Further, also the SAURON kinematic data, shown in the upper panel of Figure 4.13, show signatures of non-sphericity, particularly, a faint cold ring visible in the velocity dispersion and h_4 panels with projected radius $R \approx 15''$[1] Thus to understand how much dark mass around NGC 3379 is allowed by the kinematic data for this galaxy may require more general models than spherical ones. In this section we will present oblate axisymmetric models in the family of halo potentials considered already in the last section.

Face-on oblate model in a spherical potential

As a first step we attempt to construct a model for NGC 3379 in a massive dark halo, in which the distribution of stars is flattened along the line-of-sight. This model is required to have a small line-of-sight velocity dispersion at large radii, thus will be flattened in accordance with the virial theorem (*e.g.* Binney and Tremaine, 1987). We do not know beforehand what the required shape of this model must be, so we will use the NMAGIC method to find it for us, keeping the potential spherically symmetric. For illustration we embed this model in halo E, and will hence hereafter denote it as model E*.

To construct this model we replace the A_{lm} constraints (*cf.* Section 4.4.1), which before imposed a spherical shape on the particle distribution, by the Fourier moments of the surface brightness distribution given in Figure 4.1. They are computed from the photometry as in Section 4.3.2, on a grid in projected radius quasi-logarithmically spaced betwen $R_{\rm min} = 0.01''$ and $R_{\rm max} = 1500''$. The higher-order moments are set to zero, enforcing axisymmetry. We then start from spherical initial conditions and use NMAGIC to flatten the particle model through fitting the kinematic observables, particularly the PN velocity dispersion profile. As kinematic

[1] As can be seen from Fig. 4.13, the feature can also be reproduced in spherical models.

HALO	r_0/R_e	v_0/kms^{-1}	i	χ^2/N	χ^2_{alm}/N_{alm}	χ^2_{sb}/N_{sb}	χ^2_{sau}/N_{sau}	χ^2_{sl}/N_{sl}	χ^2_{PN}/N_{PN}	$-F$	Υ
A90	0	0	90	0.619	0.173	0.331	0.624	0.866	0.369	4899.995	8.09
A50	0	0	50	0.773	0.291	0.437	0.781	1.031	0.426	6129.759	8.12
A40	0	0	40	0.789	0.507	0.587	0.780	1.079	0.515	6634.361	8.22
B90	3	90	90	0.631	0.243	0.40	0.635	0.852	0.344	5051.231	7.923
B50	3	90	50	0.777	0.352	0.523	0.782	1.008	0.371	6196.835	7.97
B40	3	90	40	0.782	0.570	0.670	0.770	1.047	0.438	6562.924	8.10
C90	3	130	90	0.651	0.296	0.457	0.655	0.851	0.401	5291.926	7.72
C50	3	130	50	0.741	0.429	0.611	0.742	0.933	0.396	6030.503	7.82
C40	3	130	40	0.766	0.661	0.591	0.753	0.990	0.414	6478.453	7.98
D90	3	200	90	0.611	0.367	0.462	0.603	0.847	0.887	5343.843	7.26
D50	3	200	50	0.761	0.394	0.663	0.763	0.961	0.815	6394.686	7.50
D40	3	200	40	0.745	0.618	0.639	0.738	0.906	0.654	6466.793	7.693
E90	3	260	90	0.684	0.577	0.751	0.652	1.037	2.602	6325.564	6.86
E50	3	260	50	0.765	0.530	0.854	0.749	1.026	2.401	6782.397	7.20
E40	3	260	40	0.756	0.819	0.739	0.899	0.737	1.662	6806.086	7.42
DR	3	200	50	0.715	–	0.567	0.699	0.897	0.890	5990.4	7.57
ER	3	260	50	0.710	–	1.313	0.676	0.894	6.317	6219.4	6.85

Table 4.2: Table of parameters and χ^2-fit results for oblate models of NGC 3379. Columns (1)-(3) give the model code and the parameters r_0, v_0 used in equation (4.1) for the respective dark halo potential; all halo potentials are spherical ($q_\phi = 1.0$). The fourth column gives the inclination i and the next six columns list the χ^2 values per data point, for all observables [column (5)], and for the density constraints, surface brightness constraints, SAURON kinematic observables, slit kinematic observables, and PN observables separately [columns (6)-(10)]. Column (11) gives the numerical value of the merit function in equation (4.6), and column (12) the final (B-band) mass-to-light ratio. The respective number of constraints are $N = 13237$, $N_{alm} = 680$, $N_{sb} = 200$, $N_{sau} = 11214$, $N_{sl} = 1135$, $N_{PN} = 8$.

constraints, we use the SAURON, slit, and PNe velocity dispersion data. The entropy parameter is kept at the same value as for the spherical models, $\mu = 2 \times 10^3$. During this "kinematic deprojection", the spherically averaged potential generated by the particles is updated after regular time intervals, but the non-spherical terms are ignored. The DM potential is given by equation (4.1) and remains constant in time. After the correction phase, the model is again allowed to freely evolve for some time.

Figures 4.12, 4.14, 4.13 and 4.15 show how the final "self-flattened" particle model E* compares to the various data. The model fits the data as well as the best-fitting spherical models. As anticipated, the model makes the PN dispersion profile compatible with a massive dark halo potential by flattening the outer distribution of stars and decreasing the model σ along the line-of-sight. Fig. 4.16 shows that the line-of-sight (z) velocity dispersion measured in the equatorial plane is half the ϕ-dispersion in this plane; the radial dispersion still dominates. The model's flattening is illustrated in Figure 4.17, which shows the SB distribution in an edge-on projection perpendicular to the line-of-sight. The axis ratio is $q \approx 0.7$.

While this model provides an excellent fit to the photometric and kinematic data in a massive dark DM halo, it is not a completely realistic model for NGC 3379. For it is only in a spherical potential as assumed for model E* that a face-on distribution of stars can show rotation. More realistic axisymmetric models must therefore be inclined to allow for the rotation seen in the SAURON and slit data.

Self-consistent oblate models

Therefore we now consider oblate models for NGC 3379 with inclinations $i = 90°$, $i = 50°$ and $i = 40°$, in which the axisymmetric gravitational potential of the stellar component is computed self-consistently from the particles. We investigate models without DM as well as models including various DM halos as detailed in Table 4.2. The gravitational potential of the DM halo is still assumed to be spherical and is kept fixed. All models are made to fit

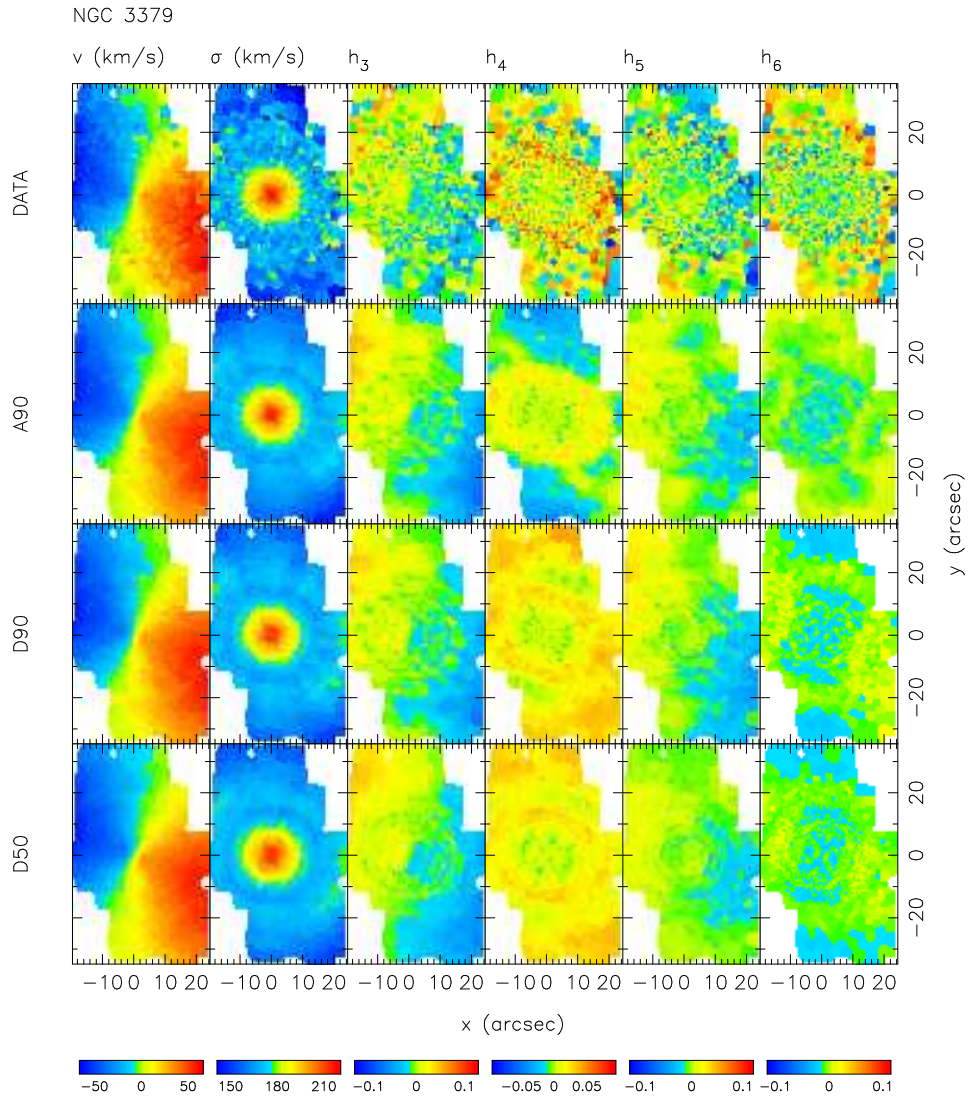

Figure 4.18: Comparison of axisymmetric models with SAURON kinematic data for NGC 3379 (top panel). Following panels are for models A90, D90, D50. Model A90 has all the mass in the stars, while the later two models include a massive halo; see Table 4.2.

the photometry, the slit and SAURON absorption line kinematic data, and the PN.S velocity dispersion profile.

The procedure employed for constructing the models is similar to that in Section 4.4.1. Again, we need to first specify the observables. We expand the deprojected luminosity density of NGC 3379 for each inclination in a spherical harmonics series and determine the expansion coefficients on the same quasi-logarithmic grid in radius as before. As observables we use the luminosity on radial shells L_k and the higher order moments A_{20}, A_{22}, $\cdots$, A_{66}, but set the $m \neq 0$ terms of the expansion to zero to force the models to remain axisymmetric. Errors for the A_{lm} coefficients are estimated as in Section 4.3.4. We thus obtain three different sets of luminosity density observables A_{lm} with corresponding errors, one for each of the three inclinations. In addition to the A_{lm}, we also fit the surface brightness itself, using the Fourier moment observables on the grid of projected radii R_k as in the previous Section 4.4.2. Errors for these Fourier moments are computed similarly as the A_{lm} errors. The kinematic constraints are identical to those used for the spherical models: they are the luminosity weighted, symmetrized Gauss-Hermite moments from the slit data and SAURON data (see Section 4.2.3), and the PNe kinematics represented by the binned line-of-sight velocity dispersion points.

To the combined set of observables we fit particle models in a similar three-step process as for the spherical models. (i) We start with the spherical particle model described in Section 4.3.2 and use NMAGIC to generate an equilibrium model with the desired luminosity distribution, as given by the deprojection of the photometry for the given inclination. (ii) We then use the resulting particle model as a starting point to generate the final set of models by fitting the photometric and kinematic constraints in the different DM halos. We use the same entropy parameter $\mu = 2 \times 10^3$ as for the spherical models. (iii) Finally, we first keep the potential constant and let the system evolve freely without changing the particle weights, and thereafter test the stability of the model.

The quality of the fit for the different halo models and inclinations is again characterized by the value of the merit function F of equation (4.6) and the values of the different χ^2 per data point, both globally and for the individual data sets. These are given in Table 4.2 and will be discussed further in Section 4.4.4. In addition to the models shown in Table 4.2, we have also constructed a similar suite of models for the unsymmetrized SAURON and slit data. These fits were of similar quality as the models for the symmetrized data, i.e., when subtracting the systematic error floors determined in Section 4.2.3 ($\chi^2_{sau}/N_{sau}(\mathrm{sys}) = 1.0$ and $\chi^2_{sl}/N_{sl}(\mathrm{sys}) = 1.0$) from the χ^2 values of the models for the unsymmetrized data, the model χ^2 values became very similar to those reported in in Table 4.2.

Figures 4.18-4.20 compare some of the final axisymmetric particle models to the SAURON, slit and PNe data. Both edge-on and inclined models again are very good matches to the SAURON and slit data, with or without dark matter halo. The PN velocity dispersion profile is fitted well by the models with the lower mass halo models B,C; halo D slightly overestimates the outer PN velocity dispersion point given by Douglas et al. (2007) but is consistent with the outer point when the "friendless" outlier point is included. Model E90 is inconsistent with the outer dispersion point of Douglas et al. (2007), consistent with Table 4.2, but is only marginally inconsistent with the data when the outlier is included. Based on this together with the likelihood results reported below, halo D is the most massive halo consistent with the PN data. Figure 4.21 shows that for this model the dark halo contributes about 60% of the total mass within the radius of the last PN data point at $\sim 7R_e \sim 15\,\mathrm{kpc}$.

Figure 4.22 shows the intrinsic velocity dispersions, streaming velocity, and anisotropy for some of the models. Because of the small projected ellipticity of NGC 3379, the edge-on models are very similar to the spherical models in the respective halo potentials and the higher circular velocity halos require large radial anisotropy to match the PN data. The inclined flattened models have similarly small $\sigma_z = \sigma_\theta$ in the model equatorial plane, but somewhat larger σ_ϕ, as expected. Also in the axisymmetric models it is the radially increasing, strong radial anisotropy

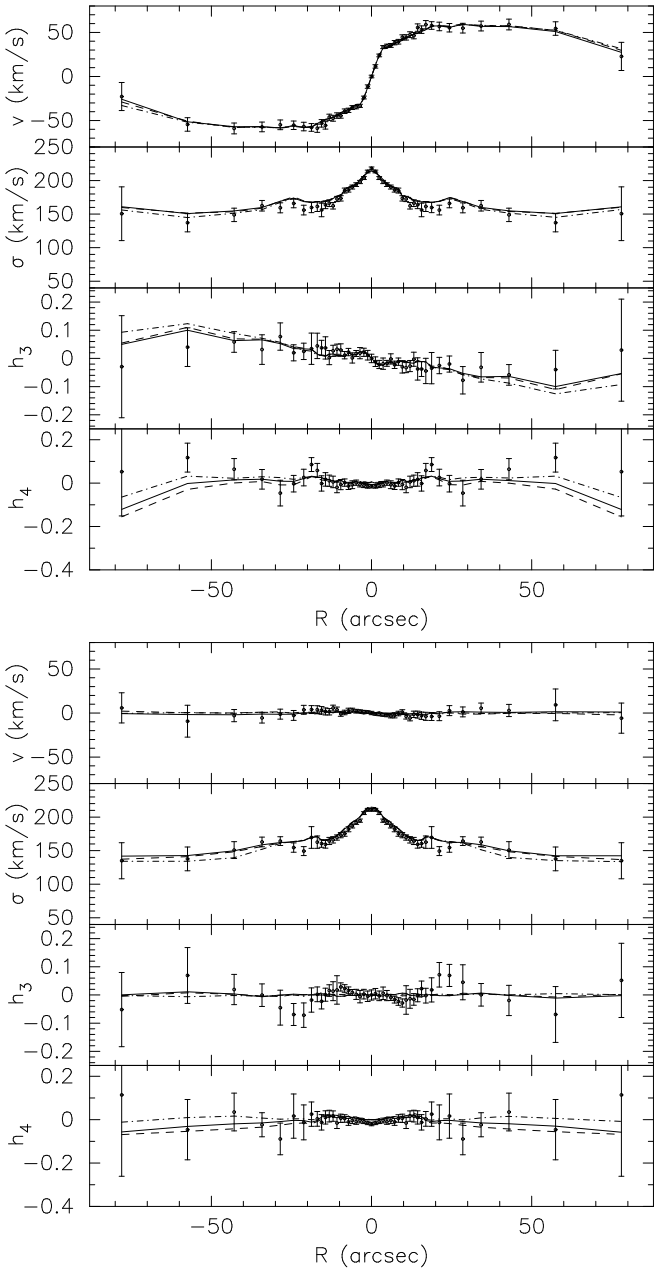

Figure 4.19: Comparison of models A90 (dashed lines), D90 (full lines) and D40 (dash-dotted lines) with the symmetrized slit data from Statler and Smecker-Hane (1999) along the major (top) and minor axes (bottom panel). The model data points are averages over the same slit cells as the target data (see Fig. 4.3), and are connected by straight line segments.

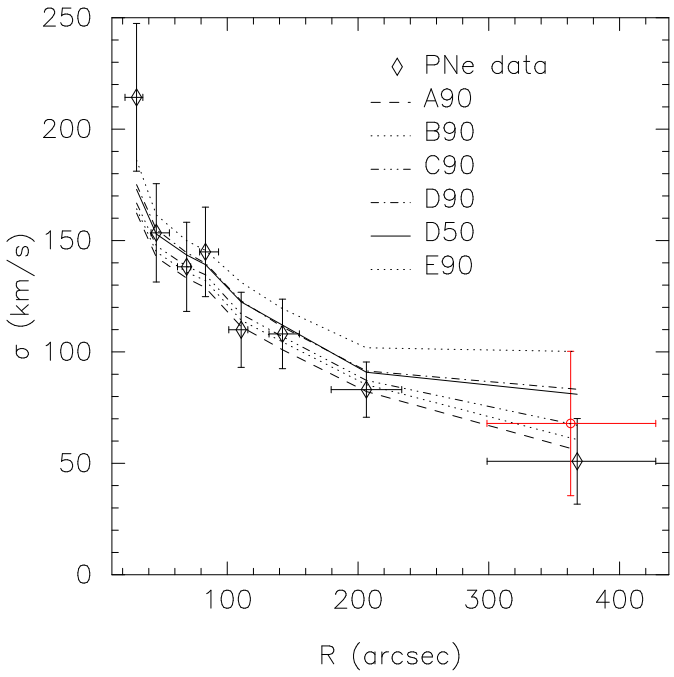

Figure 4.20: Comparison of the radial velocity dispersion profile from the PN.S data with the oblate particle models. The dashed line shows the stellar-mass only model A90. The other broken lines show models B90, C90, D90, the solid line shows model D50, and the upper dotted line shows model E90.

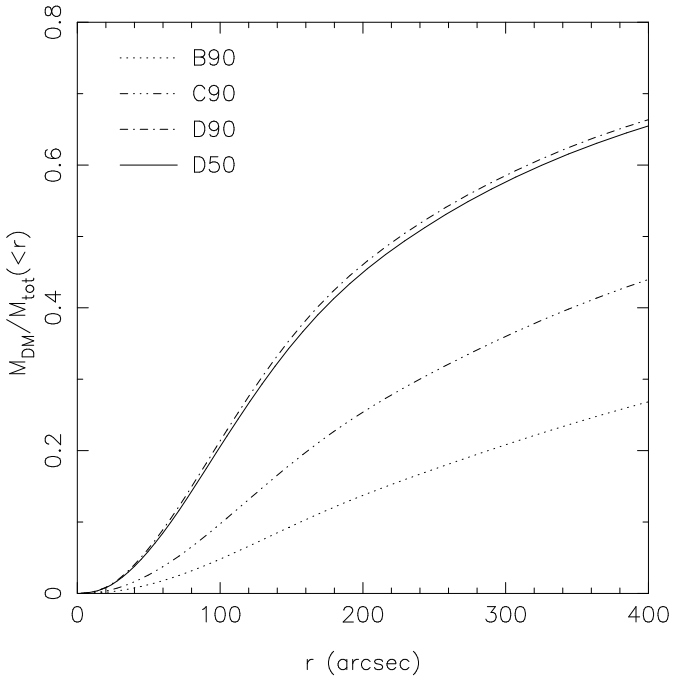

Figure 4.21: Enclosed DM fraction as function of radius for the final particle models B90, C90, D90, D50.

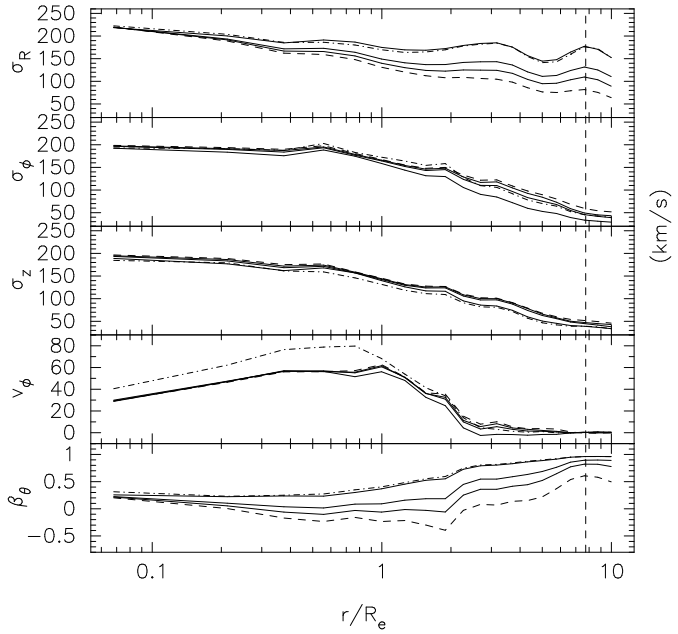

Figure 4.22: Intrinsic kinematics of the final models A90, B90 (dashed), C90, D90 (full) and D50 (dash-dotted lines). Panels from top to bottom show the radial, azimuthal, and θ velocity dispersion profiles, the mean azimuthal streaming velocity, and the meridional anisotropy profile. The models in the most massive halos are strongly radially anisotropic, as expected.

which causes the rapidly decreasing PN velocity dispersion profile in the massive dark halo potentials.

Finally, we comment briefly on the stability of these models. All models in halos A-C show no signs of any change after 5.8 Gyr of evolution following the phase-mixing after the NMAGIC fit. The D models are almost unchanged, despite the strong radial anisotropy, developing after 5.8 Gyr a percent-level triaxiality just outside the error bars of the A_{22} constraints. The models in halo E show a similar slow evolution during which they in addition develop significant positive h_4 across the entire image. As in the spherical models, the PN dispersion profiles remain unchanged during this evolution.

4.4.3 Models without axisymmetry constraint

We have constructed a small number of models for which the stellar density was not constrained to remain axisymmetric, in order to see whether the larger freedom in the orbit structure of non-axisymmetric potentials would allow the models to fit the PN kinematics also in the most massive halo E. However, we have kept the constant value PA$= 70\,\mathrm{deg}$ for the position angle in the photometry, neglecting the observed small variations $\Delta\mathrm{PA} = \pm 3\,\mathrm{deg}$, so these models do not have isophote twists. We generate these models as follows, using the full power of NMAGIC, by (i) fitting only surface brightness and kinematic data, in a similar way as for model E*, (ii) leaving all density A_{lm} terms and corresponding potential terms free to change during the fit, in order to allow the model to freely change its orientation, and (iii) using a spherical model, a model flattened along the line-of-sight, or the inclined model D40 as initial conditions.

Because we know that valid models in halo D can be found, we have first evolved a model in halo D, starting from initial conditions D*, a model that had previously been obtained exactly analogously to model E* (see Section 4.4.2). Because of the line-of-sight streaming velocities, this system rotates out of the sky plane while NMAGIC simultaneously keeps adjusting the orbit structure to match both the surface brightness and the projected kinematics. This model

converges to an almost axisymmetric model with inclination $\simeq 43\,\mathrm{deg}$, and is then completely stable over 5.8 Gyr of evolution. It matches all the kinematic data, very similar to models D40 and D50, and is listed in Table 4.2 as model DR.

Also shown in the Table are the results for model ER, which was obtained analogously starting from model E*. This model does not fit the PN data. None of our other attempts to obtain a valid model E has been successful, including one inspired by some old work on merger remnants (Gerhard, 1983a,b), following which we tried to construct a model that changes from edge-on oblate in its inner parts to face-on triaxial in its outer regions. We believe the main reason for the failure in halo E is the observed rotation of NGC 3379, of which either the sense (along the projected major axis) or the amplitude do not allow the low-inclination configurations required by the low values of velocity dispersion at large radii.

4.4.4 Likelihoods and quality of the fits to the data

We now turn to discussing the question which models are acceptable fits to the data and which models can be ruled out. To do this, it is customary to determine $\Delta\chi^2$ values relative to the best-fitting models, and determine the confidence boundaries according to the number of parameters to be determined. In our case, we essentially determine only one parameter, the halo circular velocity at $\sim 7R_e$, or v_0, so the relevant $\Delta\chi^2 = 1$ (the mass-to-light ratio of the models is optimized together with the weights). However, all our models match the Sauron and slit kinematic data to within 1σ per data point, i.e., better than the underlying "true" model. Clearly, we cannot apply a $\Delta\chi^2 = 1$ for small variations within 1σ relative to, say, the Sauron data points. Even if the best model fitted with exactly $\chi^2_{sau} \simeq 10^4$, this would make little sense: for $N_{sau} = 10^4$, $\Delta\chi^2 = 1$ corresponds to an average change per data point of $\simeq 10^{-4}\sigma$. Only if the $\Delta\chi^2 = 1$ arises because of significant mismatch of a few crucial data points would this seem reasonable. The crucial data points for the issue addressed in this paper, the dark matter halo in NGC 3379, are the PN velocities or the binned PN dispersions. Thus we focus our discussion on the merit of the models relative to these data.

Figure 4.23 shows the χ^2_{PN} and $\Delta\chi^2$ values for both the spherical and the axisymmetric models from Tables 4.1 and 4.2. For the PN dispersion points we have 7 degrees of freedom (8 data points minus 1 fitted parameter), so expect $\chi^2 = 8.18$ (68.3% probability) for a typical good model. Thus we consider any model that fits the PN velocity dispersions to better than $\chi^2 = 8.18$ as valid as the underlying "true" model and compute $\Delta\chi^2$ relative to $\chi^2_{PN} = 8.18$. The curves in Figure 4.23 are plotted for the two cases with and without the "friendless" outlier of Douglas et al. (2007) contributing to the outermost dispersion point. The models with halos A-D are allowed in both cases, while the models for halo E are consistent with the data only when the outlier is included.

So far we have compared the models only to the PN velocity dispersion profile, rather than to the LOSVDs or unbinned velocity data. Figure 4.24 shows the LOSVD histograms for the PNe in the outermost three circular annuli used for computing the PN velocity dispersion profile, superposed on the LOSVDs of models B and D in the same radial shells. In the plot for the outermost bin, the PN histogram and model LOSVD are shown with and without the 3σ "friendless" outlier according to Douglas et al. (2007). Both the near-isotropic low-density halo model B and the radially anisotropic massive halo model D are consistent with the PN velocity distributions in the first and third annuli, and both appear inconsistent with the non-zero mean motion of the PNe in the second annulus.

Table 4.3 shows the posterior likelihoods of the spherical models for the observed PN velocity data set, evaluated from the model LOSVDs in the eight radial shells used in the fits. Also listed are the likelihoods resulting from direct likelihood fits of the spherical models to the PN data, using the method described in de Lorenzi et al. (2008). Figure 4.25 shows a plot of these likelihoods as a function of the models' circular velocity at $7R_e$, the radius of the outermost PN dispersion point. Despite the small number of potentials investigated and the issue of whether

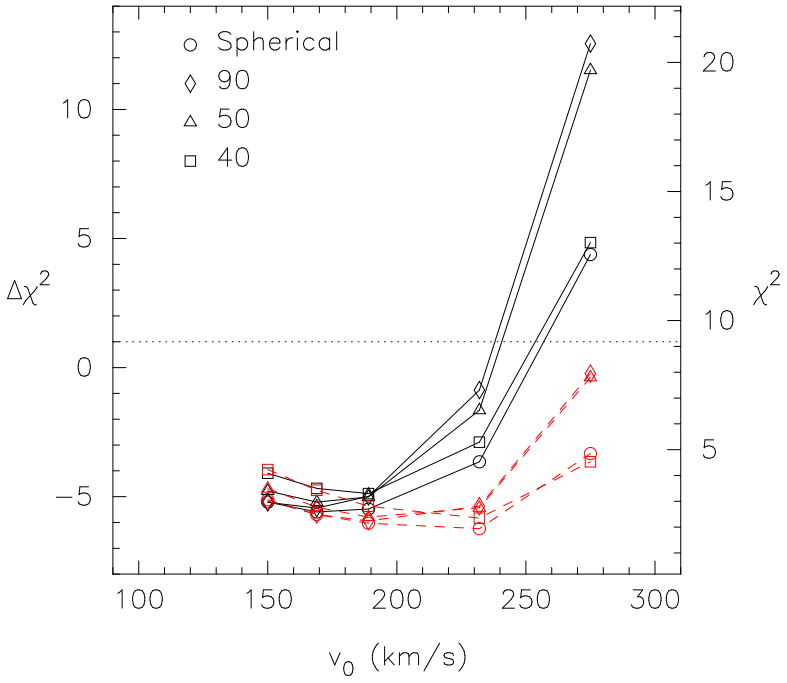

Figure 4.23: χ^2 and $\Delta\chi^2$ values of the various spherical and axisymmetric models for NGC 3379 with respect to the PN velocity dispersion data. The full black lines (red dashed lines) connect the χ^2-values obtained without (including) the 3σ "friendless" outlier of Douglas et al. (2007). $\Delta\chi^2$ is computed relative to the expected value of $\chi^2 = 8.18$ for 7 degrees of freedom.

	without outlier		with outlier	
HALO	$\ln\mathcal{L}$	$2\Delta\ln\mathcal{L}$	$\ln\mathcal{L}$	$2\Delta\ln\mathcal{L}$
A	−605.14	2.50	−611.18	4.58
B	−604.21	0.64	−609.67	1.56
C	−603.89	0.0	−608.89	0.0
D	−604.74	1.7	−609.23	0.68
E	−607.16	6.54	−611.38	4.98
A	−608.50	4.23	−613.53	5.01
B	−607.01	1.25	−611.82	1.60
C	−606.38	0.0	−611.02	0.0
D	−606.68	0.60	−611.14	0.23
E	−608.81	4.85	−613.04	4.02

Table 4.3: Likelihood values for the PN data in the spherical models. Column (1): model code. Columns (2,3): log likelihood $\ln\mathcal{L}$ and difference $2\Delta\ln\mathcal{L}$ relative to the best model C, for the PN sample not including the 3σ "friendless" outlier in the outermost shell, according to Douglas et al. (2007). Columns (4,5): same, but for the PN sample including this outlier. The top half of the table refers to posterior likelihoods of the models fitted to the PN velocity dispersion profile, the lower half gives likelihoods for similar models in which the PNe were fitted with the likelihood method of de Lorenzi et al. (2008).

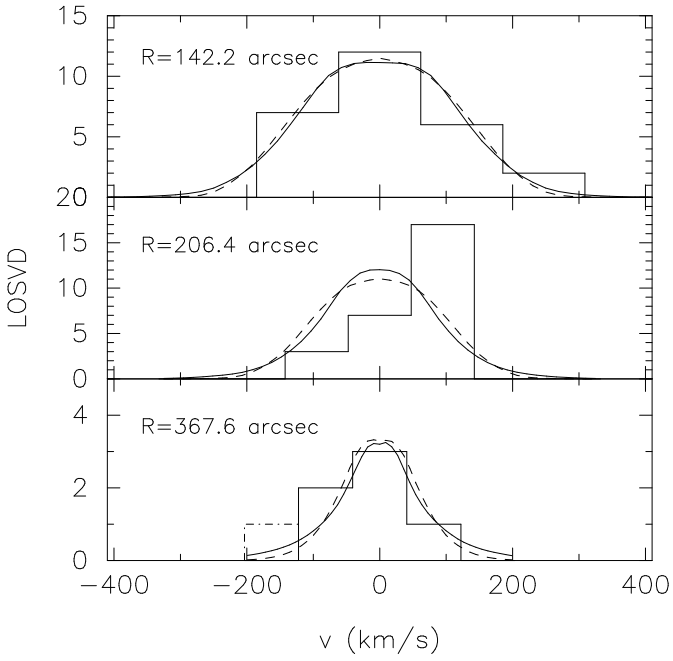

Figure 4.24: Comparison of the PNe LOSVDs in the circular annuli corresponding to the outermost three bins in the velocity dispersion profile, with the LOSVDs of the nearly isotropic, low-density halo model B, and the radially anisotropic massive halo model D in the same circular annuli. The ordinate is in units of PN number, and the model LOSVDs have been normalized to the same integral over the velocity range shown. In the middle panel for the second annulus, the mean velocity of the PNe is non-zero at the $\simeq 3\sigma$ level; both models are inconsistent with this velocity distribution. The velocity distributions in the other two panels are fully consistent with both models. In the lower panel for the outermost shell, the PN histogram is shown with (dashed) and without (solid lines) the 3σ-'"friendless"' outlier; see Section 4.2.3 and Douglas et al. (2007).

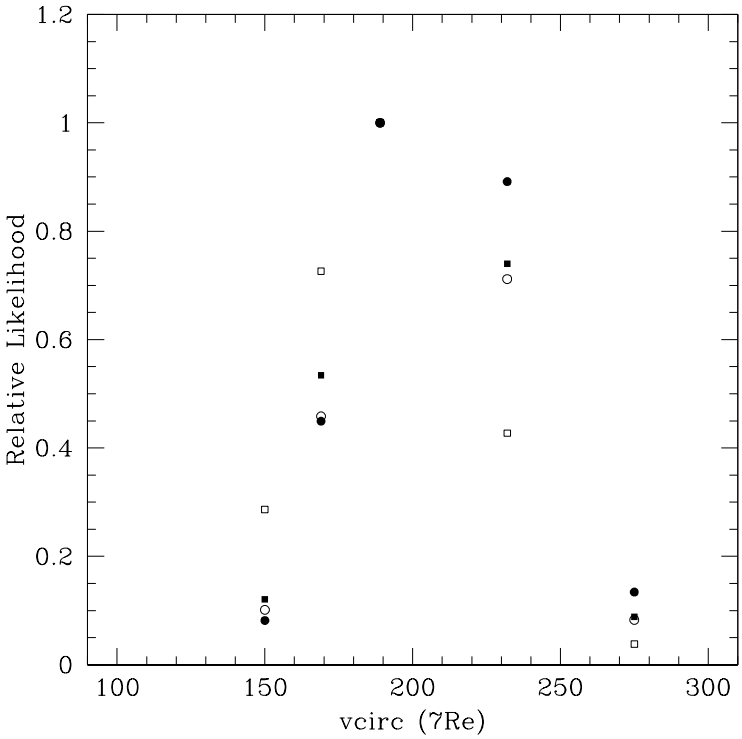

Figure 4.25: Relative likelihoods from the data in Table 4.3 as a function of the model circular velocity at $7R_e$. Open symbols show posterior likelihoods of models fitted to the binned dispersion profile, full symbols show likelihood values based on direct likelihood fits to the PN velocities. Squares show likelihoods for the PN sample without the 3σ "friendless" outlier in the outermost shell, according to Douglas et al. (2007), circles for the sample including this outlier.

the 3σ "friendless" outlier should be included, the overall shape of the likelihood function $\mathcal{L}$ is not too far from a Gaussian. Thus we can determine a confidence interval from the condition $\Delta \log \mathcal{L} > 0.5$, resulting in approximately $165\mathrm{kms}^{-1} \lesssim v_{circ}(7R_e) \lesssim 250\mathrm{kms}^{-1}$ at 1σ. This would exclude both model A without dark matter and the most massive halo model E. However, we do not believe this is a very strong result, given the influence of a single outlier on the likelihood values in Table 4.3, and the asymmetries in some of the LOSVDs (see Fig. 4.24). Note also that all models are consistent with the data at the 2σ level, for which $v_{circ}(7R_e) \lesssim 290\mathrm{kms}^{-1}$ (2σ).

4.5 Summary and conclusions

In this paper, we have carried out a dynamical study of the elliptical galaxy NGC 3379. This intermediate luminosity E1 galaxy has a rapidly declining velocity dispersion profile, which has been taken as evidence by Romanowsky et al. (2003) and Douglas et al. (2007) that this galaxy may lack the kind of dark matter halo that the current ΛCDM cosmology requires.

To explore this issue further, we have combined photometry, long slit spectroscopic data, SAURON absorption line kinematics and PN velocity dispersion data, to fit dynamical models in a sequence of potentials whose circular velocity curves at large radii vary between a near-Keplerian decline and the nearly flat shapes generated by massive halos. The combined kinematic data set runs from the center of NGC 3379 to about 7 effective radii.

For constructing the dynamical models we have used the flexible χ^2-made-to-measure particle code NMAGIC developed by (de Lorenzi et al., 2007, 2008). The NMAGIC models described in this paper consist of 7.5×10^5 particles, and for the first time incorporate integral field kinematic data for a real galaxy.

We find that a variety of dynamical models both with and without dark matter produce viable fits to all the data. For assumed spherical symmetry we find that the data are consistent both with near-isotropic systems which are dominated by the stellar mass out to the last kinematic data points, and with models in moderately massive halos whose outer parts are strongly radially anisotropic ($\beta \simeq 0.8$). In these latter models, the stellar mass distribution dominates in the center, and the dark matter fraction is $\sim 60\%$ of the total at $7R_e$.

In the spherical potentials we have also used the likelihood scheme of de Lorenzi et al. (2008) to fit the models directly to the PN velocities. From the likelihood values obtained in these fits as well as the posterior likelihoods of the models fit to the dispersion profiles, we estimate confidence limits on the halo circular velocity at $7R_e$, resulting in approximately $165\mathrm{kms}^{-1} \lesssim v_{circ}(7R_e) \lesssim 250\mathrm{kms}^{-1}$ at 1σ. This would exclude both the model without dark matter and the most massive halo model E in our sequence which has $v_{circ}(7R_e) \simeq 275\mathrm{kms}^{-1}$.

For illustration we have used NMAGIC to find the shape of a model flattened along the line-of-sight in a spherical potential including this most massive halo E, which fits all the kinematic data with high accuracy. However, all attempts to find more realistic models with this massive halo have failed, suggesting that we may have found the upper limit of the range of consistent mass distributions.

Finally, we have constructed self-consistent axisymmetric models of inclinations $i = 90°$, $i = 50°$, and $i = 40°$ in the same sequence of halos potentials. These models essentially confirm the spherical results. The edge-on models are very similar to the spherical models, becoming highly anisotropic in the more massive halos. The inclined models in addition become more flattened at large radii, which helps in decreasing the outer velocity dispersion profile. All these models are stable over Gyrs.

In summary, the kinematic data for NGC 3379 out to $7R_e$ are consistent with a variety of potentials and do not give strong constraints on the mass distribution in this galaxy. The main reason for this is the well-known degeneracy between mass and radial anisotropy which is substantial when the velocity dispersion profile falls with radius. In such cases, kinematic data

are required even further out than the presently available data set. NGC 3379 may well have the kind of dark matter halo consistent with the current ΛCDM paradigm.

CHAPTER 5

SUMMARY AND OUTLOOK

As indicated in the beginning, the two key aspects of this thesis have been: (i) To develop a made-to-measure method to construct particle models from observations, and (ii) to apply the new method to the intermediate luminosity elliptical galaxies NGC 4697 and NGC 3379 with focus on their DM contribution at large radii. Consequently, I will structure the discussion in the same way and start with the results concerning the method itself, before reporting on the astronomical results. Finally, I will give a brief outlook.

5.1 Summary

NMAGIC modelling

Syer and Tremaine (1996) proposed a made-to-measure (M2M) algorithm to construct N-particle systems from observational data and used it to generate a triaxial model from density observables. The first practical application was made by Bissantz et al. (2004), who constructed a dynamical model of the projected face-on density distribution of the Milky Way. So far, only density constraints have been considered and all models have been evolved in predetermined potentials.

In chapter 2, a χ^2-made-to-measure (χ^2M2M) algorithm was developed, extending earlier ideas by Syer and Tremaine. An important component of the new method is the use of the standard χ^2 merit function at the heart of the algorithm, which allows to assess the quality of a model fit directly. In addition, kinematic observables including higher order moments have been incorporated. Hence, kinematic and density (or surface density) constraints can be used to tailor particle models. The new χ^2M2M method was implemented in a fast, parallel code, NMAGIC. This code also incorporates an optional but fast potential solver, allowing it to recompute the potential during a model fit and, in addition, to test the stability of the final particle model. The NMAGIC implementation of the χ^2M2M algorithm is highly efficient, with a sequential fraction of only $\sim 1\%$.

The geometric flexibility and performance of NMAGIC was illustrated with a number of tests using spherical, oblate and triaxial target models. In the spherical experiments, the correct isotropic target model was recovered, independently of the adopted initial conditions. The initial model with density closer to the density of the final model had smaller final deviations from the target observables, and a narrower distribution of weights.

The oblate tests showed that a large phase-space gradient can be recovered if present, and illustrated the advantage of integral field data over slit data for constraining the model.

The triaxial experiments demonstrated that it is possible to start from a spherical model and converge to a triaxial target, and illustrated NMAGIC's ability in constructing models for triaxial elliptical galaxies with which nature confronts us. A second triaxial experiment, in which a slowly rotating model was used as a target for a non-rotating model, revealed that the residuals

in the first order kinematic moment are correlated. This gives a signature of tumbling which, at least for this triaxial system, allows to distinguish between internal stellar streaming and pattern rotation within R_e, provided a full velocity field is available. However, a more complete study of this problem is needed to firm up this result. This experiment also demonstrates the usefulness of the χ^2M2M algorithm for modelling mock (rather than real) galaxies in order to learn about their dynamics. Such an experiment would not have been practical with standard N-body simulations.

In chapter 3, I extended NMAGIC to account for seeing effects and proposed and implemented an efficient method to estimate the mass-to-light ratio Υ. Tests of this scheme using isotropic rotator input models have shown that the method recovers Υ within a few percent both for self-consistent and dark matter dominated target galaxies. In addition, a likelihood scheme was implemented, by which discrete velocity measurements can be taken into account without binning them beforehand.

The modelling of NGC 4697 and NGC 3379, presented in chapters 3 and 4, respectively, showed that the χ^2M2M/NMAGIC particle method is a very promising modelling technique. In fact, it has already gone further than the Schwarzschild method in that the gravitational potential of the stars has been allowed to vary in the modelling, the mass-to-light ratio has been adapted on the fly and the stability of the models has been checked.

Compared to the Schwarzschild method, the main advantages of the χ^2M2M algorithm as implemented in NMAGIC are that no symmetry restrictions have to be made and that no complicated procedure for orbit sampling is needed. Another advantage is that the gravitational potential can be evolved self-consistently, which further allows to test the stability of a model after the correction phase. Every χ^2M2M model corresponds to a computation of an orbit library in the Schwarzschild method. In problems where the same orbit library can be reused, Schwarzschild's method is more efficient.

The present implementation of NMAGIC is optimized for modeling nearly spherical systems. This is mainly due to the potential solver and the density observables (A_{lm}), both based on a spherical harmonics decomposition of the density distribution.

In the next two sections below, I will discuss the astronomical results from the dynamical modelling of NGC 4697 and NGC 3379.

Astronomical results

NGC 4697

Chapter 3 presented a dynamical study of the E4 galaxy NGC 4697 using surface brightness measurements and a combined kinematic data set, which runs from the center of the galaxy to about 4.5 effective radii. The kinematic data set consists of long slit spectroscopic data and discrete PNe velocity measurements.

Even though NMAGIC does not require any symmetry assumptions for the modelling, I have forced the method to generate axisymmetric particle models for NGC 4697. Both self-consistent models without dark matter, and models following a sequence of circular speed curves with increasing dark halo contributions have been investigated. The PN data have been used both binned on two different spatial grids, as well as with the new likelihood scheme, to make sure that the results are not biased by the way the PNe data are incorporated.

The main result is that models both with and without dark matter are consistent with all the data. These models fit all kinematic data with $\chi^2/N < 1$, both in potentials with only luminous matter and in potentials including sufficiently massive halos to generate nearly flat circular rotation curves. The massive dark halo models tend to fit the data slightly better in the sense of lower χ^2/N, for both the slit kinematics and the PN data, but these variations are small and not yet statistically significant. To exclude models without dark matter would require

PN velocities at even larger radii than currently available, out to an estimated $\simeq 6R_e$ from the center.

These models differ from earlier studies performed by Méndez et al. (2001) in the sense that we generate axisymmetric models instead of spherical ones and that our models are flexible with regard to anisotropy. The best-fitting models are slightly radially anisotropic, with $\beta \simeq 0.3$ at the center, increasing to $\beta \simeq 0.5$ at $\gtrsim 2R_e$. This is consistent with the value given by Dekel et al. (2005) obtained from merger simulations carried out within the ΛCDM cosmology framework.

NGC 3379

In chapter 4, the dynamical modelling of the intermediate luminosity E1 galaxy NGC 3379 was presented. The models were constructed using photometric and kinematic observations for this galaxy. Again, a combined kinematic data set was used, consisting of long slit spectroscopic data with SAURON integral field absorption line kinematics and PN velocity measurements with the PN.S instrument from Douglas et al. (2007). The combined data set runs from the center of NGC 3379 to about 7 effective radii. This is the first time that integral field SAURON kinematic data of a real galaxy has been incorporated in NMAGIC.

Both self-consistent models without dark matter, and models following a sequence of circular speed curves with increasing dark halo contributions have been investigated.

Several dynamical models, with and without DM, produce a viable fit to all the data. For assumed spherical symmetry the data is consistent with near-isotropic models dominated by stellar mass and with radially anisotropic models in moderately massive halos with DM fractions $\simeq 60$ percentage at 7 R_e. In addition, a series of of oblate models have been constructed which essentially confirm the spherical results.

The main conclusion is that the steeply declining PNe velocity dispersion profile is consistent with a variety of DM halos. It is difficult to constrain the potential in this galaxy with the present data. This is mainly due to the well known mass anisotropy degeneracy, which masks the DM distribution by preferentially populating radial orbits. Hence the possibility remains that NGC 3379 has the kind of dark matter halo that is consistent with the current ΛCDM paradigm.

5.2 Outlook

In the first part of this outlook, I discuss some of the possible technical improvements and extensions of the NMAGIC code. In the second part I give some examples of possible future applications.

5.2.1 Technical improvements

- *The profit function*

  The present implementation of the χ^2M2M algorithm uses the entropy

  $$S = -\sum_i w_i \ln(w_i/\hat{w}_i), \tag{5.1}$$

  as a profit function. The isotropic rotator experiments of chapter 3 have shown, that for the given spatial coverage of the kinematic data, a large entropy contribution in the modelling process is needed in order to obtain a smooth model. However, the large entropy value prevented the models to fit the rotation of the target model. Similar results were obtained in chapter 4, where a large entropy value prevented the model to become strongly anisotropic. Hence, a large entropy value suppresses global phase-space gradients. It is worth considering alternatives to the entropy as a profit function, which reduce local phase-space fluctuations, but allow for global phase-space gradients.

- *The dark matter halo*

  In the present work, we have represented the gravitational influence of the dark matter halo on the luminous component by an analytic logarithmic potential. Cosmological simulations reveal universal DM halo density profiles described by a NFW profile (*e.g.* Navarro et al., 1996, 1997)

$$\rho_{NFW}(r) = \frac{\rho_s}{(r/r_s)(1+r/r_s)^2}, \tag{5.2}$$

  and hence, provide a physically motivated halo model. I have implemented the NFW halo as an option in the NMAGIC code for future projects, but it has yet to be tested.

  Further, the dark matter halo could react to the luminous matter via adiabatic contraction. It may also be interesting to use live dark matter halos, represented by particle realizations made from a DF or even generated by cosmological simulations.

- *Initial conditions*

  The spherical initial conditions used in the present work were generated directly from a DF, *cf.* section A.2, assigning to each particle the same mass. For a Hernquist particle realization the number of particles within a radius r much smaller than the scale length a scales as $(r/a)^2$. This implies that there is only a small number of particles which samples the central density cusp. The resolution in the central region can be improved by using a multi-mass scheme (*e.g.* Sigurdsson et al., 1995; Magorrian, 2007), where the particle mass becomes a function of its pericenter distance.

- *Integration scheme*

  I used a "drift-kick-drift" version of a standard leapfrog integration scheme. An unattractive feature of this scheme is that it uses the same time step for all the particles. A particle on an almost radial orbit which passes close by the galaxy center, possibly harboring a black hole, requires a very small time step to be integrated accurately near its pericenter. This implies that all the particles are integrated with the same small time step, even if they are on almost circular orbits at large distances from the center of the system. This can be very time consuming because the forces have to be calculated every time step. Applying a block-time step scheme will improve the efficiency and would allow to either increase the number of particles or the number of iteration steps during an NMAGIC run. Magorrian (2007) proposed a block-time step scheme in combination with a particle mesh method using a refinement scheme which results in a gain of speed up to a factor of five.

- *Particle splitting*

  Syer and Tremaine (1996) suggested to improve their method by incorporating a scheme which kills particles with low weights and splits particles with high weights into several particles with slightly perturbed orbits. It would be interesting to study if a better convergence and a better model fit could be achieved using this method.

- *Discrete velocity measurements*

  The treatment of discrete line-of-sight velocity measurements can be extended to account for proper motion measurements, as well as any arbitrary velocity direction (*cf.* also Chanamé et al., 2007). Further, it is worthwhile to study in more detail how well the intrinsic properties of a mock galaxy are recovered from discrete measurements alone, and how the results change with the number of measured velocities and/or their spatial distribution.

5.2.2 Future applications

- *Modeling radial PNe velocities in elliptical galaxies*

  It would be interesting to model other intermediate luminosity ellipticals to compare the results concerning the DM content with the findings of Romanowsky et al. (2003), and to test the alternative idea that the PNe population may be affected by radial anisotropy, which masks the dark matter distribution.

- *Black holes*

  With an increased resolution at the center, black hole mass studies with NMAGIC may become feasible. It would be interesting to test how well one can constrain the mass of a central black hole and how this compares with Schwarzschild's method.

- *Triaxial systems*

  The geometric flexibility of NMAGIC allows to model triaxial systems. A detailed study of how well the intrinsic shape and the orientation with respect to the observer of triaxial systems can be constrained would be interesting.

- *Figure rotating stellar systems*

  In chapter 2, the kinematics of a triaxial tumbling system inside one effective radius was modeled with a non-rotating triaxial system having the same intrinsic shape. The result was that the first order kinematic moment were correlated, which gives a signature of figure rotation. A more complete study of the effects of different pattern speeds, intrinsic shapes, dark matter component and initial conditions would be necessary to strengthen the result.

- *Pseudo bulges*

  An application of the NMAGIC modeling technique to pseudo bulges using integral field kinematics with a large field of view may provide a better understanding of their intrinsic kinematics.

- *Milky Way*

  Using the original M2M method, Bissantz et al. (2004) built a stellar-dynamical model of the Milky Way's barred bulge and disk, matching the projected face-on density distribution. Rattenbury et al. (2007) presented a refined model, which was fitted also to the vertical density distribution. However, no kinematic constraints have so far been taken into account. Nonetheless, the dynamical model was in rough agreement with proper motion dispersion measurements of the Galactic bulge region. An extension of the likelihood approach to discrete proper motion measurements would be of interest for constructing dynamical models of the MW.

- *Direct comparison with Schwarzschild models*

  A direct comparison with Schwarzschild models could provide a broader understanding of several aspects of both modelling techniques.

APPENDIX A

SOME TECHNICAL DETAILS

A.1 Potential solver

Modelling stellar systems with large mass concentrations at their centers, such as elliptical galaxies, requires the force field to be computed with high accuracy at small radii. This can be achieved by computing the potential ϕ from a multipole expansion. In addition, using a surface harmonics expansion of the potential offers the possibility to enforce a certain symmetry, *e.g.* an axisymmetric potential if only the terms $m = 0$ are include.

The potential at position (r, θ, ϕ), generated by N particles with weights w_j and positions $(r'_j, \theta'_j, \phi'_j)$ [1] is given by the real part of (*cf.* Jackson, 1975; Binney and Tremaine, 1987)

$$\phi(\mathbf{r}) = -G \sum_{l=0}^{\infty} \sum_{m=0}^{l} (2 - \delta_{m0}) \frac{(l-m)!}{(l+m)!} P_l^m(\cos\theta) e^{im\phi} \left(\frac{A_{lm}}{r^{l+1}} + r^l B_{lm} \right) \tag{A.1}$$

with

$$\begin{aligned} A_{lm} &= \sum_{r'_j < r} w_j P_l^m(\cos\theta'_j) e^{im\phi'_j} {r'_j}^l \\ B_{lm} &= \sum_{r'_j > r} w_j P_l^m(\cos\theta'_j) e^{im\phi'_j} . {r'_j}^{-(l+1)} \end{aligned} \tag{A.2}$$

Many authors (*e.g.* van Albada, 1982; Villumsen, 1982; McGlynn, 1984) have performed N-body simulations based on a multipole expansions of the potential.

The direct use of equation (A.1) leads to large two-body relaxation in the simulations, caused by the finite truncation in l and by "shell-crossing", the discontinuous change of the acceleration of particles when they cross each other in radius. Different techniques have been applied to reduce these effects (*e.g.* White, 1983; McGlynn, 1984; Sellwood, 2003).

I have implemented a parallel version of the method described in Debattista (1998) and Sellwood (2003), and use it as the potential solver in the NMAGIC code. The coefficients A_{lm} and B_{lm} are computed at radii r_k, $k = 0, \cdots, n$ with $r_0 = 0$, while retaining the angular dependence of the potential. Similar to the cloud-in-cell scheme (*cf.* Hockney and Eastwood, 1988), the point particles are replaced by "clouds" smeared along the radius: for a particle with radius r'_j, the nearest grid point r_k is determined and the particle gets a finite radial extent $\delta r'_j = \frac{1}{2}(r_{k+1} - r_k)$, centered on r'_j. This is schematically illustrated in Figure A.1. The particle mass w_j is uniformly distributed over the radial extent of the "particle cloud". Hence, the mass fractions

$$f_{j,1} = \frac{1}{2} - \frac{r'_j - r_k}{\delta r'_j}, \quad \text{and} \quad f_{j,2} = \frac{1}{2} + \frac{r'_j - r_k}{\delta r'_j} \tag{A.3}$$

[1] I use subscript j to label the particles instead of i to prevent confusion with $i \equiv \sqrt{-1}$.

lie interior and exterior to r_k, respectively. Exceptions to this rule occur at the center, since no mass can be interior to $r = 0$, and at r_n, because no mass can extend beyond the outer edge of the system. Now, the contribution from each particle fragment to the interior and exterior terms

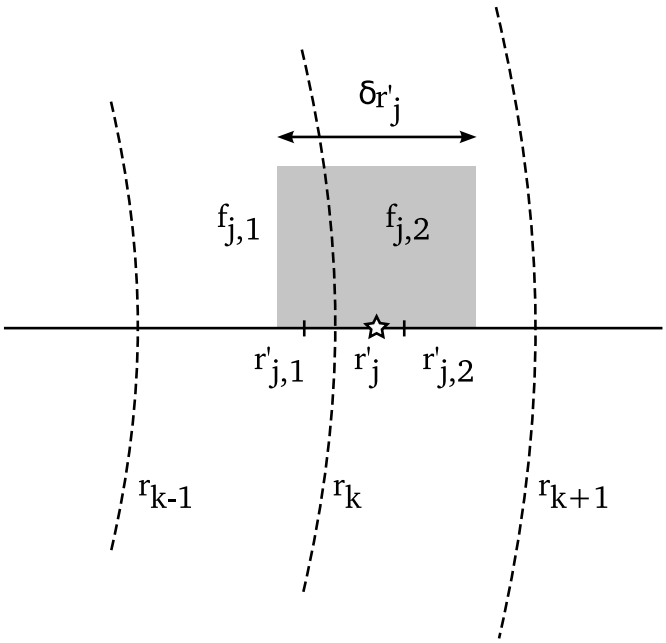

Figure A.1: Schematic view of the CIC scheme. The star denotes the particle.

on the two neighboring grid points are evaluated

$$\alpha_{lm}(k) = \sum_{\nu=1,2} f_{j,\nu} w_j P_l^m(\cos\theta_j) e^{im\phi_j} \frac{1}{r_k} \left(\frac{r'_{j,\nu}}{r_k}\right)^l$$
$$\beta_{lm}(k) = \sum_{\nu=1,2} f_{j,\nu} w_j P_l^m(\cos\theta_j) e^{i\phi_j} \frac{1}{r'_{j,\nu}} \left(\frac{r_k}{r'_{j,\nu}}\right)^l , \tag{A.4}$$

where the summation for $\alpha_{lm}(k)$ ($\beta_{lm}(k)$) is over mass fragments immediately interior (exterior) to r_k, *cf.* Figure A.1. The $r'_{j,\nu}$ denote the center of mass of the fragments. Hence, each particles contributes to $\alpha_{lm}(k)$, $\alpha_{lm}(k+1)$, $\beta_{lm}(k-1)$ and $\beta_{lm}(k)$ with exceptions at the center and the outer edge. $\alpha_{lm}(k) = 0$ because no mass can lie inside r_0.

Finally, the coefficients $A_{lm}(k)$ and $B_{lm}(k)$ are computed by summing up the contributions from all the shells interior and exterior to r_k, respectively. These are recursive sums over the radial shells

$$A_{lm}(k) = \alpha_{lm}(k) + A_{lm}(k-1) \left(\frac{r_{k-1}}{r_k}\right)^{l+1}$$
$$B_{lm}(k) = \beta_{lm}(k) + B_{lm}(k+1) \left(\frac{r_k}{r_{k+1}}\right)^l . \tag{A.5}$$

The potential at position (r, θ, ϕ) can now be computed via

$$\phi(r,\theta,\phi) = \sum_{l=0}^{\infty} \sum_{m=0}^{l} (2 - \delta_{m0}) \frac{(l-m)!}{(l+m)!} P_l^m(\cos\theta) e^{i\phi} \left(A_{lm} + B_{lm}\right),$$

where the coefficients A_{lm} and B_{lm} at radius r are obtained by linear interpolation. The potential is then differentiated to get the force field.

Particles experience forces from other particles belonging to the same shell and even self-forces. Provided that the total number of particles is large and the number of particles per bin is small, these contributions are small. Thus, the number of radial grid points should be increased with an increasing number of particles. I have replaced the coefficients $A_{lm}(k)$ and $B_{lm}(k)$ with the corresponding temporal smoothed quantities $\widetilde{A}_{lm}(k)$ and $\widetilde{B}_{lm}(k)$, *cf.* section 2.3. This further reduces the effects of two-body relaxation and particle noise.

I have parallized the method by distributing (equal) fractions of the particles over the available nodes. Once, the partial sums (A.4) have been evaluated on each processor, the only communication needed occurs, when the global values of $\alpha_{lm}(k)$ and $\beta_{lm}(k)$ are computed from the contributions of each node, *cf.* section A.4.

A comparison of a FFT potential solver with the implementation of the method described above is illustrated in Figures A.2 and A.3. The left panel in Figure A.2 shows potential contour lines in the xz-plane computed from a triaxial particle distribution. The triaxial particle distribution was generated as follows. First, a spherical Hernquist particle realization was made from DF, *cf.* section A.2 with $N = 5 \times 10^5$, truncation radius 20 and scale length $a = 1$. I squeezed the spherical particle model by 0.8 and 0.5 along the x- and the z-axes, respectively. The solid lines in Figure A.2 show the contour lines computed using a FFT potential solver using a Cartesian grid with 257^3 cells equally spaced between -25 to 25 along each direction. The dashed contours were obtained using the method described above. I used a radial grid at radii $r_k = e^{\gamma k} - 1$ with $\gamma = \log(r_{max} + 1)/n$; I use $n = 201$, $r_{max} = 25$ and $l_{max} = 2$. The right panel shows the same as the left panel but now for $l_{max} = 4$. Figure A.3 shows F_y along

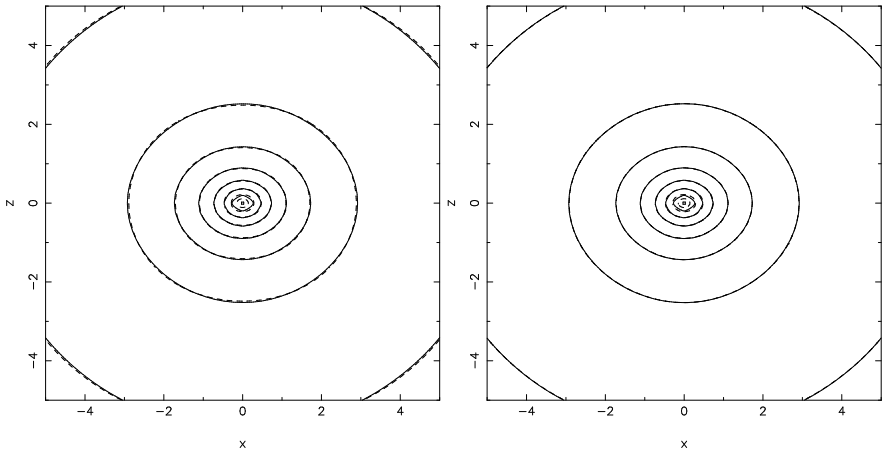

Figure A.2: (a) Left: Potential contour plot in the xz-plane for a triaxial particle distribution. The solid line was computed using an FFT whereas the dashed line was obtained using the spherical harmonic code with $l_{max} = 2$, details in the text. (b) Right: Same as a but for $l_{max} = 4$.

the x-axis computed using the FFT potential solver (solid line) and using the spherical harmonic code with $l_{max} = 4$ (dashed line). The better resolution at the center achieved with the spherical harmonic code is evident.

A.2 Initial conditions

I have adapted the method of Debattista and Sellwood (2000) to generate particle realizations from distribution functions (DFs) belonging to the family of spherical γ-models (Dehnen, 1993; Carollo et al., 1995), which are used as initial conditions for NMAGIC. The central density slope γ and the scale length a, of the model to be generated, is estimated from the observed surface brightness profile. The central surface brightness profile has $\Sigma \propto R^{1-\gamma}$ for $\gamma > 1$ and is logarithmically divergent for $\gamma = 1$. Models with $\gamma < 1$ appear to have cores and can hardly

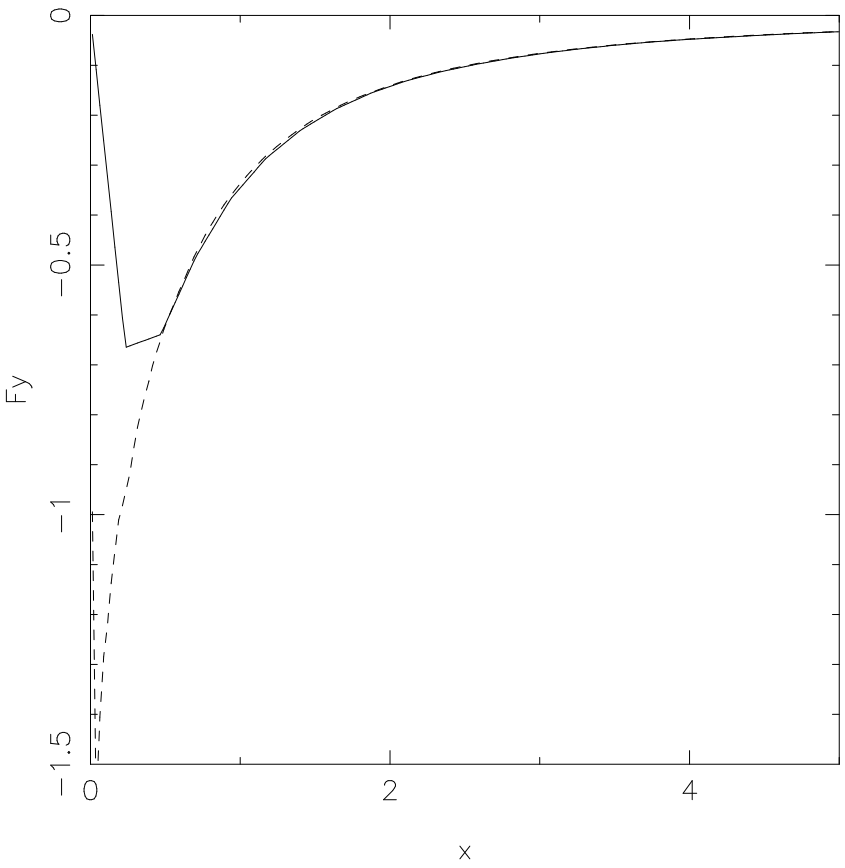

Figure A.3: F_y as function of long-axis distance. The solid line was computed using the FFT potential solver whereas the dashed line was obtained using the spherical harmonics code.

be distinguished. The scale length is estimated using $R_e/r_{1/2} \approx 3/4$ with $r_{1/2} = a(2^{1/(3-\gamma)} - 1)^{-1}$. Once, the scale length a and central density slope γ are given, the corresponding isotropic DF is determined. Selecting particles randomly from a DF (*e.g.* Kuijken and Dubinski, 1995) yields particle fluctuations $O(N^{1/2})$ in any range of the integrals, which can be reduced by applying the quiet-start procedure outlined in Debattista and Sellwood (2000). For a spherical system, the density of particles with energy E and total angular momentum L is given by

$$\mathcal{N}(E,L) = 8\pi^2 L f(E,L)\tau(E,L), \tag{A.6}$$

where f is the DF and τ is the radial period (see Binney and Tremaine, 1987). The DF is truncated at $E_{max} = \phi(r_{max})$ where ϕ is the gravitational potential of the self-consistent γ-model and r_{max} is the maximum radius of the particle realization. At that truncation, the mass enclosed is

$$m_{trun} = \int_{E_{min}}^{E_{max}} \mathrm{d}E \int_0^{L_c} \mathrm{d}L\, \mathcal{N}(E,L), \tag{A.7}$$

with $E_{min} = \phi(0)$ and L_c the angular momentum of a circular orbit at energy E. The accessible (E,L) space is divided into $n = n_E n_L$ small areas, each enclosing a fraction of mass m_{trun}/n as illustrated in the left panel of Figure A.4. The n_E cuts at energies E_j defined via

$$j\frac{m_{trun}}{n_E} = \int_{E_{min}}^{E_j} \mathrm{d}E \int_0^{L_c} \mathrm{d}L\, \mathcal{N}(E,L) \tag{A.8}$$

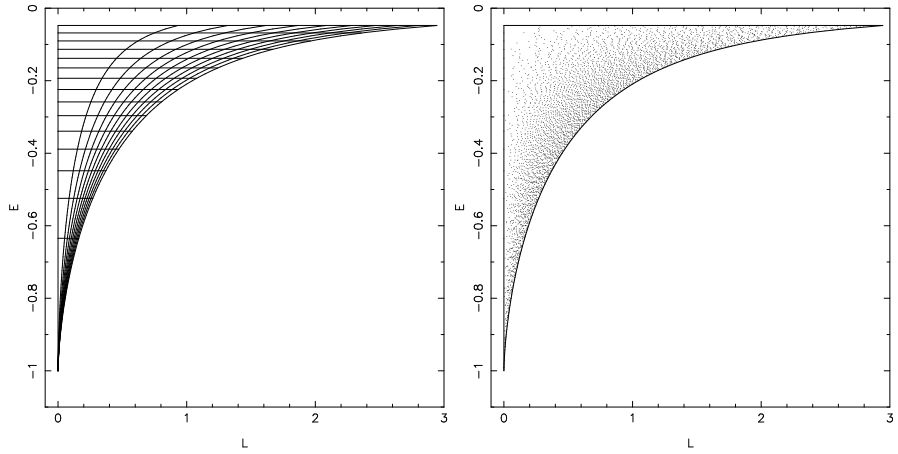

Figure A.4: (a) Left: Areas of equal mass in the (E, L) plane for a Hernquist DF. The right hand boundary indicates the limit of circular orbits and the boundary at $L = 0$ indicate the radial orbits. The upper curve shows the truncation in energy. (b) Right: Distribution of points in (E, L) plane chosen from an isotropic Hernquist DF.

and do not depend on angular momentum L. On the other hand, the boundaries $L_k(E)$ depend on energy and are defined by the relation

$$k\frac{m_{cut}}{n_L} = \int_{L=0}^{L_k} \mathrm{d}L\, \mathcal{N}(E, L), \tag{A.9}$$

where $m_{cut} = \int \mathrm{d}L\, \mathcal{N}|_E$. This defines n cells $\mathcal{C}_{jk}$ with $E \in (E_{j-1}, E_j]$ and $L \in (L_{k-1}, L_k]$ for a given energy ($E_0 = E_{min}$ and $L_0 = 0$). Now, an orbit in each cell is selected, but rather than using a regular grid, (E'_j, L'_k) is chosen at random in each $\mathcal{C}_{jk}$. First, an energy value $E'_j \in (E_{j-1}, E_j]$ is selected from the distribution $\int \mathrm{d}L\, \mathcal{N}(E, L)$, and then the corresponding angular momentum value L'_k computed via

$$(k - f)\frac{m_{cut}}{n_L} = \int_{L=0}^{L'_k} \mathrm{d}L\, \mathcal{N}(E'_j, L) \tag{A.10}$$

with $m_{cut} = \int \mathrm{d}L\, \mathcal{N}|_{E=E'_j}$ and random fraction $f \in (0, 1]$. The right panel of Figure A.4 shows such a distribution of orbits in the (E, L) plane.

Finally, each orbit has to be populated with an equal number of particles n_{EL}, making a total number of particles $N = n_E n_L n_{EL}$, each of mass $w = m_{trun}/N$. In a spherical system, a particle moves in a plane perpendicular to its angular momentum vector and it oscillates in radius between the pericenter and apocenter with period $\tau(E, L)$. The radial phase must be uniformly distributed, but the probability density varies with radius as the inverse of the radial velocity and peaks at the apocenter and pericenter. This difficulty in chosing a radius can be circumvented by numerically integrating the orbit for a random fraction of the radial period starting from its apocenter or pericenter.

The radial and azimuthal velocities are determined by (E'_j, L'_k) and the radius r, except for the sign ambiguity of the radial velocity. The azimuthal phase and the orientation of the orbit plane can be selected at random.

The left panel of Figure A.5 shows the evolution of the radial density profile of a spherical Hernquist particle realization when integrated in the analytic potential for several dynamical times. The solid line shows the analytic density profile, the dashed line shows the radial density profile at $T = 0$, the dashed-dotted line was obtained after $T = 250$ and the dotted line for $T = 500$. The lines are shifted for readability. The dynamical time at $r = a$ is $t_{dyn} = \pi$. The profiles were computed using radial bins containing 1000 particles each. The right panel shows

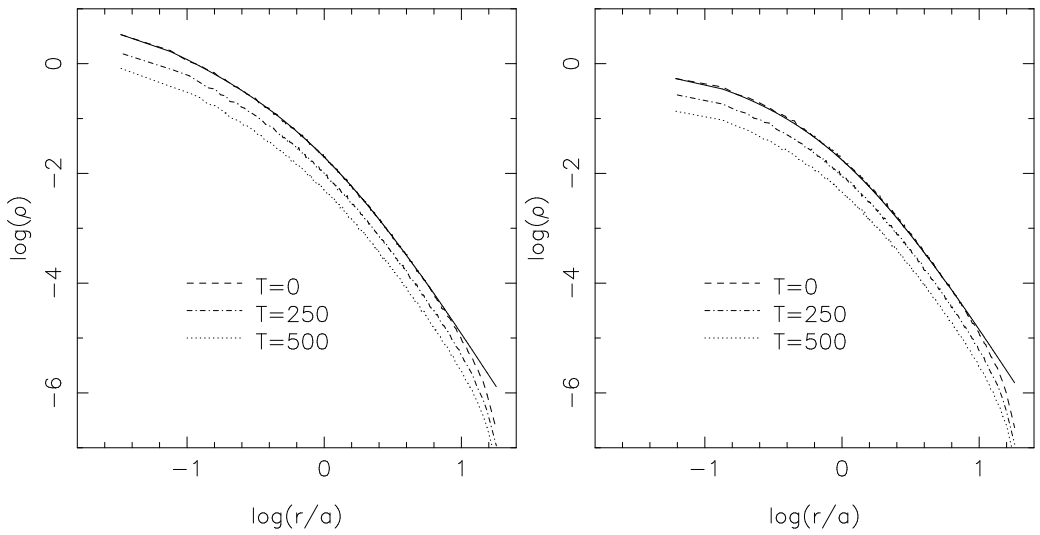

Figure A.5: (a) Left: Evolution of the radial density profile of a spherical Hernquist particle realization made from DF when integrated in the analytic potential. The solid line shows the analytic density profile, the dashed line shows the radial density profile of the ICs, the dashed-dotted line was obtained after $T = 250$ and the dotted line for $T = 500$. The lines are shifted for readability. The dynamical time at $r = a$ is $t_{dyn} = \pi$. The profiles were computed using radial bins containing 1000 particles each. (b) Right: The same as the left panel but for a Dehnen (1993) sphere with a shallow inner-power index $\gamma = 0.5$.

the same but for a Dehnen (1993) sphere with a shallow inner-power index $\gamma = 0.5$. For both models, the radial density profile remain remarkably constant over many dynamical times.

A.3 Integration scheme

The stellar particles in galaxy simulations move according to Newton's laws of motion, *cf.* Hockney and Eastwood (1988)

$$\begin{aligned} \frac{\mathrm{d}\mathbf{x}}{\mathrm{d}t} &= \mathbf{v} \\ \frac{\mathrm{d}\mathbf{v}}{\mathrm{d}t} &= \mathbf{F} \end{aligned} \tag{A.11}$$

where $\mathbf{F} = -\nabla\phi$ is the force per unit mass acting on a particle at position $\mathbf{x}, \mathbf{v}$ in phase space. The gravitational potential ϕ is generated by the hole system. I integrate the equations of motion using a "drift-kick-drift" version of the leapfrog scheme (*cf.* Magorrian, 2007)

$$\begin{aligned} \mathbf{x}_{n+1/2} &= \mathbf{x}_n + \mathbf{v}_n \frac{\delta t}{2} \\ \mathbf{v}_{n+1} &= \mathbf{v}_n + \mathbf{F}(\mathbf{x}_{n+1/2})\, \delta t \\ \mathbf{x}_{n+1} &= \mathbf{x}_{n+1/2} + \mathbf{v}_{n+1} \frac{\delta t}{2} \end{aligned} \tag{A.12}$$

where δt is a fixed time step and the subscript indicates the time level $(t = n\delta t)$. The leapfrog scheme produces a second-order accurate solution to equations (A.11) and is symplectic, reversible in time and conserves linear momentum, provided $\mathbf{F}$ obeys Newton's third law.

For the NMAGIC runs presented here, a constant time step $\delta t = 0.005$, given in dimensionless units, was used. As an illustration, I have integrated a particle in a Hernquist (1990) sphere with unit mass and scale length $a = 1$. The orbit of the particle is almost radial with

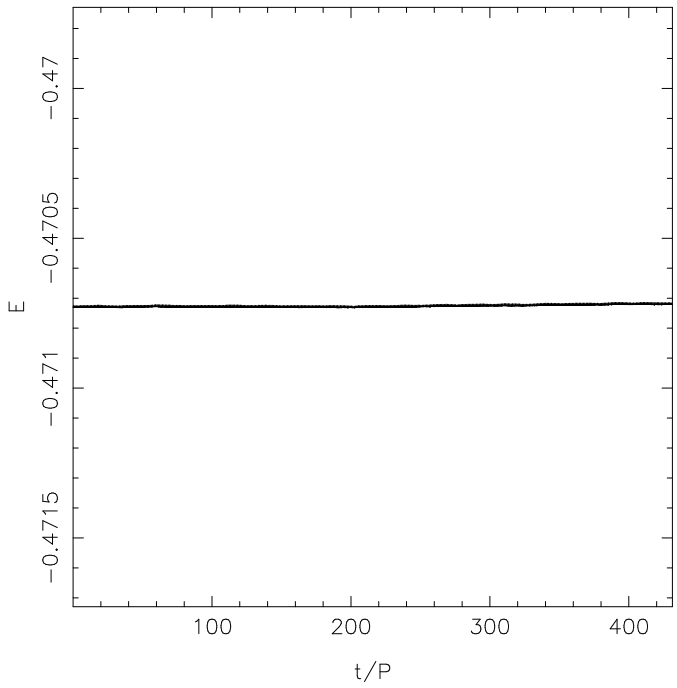

Figure A.6: Time evolution of the energy E of a particle moving along an almost radial orbit in a analytic Hernquist potential. The time is given in units of the radial period P.

pericenter distance 0.11, apocenter distance 1.1 and a radial period $P = 5.8$. Figure A.6 shows the evolution of the energy of the particle as it moves along its orbit and illustrates that no long term drift in energy is present.

A.4 Parallelization

When I had finished a first scalar version of a made-to-measure code, I performed several test runs on a standard desktop PC. These experiments were very time consuming. It is possible to reduce the computation time of a scalar program by using vector machines, which can perform operations simultaneously on linear arrays of numbers. The disadvantage of this approach is, that vector machines are generally very expensive and consequently it is difficult to get computation time contingents. A cheaper possibility to increase computation power is to use a PC clusters as a parallel computation environment, which allow numerical models to be computed with a high spatial resolution and a large number of particles. The disadvantage is that the code has to be adapted for the parallel cluster environment, *i.e.* one has to specify the distribution of memory onto the individual processors and the interprocess communications. I have parallelized the NMAGIC code using the MPI library, a library specification for message-passing, as described below.

The particles, *i.e.* their positions in phase space and their weights, are distributed equally between the available nodes, as schematically illustrated in Figure A.7. Integrating the particles along their trajectories does not require any inter-node communication, and is done on each processor separately. Communication between the different processors occurs only during an NMAGIC correction step, or when the gravitational potential is recomputed.

To compute the global value of a linear quantity Q, such as the model observables y_j or the expansion coefficients A_{lm} and B_{lm} of the gravitational potential, each node computes the contribution Q_α to Q generated by its subsample of particles, and sends Q_α to the master node (proc 0), which then computes $Q = \sum_\alpha Q_\alpha$ and distributes it to all the other nodes.

Hence, inter-node communication is only needed for the evaluation of the sum $Q = \sum_\alpha Q_\alpha$

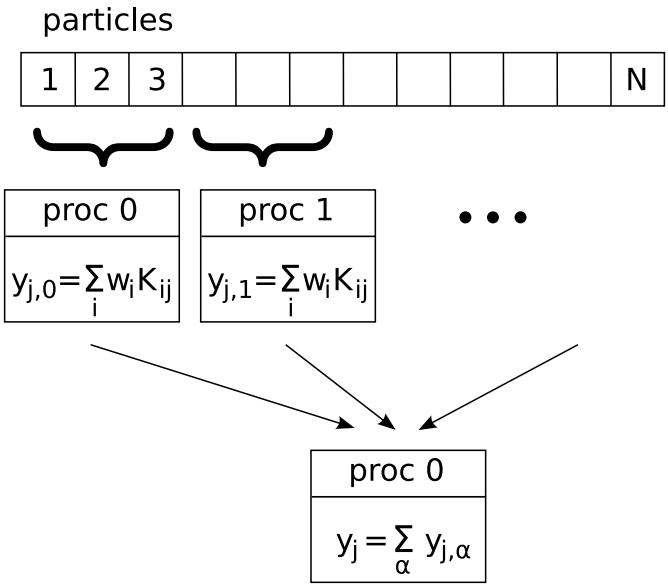

Figure A.7: Schematic representation of the parallelization scheme.

and thus the χ^2M2M algorithm is well suited to be parallized. The fraction of sequential code including communication overhead is $\approx 1\%$, *cf.* section 2.6.

Appendix B

Photometric and kinematic data of NGC 4697

B.1 Photometric and kinematic data

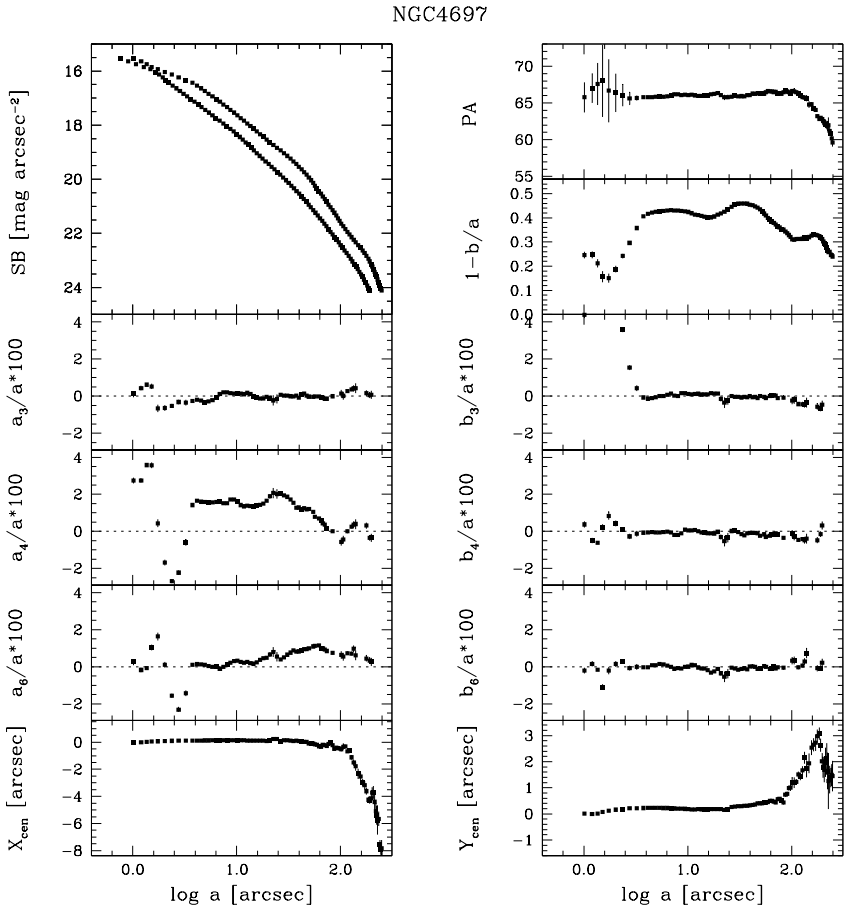

Figure B.1: Isophotal parameters of NGC 4697 as a function of the logarithm of the semi-major axis distance in arcsec. The radial profiles of the R-band surface brightness, third, fourth, and sixth cosine Fourier coefficients (a_3, a_4, and a_6), and $x-$coordinate of the center X_{cen} are plotted in the left panels (from top to bottom). The surface brightness is shown along the major (upper profile) and minor axis (lower profile). The radial profiles of the position angle (PA), ellipticity ($1 - b/a$), third fourth, and sixth sine Fourier coefficients (b_3, b_4, and b_6), and $y-$coordinate of the center (Y_{cen}) are plotted in the right panels (from top to bottom).

Table B.1: Photometric parameters of NGC 4697

a [arcsec]	μ_R^a [mag arcsec^{-2}]	e	PA [°]	Δx_c [arcsec]	Δy_c [arcsec]	Err.^{b} [arcsec]	a_3/a ×100	b_3/a ×100	a_4/a ×100	b_4/a ×100	a_6/a ×100	b_6/a ×100	Err.^{c}
1.013 ± 0.013	15.515± 0.006	0.246± 0.013	65.8± 2.0	-0.012	0.007	0.009	0.110	4.380	2.750	0.380	0.260	-0.210	0.162
1.201 ± 0.014	15.635± 0.008	0.247± 0.013	67.0± 2.0	0.000	0.000	0.010	0.430	4.850	2.750	-0.490	-0.180	0.160	0.123
1.359 ± 0.020	15.753± 0.007	0.212± 0.017	67.6± 2.9	0.019	0.019	0.014	0.620	6.790	3.580	-0.610	-0.080	-0.160	0.080
1.517 ± 0.029	15.847± 0.008	0.157± 0.023	68.0± 4.9	0.045	0.071	0.020	0.520	9.620	3.570	0.240	1.030	-1.090	0.151
1.739 ± 0.028	15.929± 0.008	0.151± 0.019	66.7± 4.3	0.069	0.129	0.020	-0.660	8.320	0.440	0.840	1.630	-0.200	0.206
2.023 ± 0.025	16.030± 0.006	0.188± 0.014	66.4± 2.6	0.083	0.162	0.018	-0.650	6.000	-1.680	0.440	0.100	0.160	0.154
2.365 ± 0.021	16.134± 0.005	0.242± 0.009	66.0± 1.5	0.095	0.190	0.015	-0.540	3.580	-2.690	0.130	-1.570	0.300	0.112
2.759 ± 0.017	16.233± 0.004	0.297± 0.006	65.6± 0.8	0.100	0.212	0.012	-0.320	1.540	-2.220	-0.270	-2.310	-0.070	0.114
3.235 ± 0.009	16.333± 0.003	0.358± 0.003	65.7± 0.3	0.109	0.221	0.007	-0.340	0.430	-0.600	-0.120	-1.430	-0.010	0.158
3.747 ± 0.007	16.436± 0.002	0.406± 0.001	65.8± 0.2	0.112	0.226	0.005	-0.260	-0.070	1.420	-0.070	0.100	-0.030	0.023
4.138 ± 0.008	16.537± 0.002	0.417± 0.002	65.8± 0.2	0.114	0.228	0.006	-0.200	-0.140	1.650	-0.060	0.140	-0.030	0.020
4.525 ± 0.008	16.637± 0.002	0.422± 0.001	65.8± 0.2	0.119	0.228	0.006	-0.250	-0.110	1.600	-0.030	0.130	0.080	0.023
4.932 ± 0.009	16.737± 0.002	0.425± 0.001	65.8± 0.2	0.126	0.228	0.006	-0.360	-0.060	1.590	-0.050	0.110	0.080	0.025
5.363 ± 0.009	16.837± 0.002	0.426± 0.001	65.9± 0.2	0.126	0.228	0.006	-0.290	-0.000	1.560	-0.050	0.040	0.150	0.027
5.835 ± 0.009	16.937± 0.002	0.428± 0.001	65.8± 0.2	0.133	0.226	0.006	-0.210	0.010	1.570	-0.030	-0.000	0.130	0.034
6.345 ± 0.010	17.037± 0.002	0.430± 0.001	65.9± 0.1	0.133	0.224	0.007	-0.070	0.080	1.590	-0.020	-0.010	0.070	0.034
6.881 ± 0.011	17.137± 0.002	0.431± 0.001	66.1± 0.1	0.138	0.217	0.007	0.120	0.130	1.620	-0.070	-0.110	-0.020	0.029
7.444 ± 0.011	17.237± 0.001	0.431± 0.001	66.2± 0.1	0.145	0.210	0.008	0.210	0.040	1.520	-0.190	-0.010	-0.110	0.039
8.056 ± 0.012	17.337± 0.001	0.430± 0.001	66.2± 0.1	0.138	0.210	0.008	0.210	0.000	1.530	-0.190	0.120	-0.070	0.039
8.706 ± 0.014	17.437± 0.001	0.428± 0.001	66.1± 0.2	0.138	0.198	0.010	0.160	0.160	1.720	-0.110	0.210	-0.090	0.038
9.398 ± 0.016	17.536± 0.001	0.427± 0.001	66.1± 0.2	0.138	0.193	0.011	0.150	0.150	1.720	0.100	0.300	-0.010	0.059
10.136 ± 0.016	17.635± 0.001	0.424± 0.001	66.1± 0.2	0.140	0.186	0.011	0.160	0.120	1.610	0.060	0.320	0.000	0.044
10.900 ± 0.015	17.736± 0.001	0.419± 0.001	66.2± 0.1	0.138	0.176	0.011	0.150	0.090	1.420	0.060	0.260	0.090	0.039
11.706 ± 0.015	17.837± 0.001	0.414± 0.001	66.0± 0.1	0.131	0.174	0.011	0.110	0.110	1.360	0.080	0.210	0.080	0.031
12.598 ± 0.017	17.937± 0.001	0.411± 0.001	66.0± 0.1	0.112	0.181	0.012	0.170	0.130	1.400	0.020	0.250	-0.040	0.052
13.531 ± 0.018	18.036± 0.001	0.407± 0.001	66.0± 0.1	0.117	0.176	0.013	0.110	0.080	1.360	-0.060	0.200	-0.090	0.039
14.530 ± 0.018	18.136± 0.001	0.405± 0.001	66.0± 0.1	0.119	0.174	0.013	0.010	0.090	1.320	-0.070	0.160	-0.100	0.028
15.595 ± 0.022	18.236± 0.001	0.403± 0.001	66.1± 0.1	0.121	0.178	0.016	-0.070	0.100	1.420	-0.090	0.250	-0.190	0.030
16.761 ± 0.027	18.335± 0.001	0.402± 0.001	66.2± 0.2	0.107	0.188	0.019	-0.130	0.160	1.430	-0.110	0.370	-0.320	0.050
18.038 ± 0.029	18.435± 0.001	0.405± 0.001	66.2± 0.2	0.105	0.193	0.021	-0.130	0.140	1.500	-0.110	0.470	-0.260	0.039
19.477 ± 0.034	18.537± 0.001	0.413± 0.001	66.4± 0.2	0.088	0.193	0.024	-0.050	0.140	1.660	-0.020	0.490	-0.120	0.034
20.955 ± 0.049	18.637± 0.001	0.419± 0.002	66.1± 0.2	0.157	0.181	0.035	-0.100	-0.140	1.890	-0.300	0.670	-0.350	0.130
22.554 ± 0.074	18.735± 0.001	0.425± 0.003	65.8± 0.3	0.248	0.162	0.053	-0.230	-0.350	2.070	-0.520	0.790	-0.540	0.270
24.352 ± 0.078	18.835± 0.001	0.433± 0.003	65.8± 0.3	0.228	0.186	0.055	-0.150	-0.220	2.020	-0.340	0.540	-0.380	0.254
26.452 ± 0.056	18.936± 0.001	0.446± 0.002	65.9± 0.2	0.093	0.264	0.040	0.070	-0.000	2.070	0.020	0.400	-0.050	0.070
28.543 ± 0.057	19.036± 0.001	0.453± 0.001	66.0± 0.2	0.150	0.274	0.040	0.030	-0.040	1.940	0.080	0.510	-0.090	0.077
30.687 ± 0.060	19.135± 0.001	0.458± 0.001	65.9± 0.2	0.147	0.290	0.042	0.020	-0.050	1.870	-0.040	0.650	-0.150	0.059
32.840 ± 0.060	19.236± 0.001	0.459± 0.001	65.9± 0.2	0.124	0.302	0.042	-0.010	-0.070	1.720	-0.140	0.760	-0.120	0.044
35.061 ± 0.062	19.336± 0.001	0.459± 0.001	65.9± 0.2	0.088	0.312	0.044	-0.020	-0.040	1.550	-0.210	0.880	-0.090	0.045
37.385 ± 0.059	19.435± 0.001	0.458± 0.001	66.1± 0.1	0.102	0.314	0.042	0.030	-0.060	1.280	-0.100	0.810	-0.140	0.066
39.678 ± 0.060	19.536± 0.001	0.455± 0.001	66.1± 0.1	0.078	0.326	0.042	-0.080	0.010	1.290	-0.080	0.830	0.020	0.050
42.182 ± 0.066	19.635± 0.001	0.453± 0.001	66.3± 0.1	0.074	0.343	0.046	0.070	-0.060	1.190	-0.070	0.860	0.020	0.071
44.663 ± 0.072	19.734± 0.001	0.448± 0.001	66.3± 0.2	0.028	0.359	0.051	0.140	-0.040	1.250	-0.070	0.940	-0.000	0.062
47.108 ± 0.073	19.834± 0.001	0.442± 0.001	66.3± 0.1	0.010	0.402	0.052	0.020	-0.100	1.190	-0.100	0.950	-0.120	0.074
49.534 ± 0.078	19.934± 0.001	0.436± 0.001	66.3± 0.2	-0.088	0.409	0.055	-0.030	0.010	1.210	-0.240	1.000	-0.110	0.045

a [arcsec]	μ_R^a [mag arcsec^{-2}]	e	PA [°]	Δx_c [arcsec]	Δy_c [arcsec]	Err.^{b} [arcsec]	a_3/a $\times100$	b_3/a $\times100$	a_4/a $\times100$	b_4/a $\times100$	a_6/a $\times100$	b_6/a $\times100$	Err.^{c}
51.950 ± 0.083	20.036± 0.001	0.428± 0.001	66.4± 0.2	-0.119	0.402	0.059	...	...	...	...	...	...	0.045
54.308 ± 0.087	20.135± 0.001	0.417± 0.001	66.2± 0.2	-0.098	0.459	0.062	-0.040	-0.040	1.060	-0.160	1.090	0.030	0.062
56.753 ± 0.092	20.235± 0.001	0.409± 0.001	66.5± 0.2	-0.167	0.424	0.065	-0.020	-0.110	0.790	-0.290	1.130	-0.020	0.065
59.253 ± 0.092	20.336± 0.001	0.399± 0.001	66.6± 0.2	-0.198	0.452	0.065	...	...	...	...	...	...	0.065
62.028 ± 0.092	20.436± 0.001	0.393± 0.001	66.6± 0.2	-0.298	0.502	0.065	-0.010	0.000	0.700	-0.240	1.150	-0.130	0.059
64.741 ± 0.082	20.536± 0.001	0.385± 0.001	66.6± 0.1	-0.345	0.505	0.058	-0.050	0.040	0.570	-0.160	0.960	-0.100	0.068
67.520 ± 0.078	20.635± 0.001	0.379± 0.001	66.5± 0.1	-0.205	0.476	0.055	-0.090	0.050	0.440	-0.190	0.990	0.010	0.048
70.445 ± 0.085	20.734± 0.001	0.372± 0.001	66.5± 0.1	-0.219	0.438	0.060	-0.140	0.030	0.360	-0.110	0.920	-0.090	0.064
73.422 ± 0.090	20.834± 0.001	0.364± 0.001	66.3± 0.1	-0.279	0.567	0.064	-0.140	-0.110	0.140	-0.170	0.850	-0.040	0.078
76.678 ± 0.085	20.936± 0.001	0.360± 0.001	66.4± 0.1	-0.140	0.583	0.060	...	...	...	...	...	...	0.078
80.086 ± 0.093	21.037± 0.001	0.354± 0.001	66.3± 0.1	-0.050	0.497	0.066	...	...	...	...	...	...	0.078
83.687 ± 0.109	21.138± 0.001	0.351± 0.001	66.4± 0.2	-0.228	0.436	0.077	-0.010	-0.080	0.010	-0.350	0.750	-0.060	0.094
87.231 ± 0.101	21.239± 0.001	0.344± 0.001	66.7± 0.1	-0.502	0.738	0.071	...	...	...	...	...	...	0.094
90.680 ± 0.120	21.339± 0.001	0.336± 0.001	66.6± 0.2	-0.398	0.769	0.085	...	...	...	...	...	...	0.094
94.336 ± 0.135	21.439± 0.001	0.329± 0.001	66.4± 0.2	-0.445	0.992	0.096	...	...	...	...	...	...	0.094
98.111 ± 0.165	21.538± 0.001	0.321± 0.002	66.3± 0.2	-0.457	1.004	0.117	...	...	...	...	...	...	0.094
101.661 ± 0.232	21.637± 0.001	0.311± 0.002	66.6± 0.3	-0.509	1.214	0.164	0.140	-0.240	-0.560	-0.110	0.640	0.340	0.200
105.981 ± 0.288	21.737± 0.001	0.309± 0.003	66.6± 0.4	-0.347	1.197	0.203	0.020	-0.200	-0.440	-0.260	0.540	0.340	0.210
111.325 ± 0.162	21.841± 0.001	0.312± 0.001	66.4± 0.2	-0.319	1.230	0.115	...	...	...	...	...	...	0.210
116.502 ± 0.166	21.944± 0.001	0.313± 0.001	66.3± 0.2	-0.664	1.511	0.117	0.270	-0.430	0.000	-0.450	0.740	-0.040	0.092
121.793 ± 0.201	22.043± 0.001	0.313± 0.002	66.1± 0.2	-0.652	1.433	0.142	...	...	...	...	...	...	0.092
127.455 ± 0.218	22.138± 0.001	0.313± 0.002	65.8± 0.2	-1.119	1.668	0.154	0.370	-0.440	0.260	-0.410	0.710	0.070	0.099
133.917 ± 0.324	22.234± 0.001	0.318± 0.002	65.7± 0.3	-1.509	2.154	0.229	0.420	-0.440	0.370	-0.480	0.970	0.290	0.170
139.843 ± 0.460	22.331± 0.001	0.314± 0.003	65.7± 0.4	-1.775	1.725	0.325	0.430	-0.340	0.400	-0.400	0.620	0.720	0.265
147.198 ± 0.536	22.430± 0.001	0.320± 0.003	64.8± 0.5	-2.335	1.937	0.379	...	...	...	...	...	...	0.265
155.523 ± 0.400	22.533± 0.001	0.326± 0.002	64.8± 0.3	-2.535	2.537	0.283	...	...	...	...	...	...	0.265
163.016 ± 0.359	22.633± 0.001	0.329± 0.002	64.2± 0.3	-2.982	2.651	0.254	...	...	...	...	...	...	0.265
170.075 ± 0.429	22.728± 0.001	0.329± 0.002	64.1± 0.3	-3.165	2.720	0.304	...	...	...	...	...	...	0.265
177.623 ± 0.365	22.827± 0.001	0.328± 0.002	63.2± 0.2	-3.611	2.977	0.258	0.160	-0.570	0.320	-0.470	0.440	-0.080	0.163
185.102 ± 0.334	22.934± 0.001	0.325± 0.002	62.8± 0.2	-4.251	3.075	0.237	...	...	...	...	...	...	0.163
190.987 ± 0.358	23.036± 0.001	0.320± 0.002	63.0± 0.2	-4.284	2.625	0.253	0.040	-0.670	-0.350	-0.140	0.320	-0.070	0.153
196.718 ± 0.432	23.132± 0.001	0.312± 0.002	62.8± 0.3	-4.146	2.013	0.305	0.070	-0.470	-0.350	0.330	0.260	0.220	0.200
202.089 ± 0.559	23.227± 0.001	0.303± 0.003	62.5± 0.4	-3.715	1.787	0.395	...	...	...	...	...	...	0.200
207.354 ± 0.675	23.323± 0.001	0.294± 0.003	62.2± 0.5	-3.703	1.692	0.478	...	...	...	...	...	...	0.200
212.802 ± 0.787	23.421± 0.001	0.290± 0.004	62.1± 0.5	-4.401	1.973	0.556	...	...	...	...	...	...	0.200
217.940 ± 0.851	23.521± 0.001	0.277± 0.004	62.0± 0.6	-5.084	2.106	0.602	...	...	...	...	...	...	0.200
222.191 ± 0.996	23.613± 0.001	0.266± 0.005	61.8± 0.7	-5.386	1.642	0.704	...	...	...	...	...	...	0.200
226.618 ± 1.524	23.707± 0.001	0.258± 0.007	62.0± 1.1	-5.745	1.259	1.078	...	...	...	...	...	...	0.200
233.406 ± 0.749	23.815± 0.001	0.260± 0.003	61.2± 0.5	-5.653	1.309	0.529	...	...	...	...	...	...	0.200
238.734 ± 0.519	23.925± 0.001	0.247± 0.002	60.9± 0.4	-7.590	1.397	0.367	...	...	...	...	...	...	0.200
243.821 ± 0.590	24.020± 0.001	0.246± 0.003	60.2± 0.4	-7.878	1.488	0.417	...	...	...	...	...	...	0.200
247.975 ± 0.827	24.104± 0.001	0.240± 0.004	59.6± 0.6	-7.811	1.447	0.585	...	...	...	...	...	...	0.200
253.321 ± 0.972	24.189± 0.001	0.245± 0.004	59.4± 0.6	-7.540	1.035	0.687	...	...	...	...	...	...	0.200

[a] Statistical errors not including systematics due to photometric calibration and sky subtraction .

[b] Error on the center coordinates from the residual rms of the ellipse fit to the isophotes: Err=rms(fit)/$\sqrt{N}$ with $N \leq 128$ the number of fitted points of the isophotes.

[c] Error of Fourier coefficients defined as Err= $\sqrt{\frac{\sum_{i=10}^{N/2}(a_i^2+b_i^2)}{N/2-10}} \times \frac{100}{a}$.

Table B.1: The kinematics of NGC 4697 along the major axis (P.A.=66°). Positive radii are to the north-east.

R (")	V (km/s)	dV (km/s)	σ (km/s)	$d\sigma$ (km/s)	h_3	dh_3	h_4	dh_4
0.38	-13.2	0.4	180.0	0.4	-0.004	0.002	0.007	0.002
0.97	-39.5	0.2	175.3	0.4	0.027	0.002	0.014	0.002
1.57	-51.8	0.2	174.4	0.4	0.041	0.002	0.017	0.002
2.27	-70.1	0.3	169.4	0.4	0.049	0.002	0.029	0.002
3.16	-83.1	0.3	163.4	0.4	0.08	0.002	0.037	0.002
4.26	-89.9	0.3	160.6	0.4	0.095	0.002	0.034	0.002
5.55	-93.8	0.4	157.9	0.5	0.105	0.003	0.037	0.003
7.14	-97.3	0.4	162.3	0.5	0.12	0.002	0.036	0.002
9.22	-94.2	0.4	163.3	0.6	0.096	0.002	0.019	0.003
12.00	-96.6	0.4	166.3	0.5	0.093	0.002	0.010	0.002
15.67	-95.5	0.4	170.5	0.6	0.080	0.002	0.004	0.003
20.63	-114.1	0.6	160.3	0.8	0.150	0.003	0.022	0.004
27.62	-109.1	0.6	157.8	0.8	0.140	0.003	-0.016	0.004
38.07	-115.1	0.7	151.9	1.0	0.122	0.004	-0.003	0.005
58.05	-108.6	1.0	143.2	1.4	0.122	0.006	-0.029	0.007
92.52	-111.5	2.9	140.9	3.7	-0.017	0.020	-0.082	0.015
-0.22	7.0	0.4	179.6	0.4	-0.024	0.002	0.015	0.002
-0.81	31.3	0.3	177.0	0.4	-0.042	0.002	0.026	0.001
-1.41	51.9	0.3	173.3	0.4	-0.061	0.002	0.029	0.001
-2.11	70.1	0.3	169.0	0.5	-0.072	0.002	0.045	0.002
-3.00	85.6	0.3	163.4	0.5	-0.100	0.002	0.052	0.002
-4.00	92.8	0.3	161.8	0.3	-0.112	0.001	0.034	0.002
-5.19	93.6	0.3	162.7	0.3	-0.112	0.001	0.041	0.002
-6.69	98.0	0.3	160.3	0.3	-0.135	0.001	0.043	0.002
-8.57	96.0	0.3	159.1	0.3	-0.114	0.001	0.034	0.002
-11.05	98.3	0.3	165.8	0.3	-0.131	0.001	0.030	0.002
-14.32	93.2	0.3	172.2	0.3	-0.126	0.001	-0.014	0.002
-18.79	103.9	0.3	172.1	0.3	-0.145	0.001	-0.011	0.002
-24.99	112.6	0.4	168.1	0.3	-0.170	0.002	0.005	0.002
-34	120.1	0.5	160.0	0.5	-0.168	0.002	-0.026	0.003
-48.87	113.7	0.7	152.5	0.6	-0.132	0.004	-0.018	0.004
-76.65	115.2	1.9	153.1	2.1	-0.087	0.012	-0.004	0.010

Table B.2: The kinematics of NGC 4697 along the minor axis (P.A.=156°). Positive radii are to the south-east.

R (")	V (km/s)	dV (km/s)	σ (km/s)	$d\sigma$ (km/s)	h_3	dh_3	h_4	dh_4
0.09	-1.3	0.2	186.3	0.2	-0.014	0.001	0.011	0.001
0.49	1.6	0.3	183.7	0.3	-0.001	0.001	0.006	0.001
1.00	2.3	0.1	179.8	0.1	-0.013	0.005	0.009	0.001
1.58	0.3	0.3	176.4	0.3	-0.007	0.001	0.005	0.001
2.27	1.6	0.3	177.9	0.3	0.001	0.001	0.037	0.001
3.25	-1.3	0.2	180.4	0.2	-0.001	0.001	0.030	0.001
4.73	4.1	0.3	184.3	0.3	-0.006	0.001	0.034	0.001
6.98	1.9	0.3	178.1	0.3	-0.019	0.001	0.015	0.001
10.66	-4.2	0.5	177.6	0.5	-0.022	0.002	0.023	0.002
17.37	5.2	0.7	175.9	0.7	-0.007	0.003	0.005	0.002
31.77	-4.6	1.4	173.2	1.4	-0.005	0.006	-0.012	0.005
-0.31	0.6	0.2	185.0	0.2	0.020	0.001	0.004	0.001
-0.80	1.0	0.1	181.9	0.1	0.018	0.005	0.006	0.001
-1.40	-1.4	0.2	176.5	0.2	0.018	0.001	0.021	0.001
-2.18	-0.8	0.3	178.9	0.3	0.013	0.001	0.027	0.001
-3.36	-1.9	0.3	176.7	0.3	-0.004	0.001	0.023	0.001
-5.13	-0.8	0.3	175.0	0.3	0.020	0.001	0.018	0.001
-7.95	1.0	0.4	175.2	0.5	0.020	0.002	0.050	0.002
-12.74	0.6	0.6	173.2	0.7	0.015	0.003	0.037	0.003
-22.55	1.9	0.9	169.7	1.0	0.017	0.004	-0.001	0.003
-49.42	4.4	2.1	158.1	2.3	0.001	0.010	-0.011	0.007

APPENDIX C

ABBREVIATIONS

Abbreviation	Meaning
CCD	Charge Coupled Device
CBE	Collisionless Boltzmann Equation
CDM	Cold Dark Matter
CIC	Cloud in cell
CMB	Cosmic Microwave Background
DF	Distribution Function
DM	Dark Matter
F77	FORTRAN 77
F90	FORTRAN 90
FCQ	Fourier Correlation Quotient
FFT	Fast Fourier Transform
FP	Fundamental Plane
FQ	Fourier Quotient
FWHM	Full Width at Half Maximum
LOS	Line-of-Sight
LOSVD	Line-of-Sight Velocity Profile
MPI	Message Passing Interface
M2M	Made-to-Measure
NGC	New General Catalogue
NMAGIC	N-particle Made-to-measure AlGorithm mInimizing Chi squared
PN	Planetary nebula
PN.S	Planetary Nebula Spectrograph
PSF	Point Spread Function
SB	Surface Brightness

BIBLIOGRAPHY

S. J. Aarseth. Dynamical evolution of clusters of galaxies, I. *MNRAS*, 126:223, 1963.

S. J. Aarseth. Direct methods for N-body simulations. In *Multiple time scales, p. 377 - 418*, page 377, 1985.

G. M. Amdahl. Validity of the single-processor approach to achieving large scale computing capabilities. In *AFIPS Conference Proceedings vol. 30 (Atlantic City, N.J., Apr. 18-20). AFIPS Press, Reston, Va.*, page 483, 1967.

M. Arnaboldi, K. C. Freeman, R. H. Mendez, M. Capaccioli, R. Ciardullo, H. Ford, O. Gerhard, X. Hui, G. H. Jacoby, R. P. Kudritzki, and P. J. Quinn. The Kinematics of the Planetary Nebulae in the Outer Regions of NGC 4406. *ApJ*, 472:145, 1996.

M. Arnaboldi, K. C. Freeman, O. Gerhard, M. Matthias, R. P. Kudritzki, R. H. Méndez, M. Capaccioli, and H. Ford. The Stellar Dynamics and Mass of NGC 1316 Using the Radial Velocities of Planetary Nebulae. *ApJ*, 507:759, 1998.

H. Awaki, R. Mushotzky, T. Tsuru, A. C. Fabian, Y. Fukazawa, M. Loewenstein, K. Makishima, H. Matsumoto, K. Matsushita, T. Mihara, T. Ohashi, G. R. Ricker, P. J. Serlemitsos, Y. Tsusaka, and T. Yamazaki. ASCA observation of three bright early-type galaxies: NGC 4472, NGC 4406, and NGC 4636. *PASJ*, 46:L65, 1994.

R. Bacon, Y. Copin, G. Monnet, B. W. Miller, J. R. Allington-Smith, M. Bureau, C. M. Carollo, R. L. Davies, E. Emsellem, H. Kuntschner, R. F. Peletier, E. K. Verolme, and P. T. de Zeeuw. The SAURON project - I. The panoramic integral-field spectrograph. *MNRAS*, 326:23, 2001.

J. E. Barnes. Galaxy Evolution - Making Ellipticals by Mergers. *Nature*, 344:379, 1990.

M. Bartelmann. Cluster mass estimates from weak lensing. *A&A*, 303:643, 1995.

K. Begemann. *HI rotation curves of spiral galaxies*. Groningen: Rijksuniversiteit, 1987, 1987.

R. Bender. Rotating and counter-rotating cores in elliptical galaxies. *A&A*, 202:L5, 1988.

R. Bender. Unraveling the kinematics of early-type galaxies - Presentation of a new method and its application to NGC4621. *A&A*, 229:441, 1990.

R. Bender and C. Moellenhoff. Morphological analysis of massive early-type galaxies in the Virgo cluster. *A&A*, 177:71, 1987.

R. Bender, S. Doebereiner, and C. Moellenhoff. Isophote shapes of elliptical galaxies. I - The data. *A&AS*, 74:385, 1988.

R. Bender, P. Surma, S. Doebereiner, C. Moellenhoff, and R. Madejsky. Isophote shapes of elliptical galaxies. II - Correlations with global optical, radio and X-ray properties. *A&A*, 217:35, 1989.

R. Bender, R. P. Saglia, and O. E. Gerhard. Line-of-Sight Velocity Distributions of Elliptical Galaxies. *MNRAS*, 269:785, 1994a.

R. Bender, R.P. Saglia, and O. Gerhard. Line-of-Sight Velocity Distributions of Elliptical Galaxies. *MNRAS*, 269:785, 1994b.

B. Binggeli. On the intrinsic shape of elliptical galaxies. *A&A*, 82:289, 1980.

J. Binney and G. A. Mamon. M/L and velocity anisotropy from observations of spherical galaxies, or must M87 have a massive black hole. *MNRAS*, 200:361, 1982.

J. Binney and M. Merrifield. *Galactic astronomy*. Princeton, NJ, Princeton University Press, 1998.

J. Binney and S. Tremaine. *Galactic Dynamics*. Princeton, NJ, Princeton University Press, 1987.

J. J. Binney, R. L. Davies, and G. D. Illingworth. Velocity mapping and models of the elliptical galaxies NGC 720, NGC 1052, and NGC 4697. *ApJ*, 361:78, 1990.

J. L. Bishop. Axisymmetric shell models with Staeckel potentials. *ApJ*, 322:618, 1987.

N. Bissantz, V. P. Debattista, and O. Gerhard. Large-Scale Model of the Milky Way: Stellar Kinematics and the Microlensing Event Timescale Distribution in the Galactic Bulge. *ApJ*, 601:L155, 2004.

R. G. Bower, J. R. Lucey, and R. S. Ellis. Precision Photometry of Early Type Galaxies in the Coma and Virgo Clusters - a Test of the Universality of the Colour / Magnitude Relation - Part Two - Analysis. *MNRAS*, 254:601, 1992.

J. S. Bullock, T. S. Kolatt, Y. Sigad, R. S. Somerville, A. V. Kravtsov, A. A. Klypin, J. R. Primack, and A. Dekel. Profiles of dark haloes: evolution, scatter and environment. *MNRAS*, 321:559, 2001.

D. Burstein, V. C. Rubin, N. Thonnard, and W. K. Ford, Jr. The distribution of mass in SC galaxies. *ApJ*, 253:70, 1982.

M. Capaccioli, E. V. Held, H. Lorenz, and M. Vietri. Photographic and CCD surface photometry of the standard elliptical galaxy NGC 3379. *AJ*, 99:1813, 1990.

M. Capaccioli, M. Vietri, E. V. Held, and H. Lorenz. Is the standard elliptical NGC 3379 a triaxial disk galaxy? *ApJ*, 371:535, 1991.

M. Cappellari, E. K. Verolme, R. P. van der Marel, G. A. V. Kleijn, G. D. Illingworth, M. Franx, C. M. Carollo, and P. T. de Zeeuw. The Counterrotating Core and the Black Hole Mass of IC 1459. *ApJ*, 578:787, 2002.

M. Cappellari, R. Bacon, M. Bureau, M. C. Damen, R. L. Davies, P. T. de Zeeuw, E. Emsellem, J. Falcón-Barroso, D. Krajnović, H. Kuntschner, R. M. McDermid, R. F. Peletier, M. Sarzi, R. C. E. van den Bosch, and G. van de Ven. The SAURON project - IV. The mass-to-light ratio, the virial mass estimator and the Fundamental Plane of elliptical and lenticular galaxies. *MNRAS*, 366:1126, 2006.

M. Cappellari, E. Emsellem, R. Bacon, M. Bureau, R. L. Davies, P. T. de Zeeuw, J. Falcón-Barroso, D. Krajnović, H. Kuntschner, R. M. McDermid, R. F. Peletier, M. Sarzi, R. C. E. van den Bosch, and G. van de Ven. The SAURON project - X. The orbital anisotropy of elliptical and lenticular galaxies: revisiting the (V/σ, ϵ) diagram with integral-field stellar kinematics. *MNRAS*, 379:418, 2007.

C. M. Carollo, P. T. de Zeeuw, and R. P. van der Marel. Velocity profiles of Osipkov-Merritt models. *MNRAS*, 276:1131, 1995.

D. Carter. The structure of the isophotes of elliptical galaxies. *MNRAS*, 182:797, 1978.

D. Carter. Weak disks in rapidly rotating elliptical galaxies. *ApJ*, 312:514, 1987.

J. Chanamé, J. Kleyna, and R. van der Marel. Constraining the Mass Profiles of Stellar Systems: Schwarzschild Modeling of Discrete Velocity Datasets. *ArXiv e-prints*, 710, 2007.

R. Ciardullo, G. H. Jacoby, and H. B. Dejonghe. The radial velocities of planetary nebulae in NGC 3379. *ApJ*, 414:454, 1993.

P. Cinzano and R. P. van der Marel. Photometric Disk-Bulge Decomposition, Line Profile Analysis and Dynamical Modelling of the Elliptical Galaxy NGC 2974. In I. J. Danziger, W. W. Zeilinger, and K. Kjaer, editors, *Structure, Dynamics and Chemical Evolution of Elliptical Galaxies*, page 105, 1993.

Y. Copin, N. Cretton, and E. Emsellem. Axisymmetric dynamical models for SAURON and OASIS observations of NGC3377. *A&A*, 415:889, 2004.

N. Cretton, P. T. de Zeeuw, R. P. van der Marel, and H.-W. Rix. Axisymmetric Three-Integral Models for Galaxies. *ApJS*, 124:383, 1999.

W. J. G. de Blok, A. Bosma, and S. McGaugh. Simulating observations of dark matter dominated galaxies: towards the optimal halo profile. *MNRAS*, 340:657, 2003.

V. De Bruyne, F. Leeuwin, and H. Dejonghe. Approximate third integrals for axisymmetric potentials using local Stäckel fits. *MNRAS*, 311:297, 2000.

F. De Lorenzi, V. P. Debattista, and O. E. Gerhard. Dynamics of Rotating Elliptical Galaxies. In L. Stanghellini, J. R. Walsh, and N. G. Douglas, editors, *Planetary Nebulae Beyond the Milky Way*, page 311, 2006.

F. de Lorenzi, V. P. Debattista, O. Gerhard, and N. Sambhus. NMAGIC: a fast parallel implementation of a χ^2-made-to-measure algorithm for modelling observational data. *MNRAS*, 376:71, 2007.

F. de Lorenzi, O. Gerhard, R.P. Saglia, N. Sambhus, V. P. Debattista, M. Pannella, and R.H. Méndez. Dark matter content and internal dynamics of NGC 4607: NMAGIC particle models from slit data and planetary nebulae velocities. *MNRAS*, 2008. submitted.

G. de Vaucouleurs. Recherches sur les Nebuleuses Extragalactiques. *Annales d'Astrophysique*, 11:247, 1948.

V. P. Debattista. The Interaction of Dark Matter with Galaxy Disks: Bars and WARPS. *Ph.D. Thesis*, 1998.

V. P. Debattista and J. A. Sellwood. Constraints from Dynamical Friction on the Dark Matter Content of Barred Galaxies. *ApJ*, 543:704, 2000.

W. Dehnen. A Family of Potential-Density Pairs for Spherical Galaxies and Bulges. *MNRAS*, 265:250, 1993.

W. Dehnen and O. E. Gerhard. Three-integral models of oblate elliptical galaxies. *MNRAS*, 261:311, 1993.

W. Dehnen and O. E. Gerhard. Two-Integral Models for Oblate Elliptical Galaxies with Cusps. *MNRAS*, 268:1019, 1994.

H. Dejonghe. The construction of analytical models for globular clusters. *A&A*, 133:225, 1984.

H. Dejonghe. Stellar dynamics and the description of stellar systems. *Phys. Rep.*, 133:217, 1986.

H. Dejonghe and T. de Zeeuw. Analytic axisymmetric galaxy models with three integrals of motion. *ApJ*, 333:90, 1988.

H. Dejonghe and D. Merritt. Inferring the mass of spherical stellar systems from velocity moments. *ApJ*, 391:531, 1992.

H. Dejonghe, V. de Bruyne, P. Vauterin, and W. W. Zeilinger. The internal dynamics of very flattened normal galaxies. Stellar distribution functions for NGC 4697. *A&A*, 306:363, 1996.

A. Dekel, F. Stoehr, G. A. Mamon, T. J. Cox, G. S. Novak, and J. R. Primack. Lost and found dark matter in elliptical galaxies. *Nature*, 437:707, 2005.

S. Djorgovski and M. Davis. Fundamental properties of elliptical galaxies. *ApJ*, 313:59, 1987.

N. G. Douglas, M. Arnaboldi, K. C. Freeman, K. Kuijken, M. R. Merrifield, A. J. Romanowsky, K. Taylor, M. Capaccioli, T. Axelrod, R. Gilmozzi, J. Hart, G. Bloxham, and D. Jones. The Planetary Nebula Spectrograph: The Green Light for Galaxy Kinematics. *PASP*, 114:1234, 2002.

N. G. Douglas, N. R. Napolitano, A. J. Romanowsky, L. Coccato, K. Kuijken, M. R. Merrifield, M. Arnaboldi, O. Gerhard, K. C. Freeman, H. R. Merrett, E. Noordermeer, and M. Capaccioli. The PN.S Elliptical Galaxy Survey: Data Reduction, Planetary Nebula Catalog, and Basic Dynamics for NGC 3379. *ApJ*, 664:257, 2007.

A. Dressler. Galaxy morphology in rich clusters - Implications for the formation and evolution of galaxies. *ApJ*, 236:351, 1980.

A. Dressler, D. Lynden-Bell, D. Burstein, R. L. Davies, S. M. Faber, R. Terlevich, and G. Wegner. Spectroscopy and photometry of elliptical galaxies. I - A new distance estimator. *ApJ*, 313:42, 1987.

G. Efstathiou and J. W. Eastwood. On the clustering of particles in an expanding universe. *MNRAS*, 194:503, 1981.

S. M. Faber and R. E. Jackson. Velocity dispersions and mass-to-light ratios for elliptical galaxies. *ApJ*, 204:668, 1976.

S. M. Faber, A. Dressler, R. L. Davies, D. Burstein, and D. Lynden-Bell. Global scaling relations for elliptical galaxies and implications for formation. In S. M. Faber, editor, *Nearly Normal Galaxies. From the Planck Time to the Present*, page 175, 1987.

S. M. Faber, S. Tremaine, E. A. Ajhar, Y.-I. Byun, A. Dressler, K. Gebhardt, C. Grillmair, J. Kormendy, T. R. Lauer, and D. Richstone. The Centers of Early-Type Galaxies with HST. IV. Central Parameter Relations. *AJ*, 114:1771, 1997.

M. Franx and G. D. Illingworth. A counterrotating core in IC 1459. *ApJ*, 327:L55, 1988.

M. Franx, G. Illingworth, and T. de Zeeuw. The ordered nature of elliptical galaxies - Implications for their intrinsic angular momenta and shapes. *ApJ*, 383:112, 1991.

M. Franx, J. H. van Gorkom, and T. de Zeeuw. Evidence for axisymmetric halos: The case of IC 2006. *ApJ*, 436:642, 1994.

J.W. Fried and G. Illingworth. Kinematics of 12 elliptical galaxies. *AJ*, 107:992, 1994.

Y. Fukazawa, J. G. Botoya-Nonesa, J. Pu, A. Ohto, and N. Kawano. Scaling Mass Profiles around Elliptical Galaxies Observed with Chandra and XMM-Newton. *ApJ*, 636:698, 2006.

R. Fux. 3D self-consistent N-body barred models of the Milky Way. I. Stellar dynamics. *A&A*, 327:983, 1997.

R. Gavazzi, T. Treu, J. D. Rhodes, L. V. E. Koopmans, A. S. Bolton, S. Burles, R. Massey, and L. A. Moustakas. The Sloan Lens ACS Survey. IV: the mass density profile of early-type galaxies out to 100 effective radii. *ArXiv Astrophysics e-prints*, 2007.

K. Gebhardt, D. Richstone, E. A. Ajhar, T. R. Lauer, Y.-I. Byun, J. Kormendy, A. Dressler, S. M. Faber, C. Grillmair, and S. Tremaine. The Centers of Early-Type Galaxies With HST. III. Non-Parametric Recovery of Stellar Luminosity Distribution. *AJ*, 112:105, 1996.

K. Gebhardt, D. Richstone, J. Kormendy, T. R. Lauer, E. A. Ajhar, R. Bender, A. Dressler, S. M. Faber, C. Grillmair, J. Magorrian, and S. Tremaine. Axisymmetric, Three-Integral Models of Galaxies: A Massive Black Hole in NGC 3379. *AJ*, 119:1157, 2000.

K. Gebhardt, D. Richstone, S. Tremaine, T. R. Lauer, R. Bender, G. Bower, A. Dressler, S. M. Faber, A. V. Filippenko, R. Green, C. Grillmair, L. C. Ho, J. Kormendy, J. Magorrian, and J. Pinkney. Axisymmetric Dynamical Models of the Central Regions of Galaxies. *ApJ*, 583: 92, 2003.

O. Gerhard, G. Jeske, R. P. Saglia, and R. Bender. Breaking the degeneracy between anisotropy and mass - The dark halo of the E0 galaxy NGC 6703. *MNRAS*, 295:197, 1998.

O. Gerhard, A. Kronawitter, R. P. Saglia, and R. Bender. Dynamical Family Properties and Dark Halo Scaling Relations of Giant Elliptical Galaxies. *AJ*, 121:1936, 2001.

O. Gerhard, M. Arnaboldi, K. C. Freeman, S. Okamura, N. Kashikawa, and N. Yasuda. The kinematics of intracluster planetary nebulae and the on-going subcluster merger in the Coma cluster core. *A&A*, 468:815, 2007.

O. E. Gerhard. N-body simulations of disc-halo galaxies - Isolated systems, tidal interactions and merging. *MNRAS*, 197:179, 1981.

O. E. Gerhard. A quasi-stable stellar system with prolate inner and oblate outer parts. *MNRAS*, 202:1159, 1983a.

O. E. Gerhard. Intrinsic principal axes twists in N-body models of elliptical galaxies. *MNRAS*, 203:19P, 1983b.

O. E. Gerhard. A new family of distribution functions for spherical galaxies. *MNRAS*, 250:812, 1991.

O. E. Gerhard. Line-of-sight velocity profiles in spherical galaxies: breaking the degeneracy between anisotropy and mass. *MNRAS*, 265:213, 1993.

O. E. Gerhard. Elliptical galaxies. In G. Contopoulos, N. K. Spyrou, and L. Vlahos, editors, *Galactic Dynamics and N-Body Simulations*, volume 433 of *Lecture Notes in Physics, Berlin Springer Verlag*, page 191, 1994.

O. E. Gerhard and J. J. Binney. On the deprojection of axisymmetric bodies. *MNRAS*, 279:993, 1996.

P. Goudfrooij, L. Hansen, H. E. Jorgensen, H. U. Norgaard-Nielsen, T. de Jong, and L. B. van den Hoek. Interstellar matter in Shapley-Ames elliptical galaxies. I. Multicolour CCD surface photometry. *A&AS*, 104:179, 1994.

R. E. Griffiths, S. Casertano, M. Im, and K. U. Ratnatunga. Weak gravitational lensing around field galaxies in Hubble Space Telescope survey images. *MNRAS*, 282:1159, 1996.

M. Hénon. L'évolution initiale d'un amas sphérique. *Annales d'Astrophysique*, 27:83, 1964.

L. Hernquist. An analytical model for spherical galaxies and bulges. *ApJ*, 356:359, 1990.

L. Hernquist. Structure of merger remnants. I - Bulgeless progenitors. *ApJ*, 400:460, 1992.

L. Hernquist and J. P. Ostriker. A self-consistent field method for galactic dynamics. *ApJ*, 386: 375, 1992.

R. W. Hockney and D. R. K. Brownrigg. Effect of Population 11 stars and three-dimensional motion on spiral structure. *MNRAS*, 167:351, 1974.

R. W. Hockney and J. W. Eastwood. *Computer simulation using particles*. Bristol: Hilger, 1988, 1988.

W. Hu and S. Dodelson. Cosmic Microwave Background Anisotropies. *ARA&A*, 40:171, 2002.

X. Hui, H. C. Ford, K. C. Freeman, and M. A. Dopita. The Planetary Nebula System and Dynamics of NGC 5128. III. Kinematics and Halo Mass Distributions. *ApJ*, 449:592, 1995.

P. J. Humphrey, D. A. Buote, F. Gastaldello, L. Zappacosta, J. S. Bullock, F. Brighenti, and W. G. Mathews. A Chandra View of Dark Matter in Early-Type Galaxies. *ApJ*, 646:899, 2006.

C. Hunter and P. T. de Zeeuw. Triaxial galaxy models with thin tube orbits. *ApJ*, 389:79, 1992.

C. Hunter and E. Qian. Two-integral distribution functions for axisymmetric galaxies. *MNRAS*, 262:401, 1993.

G. D. Illingworth and P. L. Schechter. Velocity and velocity dispersion profiles in NGC 3115. *ApJ*, 256:481, 1982.

J. A. Irwin, C. L. Sarazin, and J. N. Bregman. The X-Ray-faint Early-Type Galaxy NGC 4697. *ApJ*, 544:293, 2000.

J. D. Jackson. *Classical electrodynamics*. New York: Wiley, 1975, 2nd ed., 1975.

R. I. Jedrzejewski, R. L. Davies, and G. D. Illingworth. CCD surface photometry of the bright elliptical galaxies NGC 720, NGC 1052, and NGC 4697. *AJ*, 94:1508, 1987.

J. B. Jensen, J. L. Tonry, B. J. Barris, R. I. Thompson, M. C. Liu, M. J. Rieke, E. A. Ajhar, and J. P. Blakeslee. Measuring Distances and Probing the Unresolved Stellar Populations of Galaxies Using Infrared Surface Brightness Fluctuations. *ApJ*, 583:712, 2003.

E. Jourdeuil and E. Emsellem. Scalable N-body code for the modelling of early-type galaxies. *ArXiv e-prints*, 709, 2007.

A. J. Kalnajs. Dynamics of flat galaxies. IV - The integral equation for normal modes in matrix form. *ApJ*, 212:637, 1977.

S. M. Kent. Dark matter in spiral galaxies. I - Galaxies with optical rotation curves. *AJ*, 91: 1301, 1986.

C. S. Kochanek and G. B. Rybicki. Deprojection of axially symmetric objects. *MNRAS*, 280: 1257, 1996.

L. V. E. Koopmans, T. Treu, A. S. Bolton, S. Burles, and L. A. Moustakas. The Sloan Lens ACS Survey. III. The Structure and Formation of Early-Type Galaxies and Their Evolution since z ˜ 1. *ApJ*, 649:599, 2006.

W. Koprolin, A., and W. Zeilinger. Line-of-sight velocity distributions of 53 early-type galaxies. *A&AS*, 145:71, 2000.

A. Kronawitter, R. P. Saglia, O. Gerhard, and R. Bender. Orbital structure and mass distribution in elliptical galaxies. *A&AS*, 144:53, 2000.

K. Kuijken. An Axisymmetric Distribution Function for the Galactic Bulge. *ApJ*, 446:194, 1995.

K. Kuijken and J. Dubinski. Nearly Self-Consistent Disc / Bulge / Halo Models for Galaxies. *MNRAS*, 277:1341, 1995.

K. Kuijken and M. R. Merrifield. A New Method for Obtaining Stellar Velocity Distributions from Absorption-Line Spectra - Unresolved Gaussian Decomposition. *MNRAS*, 264:712, 1993.

T. R. Lauer, E. A. Ajhar, Y.-I. Byun, A. Dressler, S. M. Faber, C. Grillmair, J. Kormendy, D. Richstone, and S. Tremaine. The Centers of Early-Type Galaxies with HST.I.An Observational Survey. *AJ*, 110:2622, 1995.

F. Leeuwin, F. Combes, and J. Binney. N-body simulations with perturbation particles. I - Method and tests. *MNRAS*, 262:1013, 1993.

M. Loewenstein and R. E. White, III. Prevalence and Properties of Dark Matter in Elliptical Galaxies. *ApJ*, 518:50, 1999.

L. B. Lucy. An iterative technique for the rectification of observed distributions. *AJ*, 79:745, 1974.

D. Lynden-Bell. Can spherical clusters rotate? *MNRAS*, 120:204, 1960.

D. Lynden-Bell. Stellar dynamics: Exact solution of the self-gravitation equation. *MNRAS*, 123: 447, 1962.

J. Magorrian. Grommet: an N-body code for high-resolution simulations of individual galaxies. *ArXiv Astrophysics e-prints*, 2007.

J. Magorrian. Reconstructing Two-Integral Distribution Functions from Moments. *MNRAS*, 277:1185, 1995.

J. Magorrian. Kinematical signatures of hidden stellar discs. *MNRAS*, 302:530, 1999.

J. Magorrian and D. Ballantyne. Mass profiles and anisotropies of early-type galaxies. *MNRAS*, 322:702, 2001.

J. Magorrian and J. Binney. Predicting line-of-sight velocity distributions of elliptical galaxies. *MNRAS*, 271:949, 1994.

D. F. Malin and D. Carter. A catalog of elliptical galaxies with shells. *ApJ*, 274:534, 1983.

K. Matsushita, K. Makishima, Y. Ikebe, E. Rokutanda, N. Yamasaki, and T. Ohashi. Largely Extended X-Ray Emission Around the Elliptical Galaxy NGC 4636 Observed with ASCA. *ApJ*, 499:L13, 1998.

M. Matthias and O. Gerhard. Dynamics of the boxy elliptical galaxy NGC 1600. *MNRAS*, 310: 879, 1999.

S. S. McGaugh, W. J. G. de Blok, J. M. Schombert, R. Kuzio de Naray, and J. H. Kim. The Rotation Velocity Attributable to Dark Matter at Intermediate Radii in Disk Galaxies. *ApJ*, 659:149, 2007.

T. A. McGlynn. Dissipationless collapse of galaxies and initial conditions. *ApJ*, 281:13, 1984.

D. Mehlert, R.P. Saglia, R. Bender, and G. Wegner. Spatially resolved spectroscopy of Coma cluster early-type galaxies. I. The database. *A&AS*, 141:449, 2000.

Y. Mellier, B. Fort, and J.-P. Kneib. The dark matter distribution in MS 2137-23 from the modeling of the multiple arc systems. *ApJ*, 407:33, 1993.

R. H. Méndez, A. Riffeser, R.-P. Kudritzki, M. Matthias, K. C. Freeman, M. Arnaboldi, M. Capaccioli, and O. E. Gerhard. Detection, Photometry, and Slitless Radial Velocities of 535 Planetary Nebulae in the Flattened Elliptical Galaxy NGC 4697. *ApJ*, 563:135, 2001.

R. H. Méndez, D. Thomas, R. P. Saglia, C. Maraston, R. P. Kudritzki, and R. Bender. Oxygen and Neon Abundances of Planetary Nebulae in the Elliptical Galaxy NGC 4697. *ApJ*, 627: 767, 2005.

H. R. Merrett, K. Kuijken, M. R. Merrifield, A. J. Romanowsky, N. G. Douglas, N. R. Napolitano, M. Arnaboldi, M. Capaccioli, K. C. Freeman, O. Gerhard, N. W. Evans, M. I. Wilkinson, C. Halliday, T. J. Bridges, and D. Carter. Tracing the star stream through M31 using planetary nebula kinematics. *MNRAS*, 346:L62, 2003.

D. Merritt. Dynamical mapping of hot stellar systems. *ApJ*, 413:79, 1993.

D. Merritt. The Dynamical Inverse Problem for Axisymmetric Stellar Systems. *AJ*, 112:1085, 1996.

B. Moore, F. Governato, T. Quinn, J. Stadel, and G. Lake. Resolving the Structure of Cold Dark Matter Halos. *ApJ*, 499:L5, 1998.

B. Moore, T. Quinn, F. Governato, J. Stadel, and G. Lake. Cold collapse and the core catastrophe. *MNRAS*, 310:1147, 1999.

T. Naab and A. Burkert. Statistical Properties of Collisionless Equal- and Unequal-Mass Merger Remnants of Disk Galaxies. *ApJ*, 597:893, 2003.

T. Naab, R. Jesseit, and A. Burkert. The influence of gas on the structure of merger remnants. *MNRAS*, 372:839, 2006.

N. R. Napolitano, M. Capaccioli, A. J. Romanowsky, N. G. Douglas, M. R. Merrifield, K. Kuijken, M. Arnaboldi, O. Gerhard, and K. C. Freeman. Mass-to-light ratio gradients in early-type galaxy haloes. *MNRAS*, 357:691, 2005.

J. F. Navarro, C. S. Frenk, and S. D. M. White. The Structure of Cold Dark Matter Halos. *ApJ*, 462:563, 1996.

J. F. Navarro, C. S. Frenk, and S. D. M. White. A Universal Density Profile from Hierarchical Clustering. *ApJ*, 490:493, 1997.

A. Ollongren. Three-dimensional galactic stellar orbits. *Bull. Astron. Inst. Netherlands*, 16:241, 1962.

T. A. Oosterloo, R. Morganti, E. M. Sadler, D. Vergani, and N. Caldwell. Extended H I Disks in Dust Lane Elliptical Galaxies. *AJ*, 123:729, 2002.

J. A. Peacock. *Cosmological Physics*. Cosmological Physics, by John A. Peacock, pp. 704. ISBN 052141072X. Cambridge, UK: Cambridge University Press, January 1999., 1999.

R. F. Peletier, R. L. Davies, G. D. Illingworth, L. E. Davis, and M. Cawson. CCD surface photometry of galaxies with dynamical data. II - UBR photometry of 39 elliptical galaxies. *AJ*, 100:1091, 1990.

M. Pierce, M. A. Beasley, D. A. Forbes, T. Bridges, K. Gebhardt, F. R. Faifer, J. C. Forte, S. E. Zepf, R. Sharples, D. A. Hanes, and R. Proctor. Gemini/GMOS spectra of globular clusters in the Leo group elliptical NGC 3379. *MNRAS*, 366:1253, 2006.

J. Pinkney, K. Gebhardt, D. Richstone, and Nuker Team. A black hole in NGC 4697 from stellar and gas kinematics. *Bulletin of the American Astronomical Society*, 32:1437, 2000.

J. Pinkney, K. Gebhardt, R. Bender, G. Bower, A. Dressler, S. M. Faber, A. V. Filippenko, R. Green, L. C. Ho, J. Kormendy, T. R. Lauer, J. Magorrian, D. Richstone, and S. Tremaine. Kinematics of 10 Early-Type Galaxies from Hubble Space Telescope and Ground-based Spectroscopy. *ApJ*, 596:903, 2003.

W. H. Press, S. A. Teukolsky, W. T. Vetterling, and B. P. Flannery. *Numerical recipes in FORTRAN. The art of scientific computing*. Cambridge: University Press, —c1992, 2nd ed., 1992.

E. E. Qian, P. T. de Zeeuw, R. P. van der Marel, and C. Hunter. Axisymmetric galaxy models with central black holes, with an application to M32. *MNRAS*, 274:602, 1995.

N. J. Rattenbury, S. Mao, V. P. Debattista, T. Sumi, O. Gerhard, and F. de Lorenzi. Proper motion dispersions of red clump giants in the galactic bulge: observations and model comparisons. *MNRAS*, 378:1165, 2007.

H.-W. Rix and S. D. M. White. Disks in elliptical galaxies. *ApJ*, 362:52, 1990.

H.-W. Rix, P. T. de Zeeuw, N. Cretton, R. P. van der Marel, and C. M. Carollo. Dynamical Modeling of Velocity Profiles: The Dark Halo around the Elliptical Galaxy NGC 2434. *ApJ*, 488:702, 1997.

A. J. Romanowsky and C. S. Kochanek. Dynamics of Stars and Globular Clusters in M87. *ApJ*, 553:722, 2001.

A. J. Romanowsky and C. S. Kochanek. Structural and Dynamical Uncertainties in Modelling Axisymmetric Elliptical Galaxies. *MNRAS*, 287:35, 1997.

A. J. Romanowsky, N. G. Douglas, M. Arnaboldi, K. Kuijken, M. R. Merrifield, N. R. Napolitano, M. Capaccioli, and K. C. Freeman. A Dearth of Dark Matter in Ordinary Elliptical Galaxies. *Science*, 301:1696, 2003.

R. H. Rubin. Models of H II regions - Heavy element opacity, variation of temperature. *ApJS*, 57:349, 1985.

D. Rusin and C. S. Kochanek. The Evolution and Structure of Early-Type Field Galaxies: A Combined Statistical Analysis of Gravitational Lenses. *ApJ*, 623:666, 2005.

G. B. Rybicki. Deprojection of Galaxies - how much can BE Learned. In P. T. de Zeeuw, editor, *IAU Symp. 127: Structure and Dynamics of Elliptical Galaxies*, page 397, 1987.

B. Ryden. The intrinsic shapes of elliptical galaxies. *ApJ*, 396:445, 1992.

A. F. Saaf. A Formal Third Integral of Motion in a Nearly Spherical Stellar System. *ApJ*, 154: 483, 1968.

N. Sambhus, O. Gerhard, and R. H. Méndez. Kinematic Evidence for Different Planetary Nebula Populations in the Elliptical Galaxy NGC 4697. *AJ*, 131:837, 2006.

A. E. Sansom, J. E. Hibbard, and F. Schweizer. The Cold and Hot Gas Content of Fine-Structure E and S0 Galaxies. *AJ*, 120:1946, 2000.

S. Schindler, B. Binggeli, and H. Böhringer. Morphology of the Virgo cluster: Gas versus galaxies. *A&A*, 343:420, 1999.

M. Schwarzschild. A numerical model for a triaxial stellar system in dynamical equilibrium. *ApJ*, 232:236, 1979.

C. Scorza and R. Bender. The internal structure of disky elliptical galaxies. *A&A*, 293:20, 1995.

C. Scorza and R. Bender. A disk in the elliptical galaxy NGC 3610. *A&A*, 235:49, 1990.

C. Scorza, R. Bender, C. Winkelmann, M. Capaccioli, and D. F. Macchetto. Stellar disks and embedded bars in early-type galaxies. I. 2-D photometric decomposition of 28 southern early-type galaxies. *A&AS*, 131:265, 1998.

J. A. Sellwood. Bars and Dark Matter Halo Cores. *ApJ*, 587:638, 2003.

J. L. Sersic. *Atlas de galaxias australes*. Cordoba, Argentina: Observatorio Astronomico, 1968, 1968.

K. L. Shapiro, M. Cappellari, T. de Zeeuw, R. M. McDermid, K. Gebhardt, R. C. E. van den Bosch, and T. S. Statler. The black hole in NGC 3379: a comparison of gas and stellar dynamical mass measurements with HST and integral-field data. *MNRAS*, 370:559, 2006.

S. Sigurdsson, L. Hernquist, and G. D. Quinlan. Models of Galaxies with Central Black Holes: Simulation Methods. *ApJ*, 446:75, 1995.

F. Simien and R. Michard. Isophotal contours of early-type galaxies. II - Axisymmetric-bulge and thin-disk approximations. *A&A*, 227:11, 1990.

D. N. Spergel, L. Verde, H. V. Peiris, E. Komatsu, M. R. Nolta, C. L. Bennett, M. Halpern, G. Hinshaw, N. Jarosik, A. Kogut, M. Limon, S. S. Meyer, L. Page, G. S. Tucker, J. L. Weiland, E. Wollack, and E. L. Wright. First-Year Wilkinson Microwave Anisotropy Probe (WMAP) Observations: Determination of Cosmological Parameters. *ApJS*, 148:175, 2003.

D. N. Spergel, R. Bean, O. Doré, M. R. Nolta, C. L. Bennett, J. Dunkley, G. Hinshaw, N. Jarosik, E. Komatsu, L. Page, H. V. Peiris, L. Verde, M. Halpern, R. S. Hill, A. Kogut, M. Limon, S. S. Meyer, N. Odegard, G. S. Tucker, J. L. Weiland, E. Wollack, and E. L. Wright. Three-Year Wilkinson Microwave Anisotropy Probe (WMAP) Observations: Implications for Cosmology. *ApJS*, 170:377, 2007.

T. S. Statler. The Shape and Orientation of NGC 3379: Implications for Nuclear Decoupling. *AJ*, 121:244, 2001.

T. S. Statler and T. Smecker-Hane. The Stellar Kinematic Fields of NGC 3379. *AJ*, 117:839, 1999.

D. Syer and S. Tremaine. Made-to-measure N-body systems. *MNRAS*, 282:223, 1996.

J. Thomas. *Ph.D. Thesis*, 2006.

J. Thomas, R. P. Saglia, R. Bender, D. Thomas, K. Gebhardt, J. Magorrian, E. M. Corsini, and G. Wegner. Regularized orbit models unveiling the stellar structure and dark matter halo of the Coma elliptical NGC 4807. *MNRAS*, 360:1355, 2005.

J. Thomas, R. P. Saglia, R. Bender, D. Thomas, K. Gebhardt, J. Magorrian, E. M. Corsini, and G. Wegner. *MNRAS*, 2007. submitted.

J. L. Tonry, A. Dressler, J. P. Blakeslee, E. A. Ajhar, A. B. Fletcher, G. A. Luppino, M. R. Metzger, and C. B. Moore. The SBF Survey of Galaxy Distances. IV. SBF Magnitudes, Colors, and Distances. *ApJ*, 546:681, 2001.

A. Toomre and J. Toomre. Galactic Bridges and Tails. *ApJ*, 178:623, 1972.

B. Tremblay and D. Merritt. Evidence From Intrinsic Shapes for Two Families of Elliptical Galaxies. *AJ*, 111:2243, 1996.

B. Tremblay, D. Merritt, and T. B. Williams. Planetary nebulae as probes of dark matter in NGC 3384. *ApJ*, 443:L5, 1995.

T. Treu and L. V. E. Koopmans. Massive Dark Matter Halos and Evolution of Early-Type Galaxies to z ˜ 1. *ApJ*, 611:739, 2004.

M. Valluri, D. Merritt, and E. Emsellem. Difficulties with Recovering the Masses of Supermassive Black Holes from Stellar Kinematical Data. *ApJ*, 602:66, 2004.

T. S. van Albada. Dissipationless galaxy formation and the R to the 1/4-power law. *MNRAS*, 201:939, 1982.

T. S. van Albada, J. N. Bahcall, K. Begeman, and R. Sancisi. Distribution of dark matter in the spiral galaxy NGC 3198. *ApJ*, 295:305, 1985.

G. van de Ven, C. Hunter, E. K. Verolme, and P. T. de Zeeuw. General solution of the Jeans equations for triaxial galaxies with separable potentials. *MNRAS*, 342:1056, 2003.

R. P. van der Marel and M. Franx. A new method for the identification of non-Gaussian line profiles in elliptical galaxies. *ApJ*, 407:525, 1993.

R. P. van der Marel, H.-W. Rix, D. Carter, M. Franx, S. D. M. White, and P. T. de Zeeuw. Velocity Profiles of Galaxies with Claimed Black-Holes - Part One - Observations of M31 M32 NGC3115 and NGC4594. *MNRAS*, 268:521, 1994.

E. K. Verolme, M. Cappellari, Y. Copin, R. P. van der Marel, R. Bacon, M. Bureau, R. L. Davies, B. M. Miller, and P. T. de Zeeuw. A SAURON study of M32: measuring the intrinsic flattening and the central black hole mass. *MNRAS*, 335:517, 2002.

J. V. Villumsen. Simulations of galaxy mergers. *MNRAS*, 199:493, 1982.

N. Visvanathan and A. Sandage. The color-absolute magnitude relation for E and S0 galaxies. I - Calibration and tests for universality using Virgo and eight other nearby clusters. *ApJ*, 216: 214, 1977.

S. von Hoerner. Die numerische Integration des n-Körper-Problemes für Sternhaufen. I. *Zeitschrift fur Astrophysik*, 50:184, 1960.

R. H. Wechsler, J. S. Bullock, J. R. Primack, A. V. Kravtsov, and A. Dekel. Concentrations of Dark Halos from Their Assembly Histories. *ApJ*, 568:52, 2002.

M. L. Weil and L. Hernquist. Global Properties of Multiple Merger Remnants. *ApJ*, 460:101, 1996.

S. D. M. White. Simulations of sinking satellites. *ApJ*, 274:53, 1983.

G. Wilson, N. Kaiser, G. A. Luppino, and L. L. Cowie. Galaxy Halo Masses from Galaxy-Galaxy Lensing. *ApJ*, 555:572, 2001.

F. Zwicky. Die Rotverschiebung von extragalaktischen Nebeln. *Helvetica Physica Acta*, 6:110, 1933.

LIST OF FIGURES

2.1 A high level flowchart describing NMAGIC . . . 18
2.2 The performance of NMAGIC . . . 20
2.3 Spherical target: Comparison of mass profiles . . . 22
2.4 Oblate target: Comparison of mass profiles . . . 23
2.5 Kinematic major and minor axis slits for the oblate models . . . 24
2.6 Target mass and A_{20} profiles for the triaxial models . . . 25
2.7 Line-of-sight velocity field of the rotating triaxial particle model . . . 26
2.8 Time evolution of χ^2 and a set of particle weights . . . 28
2.9 Comparison of the spherical model with target observables . . . 29
2.10 Histogram of the particle weights . . . 30
2.11 Radial density profiles and differential energy distributions of a spherical model 32
2.12 Internal kinematics of a speherical model . . . 33
2.13 Radial density profiles and differential energy distributions . . . 34
2.14 Histogram of the particle weights obtained from different initial conditions . . . 35
2.15 The mass and mass A_{20} profiles for the oblate models . . . 36
2.16 Mass-weighted higher order moments along the major and minor axes . . . 37
2.17 LOSVDs along the major axis and minor axis . . . 38
2.18 Distribution of particle weights in the final oblated models . . . 39
2.19 Particle weight distributions for the oblate models . . . 40
2.20 Mass and A_{20} profiles for a triaxial experiment . . . 41
2.21 The difference between kinematics of the non-rotating triaxial models . . . 42
2.22 The difference between kinematics of the rotating triaxial models . . . 43
2.23 Difference of the line-of-sight velocity fields for the triaxial models . . . 44

3.1 The photometry of NGC 4697 . . . 49
3.2 Isophote parameter profiles of NGC 4697 compared with the deprojection . . . 51
3.3 Major and minor axis The kinematics of NGC 4697 . . . 52
3.4 Comparison between the different absorption line kinematics of NGC 4697 . . . 52
3.5 Schematic view of the slit setup . . . 54
3.6 The positions and velocities of the PN sample of NGC 4697 . . . 55
3.7 Seeing convolution test . . . 58
3.8 Comparison of the surface brightness of NGC 4697 with the γ-model . . . 62
3.9 Comparison of the kinematic of NGC 4697 and an isotropic rotator model . . . 63
3.10 Entropy tests for NGC 4697 . . . 64
3.11 Particle model fit to the isotropic rotator mock kinematic data . . . 65
3.12 Intrinsic velocity moments of the isotropic rotator particle . . . 67
3.13 Quality of the particle model fit to the isotropic rotator input model . . . 68
3.14 Direct mass-to-light ratio fits with NMAGIC . . . 68
3.15 Circular velocity curves of the potentials used for NGC 4697 . . . 69
3.16 Comparison of the photometric constraints with the final models of NGC 4697 72
3.17 Comparison of the models of NGC 4697 to the absorption line kinematic data . 73

3.18 Comparison of the PNe kinematic data of NGC 4697 with particle models . . . 74
3.19 Internal velocity moments for models of NGC 4697 74

4.1 Combined photometry of NGC 3379 80
4.2 Iso-density contours of the deprojected luminosity distribution of NGC 3379 . . 81
4.3 Schematic view of the positions with kinematic data of NGC 3379 82
4.4 Comparison of the SAURON data with the major axis kinematics. 84
4.5 Comparison of the SB profile of the mock galaxy with NGC 3379 88
4.6 Comparison of the LOSVD kinematics of mock galaxy with those of NGC 3379 89
4.7 SAURON mock kinematic data for a spherical isotropic γ-model 89
4.8 Entropy tests for NGC 3379 90
4.9 Internal kinematics of the isotropic target galaxy and its particle realization . . 91
4.10 Recovering the mass-to-light ratio of the mock galaxy 92
4.11 Circular velocity curves for the potentials used in the modelling of NGC 3379 . 93
4.12 Comparison of the SB profiles of the spherical models with the NGC 3379 . . . 95
4.13 Symmetrized SAURON kinematic data for NGC 3379 96
4.14 Comparison of the slit kinematic data of NGC 3379 with particle models 98
4.15 Comparison of the spherical models with the PN.S data 99
4.16 Intrinsic kinematics of the final spherical models 99
4.17 Edge-on SB contours of the kinematically deprojected oblate model 100
4.18 Comparison of the axisymmetric models with the SAURON data for NGC 3379 102
4.19 Comparison of oblate models with the symmetrized slit data 104
4.20 Comparison of the axisymmetric models with the PN.S data 105
4.21 Enclosed DM fraction as function of radius for the final particle models 105
4.22 Intrinsic kinematics of the final oblate models 106
4.23 χ^2 values of various models for NGC 3379 with respect to the PNe data 108
4.24 Comparison of the PNe LOSVDs in circular annuli with particle models 109
4.25 Relative likelihoods as a function of the model circular velocity at $7R_e$ 110

A.1 CIC scheme use in potential computation 120
A.2 Potential contours 121
A.3 Force resolution 122
A.4 Energy angular momentum space for a Hernquist distribution function 123
A.5 Density evolution of a spherical particle model made from distribution function 124
A.6 Time evolution of energy of a particle on an almost radial orbit 125
A.7 Schematic representation of the parallelization of NMAGIC 126

B.1 Isophotal parameters of NGC 4697 128

LIST OF TABLES

2.1 Tests of NMAGIC with model names and parameters 27

3.1 Table of parameters and fit results for models of NGC 4697 70
3.2 Table of parameters and fit results for models of NGC 4697 70

4.1 Table of parameters and fit results for models of NGC 3379 94
4.2 Table of parameters and χ^2-fit results for oblate models of NGC 3379 101
4.3 Likelihood values for the PN data in the spherical models of NGC 3379 108

B.1 The kinematics of NGC 4697 along the major axis 132
B.2 The kinematics of NGC 4697 along the minor axis 133

ACKNOWLEDGEMENTS

To write a PhD thesis is a tedious and sometimes a complicated undertaking and would be hardly possible without the (mental) support from other people. At the completion of this work, it is therefore a great pleasure to thank the people who have supported me during my PhD thesis. First, I want to thank my girlfriend Sara for her patience for always being willing to listen to the problems arisen during the PhD. I thank my parents and my brother for supporting me during my studies and during my PhD. Another thank goes to Groseli for her financial support during the last few years.

I thank Ortwin Gerhard for giving me the opportunity to write a PhD thesis in astronomy, for the scientific discussions and his effort in working through the publications. Further, I want to thank Victor P. Debattista for introducing me to FORTRAN.

Another thank goes to my colleagues Lodovico Coccato, Ayse Ulubay Siddiki and Payel Das for reading parts of this thesis.